California AHMCT Program
University of California at Davis
California Department of Transportation

REFINEMENTS OF A ROBOTIC SYSTEM FOR STENCILING OF GENERAL ROADWAY MARKINGS

Bahram Ravani, Principal Investigator
Jeffrey Hemenway, Nina Patarinska, Sean Steffensen

AHMCT Research Report
UCD-ARR-00-09-30-01

Final Report of Contract
65A0038

September 30, 2000

* This report has been prepared in cooperation with the State of California, Business and Transportation Agency, Department of Transportation and is based on work supported by Contract Number RTA 65A0038 through the Advanced Highway Maintenance and Construction Technology Research Center at the University of California at Davis.

Technical Documentation Page

1. Report No.	2. Government Accession No.	3. Recipient's Catalog No.
FHWA/CA/NT-2003/01		

4. Title and Subtitle	5. Report Date
Refinements of a Robotic System for Stenciling of General Roadway Markings	September 30, 2000
	6. Performing Organization Code
7. Author(s): Bahram Ravani, P. I.	8. Performing Organization Report No. UCD-ARR-00-09-30-01
9. Performing Organization Name and Address AHMCT Center UCD Dept of Mechanical & Aeronautical Engineering Davis, California 95616-5294	10. Work Unit No. (TRAIS) 11. Contract or Grant IA65A0038
12. Sponsoring Agency Name and Address California Department of Transportation P.O. Box 942873, MS#83 Sacramento, CA 94273-0001	13. Type of Report and Period Covered Final Report March 1999 - September 2000 14. Sponsoring Agency Code

15. Supplementary Notes

16. Abstract

The purpose of work was to refine and evaluate the feasibility of using a long reach robotic arm for use in roadway markings and stenciling operations. This was part of an effort to minimize the traffic exposure for the working crew.

The scope of work involved testing of the system and research into modifications that would be needed before using a long-reach robot arm developed for highway applications. It was determined that the long reach robotic arm required modifications due to the coupling effects of the dynamics and the end point accuracy required for proper edge definition in painting of roadway markings. Modifications were performed in the hydraulic system and in the control algorithm to improve the performance of the robot. The results were experimentally demonstrated with the robot without an end-effector closely following roadway markings. In addition, the paper design of a new end-effector was completed that used an innovative tilt mechanism for the painting gun.

17. Key Words	18. Distribution Statement
Stenciling, articulated robotic system, roadway markings, painting, robotic arm; painting end-effector	No restrictions. This document is available to the public through the National Technical Information Service, Springfield, Virginia 22161.

20. Security Classif. (of this report)	20. Security Classif. (of this page)	21. No. of Pages	22. Price
Unclassified	Unclassified	347	

Form DOT F 1700.7 (8-72) (PF V2.1, 6/30/92) Reproduction of completed page authorized

ABSTRACT

This final report documents the Advanced Highway Maintenance and Construction Technology (AHMCT) Research Center's efforts to refine a robotic system for stenciling of general roadway markings. In accordance with the AHMCT's mission to develop and deploy highway technology that saves lives and reduces costs, this was an effort to minimize the traffic exposure for the working crew. Over a two year period, a research prototype of an articulated robotic system for potential use in the process of stenciling roadway markings was developed. At the end of the project, the deliverable was a demonstration of the robotic arm (without the end-effector) capable of producing markings with end-point deviations within an inch with no abrupt changes and the paper design of an end-effector performing its function with proper coordination with the robotic arm without degrading the end-point accuracy of the system.

EXECUTIVE SUMMARY

This research project deals with refinements of a general robotic system for use in roadway markings and stenciling operations. Painted roadway markings are usually applied using a mechanical stenciling procedure by the maintenance crew working on the roadway surface. The process involves transverse marking of the pavement with word and symbol markings, limit lines, cross walk lines, shoulder markings, parking stall markings, railroad crossing markings and so on. The operation involves laying down mechanical stencils, manually painting through the stencils, and finally removing the mechanical stencils. The operation exposes the roadway crew to on-going traffic requiring them to perform delicate work directly on the roadway.

At the AHMCT center, we have developed (over a two year period) a research prototype of an articulated robotic system for potential use in the process of stenciling roadway markings. The testing of the system had indicated that modifications are necessary before the system can be considered for potential application on the roadway. Test data indicated that there are a minimum of four areas where the articulated robotic system needed modifications due to the coupling effects of the dynamics and the end point accuracy required for proper edge definition in painting of roadway markings. The first area was related to the dynamic effects of the hydraulics used to power and control the robotic arm. We had found that flow of hydraulic fluid through the lines produced dynamic effects that influenced the end point accuracy as well as the waviness of the paint markings, making the system performance not desirable. The second item was handling the undesirable structural dynamics of the arm due to its long reach articulated design needed to reach two lanes of the roadway as specified in the original design specifications. The third area was the control system that needed to be modified since end-point trajectories showed undesirable performance. Finally, the fourth area was the new design of the end-effector. The end-effector control for its rotational axis used a stepper motor design producing less than desirable accuracy in tracking since it was not a servo drive system. The structural design of the end-effector also did not have the necessary stiffness for rapid motions around curved portions of a trajectory in painting highway markings. There was a need therefore for modifications of the end-effector design to improve its control system performance as well as its structural performance.

The hydraulic system was modified by adding a hydraulic fluid accumulator to improve power delivery to the hydraulic actuators. Additionally, supply check valves were inserted to minimize fluid back-flow between the actuators. Testing the system it was found that there is a need to provide a damped motion for the arm swing. Counter balanced valves were therefore added on the exhaust side of the motors to provide the needed damping. These modifications reduced and eliminated the undesirable dynamics of the hydraulic fluids degrading system tracking and painting performance.

Initially we thought that waviness observed in the edge definition for roadway markings produced by the robotic arm could be eliminated or reduced by counterbalancing the robotic arm. We thought that the control system cannot properly keep track of all the dynamics due to the high weight of the arm when it is painting in its articulated position. A four spring counterbalance system with friction plates and swivel mounts was designed and implemented on the robotic arm. The arm was used to draw the letter S which exerts the highest demand on system dynamics. Testing the system, it was found that although counterbalancing does improve the tracking accuracy the waviness error still appeared in tracking the letter S. It was therefore decided counterbalancing would not be used in the robotic arm.

Testing and trouble shooting the overall control system of long reach stenciling robot constituted most of the planned effort in this project. It involved testing the control

system of the arm looking at the performance of the actuators, sensors, and the control software. In this part of the project the arm was tested without paint distribution using a felt pen at the end of it for making marks on sheets of paper for evaluation. We were seeking a desired accuracy of less than ¼ of an inch with no abrupt deviations. We found that the entire control system for the arm had to be changed from a dedicated microprocessor type control to a PC based system with QNX real time operating system. This new PC architecture enables us to develop a robust method for control of the arm based on scientific technique developed as part of a basic research task order within AHMCT research center. This involved using a time delayed control system where the system disturbances could be modeled and fed back into the overall control system therefore reducing tracking error. Testing indicated that the letter S could be drawn with high tracking accuracy. The waviness error was found to be less than ¼ inch throughout the trajectory. A new interface board was developed and the control system was implemented and demonstrated showing the feasibility of this approach.

The early end-effector of the robotic system utilized a stepper-motor to change the orientation of the paint spray fan. This stepper-motor setup held a maximum rotation rate of approximately 0.25 revolutions/second that limited the linear speed of the arm during painting of tight curves. An example of a tight curve is the top and bottom of the letter "O". Additionally, the end-effector unit itself had undesirable rigidity and vibratory characteristics that limited the accuracy of painted marks. The end effector was modified to a servo based unit. After the modification was performed a notification was received by AHMCT from a company in the Bay area that the system infringed on their patent on using a rotational joint to provide a tilting motion of the spray gun for painting a surface. A redesign of the end effector was therefore considered where a rotational joint would not be used to provide the necessary tilting motion for the spray gun. The detailed design of the new system was developed that would use an innovative four bar linkage design with a linear motion providing the tilt type action for the end-effector. The ground link of the four bar mechanism is attached rigidly to the arm of the robot. The platform link carries the spray gun and its motion supplies the tilt necessary to paint uniformly when the stenciling process requires sharp turns. Special consideration of the link lengths during the initial design led to the synthesis of a special four bar mechanism known as Robert's Mechanism. Robert's Mechanism possess a near straight line motion of a point located upon the platform link. The straight line motion was exploited to create a direct way of controlling the motion of the four bar mechanism using a ball screw mechanism. A servo motor with encoder feedback drives the rotation of the ball screw. The servomotor drive interfaces with an onboard Intel personal computer to determine proper position commands for the tilt mechanism servomotor based upon the trajectory planning and current positions of the other robotic joints.

The deliverables in this project involved a demonstration of the robotic arm (without the end-effector) capable of producing markings with end-point deviations within ¼ of an inch with no abrupt changes and the design of an end-effector performing its function with proper coordination with the robotic arm without degrading end-point tracing accuracy of the system.

TABLE OF CONTENTS

DISCLAIMER/DISCLOSURE

The research reported herein was performed as part of the Advanced Highway Maintenance and Construction Technology (AHMCT) Research Center, within the Department of Mechanical and Aeronautical Engineering at the University of California, Davis, and the New Technology and Research Program at the California Department of Transportation. It is evolutionary and voluntary. It is a cooperative venture of local, state and federal governments and universities.

The contents of this report reflect the views of the author(s) who is (are) responsible for the facts and the accuracy of the data presented herein. The contents do not necessarily reflect the official views or policies of the State of California, the Federal Highway Administration, or the University of California. This report does not constitute a standard, specification, or regulation.

Section I:

Introduction, Hydraulic System Improvements, Structural Dynamics and Control System Improvements, End-Effector Improvements, Deliverables

Introduction

The mechanical design and construction of the AHMCT's Long Reach Roadway Sign Stenciling Robotic Arm was completed in a previous contract. During operational testing, it was determined that the edge definition accuracy in painting certain roadway markings exceeded the path following accuracy of the robotic arm. This project was aimed at providing modifications to address the path following accuracies of the robotic arm and developing an operational end-effector for the robotic arm.

Painted roadway markings are usually applied by roadway maintenance crew members using a mechanical stenciling procedure. The process involves transverse marking of the pavement with word and symbol markings, limit lines, cross walk lines, shoulder markings, parking stall markings, railroad crossing markings and so on. The operation involves laying down mechanical stencils, manually painting through the stencils, and finally removing the mechanical stencils. The operation exposes the roadway crew to on-going traffic requiring them to perform delicate work directly on the roadway. In an effort to minimize the traffic exposure to the working crew, AHMCT research center at the University of California at Davis have started the development of a research prototype of a long reach robotic system for roadway sign stenciling. This roadway sign stenciling robotic arm is shown in Figure 1 and is intended to remove the working crew from the roadway surface during the process of painting roadway

Figure 1. A view of AHMCT's roadway sign stenciling robotic arm.

markings. This robotic system was developed over a two year period as a research prototype for evaluation of using long reach robotic arm technology in painting roadway markings.

During operational testing, it was observed that there was coupling of the dynamics associated with long reach articulated structure of the robot and its end-effector and that associated with the movement of the hydraulic fluid used to control and power the arm motion. This project was therefore launched to assess some of these issues and develop the control and design technologies that would pave the way for use of articulated robotic arm technology for roadway maintenance operations in general and painting roadway markings in particular. At AHMCT research center, we have successfully developed, in the past, gantry type robot technology for painting on the roadway surface [1-2]. Such gantry technology has also been developed commercially [3-5]. There has however been no reported development in using articulated arm technology for such a purpose. The gantry robotic technology has a major drawback in its utility for roadway maintenance applications requiring long reach such as painting within two roadway lanes. The drawback is really associated with the size of the gantry system making its foot print comparable to its workspace. This makes it difficult to have the robotic system carried by a vehicle for deployment on the roadway. The articulated system however can be easily mounted and carried on the maintenance vehicle as shown in the AHMCT's robot design in Figure 1.

In this project we have explored modification of the robotic system of Figure 1 in four areas namely hydraulic system improvements, structural design of the system, control system design, and finally the design of an operational end-effctor. These are described in the remaining of this report.

Hydraulic System Improvements:

In the initial testing of the AHMCT long reach robotic arm, we found that flow of hydraulic fluid through the lines produced dynamic effects that influenced the end point accuracy as well as the waviness of the paint markings, making the system performance not desirable. The hydraulic system was therefore modified by adding a hydraulic fluid accumulator to improve power delivery to the hydraulic actuators. This smoothed out pressure variations in the line. Additionally, supply check valves were inserted to minimize fluid back-flow between the actuators. Testing the system it was found that there is a need to provide a damped motion for the arm swing. Counter balanced valves were therefore added on the exhaust side of the motors to provide the needed damping. A schematic diagram of the modified hydraulic system for the robotic arm is shown in Figure 2. This figure shows the complete system including the hydraulic sub-system used for stabilizer feet on the maintenance vehicle used to fix the position of the maintenance truck while the arm is in operations (see Figure 1). These modifications reduced and eliminated the undesirable dynamics of the hydraulic fluids improving system tracking and painting performance. The improvements however were not sufficient to meet the design specifications of the robot as being capable of producing markings with end-point deviations within ¼ of an inch with no abrupt changes.

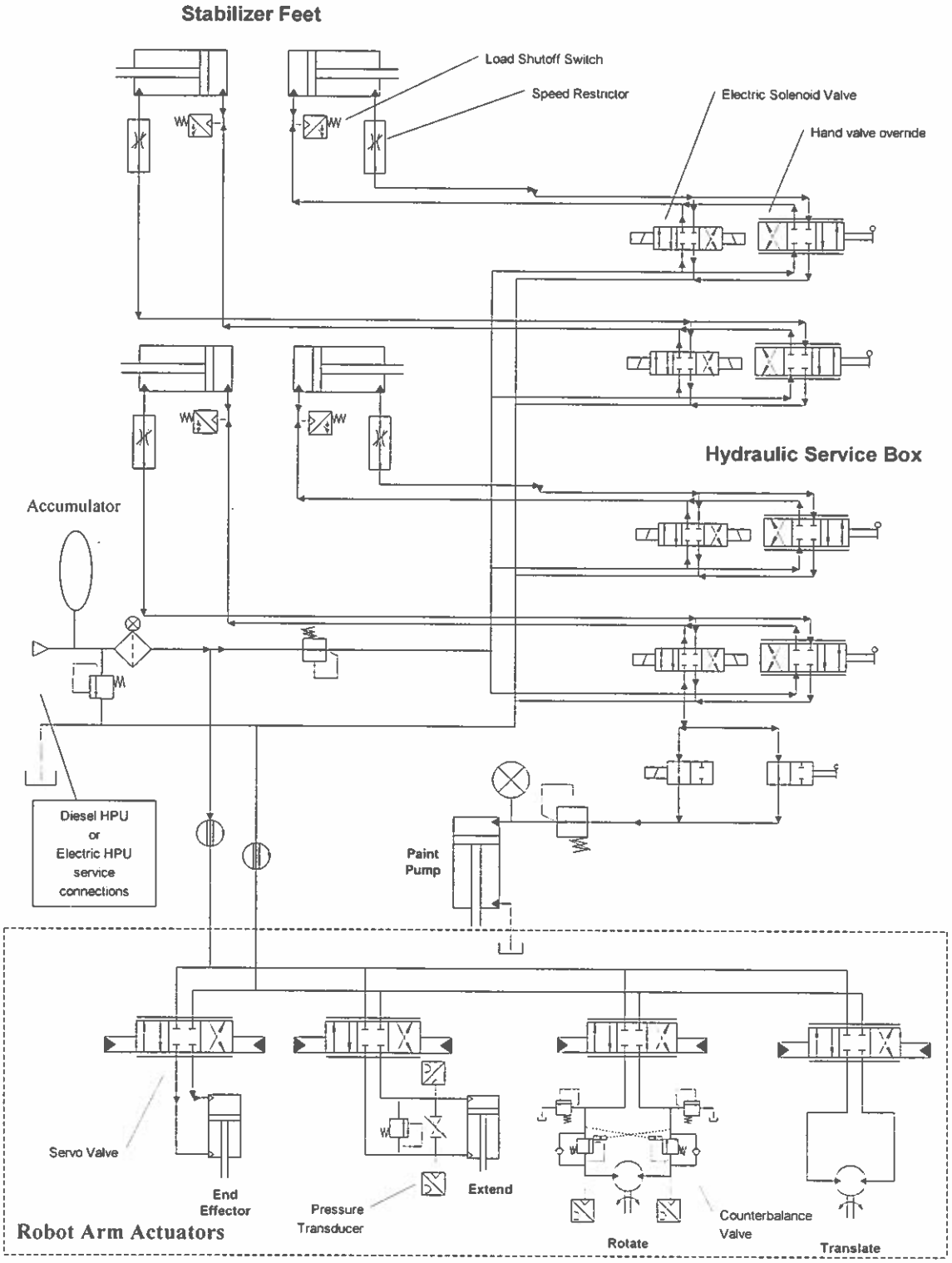

Figure 2. A schematic of the Hydraulic System of the AHMCT's Sign Stenciling Robotic Arm.

Structural Dynamics and Control System Improvements

Initially we thought that waviness observed in the edge definition for roadway markings produced by the robotic arm could be eliminated or reduced by counterbalancing the robotic arm. We thought that the control system cannot properly keep track of all the dynamics due to the high weight of the arm when it is painting in its articulated position. A four spring counterbalance system with friction plates and swivel mounts was designed and implemented on the robotic arm. The arm was used to draw the letter S which exerts the highest demand on system dynamics. Testing the system, it was found that although counterbalancing does improve the tracking accuracy the waviness error still appeared in tracking the letter S. It was therefore decided counterbalancing would not be used in the robotic arm. The details of the work on counterbalancing and the test results associated with it are documented in the attached appendix A.

Testing and trouble shooting the overall control system of long reach stenciling robot constituted most of the planned effort in this project. It involved testing the control system of the arm looking at the performance of the actuators, sensors, and the control software. In this part of the project, the arm was tested without paint distribution using a felt pen at the end of it for making marks on sheets of paper for evaluation. We were seeking a desired accuracy of less than ¼ of an inch with no abrupt deviations. We found that the entire control system for the arm had to be changed from a dedicated microprocessor type control to a PC based system with QNX real time operating system. This new PC architecture enables us to develop a robust method for control of the arm based on scientific technique developed as part of a basic research task order within AHMCT research center. This involved using a time delayed control system where the system disturbances could be modeled and fed back into the overall control system therefore reducing tracking error. Testing indicated that the letter S could be drawn with high tracking accuracy. The waviness error was found to be less than ¼ inch throughout the trajectory. A new interface board was developed and the control system was implemented and demonstrated showing the feasibility of this approach. The details of the scientific aspects of this method are described in the attached appendix B. A user guide was also developed for the final control system implemented on the robotic arm. This user guide is provided as a separate document entitled: Controller_User_Guide and it is attached.

End-Effector Improvements

The current end-effector of the robotic system utilized a stepper-motor to change the orientation of the paint spray fan. This stepper-motor setup has a maximum rotation rate of approximately 0.25 revolutions/second that limited the linear speed of the arm during painting of tight curves. An example of a tight curve is the top and bottom of the letter "O". Additionally, the end-effector unit itself had undesirable rigidity and vibratory characteristics that limited the accuracy of painted marks. The end effector was modified to a servo based unit. After the modification was performed a notification was received

by AHMCT from a company in the Bay area that the system infringed on their patent on using a rotational joint to provide a tilting motion of the spray gun for painting a surface. A redesign of the end effector was therefore considered where a rotational joint would not be used to provide the necessary tilting motion for the spray gun. The detailed design of the new system was developed that uses an innovative four bar linkage design with a linear motion providing the tilt type action for the end-effector. The new end-effector design is depicted in Figure 3 below.

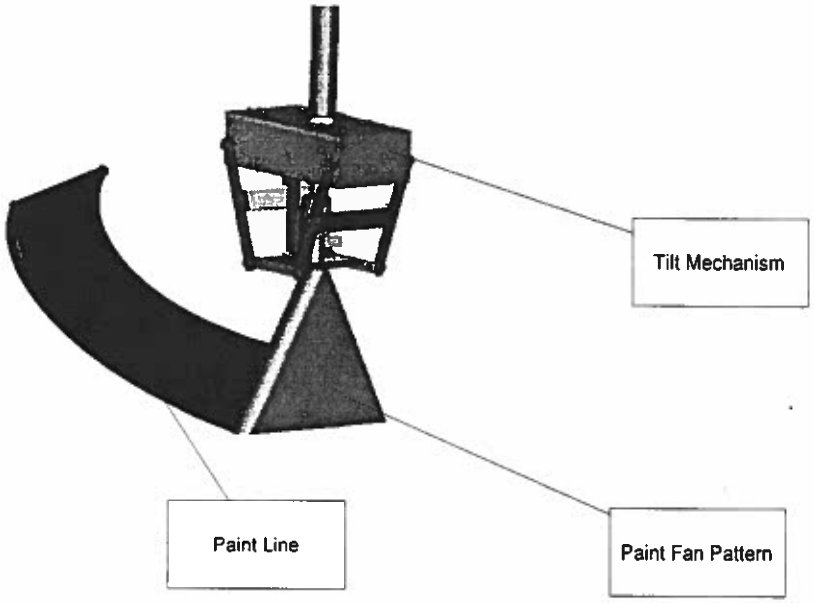

Figure 3. The new proposed End-Effector Design using Four Bar Linkages to achieve a tilt motion for the paint spray gun.

Deliverables

The deliverables in this project involved a demonstration of he robotic arm (without the end-effector) capable of producing markings with end-point deviations within ¼ of an inch with no abrupt changes and the design of an end-effector performing its function with proper coordination with the robotic arm without degrading end-point tracing accuracy of the system. It also included the user guide and the documentation for the controller as attached as well as this final report.

Section II:

Nonlinear control of the AHMCT's Long-Reach Roadway Sign Stenciling Robotic Arm

Nonlinear Control of the AHMCT's Long-Reach Roadway Sign Stenciling Robotic Arm

1 Introduction

The mechanical design and construction of the AHMCT's Long Reach Roadway Sign Stenciling Robotic Arm was completed in a previous contract. During operational testing, it was detemined that the edge defintiion accuracy in painting certain roadway markings exceed the path following accuracy of the robotic arm. As part of a new project aimed at developing the end effector and addressing these accuracy problems, development of a more advanced nonlinear control system was undertaken for this robotic system. This report describes the details of the new control system. This control system was implemented on the robotic arm and showed that it overcomes all previous inaccuracy problems.

The kinematic structure of the mechanism used in the long reach stenciling robotis arm is shown in Figure 1. This is a pantograph mechanism with a rotatable base. The use of the pantograph mechanism allows localizing the actuators for the tip motion at the base and there fore reducing the overall weight of the long reach portionof the system. It also provides for amplification of the motion at the end as compared to the actuator stroke needed at the base. The stronke at the base is the input to the system and is the linear motion q_2 of the hydraulic cylinder, which yields a scaled linear motion of the end-effector E in the same direction. Together with the rotation q_1 of the hydraulic motor the System has two degrees of freedom i.e. free translational motion of the end-effector E in a plane perpendicular to the axis of the hydraulic motor.

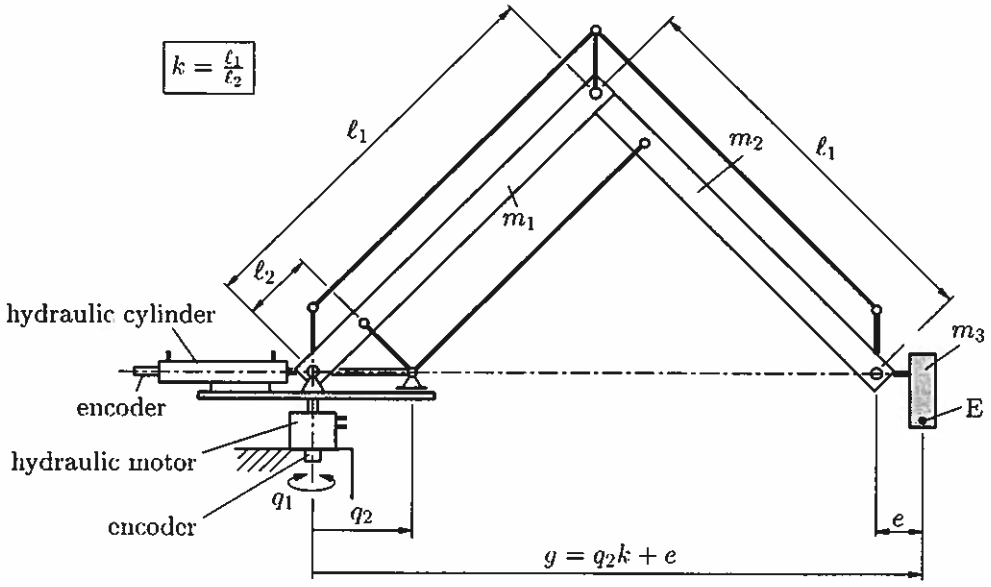

Figure 1: System

2 Hydraulic System

The hydraulic system for the long reach stenciling robot consists of an oil supply unit and two actuator units (hydraulic cylinder and hydraulic motor), which are shown in Figure 2. For the development of the new control system, it is assumed, that the oil supply unit always provides a constant pressure p_0. Each of the actuator units consists of an actuator, a servovalve and two relief valves for the two sides A and B of the actuator. For the implementation of the new controller each actuator unit has two pressure-transducers, again for side A and B.

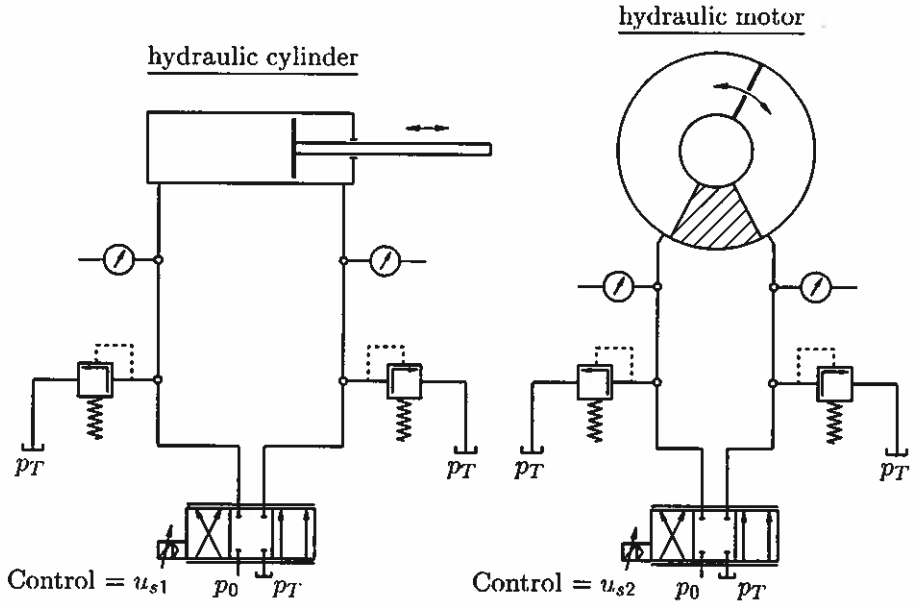

Figure 2: hydraulic actuator units

3 Dynamics of the several Components

3.1 Equations of Motion for the Mechanical System

As shown in Figure 3, for the derivation of the equations of motion it is assumed, that only the main-arms of the robot and the end-effector have mass properties $(m_1, \Theta_{S_1}, m_2, \Theta_{S_2}, m_3, \Theta_{S_3})$. The other masses are neglected, because they are very small in relation to the main-arm-masses.

The investigation of the kinematics in the x, y, z coordinate system (see Figure 3) yields the following relations:

$$\mathbf{r}_1 = \frac{1}{4}\begin{bmatrix} kq_2\cos q_1 \\ kq_2\sin q_1 \\ k\sqrt{4\ell_2^2 - q_2^2} \end{bmatrix} ; \mathbf{r}_2 = \frac{1}{4}\begin{bmatrix} 3kq_2\cos q_1 \\ 3kq_2\sin q_1 \\ k\sqrt{4\ell_2^2 - q_2^2} \end{bmatrix} ; \mathbf{r}_3 = \begin{bmatrix} (kq_2 + e)\cos q_1 \\ (kq_2 + e)\sin q_1 \\ -f \end{bmatrix} \quad (1)$$

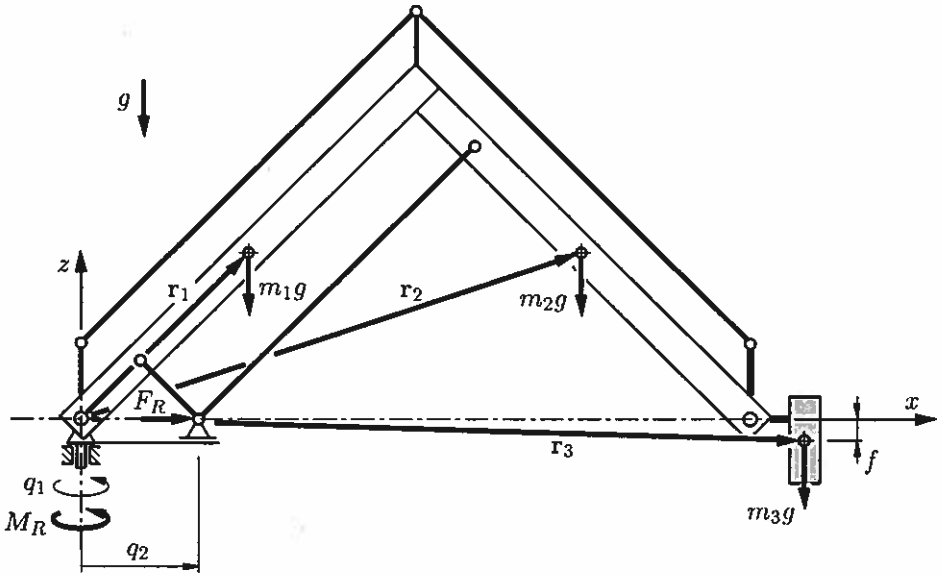

Figure 3: system for equations of motion

$$\boldsymbol{\omega}_1 = \frac{1}{t}\begin{bmatrix} -\dot{q}_1 q_2\sqrt{4\ell_2^2 - q_2^2} \\ 2\ell_2\dot{q}_2 \\ \dot{q}_1(4\ell_2^2 - q_2^2) \end{bmatrix} ; \boldsymbol{\omega}_2 = \frac{1}{t}\begin{bmatrix} \dot{q}_1 q_2\sqrt{4\ell_2^2 - q_2^2} \\ -2\ell_2\dot{q}_2 \\ \dot{q}_1(4\ell_2^2 - q_2^2) \end{bmatrix} ; \boldsymbol{\omega}_3 = \begin{bmatrix} 0 \\ 0 \\ \dot{q}_1 \end{bmatrix} \tag{2}$$

with $t = 2\ell_2\sqrt{4\ell_2^2 - q_2^2}$.

The gravity forces decomposed in the x, y, z system are:

$$\mathbf{F}_1 = \begin{bmatrix} 0 \\ 0 \\ -m_1 g \end{bmatrix} ; \mathbf{F}_2 = \begin{bmatrix} 0 \\ 0 \\ -m_2 g \end{bmatrix} ; \mathbf{F}_3 = \begin{bmatrix} 0 \\ 0 \\ -m_3 g \end{bmatrix} \tag{3}$$

The next step is to formulate the Lagrange Equations of the Second Class

$$\frac{d}{dt}\left(\frac{\partial T}{\partial \dot{q}_j}\right) - \frac{\partial T}{\partial q_j} = Q_j \quad ; \quad j = 1, 2 \tag{4}$$

where q_j represents the components of the vector $\mathbf{q} = [q_1, q_2]^{\mathrm{T}}$ of generalized coordinates of the system.

To evaluate this equation the kinetic energy T and the generalized forces Q have to be calculated.

Kinetic energy:

$$T = \frac{1}{2}\sum_{i=1}^{3} m_i \dot{\mathbf{r}}_i^2 + \frac{1}{2}\sum_{i=1}^{3} \boldsymbol{\omega}_i^{\mathrm{T}} \Theta_{Si} \boldsymbol{\omega}_i \tag{5}$$

Generalized forces:

$$\delta A = \sum_{i=1}^{3} F_i \delta r_i + M_R \delta q_1 + F_R \delta q_2 \tag{6}$$

On the other hand

$$\delta A = \sum_{j=1}^{2} Q_j \delta q_j \tag{7}$$

Comparison of the coefficients between equations (6) and (7) yields Q_1 and Q_2. F_R and M_R (see Figure 3) are the resulting force and moment respectively acted from the hydraulic actuators to the mechanical system.

Evaluating equation (4), the equations of motion can be brought in the following form:

$$\mathbf{A}(\mathbf{q})\ddot{\mathbf{q}} + \mathbf{C}(\mathbf{q}, \dot{\mathbf{q}})\dot{\mathbf{q}} + \mathbf{g}(\mathbf{q}) = \boldsymbol{\tau} - \mathbf{J}^{\mathrm{T}}\mathbf{f}_e + \mathbf{d} \tag{8}$$

with

$\mathbf{A}$	:	mass inertia matrix
$\mathbf{C}$	:	matrix of Coriolis and centrifugal terms
$\mathbf{g}$	:	vector of generalized gravity forces
$\boldsymbol{\tau}$	:	vector of generalized joint forces; $\boldsymbol{\tau} = [M_R, F_R]^{\mathrm{T}}$
$\mathbf{f}_e$	:	vector of external forces on the end-effector
$\mathbf{d}$	:	vector of unknown generalized disturbance forces

For the simulation of the system it is assumed, that f_e and d are negligible.

3.2 Hydraulic Actuators

The dynamics of the hydraulic components are described in a lot of publications. The here specified equations are from [2]. Because of the similarity between hydraulic cylinders and motors, here only the equations for the hydraulic cylinder are discussed. The cylinder shown in Figure 4 produces a resulting force F_R

$$F_R = (p_A - \alpha p_B)A - F_F \tag{9}$$

with

p_A	:	pressure in chamber A
p_B	:	pressure in chamber B
A	:	piston area in chamber A
α	:	ratio of piston areas of chambers A and B
F_F	:	friction force

The model of the friction force F_F consists of a constant *Coulomb friction* F_R, an exponentially decreasing part of *stiction* F_H and a part $d\dot{x}$ *viscous friction*:

$$F_F = d\dot{x} + F_C \operatorname{sign}(\dot{x}) + F_H \exp\left(-\frac{|\dot{x}|}{c}\right) \operatorname{sign}(\dot{x}) \tag{10}$$

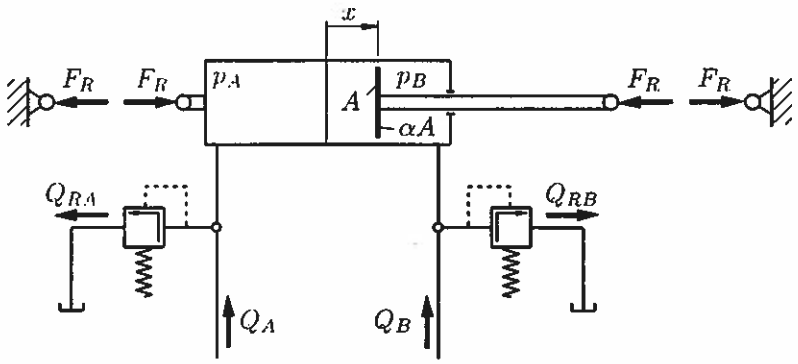

Figure 4: hydraulic actuators

Neglecting leakage in the actuator, the differential equations for the pressure variables p_A and p_B are:

$$\dot{p}_A = \frac{E'_{oil}(p_A)}{V_{0A} + Ax} \left[Q_A - A\dot{x} - Q_{DA}(p_A) \right] \tag{11}$$

$$\dot{p}_B = \frac{E'_{oil}(p_B)}{V_{0B} - \alpha Ax} \left[Q_B + \alpha A\dot{x} - Q_{DB}(p_B) \right] \tag{12}$$

with

Q_A, Q_B	:	flows from the servovalve to chamber A and B respectively (see section 3.3)
E'_{oil}	:	substitute fluid bulk modulus (see equation (13))
V_{0A}, V_{0B}	:	oil volume of chamber A and B by $x = 0$ including pipe and dead volumina
Q_{DA}, Q_{DB}	:	oil flows through relief valves on side A and B (see equation (14))

$$E'_{oil} = \frac{1}{2} E_{oil} \log \left(100 \left(0.9 \frac{p_c}{p_\kappa} + 0.03 \right) \right) \tag{13}$$

$$Q_{Dc} = \begin{cases} G(p_c - p_{max}) & \text{for } p_c > p_{max} \\ 0 & \text{for } p_c \leq p_{max} \end{cases} \tag{14}$$

with

E_{oil}	:	fluid bulk modulus of pure oil
p_κ	:	pressure constant
G	:	flowgain
p_{max}	:	maximum pressure of relief valve
index c	:	for chamber A or B

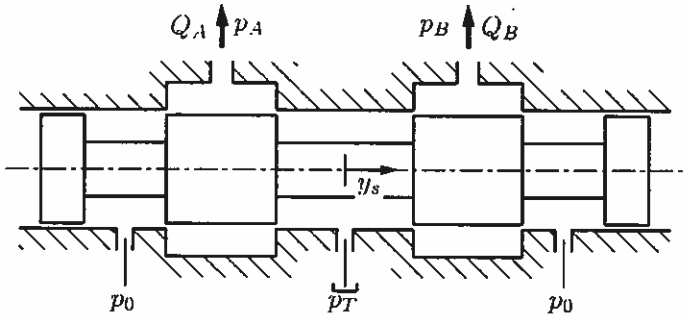

Figure 5: Servovalve

3.3 Servovalve

Neglecting leakage in the valve, the flow Q_A and Q_B into sides A and B of the actuator is

$$Q_A = \begin{cases} B_v y_s \operatorname{sign}(p_0 - p_A)\sqrt{|p_0 - p_A|} & \text{for } y_s \geq 0 \\ B_v y_s \operatorname{sign}(p_A - p_T)\sqrt{|p_A - p_T|} & \text{for } y_s < 0 \end{cases} \tag{15}$$

$$Q_B = \begin{cases} -B_v y_s \operatorname{sign}(p_B - p_T)\sqrt{|p_B - p_T|} & \text{for } y_s \geq 0 \\ -B_v y_s \operatorname{sign}(p_0 - p_B)\sqrt{|p_0 - p_B|} & \text{for } y_s < 0 \end{cases} \tag{16}$$

with

B_v	:	valve orifice coefficient
y_s	:	spool position (see Figure 5)
p_A, p_B	:	pressures in chamber A and B
p_0	:	supply pressure
p_T	:	reservoir pressure

As in [4], the spool valve displacement y_s is related to the control input u_s by a first-order system given by

$$\tau_s \dot{y}_s = -y_s + K_s u_s \tag{17}$$

where τ_s and K_s are the time constant and gain of the servovalve dynamics, respectively.

$\ddot{A}$

4 Block Diagram of the Robot without Controller

Assembling all the components discussed in sections 3.1, 3.2 and 3.3, results in the block diagram shown in Figure 6 for the robot, which has been implemented in SIMULINK. Each servovalve includes one and each hydraulic actuator two integrators for the the pressures in chamber A and B. Furthermore, the mechanical system possesses four integrators, two for each generalized coordinate. The inputs of the robot are the two control inputs u_s of the servovalves. The output is the resulting motion of the robot. The measured feedback magnitudes for the here investiagated controller are the joint-positions and actuator-pressures, labeled as outward arrows in Figure 6.

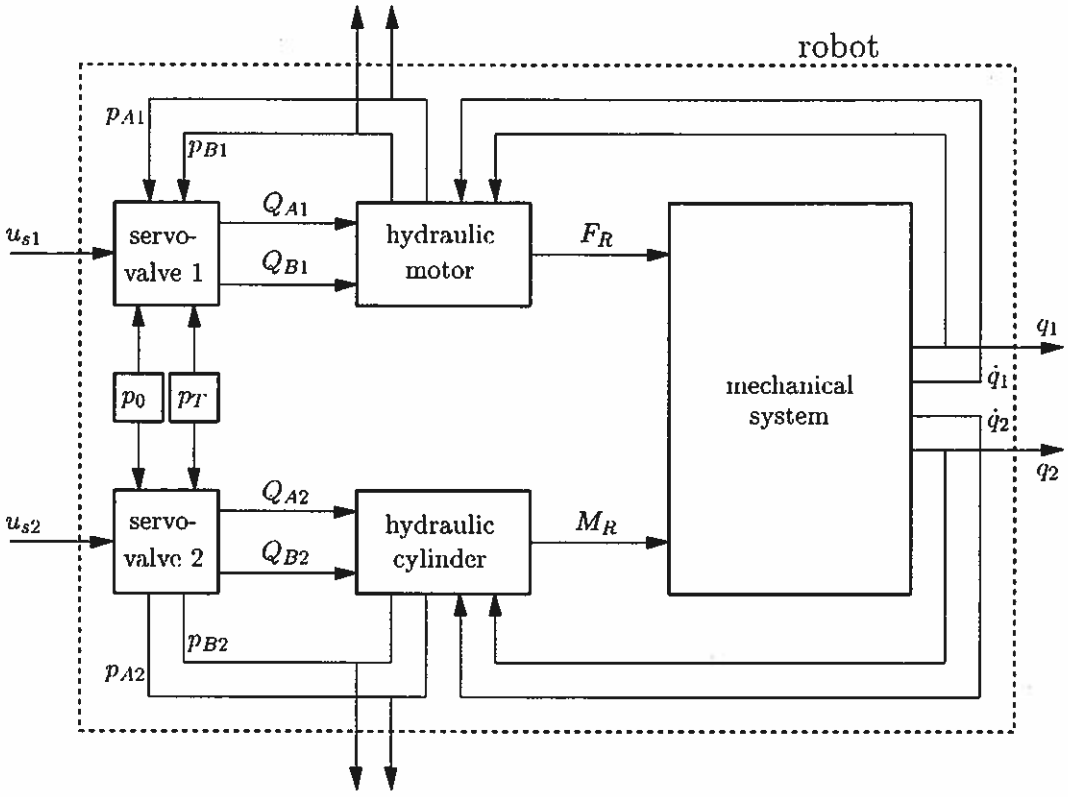

Figure 6: block diagram of the robot without controller

5 Controller

The controller shown in Figure 7 consists of two parts. (1) A so-called Simplified Cartesian Computed-Torque (SCCT) controller ([1]), which calculates the desired force and moment in the actuators and (2) a nonlinear controller for the hydraulic subsystem to reach the desired force and moment ([3]).

5.1 Simplified Cartesian Computed Torque (SCCT) Control

This controller yields the equivalent linearizing dynamic cancellation of the well-known Cartesian computed torque controller, yet is far simpler to compute, and at the same time inherently robust with respect to manipulator dynamic parameter uncertainty. This SCCT controller requires only knowledge of the bounds of the manipulator joint inertia matrix.

The robot dynamic model in equation (8) can be rewritten as

$$\bar{\mathbf{A}}\ddot{\mathbf{q}} + \boldsymbol{\eta}(\mathbf{q}, \dot{\mathbf{q}}, \ddot{\mathbf{q}}, t) = \boldsymbol{\tau} \tag{18}$$

where $\bar{\mathbf{A}}$ is a constant approximation to the configuration dependent inertia matrix $\mathbf{A}(\mathbf{q})$,

and $\boldsymbol{\eta}(\mathbf{q}, \dot{\mathbf{q}}, \ddot{\mathbf{q}}, t)$ represents a composite disturbance and joint coupling term given by

$$\boldsymbol{\eta}(\mathbf{q}, \dot{\mathbf{q}}, \ddot{\mathbf{q}}, t) = (\mathbf{A}(\mathbf{q}) - \bar{\mathbf{A}})\ddot{\mathbf{q}} + \mathbf{C}(\mathbf{q}, \dot{\mathbf{q}})\dot{\mathbf{q}} + \mathbf{g}(\mathbf{q}) + \mathbf{J}^{\mathrm{T}} f_e - \mathbf{d}(t) \tag{19}$$

Application of control law

$$\boldsymbol{\tau} = \bar{\mathbf{A}}\mathbf{u} + \boldsymbol{\eta}(\mathbf{q}, \dot{\mathbf{q}}, \ddot{\mathbf{q}}, t) \tag{20}$$

yields joint acceleration $\ddot{\mathbf{q}} = \mathbf{u}$

To simplify the controller computation, and reduce the need for *a priori* knowledge of the robot dynamics, it is assumed that $\boldsymbol{\eta}(\mathbf{q}, \dot{\mathbf{q}}, \ddot{\mathbf{q}}, t) \triangleq \boldsymbol{\eta}(t)$ is a continuous function with respect to t, and can be approximated by a time-delayed version as

$$\hat{\boldsymbol{\eta}}(t) = \boldsymbol{\eta}(t - \lambda) \approx \boldsymbol{\eta}(t) \tag{21}$$

The last approximation arises from the assumption of continuity, and the choice of a small time delay λ. For the here presented simulations we used $\lambda = 10$ ms, which is the same than the control sampling time.

With this estimate for $\boldsymbol{\eta}$ the control law is now computed as

$$\boldsymbol{\tau} = \bar{\mathbf{A}}\mathbf{u} + \hat{\boldsymbol{\eta}}(t) \tag{22}$$

and

$$\hat{\boldsymbol{\eta}}(t) = \tau(t - \lambda) - \bar{\mathbf{A}}\ddot{\mathbf{q}}(t - \lambda) \tag{23}$$

This estimation scheme relies on previous values of τ and $\ddot{\mathbf{q}}$. $\ddot{\mathbf{q}}$ is estimated by a central difference algorithm from samples of the joint position q.

The next step is to calculate the desired joint accelerations u in equation (22). Given a desired Cartesian path, $\mathbf{r}_d = [x_d, y_d]^{\mathrm{T}}$ with associated desired velocity and acceleration, to achieve a desired second-order error dynamic, we choose

$$\boldsymbol{\nu} = \ddot{\mathbf{r}}_d + \mathbf{K}_d(\dot{\mathbf{r}}_d - \dot{\mathbf{r}}) + \mathbf{K}_p(\mathbf{r}_d - \mathbf{r}) \tag{24}$$

where $\mathbf{K}_d$ and $\mathbf{K}_p$ are positive definite gain matrices selected to provide the desired gain and damping. With this, the desired joint acceleration can be calculated as

$$\mathbf{u} = \mathbf{J}^{-1}(\boldsymbol{\nu} - \dot{\mathbf{J}}\dot{\mathbf{q}}) \tag{25}$$

where $\mathbf{J}$ is the robot Jacobian matrix.

The so computed force vector $\boldsymbol{\tau}$ is the desired input vector $\boldsymbol{\tau}_d = [F_{R_d}, M_{R_d}]^{\mathrm{T}}$ for the nonlinear controller of the hydraulic subsystem (see Figure 7).

5.2 Nonlinear Controller for the Hydraulic Subsystem

Because of the similarities of the hydraulic cylinder and the hydraulic motor, here only the cylinder is investigated. Differentiating the fluid force $F_{F\ell}$ on the piston of the hydraulic cylinder (see sections 4 and 5) yields

$$\dot{F}_{F\ell} = (\dot{p}_A - \alpha \dot{p}_B).A \tag{26}$$

For the derivation of the control law it is assumed, that the control u_s applied to the spool valve is directly proportional to the spool position y_s, i.e. that the time constant τ_s in equation (17) goes to zero. This makes sense, if the dynamics of the valve motor/flapper are fast enough to be neglected (see [2]).

Together with equations (11), (12), (15), (16), (17), neglecting the flows through the relief valves Q_{DA} and Q_{DB}, assuming a constant fluid bulk modulus E_{oil} and only positive pressure-differences in the roots of equations (15) and (16), we have

$$\dot{F}_{F\ell} = -\dot{x} \underbrace{E_{oil}A^2 \left(\frac{1}{V_{0A} + Ax} + \frac{\alpha^2}{V_{0B} - \alpha Ax} \right)}_{M} + \frac{1}{N}(x, p_A, p_B,)u_s \tag{27}$$

where

$$\frac{1}{N} = \begin{cases} E_{oil}AB_vK_s \left(\frac{1}{V_{0A}+Ax}\sqrt{p_0 - p_A} + \frac{\alpha}{V_{0B}-\alpha Ax}\sqrt{p_B - p_T} \right) & \text{for} \quad u_s \geq 0 \\ E_{oil}AB_vK_s \left(\frac{1}{V_{0A}+Ax}\sqrt{p_A - p_T} + \frac{\alpha}{V_{0B}-\alpha Ax}\sqrt{p_0 - p_B} \right) & \text{for} \quad u_s < 0 \end{cases} \tag{28}$$

Choosing u_s as

$$u_s = N \left(\dot{F}_{F\ell_d} - k_F(F_{F\ell} - F_{F\ell_d}) + \dot{x}M \right) \tag{29}$$

yields

$$\dot{F}_{F\ell} = \dot{F}_{F\ell_d} - k_F(F_{F\ell} - F_{F\ell_d}) \tag{30}$$

This guarantees exponential force stabilization, as shown in [3]. k_F is a positive force error gain and $F_{F\ell_d}$ is the desired fluid force

$$F_{F\ell_d} = F_{R_d} + \hat{F}_F \tag{31}$$

where $\hat{F}_F$ is an estimate of the friction forces in the cylinder and F_{R_d} is the component for the hydraulic cylinder of the desired vector τ_d, which is the output from the SCCT controller.

This nonlinear controller was found to provide a path following capability for the stenciling robotic arm that met the edge definition stenciling requirement of Caltrans for all roadway markings. The system was tested in our laboratory with Caltrans project monitors and would provide path for setnciling theletter S which would meet all the edge definition requirements.

References

[1] T. A. Lasky. *Force-Tracking Impedance Control of Robot Manipulators.* PhD thesis, University of California, Davis, December 1995.

[2] M. Schneider. *Modellbildung, Simulation und nichtlineare Regelung elastischer, hydraulisch angetriebener Grobmanipulatoren.* Fortschritt-Berichte VDI, Reihe 8 Nr.756. VDI-Verlag, Düsseldorf, 1999.

[3] Garett A. Sohl and James E. Bobrow. Experiments and simulations on the nonlinear control of a hydraulic servosystem. *IEEE Transactions on Control Systems Technology*, 7(2):238–247, March 1999.

[4] Bin Yao, Fanping Bu, John Reedy, and George T.-C. Chiu. Adaptive robust motion control of single-rod hydraulic actuators: Theory and practice. *IEEE/ASME Transactions on Mechatronics*, 5(1):79–91, March 2000.

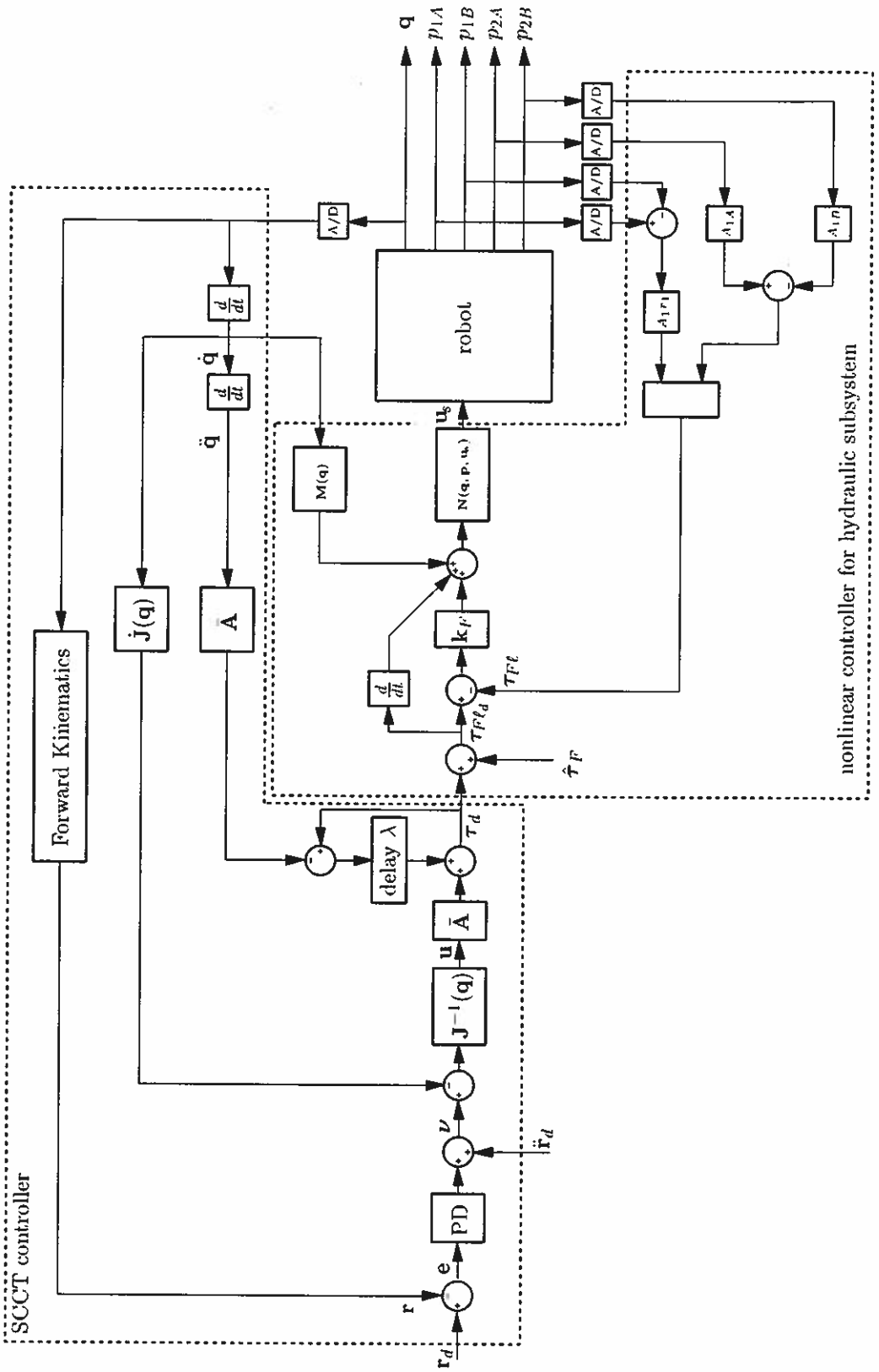

Figure 7: Controller

SECTION III

USER GUIDE AND DOCUMENTATION FOR THE NEW CONTROLLER

Refinements of a Robotic System for Stenciling of General Roadway Markings

User Guide and Documentation for the New Controller

Principal Investigator: Professor B. Ravani
AHMCT (Advanced Highway Maintenance and Construction Technology) Research Center
Department of Mechanical & Aeronautical Engineering
University of California-Davis
Davis, CA 95616

Controller for the stenciling robot

The controller consists of:

a) a PC with a QNX real time operating system
b) a motion control input/output board (within the PC) with:
   - 8 channels of encoder input
   - 8 channels of analog output
   - 8 channels of analog input
   - 32 bits digital input and output
c) an interface board for the connection between robot and motion control input/output board. This board contains also the necessary amplifiers (see Figure 1)

The robot comprises a set of joints: (1) a prismatic joint for the transverse motion of the base of the pantograph mechanism, (2) a revolute joint for the rotation of the base, and (3) a further prismatic joint for the extension of the robot. All three joints contain a encoder to get the actual joint position. Joints (2) and (3) comprise also pressure transducers, two for each joint (for the two chambers of the hydraulic actuators). All three joints are connected to the interface board, but only joints (2) and (3) are currently used in the control program. For safety reasons the prismatic joint (3) also comprises a additional valve that only opens, if it is connected to a 12 V voltage. If it is closed, no extension of the robot arm is possible. To open the valve, the control program must write TRUE to a certain digital Output channel, the switch on the interface board has to be ON (see Figure 1) and the limit switch on the extension joint must not be interrupted.

Interface board

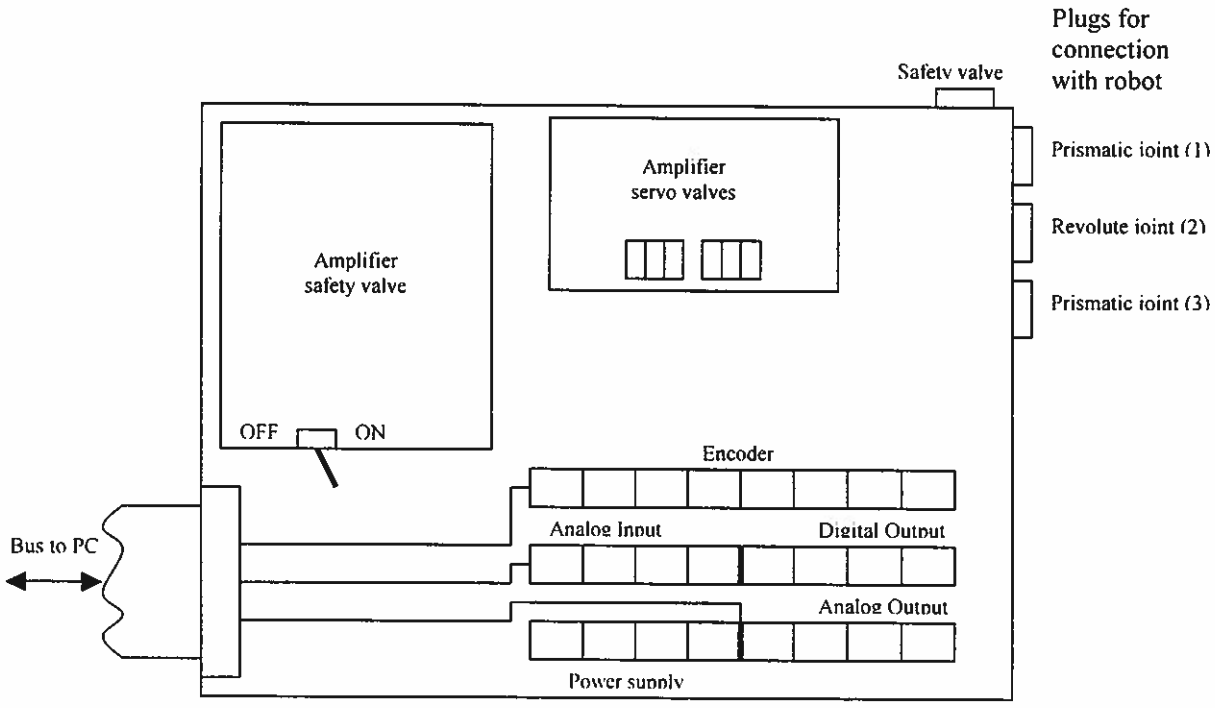

Figure 1. Interface board

The interface board is the connection between the robot and the motion control input/output board. On the right upper corner the wires from the valves, encoders and pressure transducers are connected via plugs. On the left lower corner the bus to the input/output board is drawn in. Furthermore there are the necessary amplifiers for the safety valve (includes also the switch for this valve) and the servo valves mounted. On the right lower corner all the connectors are mounted. Only a few are used now, so if there are any additional axis to control, they can be connected to the free places. Caution, **the labeling is not always correct, so the best way is to write a voltage to an channel and to measure it on the board to find the right connector, or the opposite way, attach a defined voltage to an connector an read all channel from the program to see, which is the right one**

Control program

There are four different control algorithms implemented, which can be found in the directories:

```
/home/six/robot/sjct
                  pid
                  dynInv
                  scct
```

In the directory `/sjct` the implemented control algorithm is a combination of a PID controller for the extension and a so called Simplified Joint Computed Torque (SJCT) method for the rotation. This algorithm yields the most stable and accurate behavior. In the `/pid` directory, PID controllers are realized for either joints. The result is also a stable behavior, but with lower accuracy. The directory `/dynInv` comprises a combination of a PID controller for the extension and a simple form of Dynamic Inversion for the rotation. The result is a very accurate but for large extensions not very stable controller. The last implemented controller can be found in the directory `/scct`. This is a so called Simplified Cartesian Computed Torque (SCCT) controller. The resulting behavior is very unstable, hence, this controller should not be used without changes!!

As mentioned before, the combination PID with SJCT in the directory `/sjct` yields the best results. Hence, the code of this controller is shown bellow and will be explained. The other programs have the same structure, the only difference is the code in the function `void controlLaw()`.

The control program **SjctPid.cpp** is a C++ program with two threads. A timer is attached to each of the threads. One of the threads is used only to write actual data on the screen every second, in the second one all the necessary operations to control the robot are performed. That means, that the timer of the second thread is responsible for the sampling frequency. To change the sampling frequency you have to modify the two lines:

```
const double T = 0.005;     //sampling time -> see Timer
.
.
timer.it_value.tv_nsec = 5000000; //5 msec or 200 Hz sampling frequency
```

At each sampling step, the control-thread processes the following code:

```
int PIDthread (void* arg)
{
  for (;;)
  {
    Receive (proxy, 0, 0);
    readValues();
    if(LAW_ON)
      controlLaw();

    writeDA();
  }
}
```

The function void `readValues()` has the following form:

```
void readValues()
{
//Pressures -> from analog inputs, channels 2, 3, 4, 5
  pA1_a= (stg.pollReadVoltage(3)-1.0)*5.175e6; // [pascal]
  pB1_a= (stg.pollReadVoltage(2)-1.0)*5.175e6;
  pA2_a= (stg.pollReadVoltage(4)-1.0)*5.175e6;
  pB2_a= (stg.pollReadVoltage(5)-1.0)*5.175e6;
//Encoders
  //read q1_a (rotation) -> channel 1
  stg.resetIDL(1);
  stg.latchEncoder(1);
  q1_a=(stg.readEncoder(1))*7.1399e-5;//2Pi=88000 Pulses ->[rad]

  //read q2_a (extension)-> channel 3
  stg.resetIDL(3);
  stg.latchEncoder(3);
  q2_a=1.55 + (1.05833e-4*(stg.readEncoder(3))); // 0.105833 mm/pulse
}
```

In this function at first the actual pressures of the joints (2) and (3) are read via the input/output board (asnalog input channels 2, 3, 4, 5). Afterwards the encoder values of the joints are read (channels 1, 3) and converted into radians and meters respectively. Caution, **the value `q2_a` is the extension of the endeffector and not the position of the hydraulic cylinder.**

If the variable `LAW_ON` is TRUE, the function `controlLaw()` is the next to be processed. How to set the variable `LAW_ON` to `TRUE` or `FALSE` will be explained later. The function has the following form:

```
void controlLaw()
{
  //desired trajectory generation
  if(LIN_EXE)      //linear motion to point
  {
    if(step<steps)
      {
      step++;
      x_d=x_b+step*dx;
      y_d=y_b+step*dy;
    }
      else
      {
        LIN_EXE=0;
      x_d=x_e;
      y_d=y_e;
        cout << "endpoint reached" << endl;
      }
  }
  if(S_EXE) // 'S' motion
  {
    if(step<steps)
      {
      step++;
      x_d=x_b+R*sin(step*dphi);
        if(step<(steps/2))
        y_d=y_b+R-R*cos(step*dphi);
        else
        y_d=y_b+3*R+R*cos(step*dphi);
    }
      else
      {
        S_EXE=0;
      x_d=x_b;
      y_d=y_b+4*R;
        cout << "endpoint reached" << endl;
      }
  }

  //calculate ys1 and ys2 [+/- 1]
  if(q1_a<0.7854 || q1_a>2.3562)  //for safety
  {
    ys1=zero1;
    ys2=zero2;
  }
  else
  {
    //torque joint controller for hydraulic motor
    q1_d=atan2(y_d,x_d);
    q2_d=sqrt(x_d*x_d+y_d*y_d);

    q1_D_1 = q1_D;
    q1_D   = (q1_a - q1_1) / T ;
```

```
    q1_1   = q1_a;
    q1_DD  = (q1_D - q1_D_1) / T;

    e_q1_2=e_q1_1;
    e_q1_1=e_q1_0;
    e_q1_0=q1_d-q1_a;

      A1 = m * q2_a;
    q1_DD_d     +=   (a0*e_q1_0   +   a1*e_q1_1   +   a2*e_q1_2);   //desired
accelleration

    Q1_d_1 = Q1_d;
    Q1_d  += A1*(q1_DD_d-q1_DD);      //desired torque

    //nonlinear pressure control law (Bobrow)
    Q1_a  = (pA1_a - pB1_a) * 6.214e-5;
    vA1_a = 5e-4 + (q1_a * 6.214e-5);
    vB1_a = 8.04e-4 - (q1_a * 6.214e-5);
    num1  = ((Q1_d - Q1_d_1) / T)  - kF_q1 * (Q1_a - Q1_d)
           +6.1782 * q1_D * ((1.0/vA1_a) + (1.0/vB1_a));

    ys1=0;
    if (num1 >= 0.0)
    {
      if((2.069e7-pA1_a)&&(pB1_a-1e5) >= 0)
      {
        z1  = 2.379e-2 * (sqrt (2.069e7 - pA1_a)/vA1_a +
                  sqrt (pB1_a - 1e5) / vB1_a );
          ys1=-num1/z1;
      }
    }
    else
    {
      if((pA1_a-1e5)&&(2.069e7-pB1_a) >= 0)
        {
        z1 = 2.379e-2 * (sqrt (pA1_a - 1e5) / vA1_a +
                  sqrt (2.069e7 - pB1_a) / vB1_a);
          ys1=-num1/z1;
        }
    }

    if(ys1>0.2)
        ys1=0.2;
    else
      if(ys1<-0.2)
          ys1=-0.2;

    //PID controller for hydraulic cylinder
    e_q2_2=e_q2_1;
    e_q2_1=e_q2_0;
    e_q2_0=q2_d-q2_a;

    ys2+= kP_q2*(e_q2_0-e_q2_1)
```

```
            +kI_q2*(e_q2_0)
            +kD_q2*(e_q2_0-2.0*e_q2_1+e_q2_2);

    if(ys2>1)
        ys2=1.0;
    else
    if(ys2<-1)
        ys2=-1.0;
  }
}
```

The first part is responsible for the generation of a desired trajectory, depending on the variables `LIN_EXE` and `S_EXE` . There are two kinds of implemented trajectories, (1) linear motion between two points and (2) S-motion. How to set the variables `LIN_EXE` and `S_EXE` to `TRUE` will be explained later. As mentioned before, the here implemented control algorithm is a PID controller for the extension and a SJCT controller for the rotation. The PID controller calculates from the actual error between the desired and actual position of the extension joint and the errors from one and two sampling steps before directly the desired voltage `ys2 [+-1]` to the servo valve. The SJCT controller calculates from the error in the position at first a desired acceleration `q1_DD_d` with a PID law. With this acceleration a desired torque is calculated with the SJCT method including a variable inertia estimate `A1`:

```
    A1    = m * q2_a;
  Q1_d_1 = Q1_d;
  Q1_d  += A1*(q1_DD_d-q1_DD);      //desired torque
```

The next step is to calculate the necessary voltage to the servo valve to get the desired torque. Therefor a nonlinear control law from G. A. Sohl and J. E. Bobrow is used. The paper is attached to this documentation.
The last function call in the control-thread is `writeDA()`,

```
void writeDA()
{
  stg.writeVoltage(6,5.0*ys1);  // valve hydraulic motor
  stg.writeVoltage(5,5.0*ys2);  // valve hydraulic cylinder
}
```

which writes the necessary voltages to the servo valves via input/output board (analog output channels 5 and 6).

To communicate with the program, the program waits in an endless loop for commands via keyboard. The possible commands can be found in the `void help()` function:

```
void help()
{
//commands
 cout << endl;
 cout << "Enter the following characters:" << endl;
 cout << "-----------------------------" << endl;
 cout << "'h' -> for help" << endl;
 cout << "'i' -> to enter value ys1 (hydraulic motor)" << endl;
 cout << "'z' -> to reset encoders (when retracted " << endl;
 cout << "       endeffector is in symmetry plane of vehicle)" << endl;
 cout << "'r' -> to turn controller ON" << endl;
 cout << "'s' -> to turn controller OFF" << endl;
 cout << "'p' -> to move linear to a point" << endl;
```

```
 cout << "'l' -> to perform a 'S' motion" << endl;
 cout << "'e' -> to exit from execution of linear and 'S' motion" << endl;
 cout << "'q' -> to quit the program (turn hydraulic OFF first!!)" << endl;
}
```

By entering `r`, the variable `LAW_ON` will be set `TRUE` and the control law is turned on. Entering `p` asks for the desired end position coordinates and sets the variable `LIN_EXE` to `TRUE`. Entering `l` sets the variable `S_EXE` to `TRUE` and yields a S-motion.
The variable `vel` defines the path velocity for linear and S-motions. All control gains and constants can be found a the head of the program.

How to use the robot

A) Turning it on

1.) Turn switch on Interface board for safety valve off (see Figure 1)
2.) Turn on all electric devices on the table (power supply, transformer, PC, monitor)
3.) Login as user `six`, no password is necessary
4.) Type `su` to get the necessary super user rights
5.) Chance to the directory `/home/six/robot/sjct` and start the program **SjctPid** (if you make chances and want to compile the program type: `make SjctPid`)
6.) Remove the chain from the robot and make sure, that the end limit switch on extension joint (3) is activated with a screw
7.) Turn switch on Interface board for safety valve on (see Figure 1). **Look carefully to the robot. If it is extending, turn the switch off and start program new.**
8.) Turn power for the hydraulic on (switch is mounted on the wall). The result is, that the robot is retracting and maybe rotating very slow. The reason therefor is, that the offset voltage of the two valves is a little bit temperature depending. You can change this offsets by modifying the variables:

```
const double zero1 = 0.03; //valve offset revolute joint (2)
const double zero2 =-0.37; //valve offset extension joint (3)
```

`zero2 =-0.37` yields the desired retraction of the robot arm.

There is a emergency stop switch next the table, to turn off the power. During the power is on, leave always one foot near this switch!!

9.) Bring retracted robot in middle position (symmetry plane of the vehicle). To reach this, type `i` and press return. Now you are asked for a desired voltage to the valve for the revolute joint (2). **Caution**, enter only values of +-0.05. Positive voltages yield clockwise rotations.
10.) If retracted robot is in middle position and not moving any more, enter `z` to reset the encoders. With this command you also set the origin and orientation of the world coordinate system. The z-axis is collinear with the axis of the revolute joint(2), and the y-axis is aligned to the endeffector
11.) Now you can start the control law by entering `r`.
12.) Enter `p` to move linear to a desired point
13.) Enter `l` to perform a S-motion in positive y direction

B) Turning it off

1.) turn of the power first (with emergency stop)
2.) **very important**, turn of the switch for the safety valve on the interface board (see Figure 1). Otherwise the robot begins to extend until end limit switch is interrupted
3.) at last enter `q` to exit from the program

Section IV:

Appendix A

Mechanical Designs for Generating Smooth Trajectories for a Roadway Painting Robot

Appendix B

Kinematic Study of the Big Articulated Robotic System (BASRS)

Appendix C

Mechanical Redesign of Big Articulating Stenciling Robot End Effecter Employing a Novel Mechanism for Paint Spray Gun Orientation Control

Section IV:

Appendix A

Mechanical Designs for Generating Smooth Trajectories for a Roadway Painting Robot

Contents

List of Figures

List of Tables

Jeffrey J. Hemenway
September 1999
Mechanical Engineering

Mechanical Designs for Generating Smooth Trajectories for a Roadway Painting Robot

Abstract

This paper consists of two parts. In Chapter 2, a possible counter-balancing technique for a large-scale articulating robot is examined. Chapter 3 discusses the mechanical redesign of a shaft system on the robot end-effector to minimize existing deflections during operation.

Chapter 2 contains a complete description of how to investigate the counter-balancing of a robot. It begins by discussing the need for such a mechanism, and then proceeds to analyze what the necessary output of such a balance would be, and by what possible methods it might be mounted to the robot. The chapter concludes with the analysis of a counter-balance that was actually built, and the effects it had on robotic performance. Throughout the analysis, an emphasis was placed on safety, as the operation of such a large robot presents many possible safety hazards in the event of an unexpected failure.

In Chapter 3, a redesign of the current end-effector shaft system is proposed to increase lateral stiffness. This is to minimize observed deflections that occur when the shaft is rotated at high speeds. First, the current level of deflection is determined

analytically, and then a potential redesign is analyzed in the same manner, to provide a comparison of potential before-and-after results. The design is then fabricated, and examined experimentally, to determine what changes have actually occurred in the deflection of the shaft system.

Chapter 1

Introduction

The Advanced Highway Maintenance and Control Technology (AHMCT) department at the University of California, Davis, is currently developing a system of automating the creation of roadway markings. The current method of producing these markings consists of laying stencils on the pavement, and applying paint via spray gun. This system has a number of disadvantages, including lack of accuracy, lack of speed, and lack of safety for the workers involved. The system under development by AHMCT seeks to remedy these problems by creating a robotic system capable of recreating these roadway markings. This system, the Big Articulating Stenciling Robot (BASR), has a reach of approximately 18 ft., and is situated in the back of a large flat-bed truck.

The arm itself is a simple three degree-of-freedom system, allowing for extension of the arm, rotation at the base, and translation of the base horizontally (Figure 1.1). The translation of the base is used solely to position the arm between successive markings, and is not used during the actual painting process. This reduces the effective number of

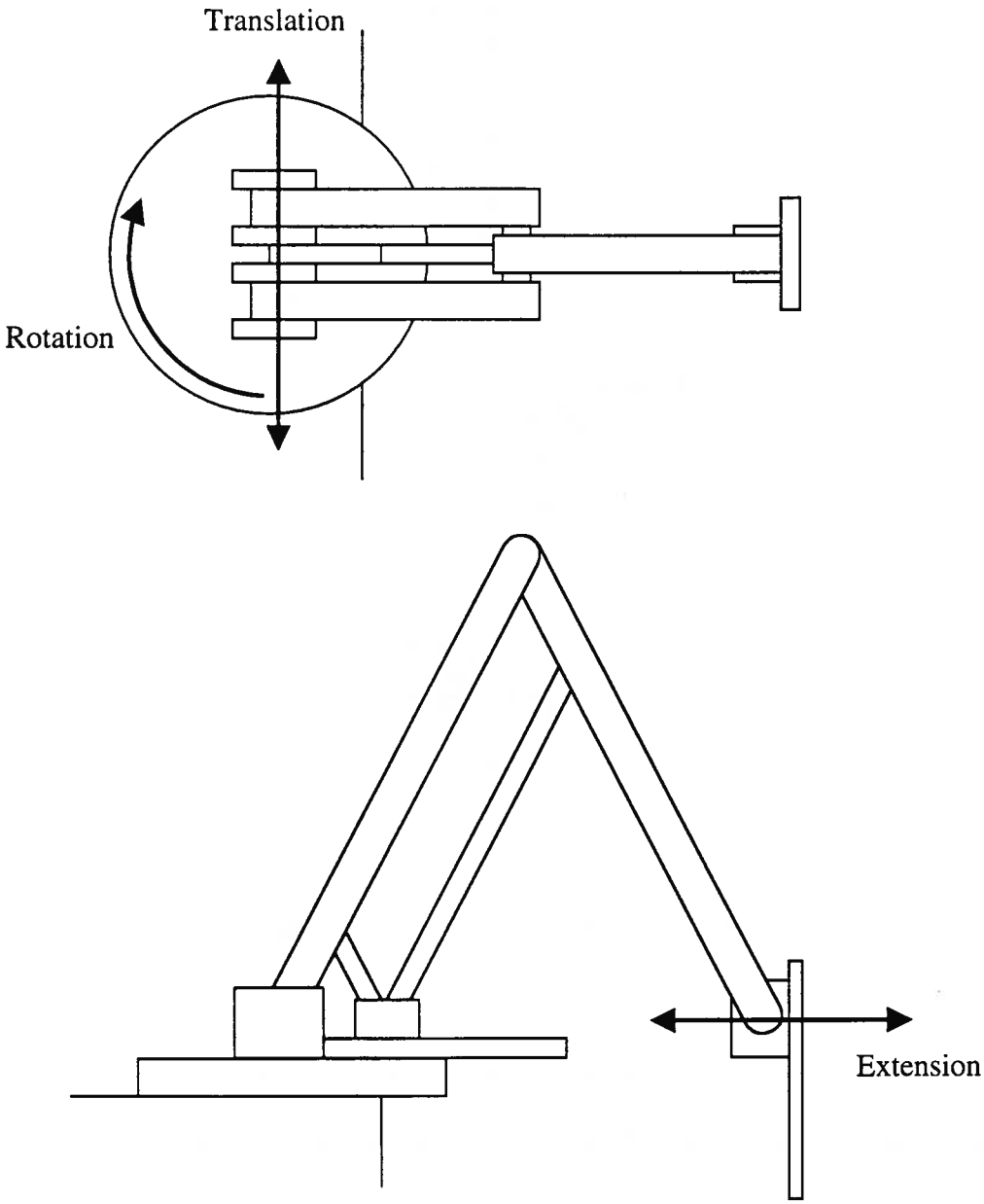

Figure 1.1: Degrees of Freedom of the BASR Arm

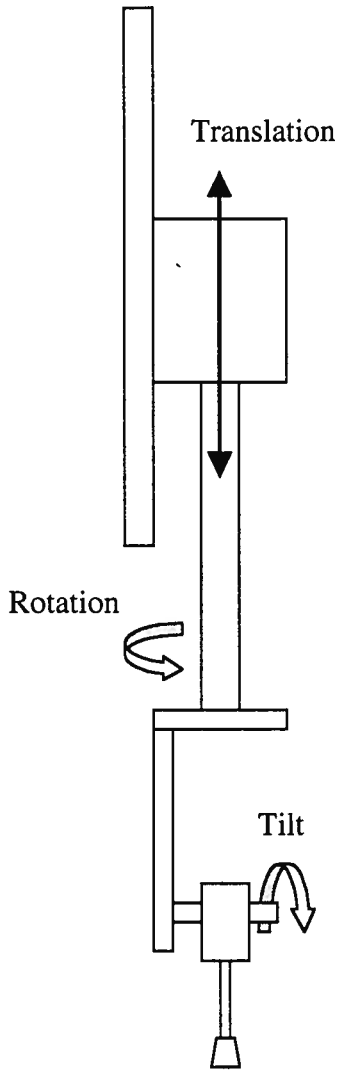

Figure 1.2: Degrees of Freedom of End-Effector

DOF of the arm to two. At the end of the arm sits an end-effector, which holds and manipulates the paint gun. The end-effector allows vertical translation of the paint gun, as well as rotation about the vertical axis, and rotation about a horizontal axis (used for tilt). The arm joints, as well as the vertical translation of the paint gun, are powered

by hydraulics. The two rotations on the end-effector are achieved through electric stepper motors.

BASR is currently in the testing and trouble-shooting stage of development. The primary problem currently under investigation is low-quality performance. The robot will paint markings, but the markings have not yet achieved the smoothness of those generated by the current stenciling process. The edges of the markings appear jagged, and the overall shape of the markings, while recognizable, falls far below what is deemed acceptable.

Of a number of possible factors that could influence markings quality (including lack of control system optimization, lack of stiffness in the robot arm, and inability of the hydraulic actuator controlling extension to move such a large mass), the two that will be addresses in this thesis are the lack of counter-balancing of the robotic arm, and deflection of the shaft upon which the paint gun is mounted.

Chapter 2

Development of Counter Balance

2.1 Current Problems with the Robot

2.1.1 Performance Issues

The performance specifications, as dictated by CalTrans, require that the markings made by the stenciling robot be indistinguishable from (or as close as possible to) the markings currently in use. This mandates that the motion of the robot be smooth and accurate. It is undetermined exactly what tolerances are required to achieve "smooth and accurate" motion, but it is suspected, given previous data, that errors in extension be less than 5 millimeters, and errors in rotation be within a few tenths of a degree. The data shown in Figure 2.1, for example, represents maximum rotational errors of approximately 0.08 degrees, and maximum extension errors of 10 mm. The data is taken from sensors mounted at the base, and has been extrapolated into Cartesian space to give a better

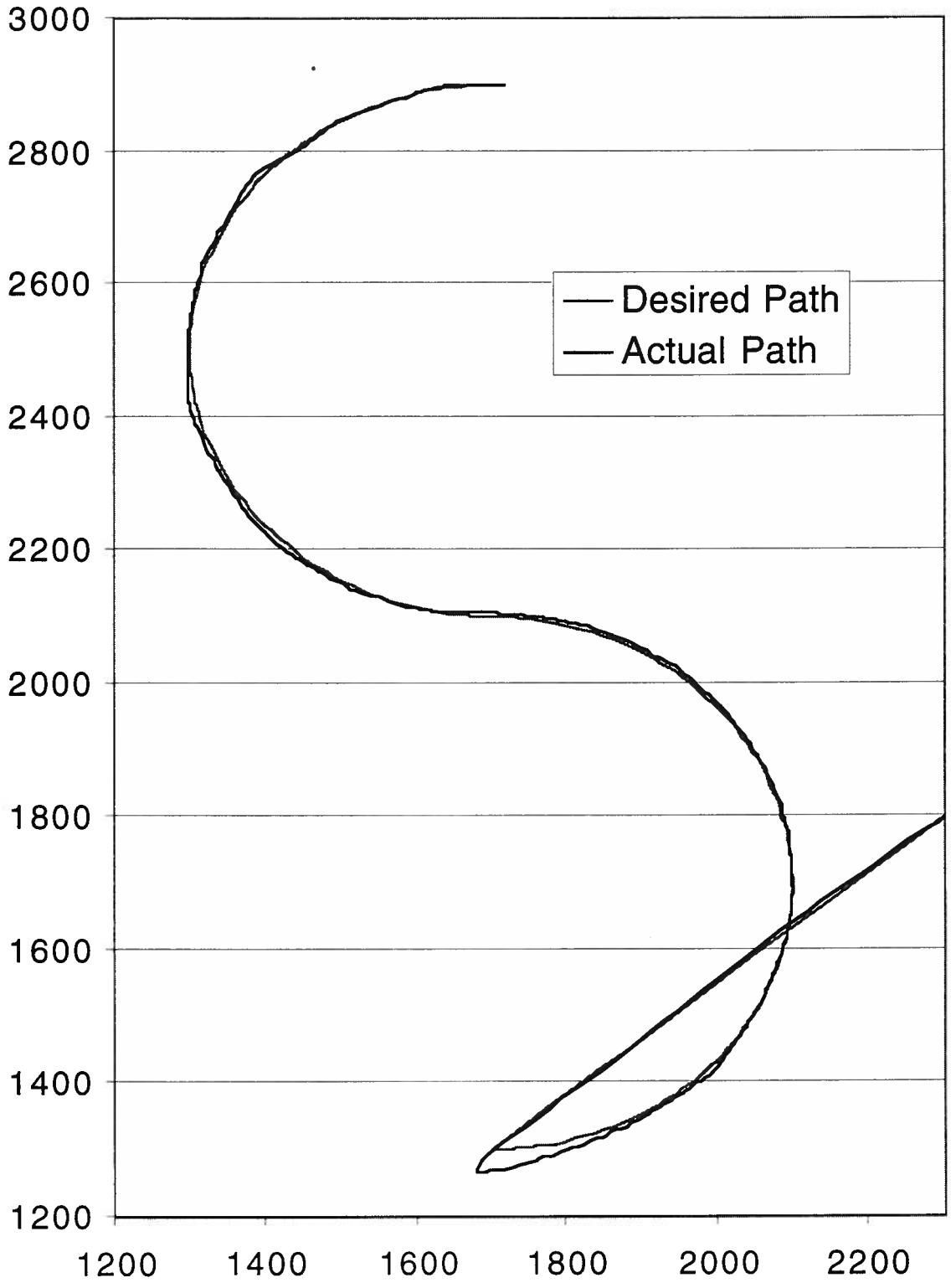

Figure 2. 1: Current Robot Arm Performance

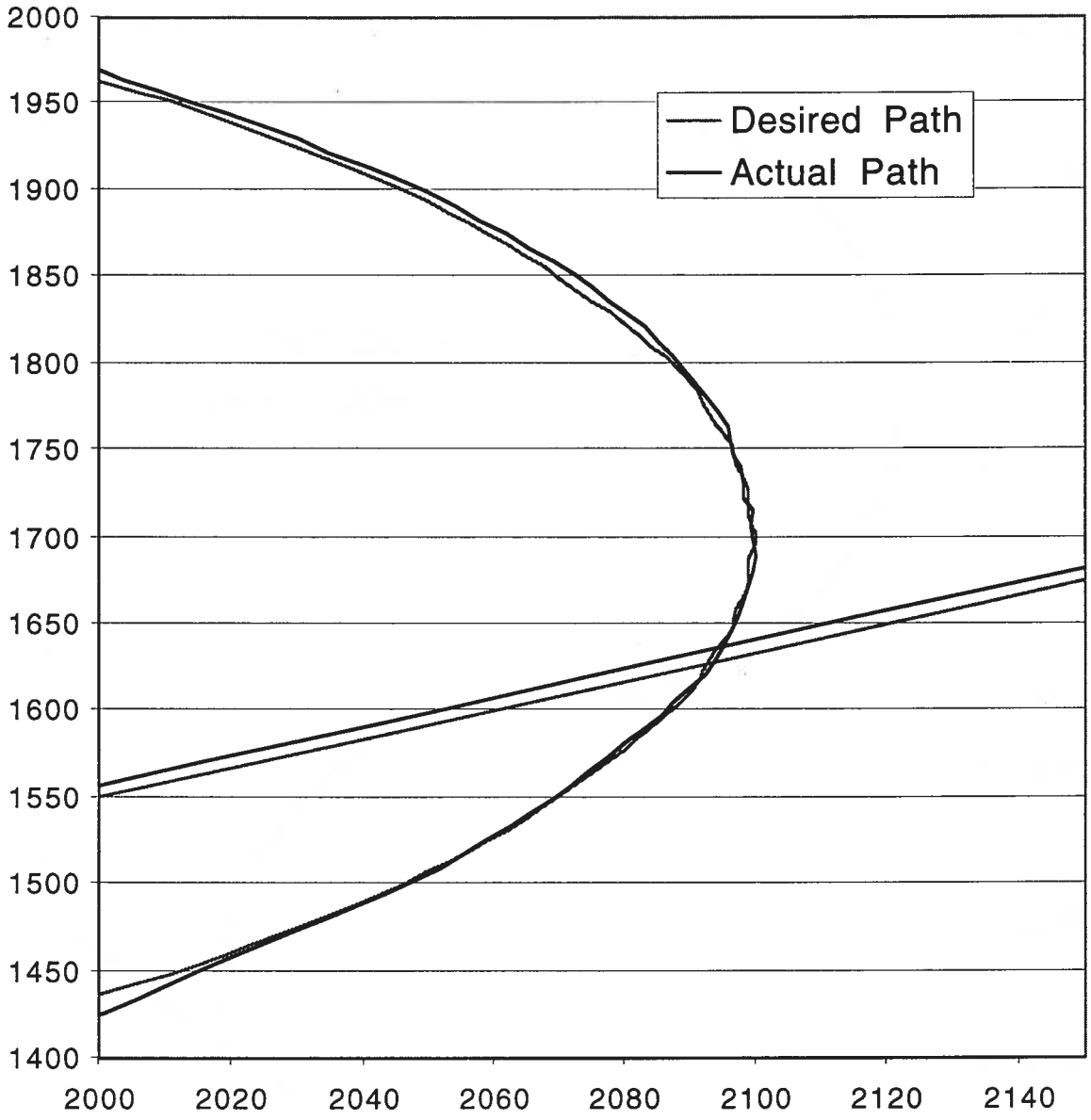

Figure 2.2: Detail of Performance Plot Demonstrating Wag

representation of what the robotic motion actually looks like. Even these small errors generate unacceptable markings. There are two possible ways in which this motion may be improved: by reducing the net error in either rotation or extension (or both), or by forcing the overall quality of the motion to be smoother (reducing the "wag").

Reducing the net error may be possible in a number of ways. One is to reduce the speed of the robot. Unfortunately, there is a lower limit to the speed of the robot. As the robot moves more and more slowly, the paint is laid on more and more thickly. If the robot moves too slowly, the paint begins to run, producing very unsightly markings. The robot is currently running at speeds very close to this minimum, and therefore this is not a viable option. Another way to reduce error may be to adjust the control system itself. Many modifications have already been made, however, and the data shown represents what is believed to be the optimum condition of the control system.

Reducing the wag is what I believe to be of greater importance. As the performance requirements of the robotic motion are rather subjective (it is required that the markings created be "indistinguishable" from current markings), net errors of a centimeter here and there may not be of supreme importance, as longs as the motion is smooth and steady. Upon close examination of the test data (Figure 2.2), it is apparent that a great deal of wag is present. This problem of wag may be addressed much as the problem of net error, as mentioned above; however, the limitations of those methods were already discussed. Another way in which this problem may be approached is from a mechanical standpoint, i.e., making changes in the mechanical system itself, to alleviate some of the strain on the hydraulic actuators. It is this final method that will be discussed for the remainder of the chapter.

2.1.2 Safety Issues

Another problem with the current robotic system is its level of safety. In its current state, a failure of the hydraulic system would allow the robot to extend to its full capacity at a high speed, which could cause serious injury to anyone standing in its path. It is desired to remedy this safety hazard to minimize the risk of injury during unforeseen failures of the system.

2.2 Evidence Justifying the Need for a Counter Balance

It is believed that some sort of counter-balancing system for the robotic arm would alleviate some of the wag (and possibly some of the net error) found in the robot's motion. This belief is based upon both observations of the robot's movement, and the nature of the mechanical design of the arm itself.

From a mechanical standpoint, the arm suffers from a great mass imbalance. If left unsupported, it is obvious that the arm will extend, under it's own weight, as far as its design allows (approximately 17.5 feet, from base to end-effector). At its full extension, the arm requires an enormous amount of force to pull it back in. At full retraction, it requires substantially less force to hold it in position, but it still has a tendency to extend.

Looking at test data for the robot's movement, as well as observing the results of painting experiments, the robot appears to perform better while extending than while retracting. From Figure 2.3, it can be seen that the performance during extension is

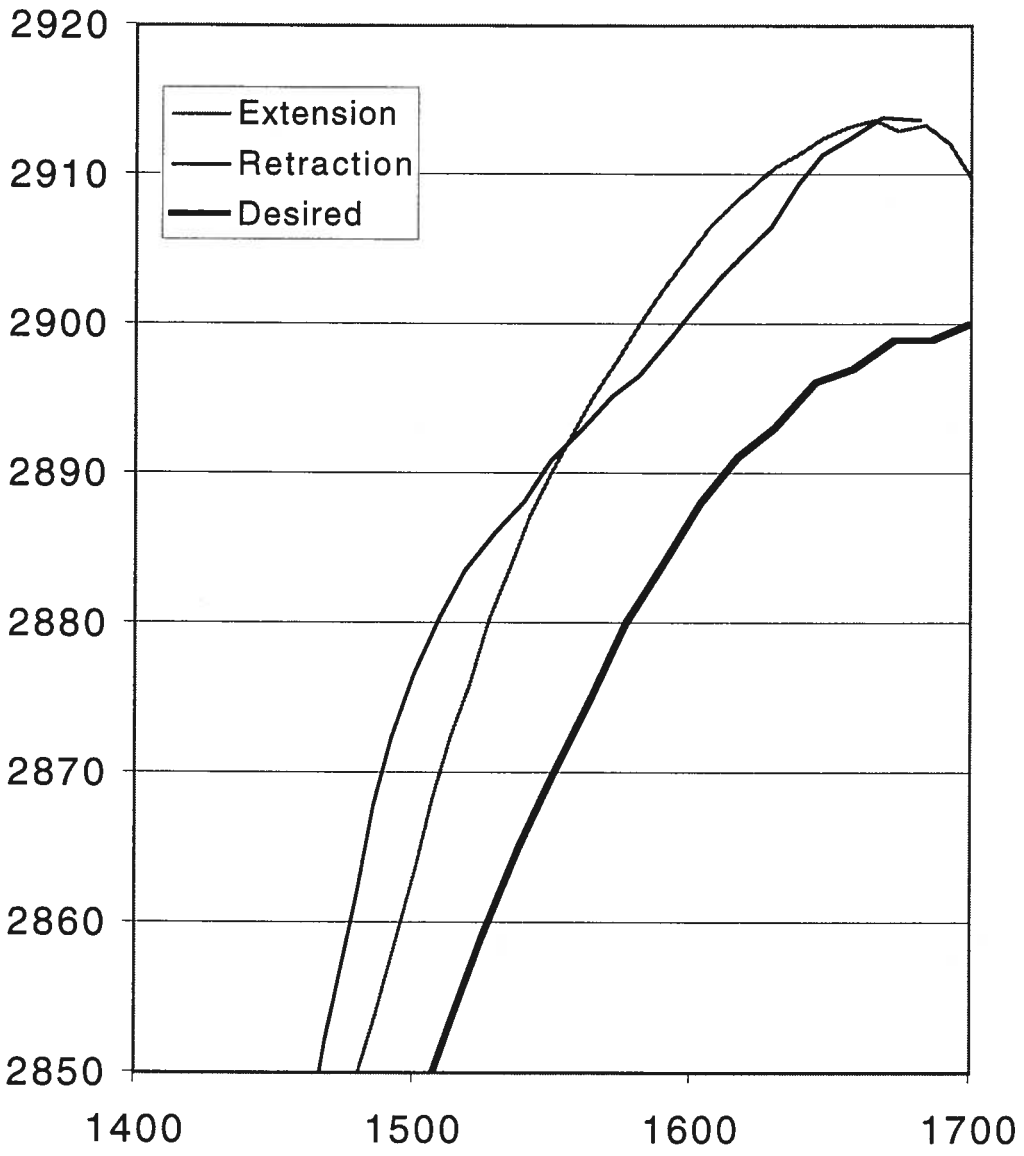

Figure 2.3: Detail Plot of Retraction Performance vs. Extension Performance

marginally smoother than that during retraction. This could be the result of the added strain on the hydraulic actuator of having to pull in the massive weight of the arm. The strain would be lessened during extension, as the actuator would have the assistance of gravity to help move the arm along. The strain on the actuator would still exist during extension, however, as it would need to slow the extension. A counter-balance would absorb some of this tendency towards extension, lessening the burden on the actuator, and improving the overall performance during both extension and retraction.

In addition to performance improvements, a counter-balance would dramatically improve the safety of the robot. It would either slow the extension to the point where it could no longer do serious harm, or stop it altogether, by providing an equilibrium point for the arm somewhere between the extremes of full extension and full retraction.

2.3 Development of Necessary Counter-Balance Forces

Before a successful counter-balance can be designed, it is necessary to determine what type of force output is desired. This can best be achieved by plotting the force required to keep the arm in equilibrium as a function of its extension. In addition, the force required will depend on where the force is applied, and how it is oriented. Two different scenarios were examined in an attempt to find the most efficient and cost effective means of producing a counter-balance. (Figure 2.4) The first scenario involved a base-mounted counter-balance, which provided a force directly along the axis of the hydraulic actuator. The second scenario used a counter-balance attached to both the base, and the arm itself.

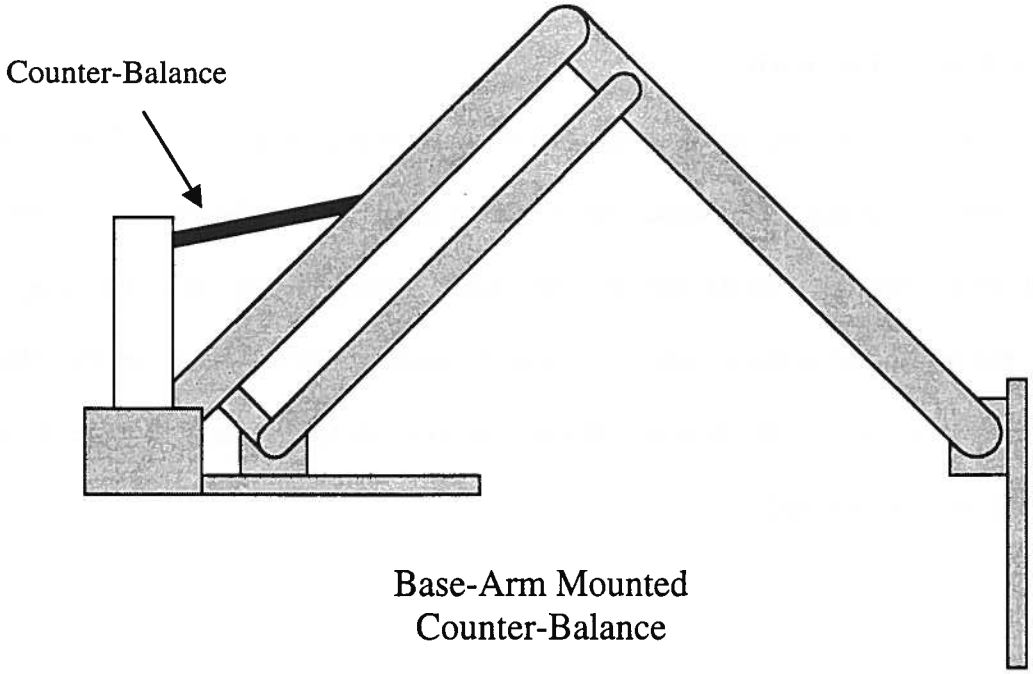

Base-Arm Mounted
Counter-Balance

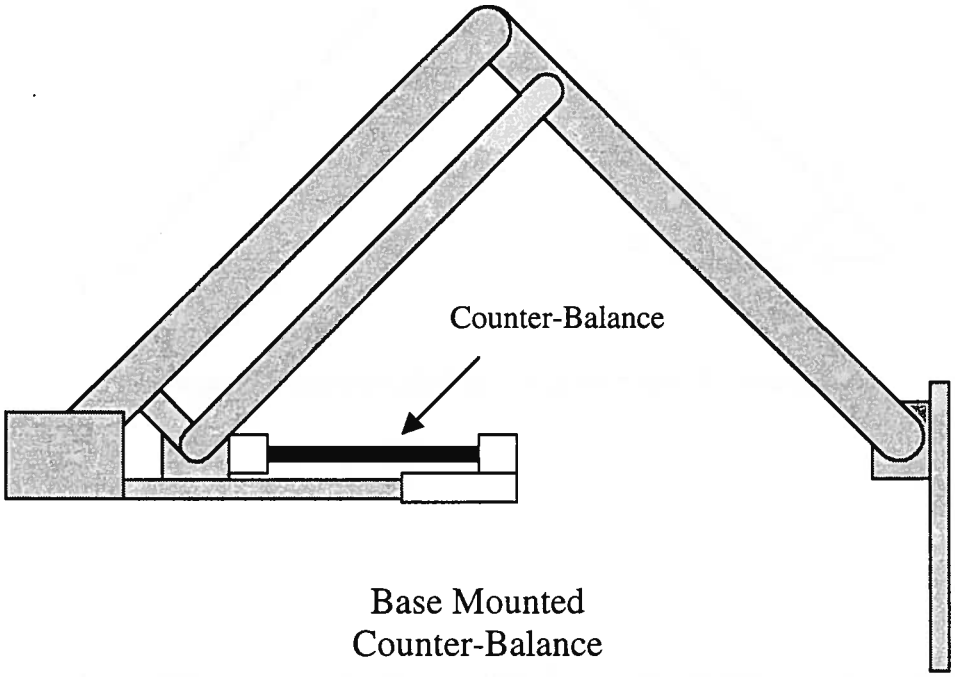

Base Mounted
Counter-Balance

Figure 2.4: Two Possible Mounting Types For the Counter-Balance

2.3.1 Base-Mounted Scenario

In order to determine the force required to keep the arm in static equilibrium, the Lagrange method was used. The equations of motion were found in the case of the robot extending under the force of its own weight, with a force F being applied in the x-direction at point C. After the equations were determined, it was assumed that the robot was stationary, i.e., $\dot{x} = \ddot{x} = 0$. It was then possible to solve for the applied force, F, in terms of the position of point C.

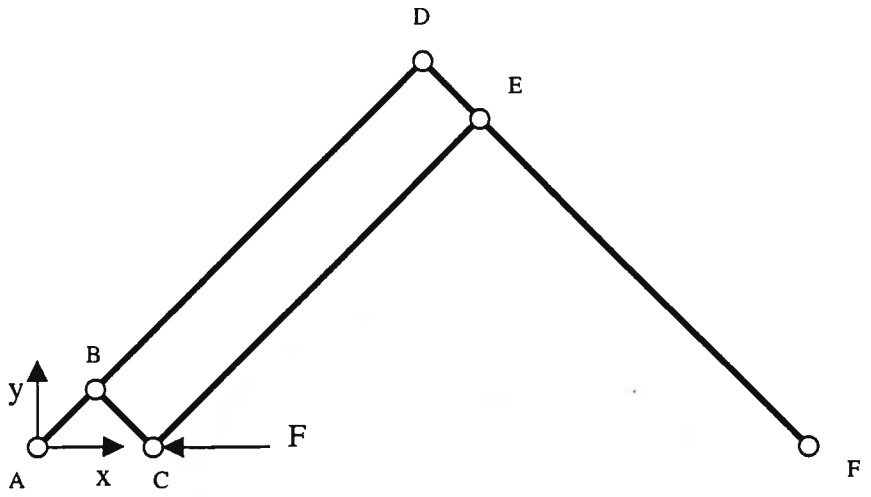

Figure 2.5: Schematic of the Robotic Arm Linkage

Above is a diagram of the BASR arm configuration. The robot consists of five links: BC, DF, CE, and two at AD. Each arm has a mass, m, a moment of inertia, I, and a length. The lengths of links AD and DF are equal, and will be assigned the variable L.

The length of link BC will be given the variable d. From the geometry, it can then be determined that link CE has length (L – d).

In order to apply the Lagrangian method to this problem, it is necessary to determine the kinetic energy, T*, of the system, as well as the potential energy, V. It can be shown that T* can be expressed as a function of x and $\dot{x}$, and further, that the expression for T* is linear in $\dot{x}^2$, that is,

$$T^* = [f(x)]\dot{x}^2 \tag{1}$$

The potential energy of the system can be expressed as

$$V = 2m_{AD}gh_{C,AD} + m_{BC}gh_{C,BC} + m_{CE}gh_{C,CE} + m_{DF}gh_{C,DF} \tag{2}$$

where m_{ij} is the mass of link i-j, and $h_{C,ij}$ is the height of the center of gravity of link i-j. For link AD, the height of the CG is given as

$$h_{AD} = \frac{1}{2}L\sin\theta. \tag{3}$$

(see Figure 2.6)

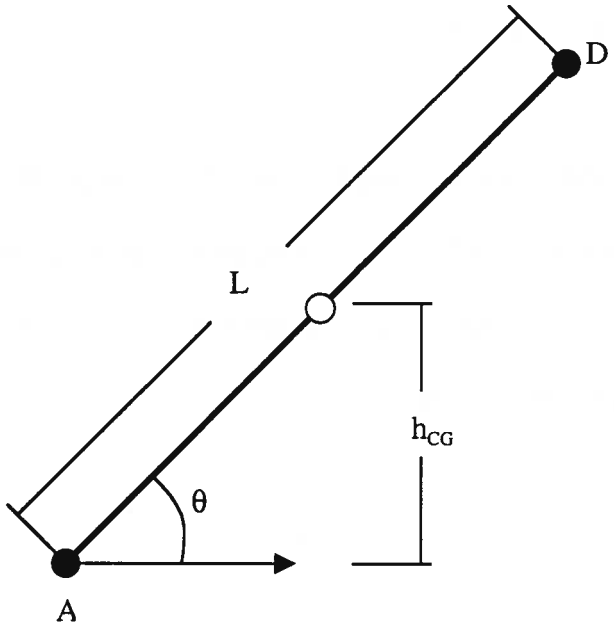

Figure 2.6: Schematic of Arm Link AD

sinθ can be found by examining link BC, shown in Figure 2.7:

$$\sin\theta = \frac{y}{d} = \frac{\sqrt{d^2 - (x/2)^2}}{d} = \frac{\sqrt{4d^2 - x^2}}{2d} \tag{4}$$

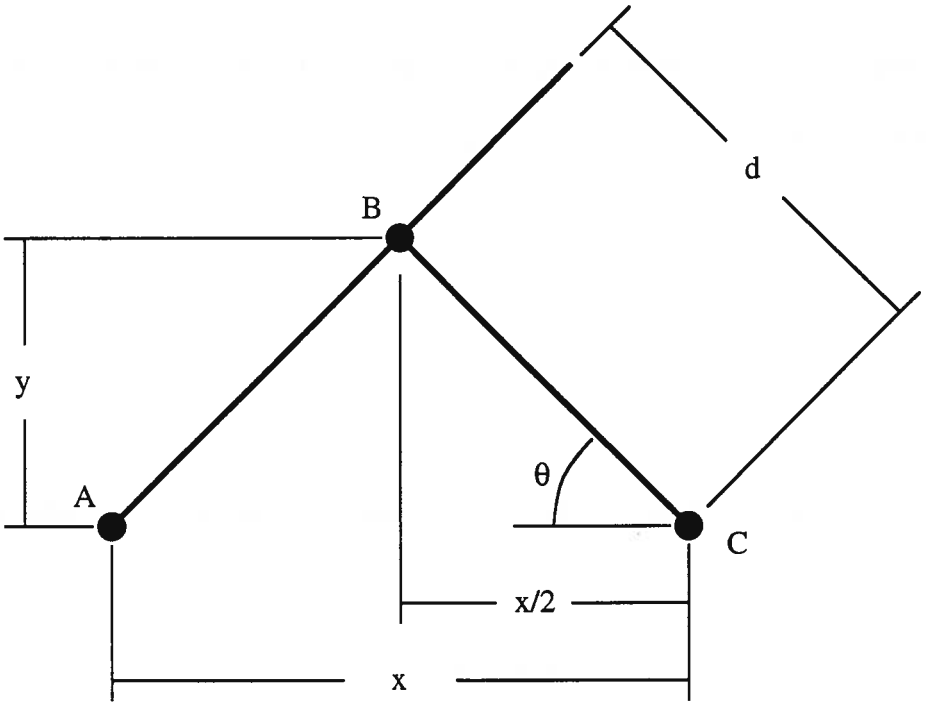

Figure 2.7: Schematic of Arm Link BC

Substituting (4) into (3) yields

$$h_{C,AD} = \frac{2m_{AD}gL\sqrt{4d^2 - x^2}}{4d} \tag{5}$$

Similar expressions can be found for $h_{C,BC}$, $h_{C,CE}$ and $h_{C,DF}$. Placing these expressions back into (2) and simplifying.

$$V = \left[\frac{g}{4d}\left(2m_{AD}L + m_{BC}d + m_{CE}(L-d) + m_{DF}L\right)\right]\sqrt{4d^2 - x^2} \tag{6}$$

The bracketed term is a constant, dependent upon the physical dimension of the robot. For the sake of simplicity, it will be referred to as the constant B, that is:

$$V = B\sqrt{4d^2 - x^2} \tag{7}$$

From these two terms, the kinetic and potential energies, the Laplacian can be found,

$$\mathrm{L} = T^* - V = f(x)\dot{x}^2 - B\sqrt{4d^2 - x^2} \tag{8}$$

The equation of motion can then be determined as follows:

$$\frac{d}{dt}\left(\frac{\partial L}{\partial \dot{x}}\right) - \frac{\partial L}{\partial x} = \Xi_x \tag{9}$$

where Ξ_x in this case can be shown to be –F. Performing the necessary operations upon (8) and substituting into (9),

$$2f(x)\ddot{x} - \frac{df}{dx}\dot{x}^2 - \frac{Bx}{\sqrt{4d^2 - x^2}} = -F \tag{10}$$

This equation may be further simplified, since we are interested only in the static behavior of the system. If the arm is in equilibrium, i.e., not moving, then all time-derivatives of x are equal to zero. Thus, equation (10) simplifies to

$$F = \frac{Bx}{\sqrt{4d^2 - x^2}} \tag{11}$$

Finally, by using the values for L, d, and the various masses, the final form of the force equation may be given:

$$F(x) = \frac{709.9x}{\sqrt{676.0 - x^2}}, \quad 7.5 < x < 25.5 \tag{12}$$

where x is in inches and F is in pounds. This equation represents the force that needs to be applied to point C in order to keep the arm from extending under its own weight. The range for this equation, 7.5 to 25.5 inches, represents full retraction and full extension, respectively, as measured between point A and point C.

2.3.2 Arm-to-Base Mounted Scenario

For this case, a set-up such as that seen in Figure 2.8 is assumed. The counter-balance would be attached at points G and H, such that the force would be tangent to the line GH. The method of Lagrange may be applied in this case, as well. The only difference in the equations would be in the value of Ξ_x. To determine its value, it is

necessary to re-evaluate the amount of work done by the counter-balance when the extension of the robot is displaced a small amount, Δ.

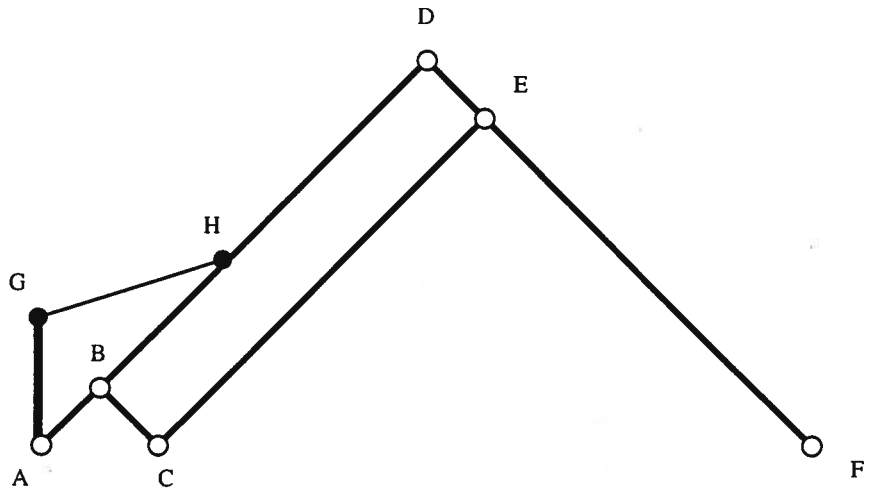

Figure 2.8: Schematic of Base-Arm Mounted Counter-Balance

First, it should be noted that a simplification can be made. It is apparent that any force applied tangent to the arm, i.e. along the link AD, will provide no help in balancing the robot. Therefore, it is necessary only to analyze a force normal to the arm at point H. The work performed by the counter-balance over a small displacement, Δ, is given by

$$\Xi_x = F_n a \delta\theta, \tag{13}$$

F_n being the component of force normal to link AD, and $a\delta\theta$ being the displacement of point H. From Figure 2.9,

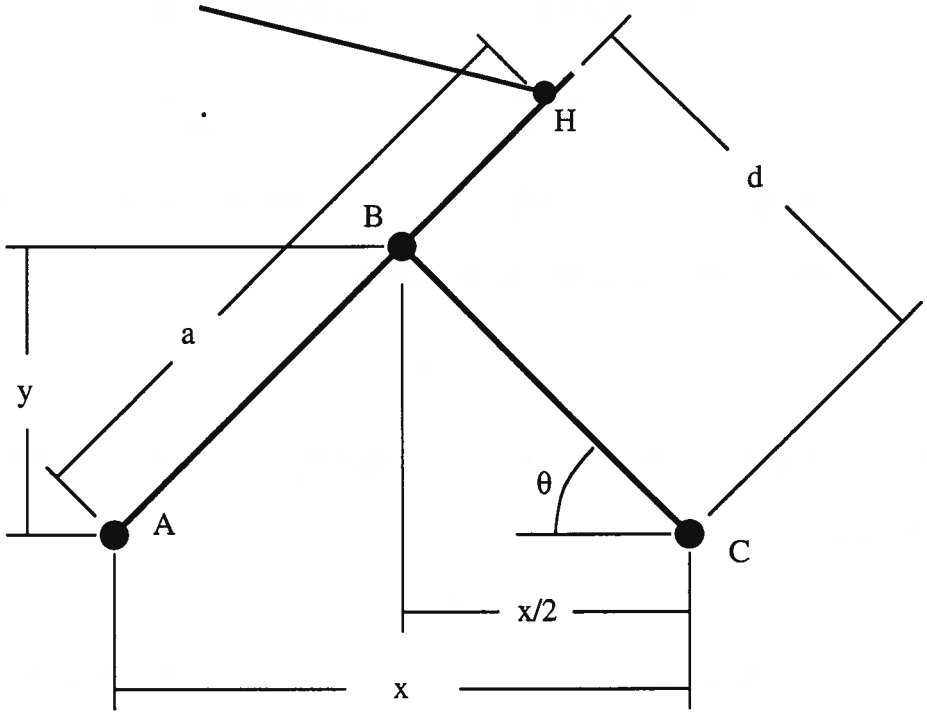

Figure 2.9: Detail Geometry of Base-Arm Mounted Counter-Balance

it can be shown that

$$\sin\theta = \sqrt{1-(x/2d)^2}, \tag{14}$$

and further, that

$$\delta\theta = \frac{-\Delta}{\sqrt{4d^2 - x^2}}. \tag{15}$$

The amount of work done by the force F_n when point C goes through a displacement Δ, then, is

$$\Xi_x = \frac{aF_n}{\sqrt{4d^2 - x^2}}. \tag{16}$$

Using this new value for Ξ_x, equation (10) may be modified, yielding

$$2f(x)\ddot{x} - \frac{df}{dx}\dot{x}^2 - \frac{Bx}{\sqrt{4d^2 - x^2}} = -\frac{aF_n}{\sqrt{4d^2 - x^2}}. \quad (17)$$

Applying the same conditions as before (i.e. all accelerations and velocities are zero) and simplifying presents the surprisingly simple result:

$$F_n = \frac{B}{a}x, \quad (18)$$

which, when supplying values for B and a (assuming point H to lie at the midpoint of AD), becomes

$$F_n = 12.91x \text{ lbs.}, \ 7.5" < x < 25.5" \quad (19)$$

The geometry of the counter-balance makes it prohibitively difficult to find an explicit equation for the *total* force output required, or at least an explicit function that is simple enough to be meaningful; however it is simple to produce a plot showing the required force as a function of extension (see Figure 2.10). Note that although equation (19) gives a linear relation between force and extension, this represents only the normal component of the required output force. Due to the geometry of the counter-balance, the actual output force is non-linear.

2.4 Design of Counter-Balance

There were four major stages in the design of the counter-balance, once the required forces were calculated. First, the pros and cons of each mounting scenario needed to be weighed, to determine the most efficient and cost-effective method.

Second, a conceptual design was to be established, and its feasibility examined. Third, it was required to create a failure-based design of the counter-balance. Lastly, the conceptual and failure-based designs needed to be combined to create a working prototype for the counter-balance.

2.4.1 Selection of Mounting Method

There were three primary factors in selecting an acceptable mounting method for the counter-balance. One is, of course, the effectiveness of the balance in reducing the mass imbalance of the robotic arm. Another factor is the cost of the balance. It was desired to produce the counter-balance as inexpensively as possible, to allow for easier mass-production of the robots. Lastly, and perhaps less obvious, the counter-balance needs to be easily mounted and dismounted, preferably with as few changes to the robot as possible. It is also required that the counter-balance be mountable without dismantling the robot, in whole or in part. Each of the two methods presented various strengths and weaknesses.

Before discussing the benefits and drawbacks of each method, it is first necessary to discuss possible ways of developing the counter-balance force. The two ways examined were springs and air-cylinders.

Springs possess the inherent benefit of being inexpensive. Large springs, suitable for our purposes, may be purchased for approximately $15 - $40. Miscellaneous costs for the creation of the mounting construct would most likely be in the neighborhood of $200. They are relatively easy to connect and disconnect, and it is simple to determine with

great accuracy what behaviors they will demonstrate. Their force output is linear, however, which would make them a poor choice for the base-mounted scenario, as the required force output in the case is extremely non-linear. They would, though, be well suited for the arm-to-base mounted case, in which the force needed as relatively linear. Figure 2.10 shows a sample comparison of the force needed and the force supplied by springs, assuming a spring constant of 60 lb/in.

Air cylinders, on the other hand, are considerably more expensive. A search of various air-cylinder manufacturers revealed a price for air-cylinders to be in the area of $800 - $1200 each. The cost of constructing the mount would, again, likely fall in the realm of $200. They are considerably more bulky, and would be more difficult to mount in the arm-to-base scenario; however, in the base-mounted situation, they would be comparatively simple to fix to the arm. Perhaps the greatest benefit of using air-cylinders is in the nature of the supplied force output. Figure 2.11 shows a comparison of force supplied to force required in the base-mounted case. In this comparison, the ends of the cylinders have been sealed, trapping the air in the cylinders' compartments. Pairs of both 5"- and 4"-cylinders have been shown. Pairs of cylinders are chosen over a single-cylinder solution to provide a symmetry in the counter-balance's design, as there would not be enough room to mount a single cylinder along the axis of the hydraulic actuator (there would be interference with the end-effector during full retraction). As far as ease of mounting, it would be simple to design a suitable mount for the cylinders; though it would most likely be necessary to weld mounting brackets onto the base of the arm. This is because drilling into the steel base with hand-drill would be required otherwise, and it would be difficult to perform this task accurately, given the lack of space in that region.

From these facts, it can be seen that the question of "base-mounting or arm-mounting?" is in fact a question of "springs or cylinders?" While the cylinders have the advantage in the performance area (as can be seen from a comparison of Figures 2.10 and 2.11), the springs have a much greater advantage in the area of cost effectiveness, being up to a couple thousand dollars less. The springs also have an advantage in the field of mounting simplicity, as no modifications would need to be made to the robot, other than a few holes drilled in the base (unlike the cylinders, they there is ample access to the region that needs to be drilled). And, the springs are simple to disconnect, coming off in a matter of minutes, and the entire mechanism could be far more petite, as lower forces are generated (up to 700 lbs, as opposed to upwards of 2500 lbs). From this analysis, it appears that a spring-based counter-balance mounted from base to arm is the best choice, and the rest of this section will focus on the design of such a solution.

2.4.2 Conceptual Design of the Counter-Balance

There are two major design criteria for the counter-balance: it needs to be strong enough to withstand the stresses produced by the force of the springs; and it needs to be capable of fitting within the confines of the current robot design, without interfering the robot's performance. To mount the balance to the base is relatively simple, as the sturdy nature of the base (consisting of 1.5" steel plates) makes it an ideal mounting surface. To mount the balance to the arm, however, requires a more thoughtful plan, as the region of the arm to which the balance would be fixed consists of nothing more than 1/4" thick aluminum tubing, which is unsuitable for drilling. Also, hydraulic lines run along the length of the arm, approximately 3/4" above the surface, restricting access.

To solve the problems of both limited access and limited material strength, friction plates were decided upon. Two 1/4" plates were mounted on the top and bottom surfaces of the arm, and bolted together tightly enough such that the friction generated during operation of the balance would fix the plates in place. The springs themselves could then be fixed to the plates (see Figure 2.12).

To construct the section of the balance that fixes to the base, a tower constructed of steel plate was decided upon. The plate could be bent into a U-shape, which would prove sturdy, while allowing access to the mounting bolts in the base of the tower. To further strengthen the base mounting, tensile straps may be fixed to the top of the tower, and attached to the base of the robot.

Another issue that needs to be addressed is the fact that, as the robot undergoes extension, the orientation of the springs changes with respect to both the base and the arm. For this reason, swivels need to be placed on both mounting constructs to allow for re-orientation of the springs. These swivels will also ensure that the springs will undergo the same displacements, which will provide symmetry in the distribution of the forces (see Figure 2.12). The final conceptual design can be seen in Figure 2.13.

2.4.3 Failure-Based Design of the Counter-Balance

Looking at the preliminary design of the counter-balance, there are two critical areas that need to be designed for possible failure, both from fatigue, and from yielding.

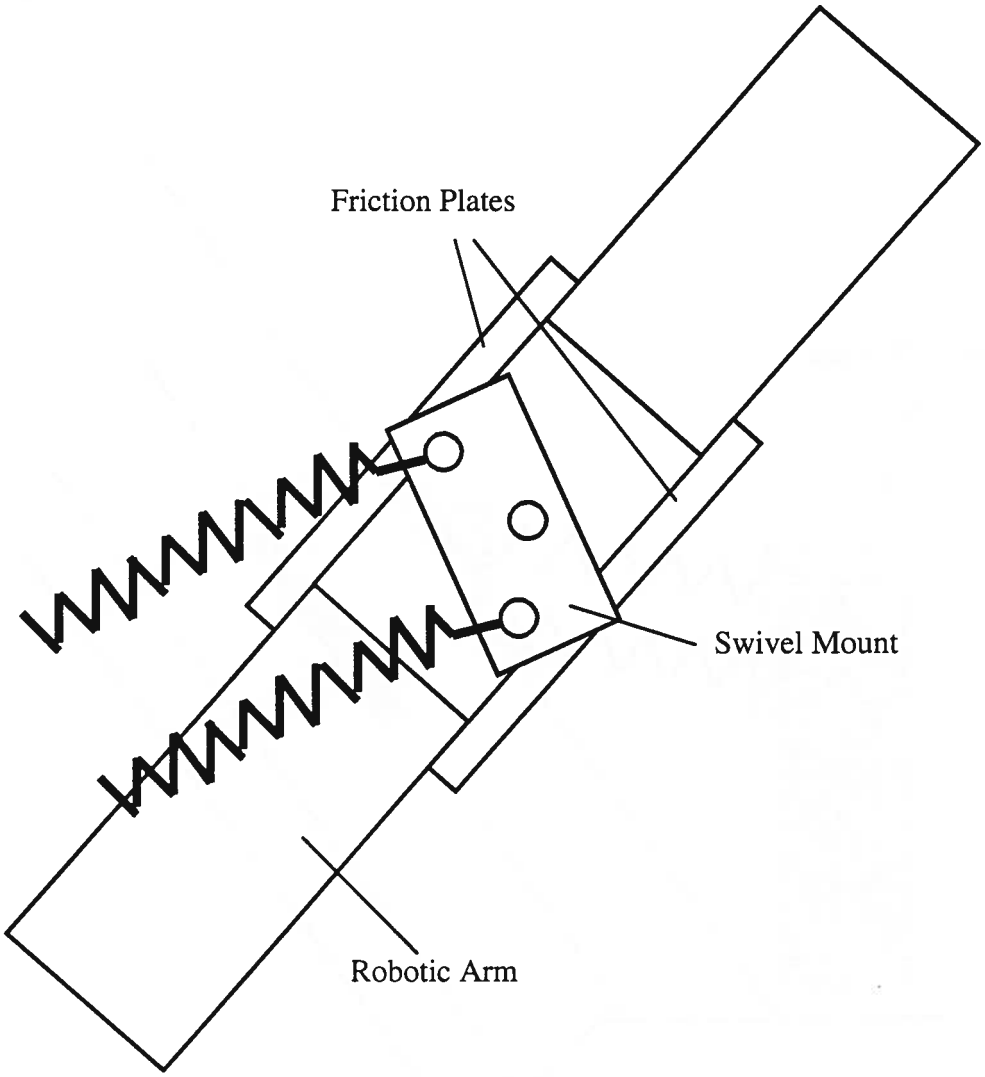

Figure 2.12: Detail of the Counter-Balance Friction Plates

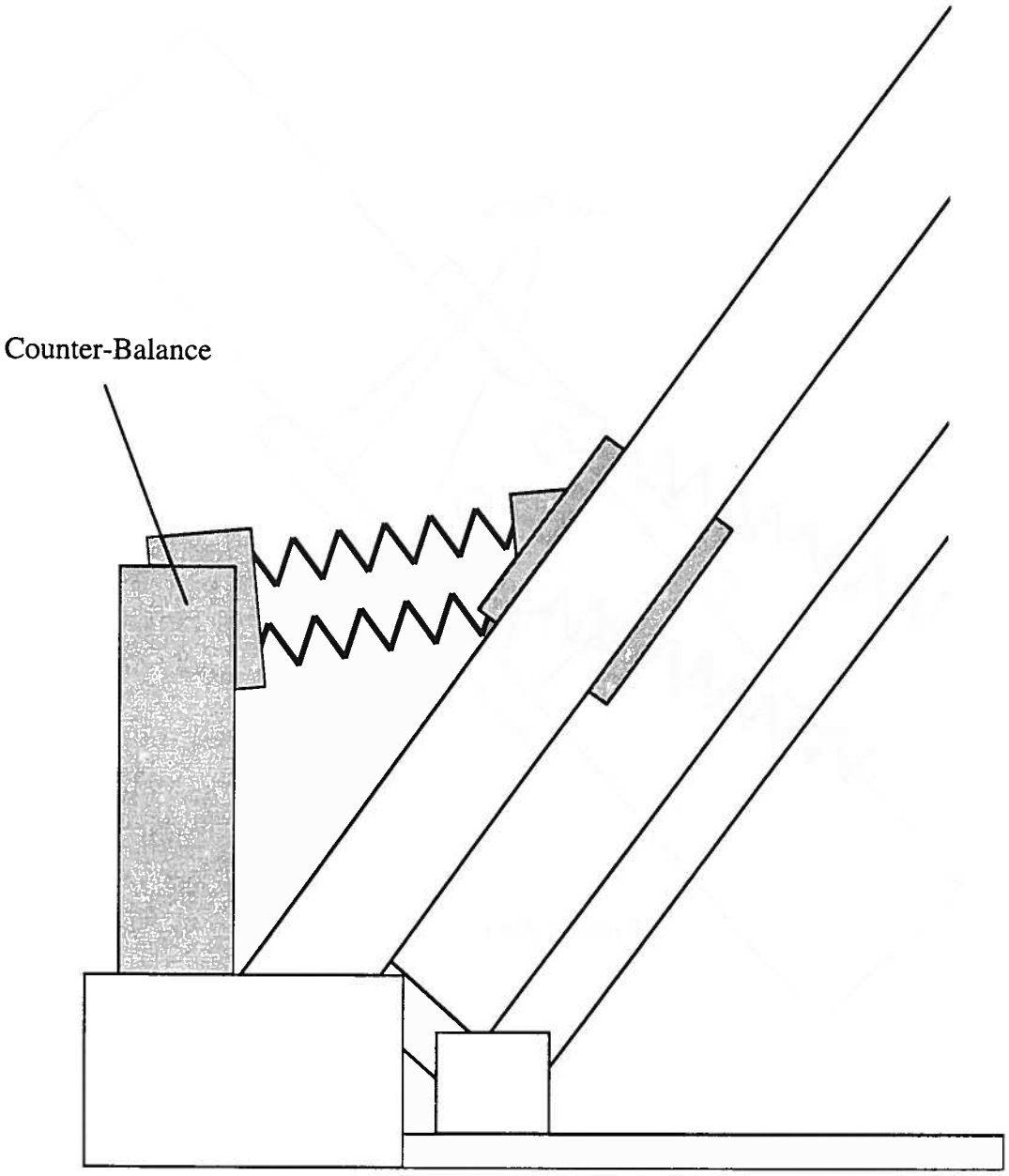

Figure 2.13: Conceptual Design of Counter-Balance

The first is the mounting of the tower; the second is the swivel rod that holds the mounting construct for the springs.

2.4.3.1 Design of Tower

A free-body diagram of the tower appears below:

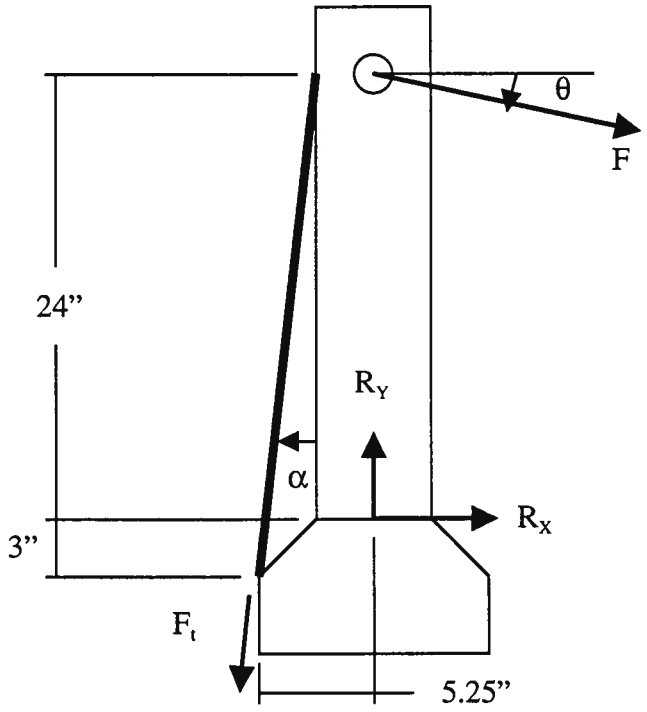

Figure 2.14: Free-body Diagram of the Counter-Balance Tower

In this diagram, the forces R represent the reaction forces on the bolts that hold the tower in place, and F_t is the tensile force in the tension straps. Summing moments and forces yields the following system of equations:

$$\begin{aligned} R_Y - F\sin\theta - F_t\cos\alpha &= 0 \\ R_X - F\cos\theta + F_t\sin\alpha &= 0 \\ 24(F\cos\theta) - 5.25(F_t\cos\alpha) + 3(F_t\sin\alpha) &= 0 \end{aligned} \tag{20}$$

The value for F will reach a maximum of 2300 lbs when θ is equal to 13.2 degrees. Using these numbers, as well as the value for α of 6.3 degrees, the reaction forces are found to be:

$$\begin{aligned} R_X &= 570.0 \ \ lb \\ R_Y &= 4920 \ \ lb \\ F_t &= 4694 \ \ lb \end{aligned} \tag{21}$$

The reaction force R_Y will be a compressive force upon the base of the tower, and will not present a problem. Similarly, the force R_X will be held by 3/8" hardened steel bolts, and is not critical. However, the 4694 lb tensile load in the tension straps may present a problem, and a failure analysis should be performed here, both for yielding and for fatigue.

To design for yielding, it is first necessary to determine the critical stresses in the strap. Since the strap is of uniform shape and thickness throughout, it is simply necessary to find the tensile stress at any point along the strap's length. The equation for tensile stress in a beam is given by

$$\sigma_a = \frac{F_t}{A}, \tag{22}$$

where A is the cross-sectional area of the strap. To assure that the strap does not fail under yielding, it is required that

$$\frac{\sigma_{all}}{\sigma_a} > n, \tag{23}$$

where n is the factor of safety desired. For safety purposes, a factor of safety of 5 will be used in this analysis. Using the maximum tensile stress for hot-rolled AISI 1040 steel (74kpsi), and the previously determined value for the tensile force, and solving for the area:

$$A > \frac{nF_t}{\sigma_{all}} = \frac{(5)(4694lb)}{74000psi} = 0.317in^2 \tag{24}$$

Therefore, any strap with a cross-sectional area greater than 0.317 in^2 will be sufficiently safe.

To design for fatigue, it will be necessary to determine the yield strength of the material, by applying several modifying factors (based on the nature of the loading) to the tensile strength. The tensile strength, as stated above, is 74 kpsi. The equation for the yield strength, then, is

$$S_e = k_a k_b k_c k_d k_e S_{ut} \tag{25}$$

where:

S_{ut} = tensile strength of the material

k_a = surface factor (determined by the finish of the material)

k_b = size factor (determined by the geometry of the material)

k_c = loading factor (determined by the nature of the load)

k_d = temperature factor (determined by temperature conditions)

k_e = misc. factor (includes factors such as stress concentration, corrosion, etc.)

The temperature factor will be 1.0, since the counter-balance will not be used in extreme temperatures. The miscellaneous factor will also be 1.0, due to the absence of any relevant conditions. The size factor will be 1.0, as well, because it does not apply to

tensile loading. The loading factor will be 0.923, which corresponds to tensile loading. The surface factor is defined as

$$k_a = aS_{ut}^{\ b} \tag{26}$$

with a = 14.4 and b = -0.718 (values defined for hot-rolled steel). Using these values yields a surface factor of 0.655. Substituting these modifying factors into equation (25) provides a yields strength of S_e = 44.7 kpsi.

The value of maximum axial load used for the fatigue analysis will be different than the one used in the yielding analysis. This is because the arm rarely extends so far as to generate these stresses. The maximum extension the arm will experience during normal operation is roughly 2/3 of its full range. Therefore, a load value of 2551 lbs, corresponding to this extension, will be used.

The Goodman criteria will be used in this analysis, as it is a good example of a conservative analysis, and is suitable for a situation such as this, in which safety is of prime concern. The Goodman criteria is as follows:

$$\frac{\sigma_a}{S_e} + \frac{\sigma_m}{S_{ut}} < \frac{1}{n} \tag{27}$$

In this equation, σ_a and σ_m represent the amplitude and mean of the stress fluctuations, respectively. In this case, since the stress varies between 0 and the maximum stress, each of these stresses will be equal to half the maximum stress. Substituting equation (22) for the axial stress, and solving for the area,

$$A > \frac{nF_t}{2}\left(\frac{1}{S_e} + \frac{1}{S_{ut}}\right) \tag{28}$$

which yields a minimum area of A = 0.229 in^2. Since the minimum area determined in the yielding analysis is the greater than that in the fatigue analysis, it will be used. Straps with dimensions of 1.5" x 0.25" will suffice, and were used in the final design.

2.4.3.2 Design of Swivel Rod

Similarly to the tower, the swivel rods need to be designed for both yielding and fatigue. From the diagram of the spring mount below, it can be seen that rod B is the critical member, as it will be susceptible to twice the load of rods A and C.

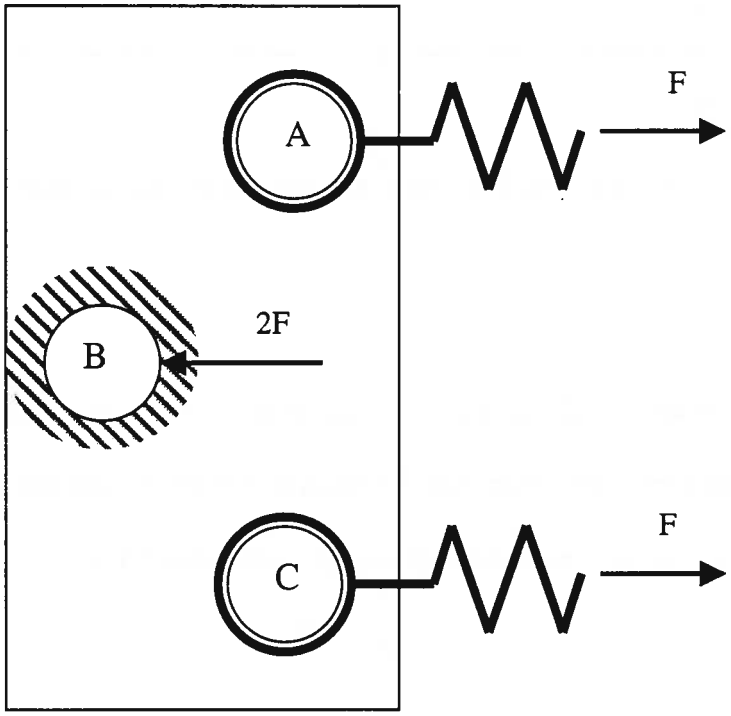

Figure 2.15: Counter-Balance Spring Mount

Because of this, it will only be necessary to design rod B, as all rods will be identical.

From the free body diagram of the rod shown below, with a known maximum force F on the spring mount of 2300 lbs., and using the symmetry of the problem, the reaction forces (R1 and R2) at the pins may be determined to be 1150 lbs. It is apparent

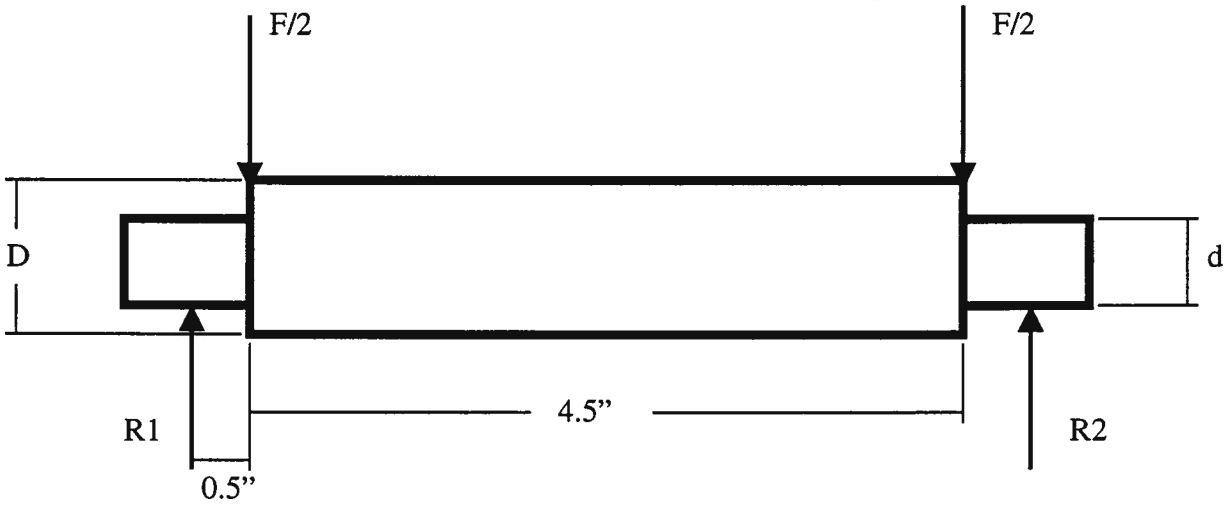

Figure 2.16: Free-Body Diagram of the Swivel Rod

that the critical stresses will occur in the pins, at the junction of the pin and the body of the rod. The moment at this point will be equal to 575 lb-in., and the stress here may be calculated as for a simple beam with cross-sectional moment, I, as

$$\sigma = \frac{My}{I}, \tag{29}$$

where M is the moment, and y is the distance from the center axis of the rod. Since the maximum stress will occur at the surface of the pin, and I may be given as $I=\pi d^4/32$,

$$\sigma = \frac{M(d/2)}{\pi d^4/32} = \frac{16M}{\pi d^3} \tag{30}$$

Using this equation for the stress in equation (23), and assuming a value for the allowable stress of 11 kpsi (2024 aluminum alloy), and a safety factor of 5,

$$d > \sqrt[3]{\frac{16Mn}{\pi\sigma_{all}}} = 0.698in \tag{31}.$$

To find the minimum radius for fatigue, equation (25) is again used to find the endurance strength. In this case, k_a = 0.973 (machined finish), k_b = 0.901 (using the equation $k_b = (d/0.3)^{-0.1133}$, and guessing a value for d of 0.75 in.), k_c = 1.0 (for bending), k_d = 1.0, and k_e = 0.755 (due to stress concentration at the junction of the pin and the body of the rod). Inserting these numbers into equation (25), a value of S_e = 29.8 kpsi is found.

The Goodman criteria (equation (27)) will again be used, with the amplitude and mean of the loading once again equal to half the maximum stress,

$$\sigma_a = \sigma_m = \frac{8M}{\pi d^3} \tag{32}$$

Plugging everything into equation (27), and solving for the diameter, d:

$$d = \sqrt[3]{\frac{8}{\pi} Mn\left(\frac{1}{S_e} + \frac{1}{S_{ut}}\right)} \tag{33}$$

Inserting values reveals a minimum value for the diameter of d = 0.742 in. A diameter of d = 0.750 will be used for the pins, which satisfies both yielding and fatigue criteria.

2.4.4 Final Design of the Counter-Balance

From the failure analysis above, the final design pictured in Figure 2.17 was developed. The spring mounts are designed to hold up to four springs, but a two spring configuration may also be used, with one spring on each rod instead of two. Of special interest is the friction plate, which is most likely the weakest element of the counter-balance. It is believed to provide sufficient friction force to keep from sliding, based on a previously built counter-balance (designed by Richard Blank) that contained similar friction plates, and was able to keep from sliding. The plates in this design have been made wider along the axis of the arm, to provide additional friction force. Even in the event that the plates cannot supply enough force to remain stationary, they will simply slide down along the arm, and will neither cause damage to the structure of the robot, nor present any safety risk to people in the surrounding area.

As an added precaution, the rods in the swivel mounts that are in contact with the base and arm mounts have been made from steel, rather than aluminum. It was decided that these were of critical importance, as a failure here could cause the springs to fly from the robot, possibly causing injury. The rods in contact with the springs are still constructed of aluminum, as they face only half the load of the critical rods.

Cables have also been inserted through the length of each spring, and mounted to the swivel mounts. This is to prevent a failure in the springs from sending broken spring parts sailing into nearby persons.

Installation of the counter-balance required two people and a couple of hours. Most of this time was spent securing the friction plates, so as to insure that the springs are taut at full retraction. The installation can be performed by one person, but will take

more time, perhaps on the order of three hours total. As an additional measure of convenience, the springs are mounted with spring clips, such that they may be removed without detaching the base or arm mounts. This allows testing or maintenance to be performed without the springs, without having to remove more than necessary. Removal of the springs requires about 5 minutes, and replacing them requires about 10.

2.5 Testing of Counter-Balance

Several tests were performed with the counter-balance on, in both 3- and 4-spring configurations, to test the effects of various spring constants. There were three basic geometry tests performed, as well as a test run of the letter 'S'. The geometry tests consisted of two arcs, drawn both during extension and retraction, and a circle (Figure 2.17). These tests represent extreme motions, and reflect performance requirements that should not actually be necessary during normal operation. The test run of the 'S' represents the most demanding of the markings that will be painted in everyday use. It uses three of the five primitives determined to be necessary for all roadway markings. Other letters had not been optimized for testing as of this writing.

Results of the geometry tests occur in Figures 2.18-2.20, with details of the plots shown in Figures 2.21-2.23. From these plots, two things are readily apparent. One is that the counter-balance does little to reduce the overall level of error in the motion of the robot. Therefore, it is difficult to discern any appreciable difference between the motions on a large scale. Do determine whether or not the counter-balance eliminates any of the wag of the robot, it is necessary to examine the detail drawings of these motions.

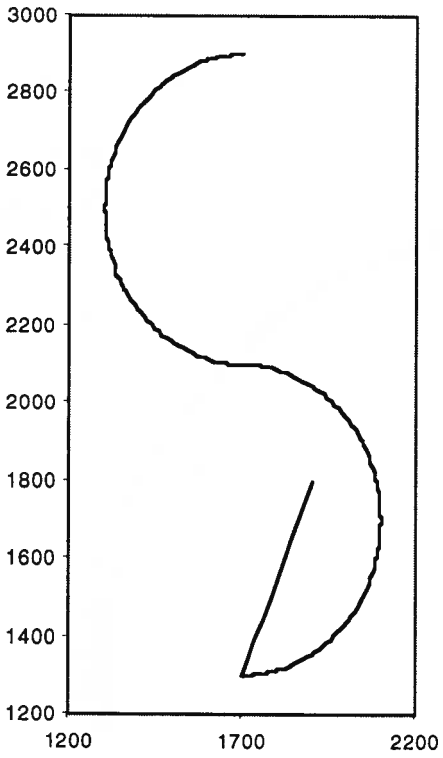

2 Arcs (Extension)

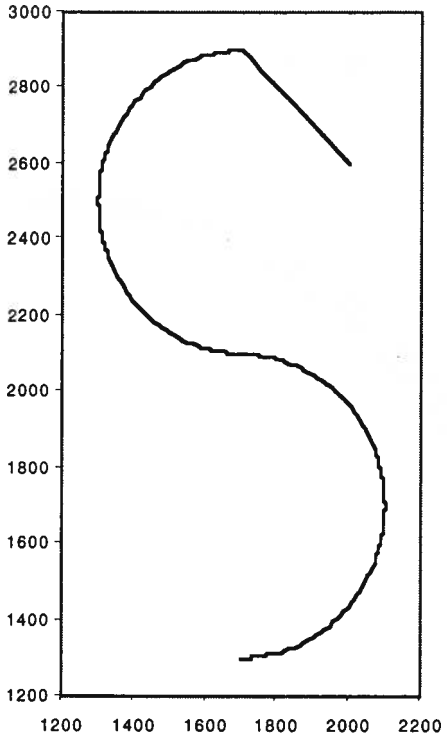

2 Arcs (Retraction)

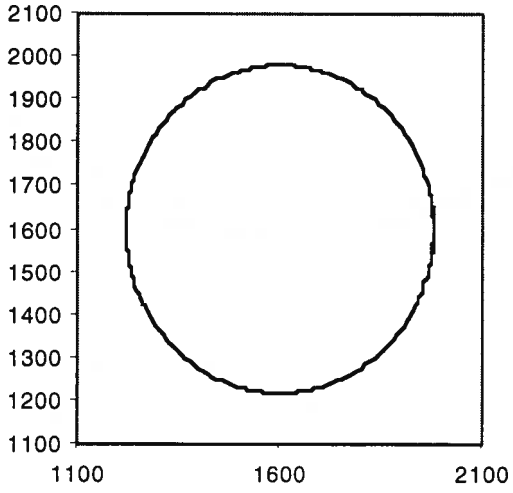

Circle

Figure 2.17: Desired Patterns for Geometry Tests

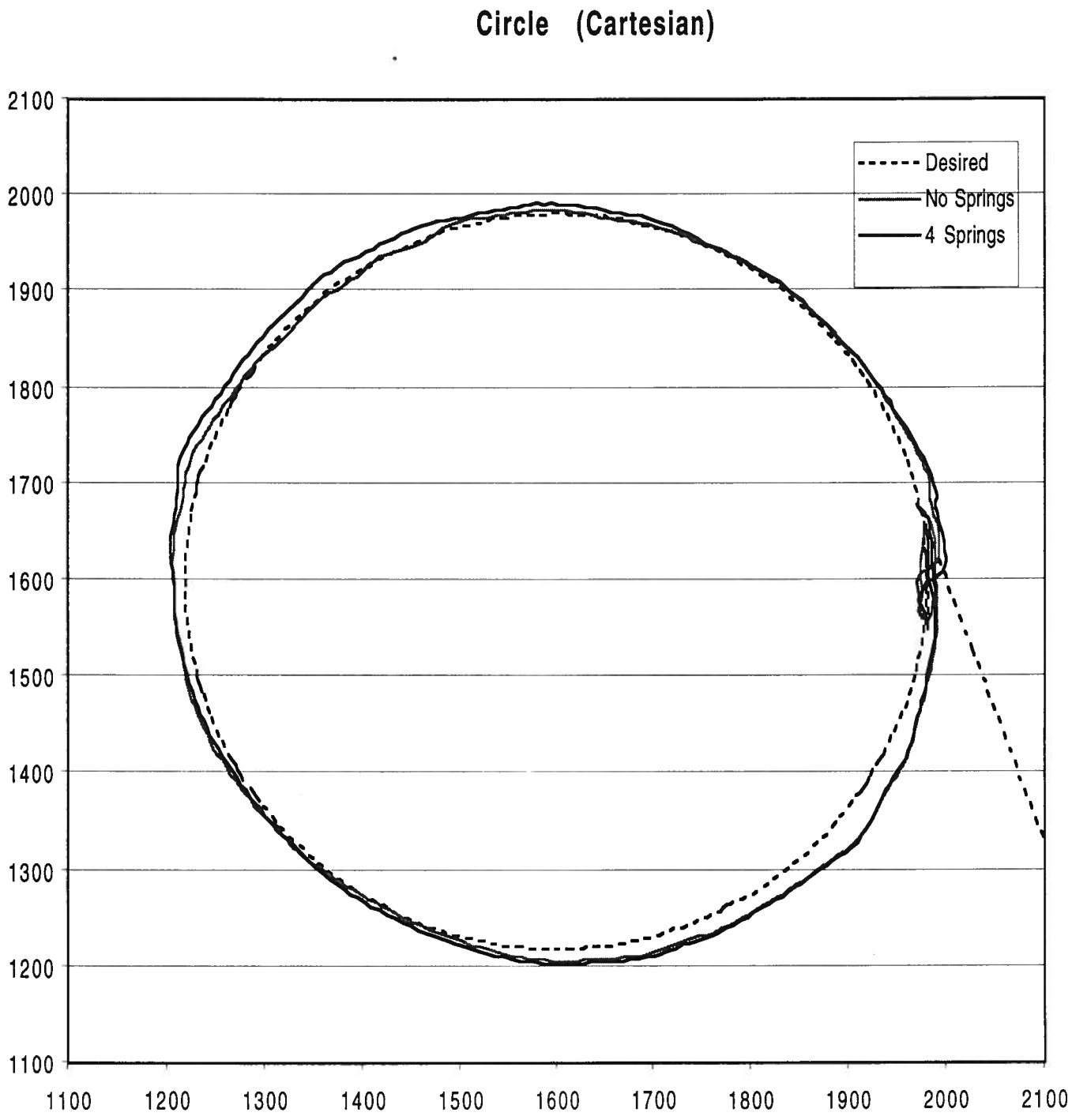

Figure 2.18: Counter-Balance Performance Test (Circle)

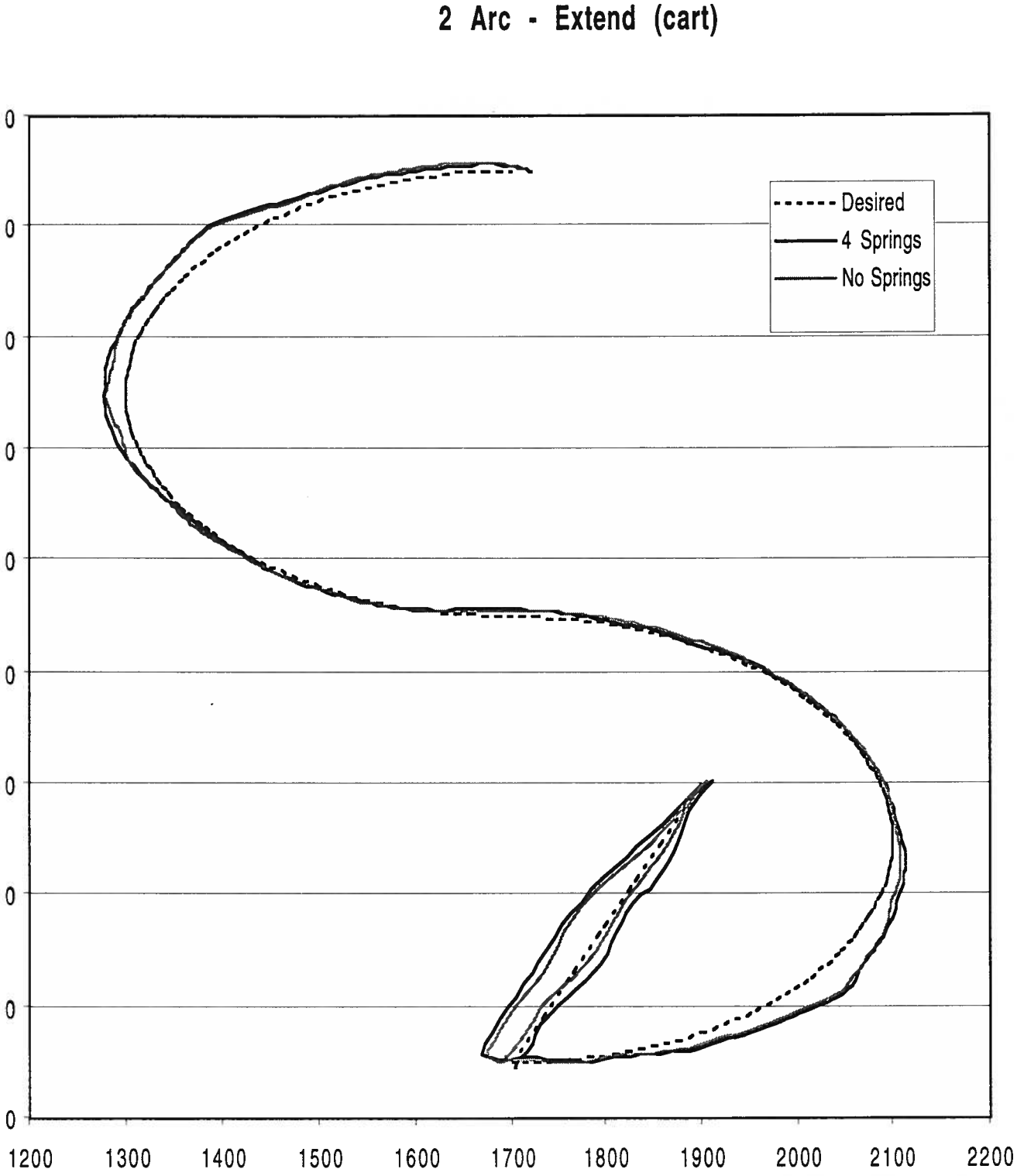

Figure 2.19: Counter-Balance Performance Test (2 Arcs During Extension)

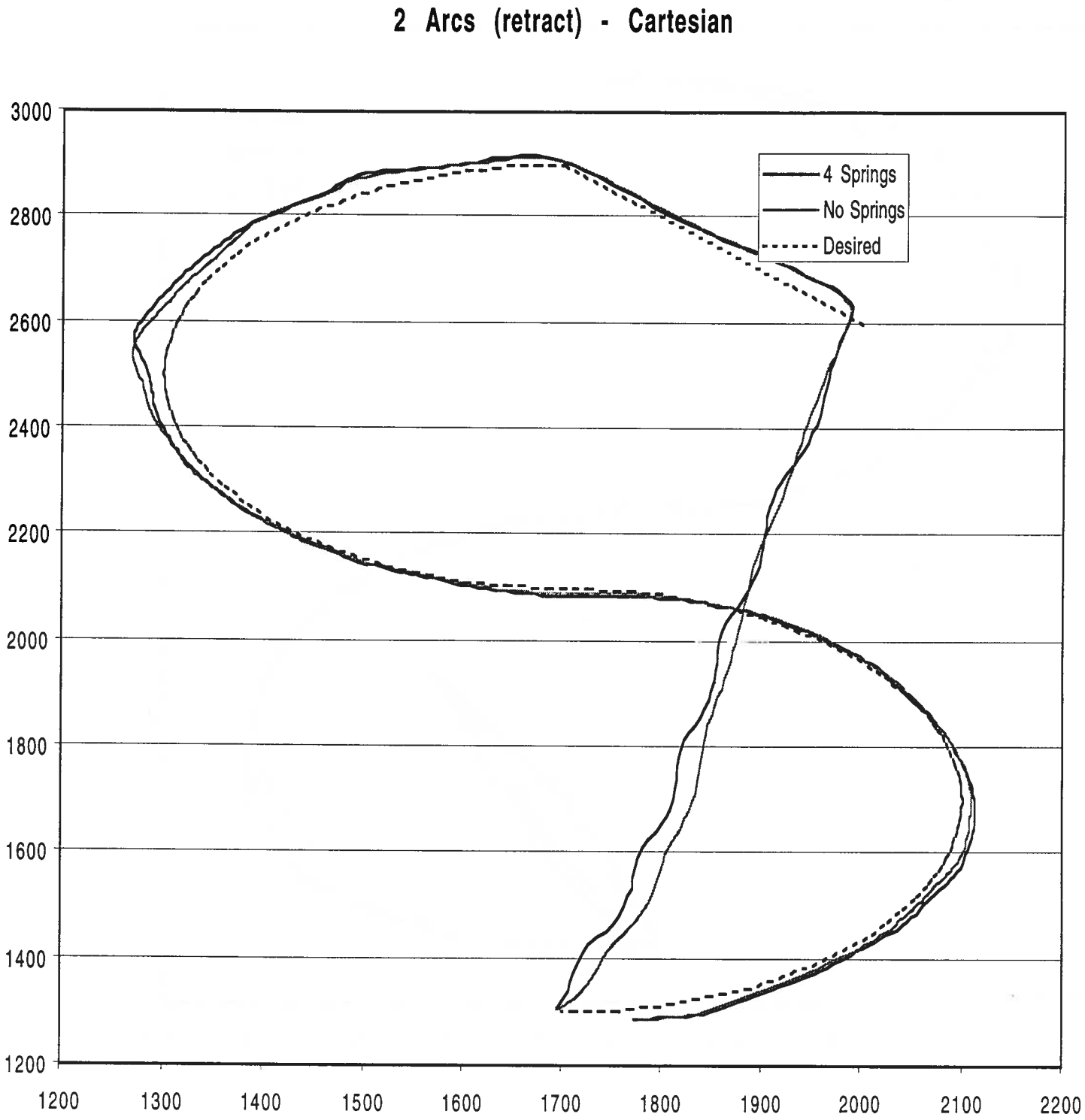

Figure 2.20: Counter-Balance Performance Test (2 Arcs During Retraction)

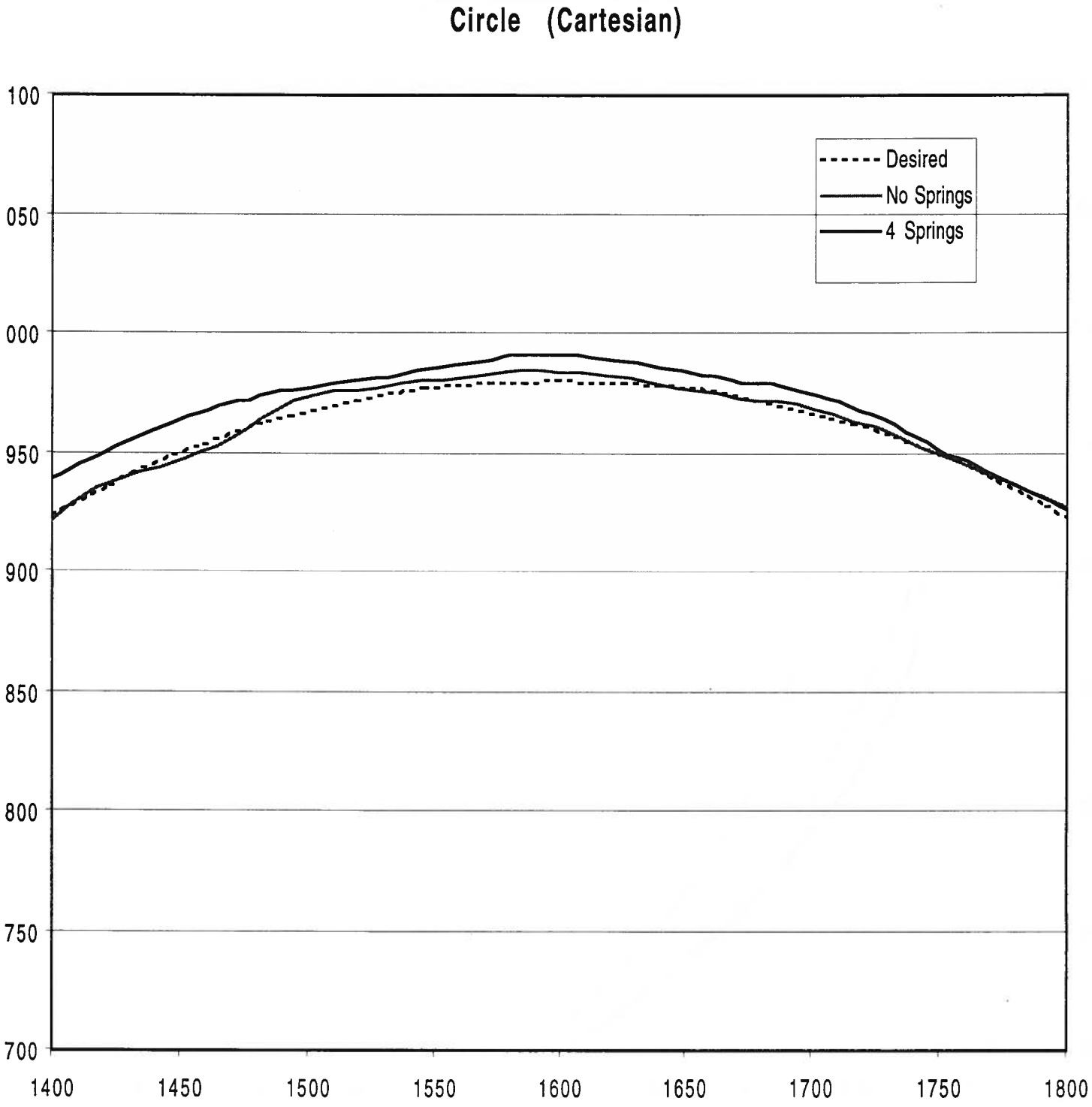

Figure 2.21: Performance Detail (Circle)

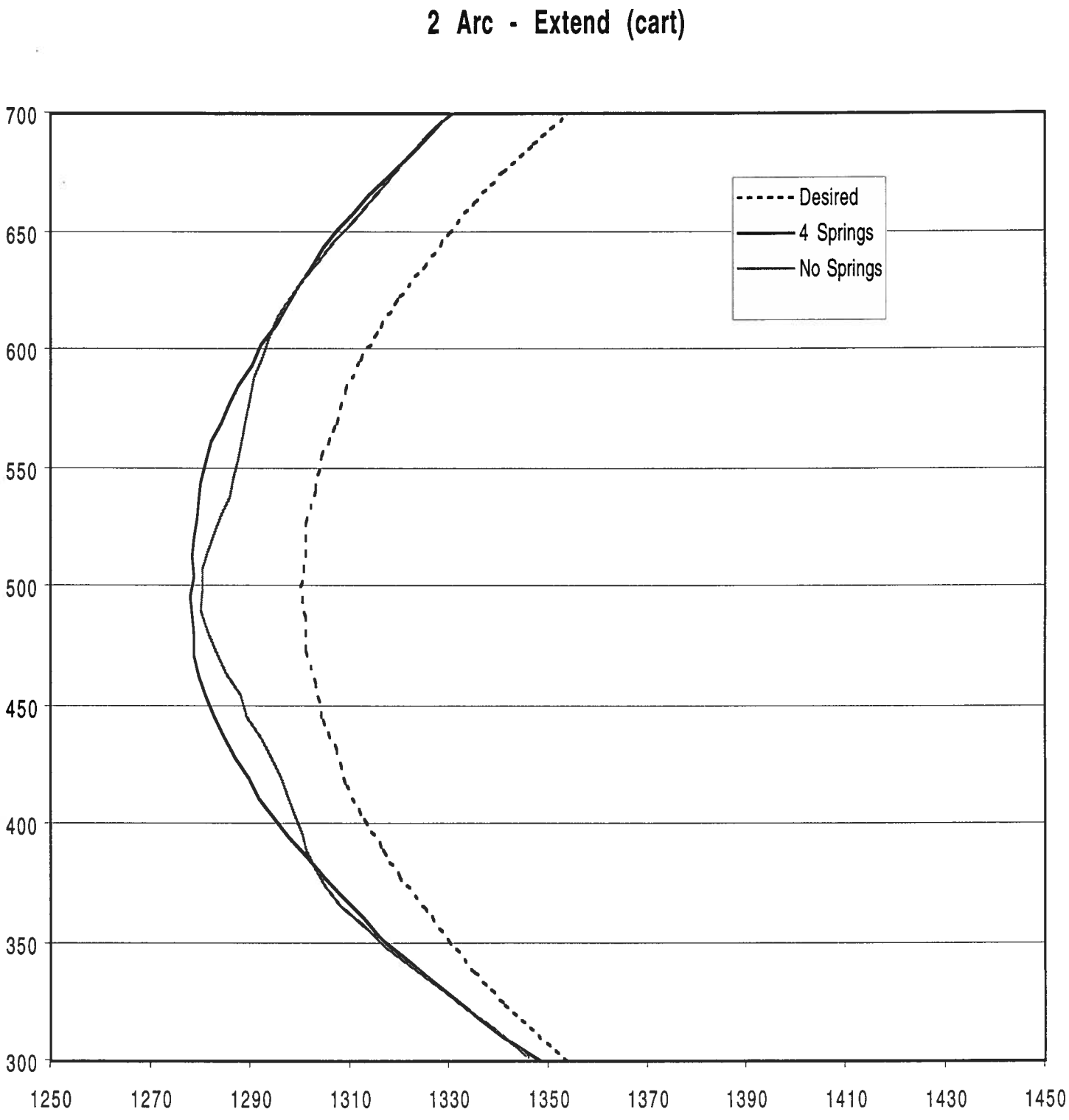

Figure 2.22: Performance Detail (2 Arcs During Extension)

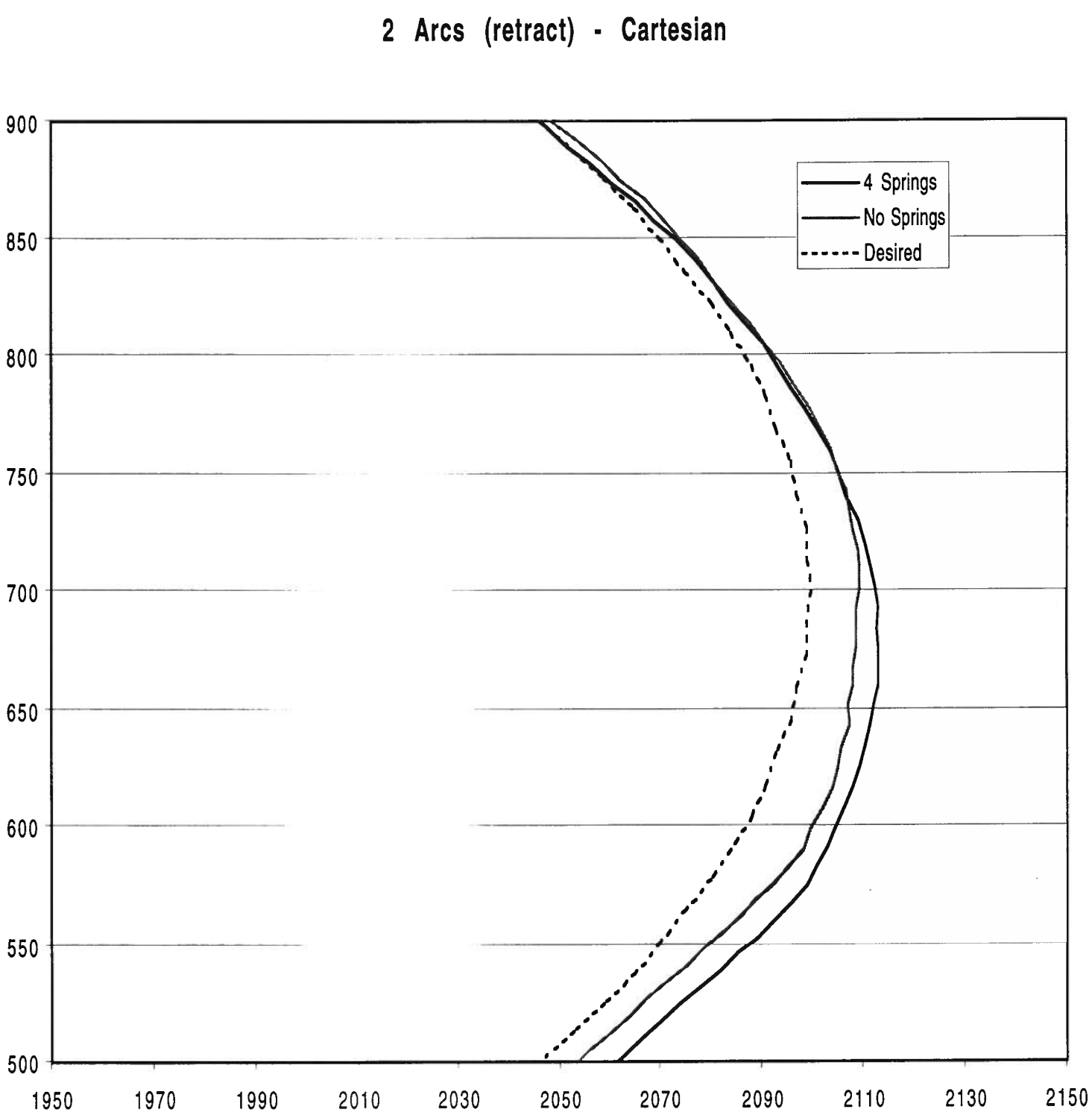

Figure 2.23: Performance Detail (2 Arcs During Retraction)

From the details of the performance plots, it can be seen that the counter-balance appears to have a beneficial effect on the robot wag. The balance does add a small amount of error to the motion of the robot, but it does so in a manner that improves the overall smoothness, while maintaining the integrity of the intended shape.

The plot of the letter 'S' appears in figure 2.24, with a detail plot in figure 2.25. Here, some problems are encountered – most notably the large waves that occur throughout the motion. There are three possible explanations for this: first, the waves may be the result of the control system not being optimized for this particular mechanical system; second, the springs may be enhancing the oscillations already present in the motion, thereby causing large-scale vibrations when the robot moves near the springs' natural frequency; or third, the hydraulic actuator may require loading, and the removal of most or all of that loading may be causing the actuator to overcompensate during motion. If the first case is true, then simply adjusting the gains would show a decrease in these vibrations. If the second is true, then the springs may be adjusted such that their natural frequency is substantially above that of the robot's motion. This may cause problems, though, as stiffer springs could generate more counter-balancing force than is desirable. If the third case is the problem, then the springs may be made less stiff, to allow some loading to remain on the actuator. If the problem is actually some combination of these three cases, however, difficulties may arise, as the listed solutions to cases 2 and 3 are mutually exclusive.

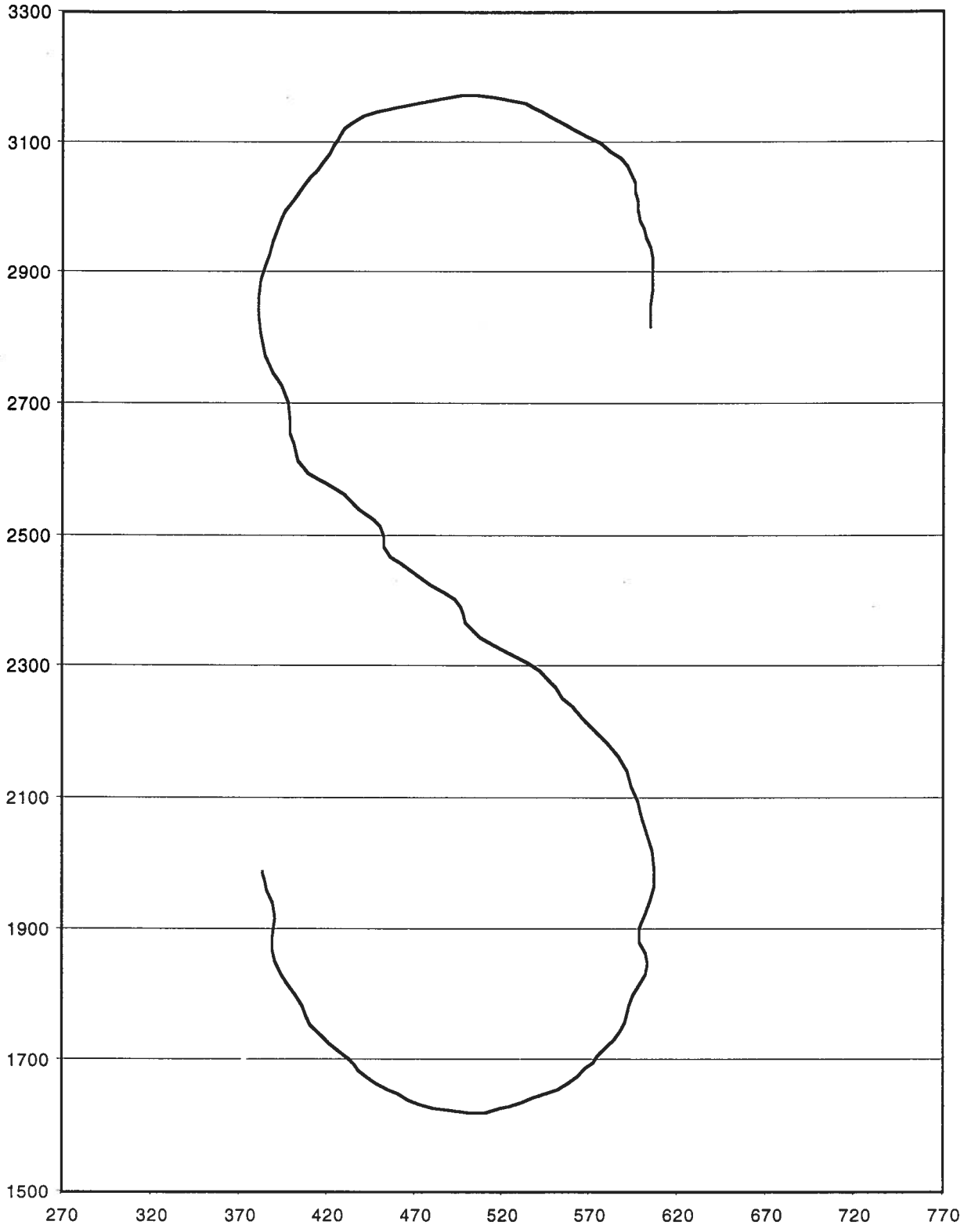

Figure 2.24: Performance Plot (Letter 'S')

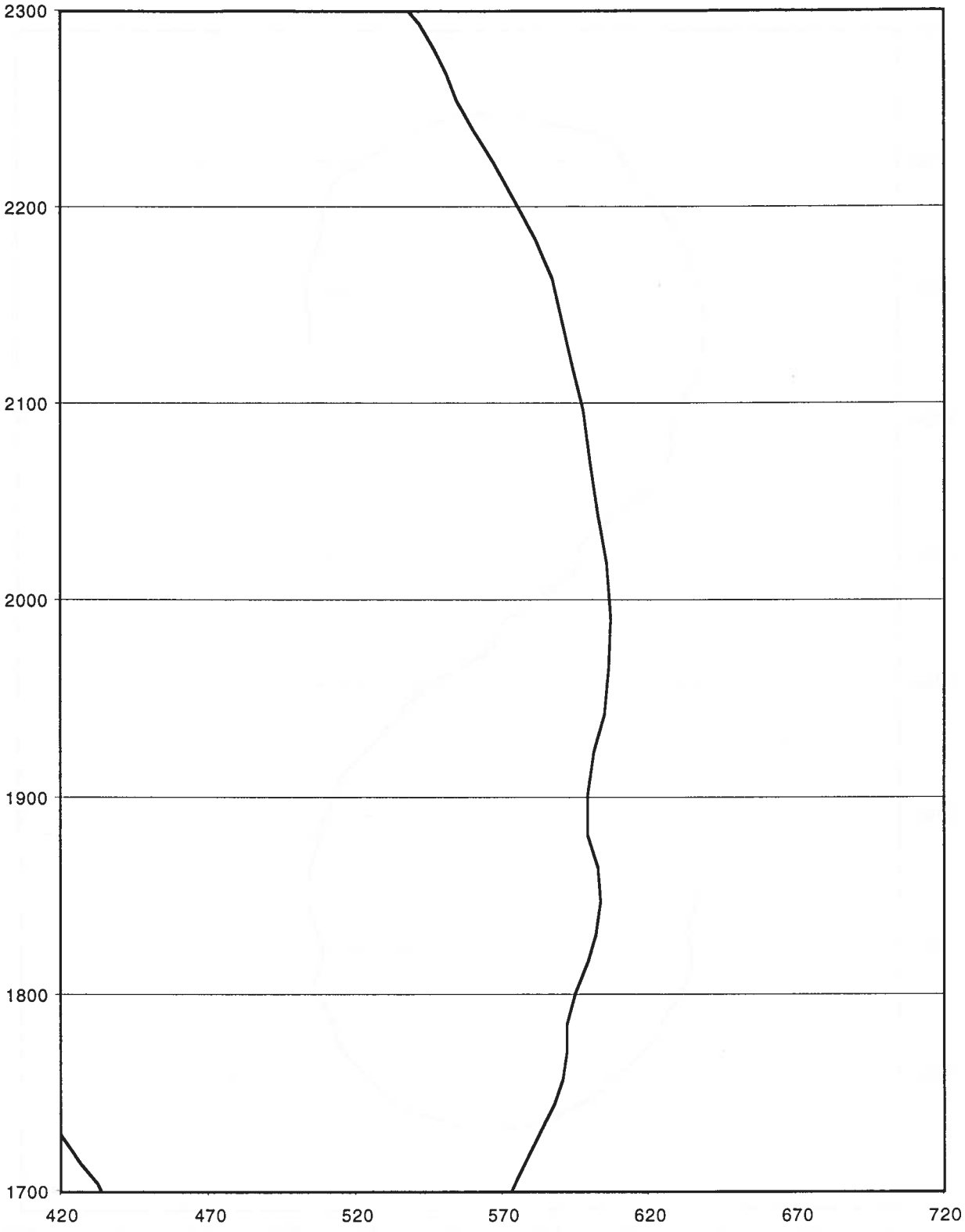

Figure 2.25: Performance Detail (Letter 'S')

Chapter 3

A Mechanical Redesign of the End-Effector Rotary Shaft

3.1 Problems with Current Rotary Shaft System

The end-effector provides three degrees of freedom to the paint gun: translation along the vertical axis (achieved via hydraulic actuator), rotation about the vertical axis (achieved via stepper motor), and tilt along another axis (also achieved via stepper motor) (Figure 3.1). These three degrees of freedom, in conjunction with the two provided by the robotic arm, allow the paint gun to be placed in any position required for any roadway markings.

The current problem with the end-effector lies in the rotation about the current axis. The center of gravity of the construct that holds the paint gun is offset from the axis of rotation by approximately 3" (see Figure 3.2). This imbalance, in conjunction with the long and slender nature of the rotary shaft upon which this construct is mounted, leads to a wobbling motion apparent in the rotation about the axis. At low speeds, the wobble is

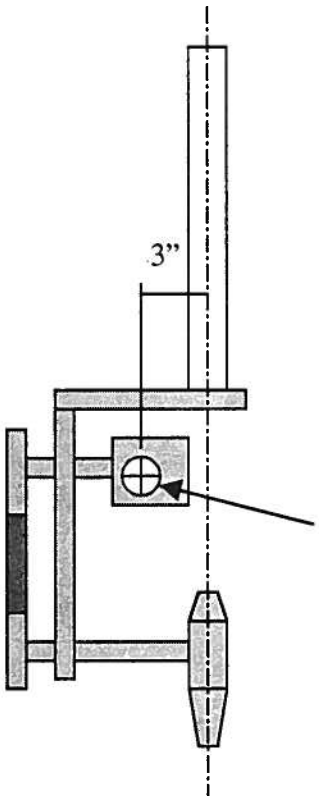

Figure 3.2: Mass Imbalance in Paint Gun Construct of the End-Effector

negligible, but at higher speeds (approximately 1 rpm), the wobble is considerable. It is not certain how much of an effect this wobbling would have upon the quality of painted markings, but it is assumed that there would be some detriment. It is thus desired to minimize the wobble.

There are two obvious ways two fix this problem. The first is to redesign the paint gun mount and tilting system so that the center of mass lies directly below the rotary shaft. The simplest way to do this would be to add a counter-weight to the side of the mount opposite the mass imbalance. The mass of this construct is about 12 lbs. At a distance of 3" from the axis of rotation, this means a counter-moment of 36 lb-in is required. In order to do this without adding excessive bulk, though, the counter-weight would need to be placed relatively close to the axis of rotation, i.e., within a few inches. This translates to an extra 10 lbs. or so being added to the weight of the construct. This is undesirable, for two reasons: first, adding more mass to the end-

effector will increase the amount of mass that needs to be manipulated by the robotic arm, and could lead to lowered performance; secondly, and more importantly, it adds to the mass that must be moved by the stepper motor, and the increased torque requirements would certainly impact the quality of the rotation. If the paint gun mount, then is to be modified, it must be completely redesigned. This is also undesirable, as it would lead to a considerable loss of time and resources. This will therefore only be considered as a last resort.

The second approach to this problem is to increase the stiffness of the shaft system that transmits the rotation from the stepper motor to the mount. This system consists of only three parts (the shaft itself, and mounting constructs on either end), all of them fairly simple to create, compared to approximately a dozen mating parts in the gun mount. It is also easy to access the shaft system, and adding extra bulk will not interfere with the operation of the robot. Also, small amounts of weight may be added to the system without appreciably increasing the torque requirements of the stepper motor, as the torque required to spin the shaft is small compared to that required to spin the gun mount. It is this method that will be approached in the remainder of this chapter.

3.2 Design of a New Shaft System

In order to effectively design the new shaft system, two things must be known: first, what deflections the current shaft system is undergoing; and second, what deflections are desired. To determine what deflections are currently occurring in the shaft, the shaft will be treated as a simple beam of varying cross-section, with constant forces being applied to the system. After

the deflections are determined, it will be possible to determine a desired maximum deflection based on a fraction of the current.

3.2.1 Deflections in the Current Shaft System

As stated before, the shaft system will be treated as a simple beam. All junctions between mating pieces are very stiff; therefore it will be assumed that the matings of the pieces are perfectly rigid, and that any deflections are due to bending in the shaft itself. An assembled and disassembled drawing of the current shaft system appears in Figure 3.3. A free-body diagram of the shaft system, shown as a single rigid piece, appears in Figure 3.4.

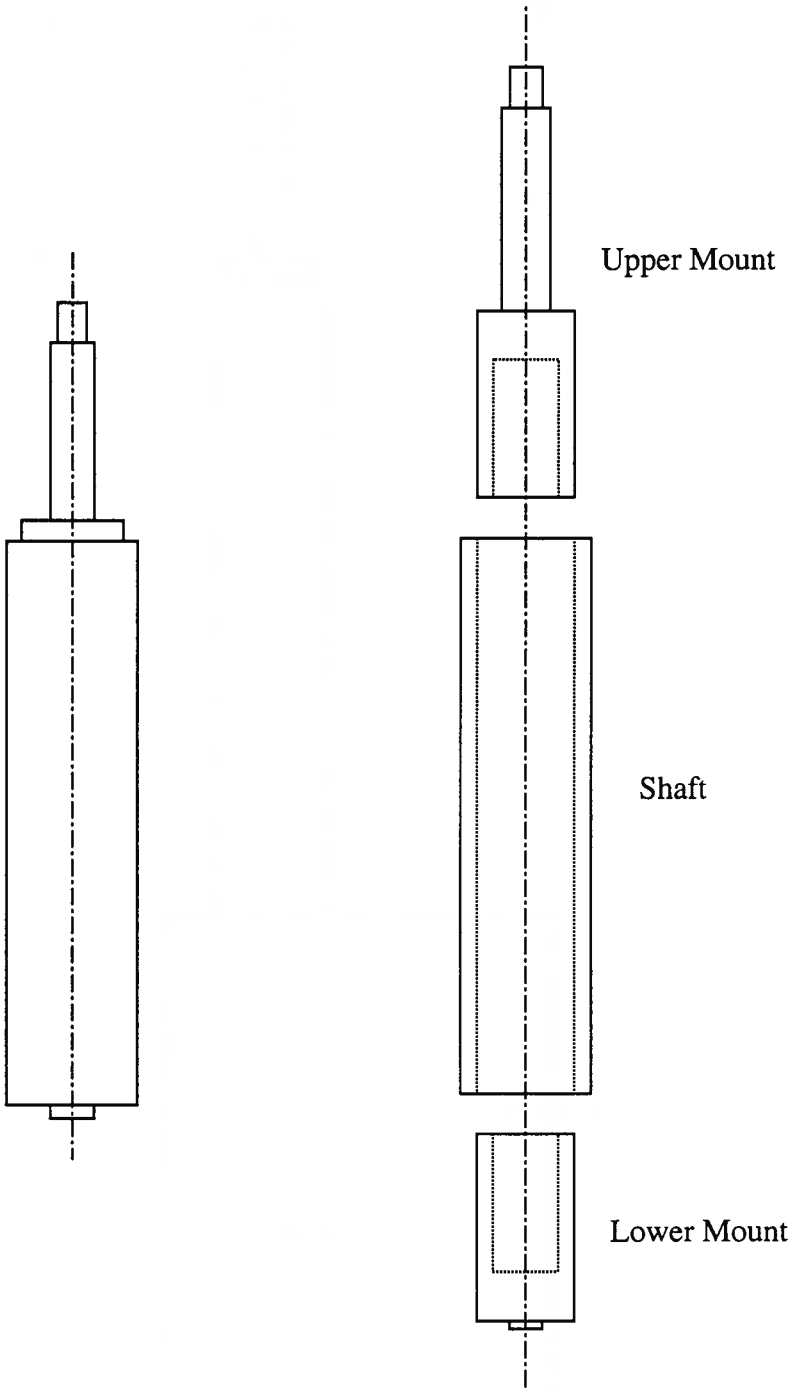

Figure 3.3: Assembled and Exploded Views of End-Effector Shaft System

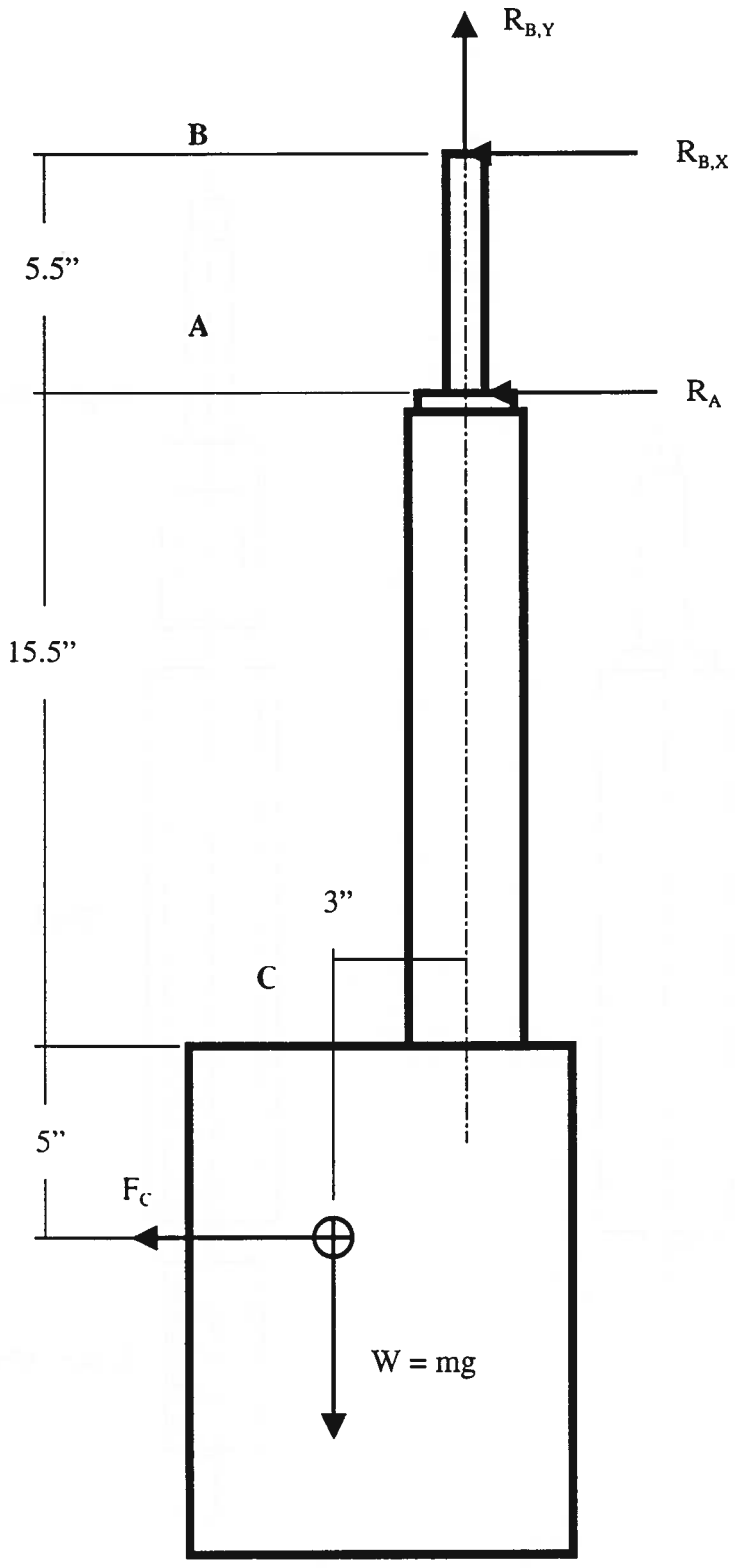

Figure 3.4: Free-Body Diagram of the Shaft System

In this diagram, W represents the weight of the paint gun mount (12.0 lbs.), F_C is the side load resulting from the centripetal acceleration of the mount, and the forces R are the reaction forces from the shaft supports. The force F_C can be found simply as

$$F_C = m\omega^2 r, \tag{1}$$

where m is the mass of the paint gun mount, ω is the angular velocity of the shaft, and r is the distance between the axis of the shaft and the CG of the gun mount. The maximum angular velocity will be taken to be 1 rpm, or 6.28 rad/sec. This Figure represents a value moderately higher than what the shaft needs to achieve during normal operating conditions. Using this value, as well as those for the mass and distance, yields a maximum value of $F_C = 3.66$ lbs.

To find the deflection at C, it is first necessary to find the reaction forces at A and B. Summing forces in the x- and y-directions, and moments about A, yields the following system of equations:

$$\begin{aligned} \Sigma F_X &: \; R_A + R_{B,X} + F_C = 0 \\ \Sigma F_Y &: \; R_{B,Y} - W = 0 \\ \Sigma M_A &: \; R_{B,X}(5.5") + W(3") - F_C(20.5") = 0 \end{aligned} \tag{3}$$

Substituting the values for F_C and W gives the reactions:

$$\begin{aligned} R_A &= -10.48 lbs \\ R_{B,X} &= 6.82 lbs \\ R_{B,Y} &= 12 lbs \end{aligned} \tag{4}$$

These reaction forces may now be used to find the deflection at point C.

The deflection at a point due to bending may be found using the equation [McGraw]:

$$y'' = \frac{M}{EI} \tag{5}$$

Here it is assumed that the deflections are small. The moment at a point along the beam is shown below in Figure 3.5, and can be determined explicitly as

$$M = \begin{cases} 6.82x \ \ lb-in, & 0" < x < 5.5" \\ 37.51 - 1.876x \ \ lb-in, & 5.5" < x < 21" \end{cases} \tag{6}$$

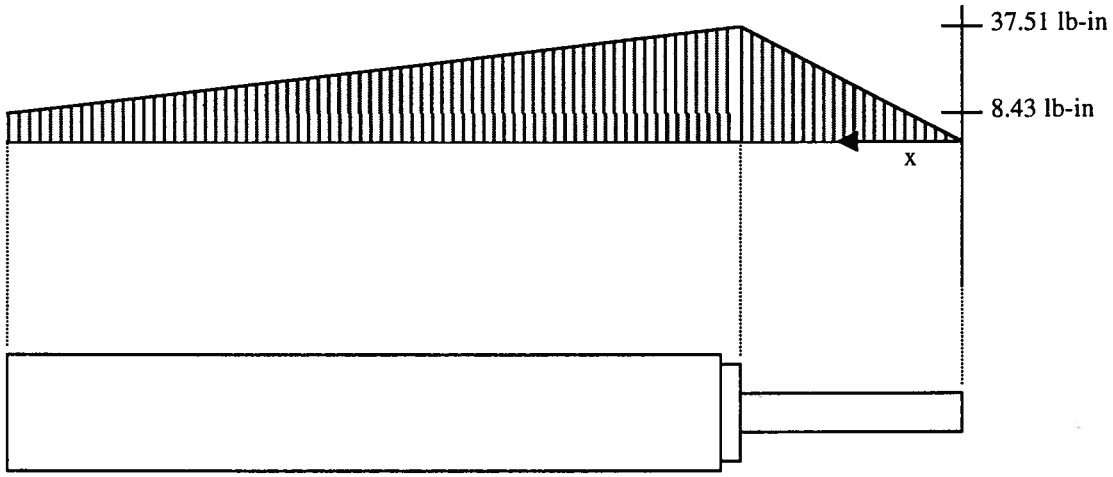

Figure 3.5: Moment Diagram of End-Effector Shaft System

The value used for E is 10.3 Mpsi, the standard for aluminum. The value for I, however, varies along the length of the shaft system, as the cross section perpendicular to the shaft axis changes several times. A cross sectional diagram along the axis, shown in Figure 3.6, shows this variation. I for each section is given by the following equations:

$$I = \frac{\pi}{32} d^4 \text{ (for a solid cylindrical cross-section)} \tag{7}$$

$$I = \frac{\pi}{32}\left(d_o^4 - d_i^4\right) \text{ (for a hollow cylindrical cross-section)} \tag{8}$$

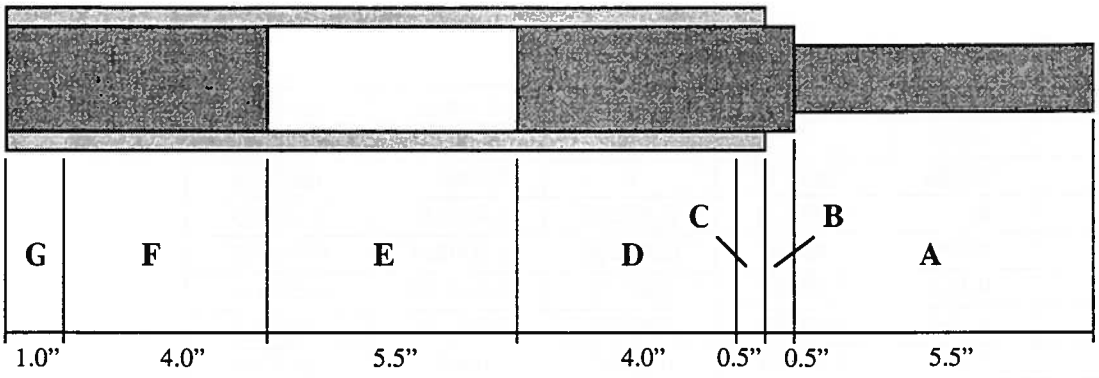

Figure 3.6: Division of Shaft System into Sections of Constant *I*

Note that sections F and G are actually of the same cross section, and could be lumped into one section. The same is true for sections C and D. They have been divided to provide a better comparison between the old and new shaft systems in the following section.

For each section, equation (5) must be integrated twice, using the appropriate values for *M* and *I*, and applicable boundary conditions. For section A, these boundary conditions are y=0 at each end, since the ends of section A are rigidly mounted. For each other section, the boundary conditions will be that the displacement, y, and the slope, y', at the right end of that section match the respective values at the left end of the previous section. Using this method, and working along the shaft from right to left, the displacement at point C may be determined. Values for the displacement and slope at each end of each section appear in Table 3.1 below.

Section	I (in^4)	y_{left} (in)	y_{right} (in)	dy/dx_{left}	dy/dx_{right}
A	0.0311	0	0	0.000215	-0.000107
B	0.0980	0.000112	0	0.000233	0.000215
C	0.240	0.000234	0.000112	0.000248	0.000233
D	0.209	0.00139	0.000234	0.000314	0.000248
E	0.142	0.00408	0.00139	0.000528	0.000314
F	0.209	0.00687	0.00408	0.000709	0.000528
G	0.240	0.00780	0.00687	0.000930	0.000709

Table 3.1: Deflection of Shaft System in Each Segment

From this table, it can be seen that the deflection at point C is 0.0078". However, this is not the final deflection at the paint gun. Using the slope at this point, and assuming that the paint gun mount is perfectly rigid,

$$y_{gun} = y_C + l_{C-gun}\left.\frac{dy}{dx}\right|_C \tag{9}$$

with $l_{C\text{-}gun}$ being the distance from point C to the end of the paint gun, about 15". This results in a total maximum deflection at the paint gun of 0.0218".

Recall that this analysis treated the shaft system as a single piece. In reality, there is a difference between the inner diameter of the shaft, and the outer diameter of the shaft mounts, of approximately 0.005". This allows small angles, θ_1 and θ_2, to exist between the shaft and its mounts, as shown in Figure 3.7. These angles may be determined to be

$$\begin{aligned}\theta_1 &= \tan^{-1}(0.005/4.5) = 0.0011 rad \\ \theta_2 &= \tan^{-1}(0.005/5.0) = 0.0010 rad\end{aligned} \tag{10}$$

The deflection due to mechanical imperfection, then, may be calculated to be

$$\delta = l_1\theta_1 + l_2(\theta_1 + \theta_2) \tag{11}$$

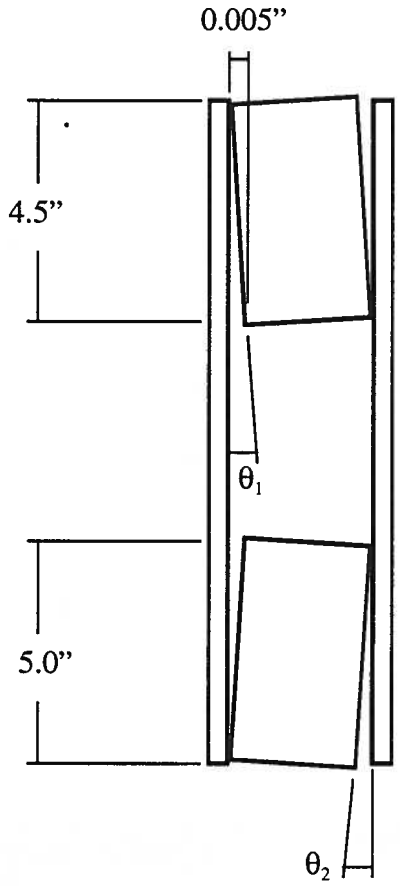

Figure 3.7: Imperfections in Shaft System Design

where l_1 is the length of the shaft (15"), and l_2 is the distance from the lower end of the shaft to the paint gun (15"). Note that equation (11) makes use of small angle approximations. This deflection, then, is $\delta = 0.0482$". Combining this with the deflection due to bending, a total deflection at the paint gun of 0.0700", a little under 3/32". If the distance between the spray gun and the ground is also taken into account (approximately 20"), then the distance l_2 changes, as well as the bending deflection, yielding a net offset of $\delta_{\text{ground}} = 0.124$" almost 1/8" of displacement. There will be negligible deflection due to tolerancing concerns at the interfaces between the lower shaft mount and the paint gun mount, and between the upper shaft mount and the bearings with which it mates, as those are very snug fits.

3.2.2 Proposed Changes in the Shaft System

There are three possible ways to decrease the deflection in the shaft system: first, the shaft may be machined from a stiffer material, such as steel; second, the thickness of the shaft may be increased; and third, the tolerances between the mating parts may be decreased. Using a stiffer material would certainly decease bending deflection, but would also add to the weight of the shaft system, which is undesirable, as stated previously. Changing the geometry of the shaft may be done in such a way that the stiffness is increased, while the mass is kept the same. And lowering the tolerances simply requires more care to be put into the machining of the parts.

In changing the geometry, the design shown in Figure 3.8 is proposed.

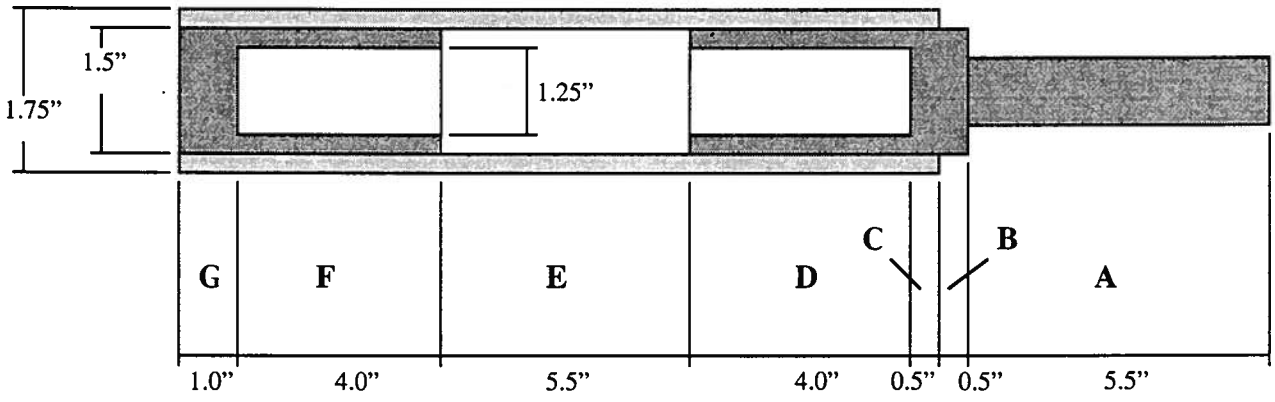

Figure 3.8: Proposed Redesign of Shaft System

Of particular interest are the hollowed out sections of the upper and lower shaft mounts. These allow their respective sections to maintain a higher stiffness while maintaining a minimal increase in mass. The masses of the shaft mounts actually remain constant, while the mass of the shaft itself increases by only 0.294 lbs. The total mass of the shaft system increases from 1.69 lbs. to 1.99 lbs. This should be an acceptably low increase in weight.

Table 3.2 details the changes in I, as well as the change in deflection, for each section of the system.

	Previous Design		Proposed Design	
Section	I (in^4)	y(in)	I (in^4)	y(in)
A	0.0311	0	0.0311	0
B	0.0980	0.000112	0.497	0.000108
C	0.240	0.000234	0.921	0.000219
D	0.240	0.00139	0.681	0.00117
E	0.142	0.00408	0.424	0.00284
F	0.240	0.00687	0.681	0.00435
G	0.240	0.00780	0.921	0.00479
Deflection at Paint Gun	**0.0218"**		**0.0114"**	
Deflection at Ground	**0.0404"**		**0.0201"**	

Table 3.2: Changes in Shaft Deflection Due to Geometry Changes

It is also recommended that tolerances in the mating dimensions be reduced from 0.005" to 0.002". Using the same analysis performed before, with these new tolerances, the deflection due to tolerance could be reduced from 0.0820" (at the ground) to 0.0362". The change in tolerance, combined with the change in design proposed above, would ultimately reduce the error at the ground from 0.124" to 0.0563", a difference of approximately 55%.

3.3 Observed Results of Shaft System Alterations

Due to time constraints, no quantitative tests were performed prior to the replacement of the old shaft system; therefore, no quantitative comparisons may be made between the two.

However, from a purely qualitative standpoint, the performance appeared to improve greatly upon installation of the new, more rigid system. The degree of wobble in the paint gun has been reduced from very noticeable to barely noticeable. At higher speeds, there is still some evidence of deflection, but it is much less pronounced, and the motion appears steadier; all significant vibrations appear to have been eradicated. As no painting tests were performed before the redesign of the shaft system, it is impossible to infer what degree of improvement has been made to the quality of the markings; but it is assumed that other factors - such as vibration of the robotic arm, errors in the control system, and irregularities in the paint gun pressure – will have a more pronounced effect on the smoothness of the markings than will any remaining deflection in the end-effector.

Chapter 4

Conclusions and Recommendations

4.1 Conclusions

A large scale robot such as BASR has many complicated elements that must be fine-tuned in order to insure maximum performance. For a robot of this magnitude to be able to perform well enough to produce high quality roadway markings, the motion must be very precise, a task that becomes more difficult as the size of the system increases. Two possible sources of error – an inability of the robot to move precisely due to lack of counter-balancing, and deflections in the shaft holding the paint gun – were addressed in this paper.

In attempting to counter-balance the robot, it was determined that while it is possible to reduce the load on the hydraulic actuator with a spring system, such a system may introduce side-effects that can adversely affect the robot's performance. The safety of the system was increased, as the counter-balance eliminated the danger of a hydraulic failure releasing pressure on the arm, and allowing it to extend unrestrained. However, the spring system may have created unwanted tendencies towards oscillation, as well as

removing too much load from the actuator. Further testing will be necessary to determine which of these effects, if any, is actually present.

In redesigning the end-effector shaft, the stiffness of the system was increased, which provided a noticeable but unmeasured lessening of wobble during paint gun rotation. In addition, this extra stiffness was achieved with minimal increase to the mass of the system – an important requirement in maintaining acceptable performance during manipulation of the paint gun. It is assumed with a high degree of certainty that the design of the end-effector is adequate for the purposes of the robot, and that any perceived errors in the quality of roadway markings are the result of some other aspect of the robotic system.

4.2 Recommendations

Further testing needs to be done to determine what effects the counter-balance truly has on the robot's performance. It is suggested that tests be performed with differing numbers and stiffnesses of springs, so as to provide ample to data upon which to base further conclusions. The critical characteristics of the counter-balance are the effective spring constant of all the springs taken together, and the degree of pre-loading that is placed on the springs. It may be that the current effective spring constant is too high, and that a lower value is needed for optimal performance. It may also be that some damping added to the counter-balance will improve the performance by damping the

oscillations that appear during certain motions of the arm. Such dampers could be mounted in a fashion similar to that in which the springs are mounted. Ultimately, the counter-balance may provide more problems and solutions, and it may be better to seek alternative solutions to the performance problems. In that case, it is highly recommended that some sort of alternative safety precautions be added to the robot to eliminate potential hazards that unexpected hydraulic failure could cause.

Section IV:

Appendix B

Kinematic Study of the Big Articulated Robotic System (BASRS)

A Kinematic Study of the Big Articulated Stenciling Robotic System (BASRS)

BY

NINA SIMEONOVA PATARINSKA

M.S. (Technical University of Sofia) 1994

THESIS

Submitted in partial satisfaction of the requirements for the degree of

MASTER OF SCIENCE

in

MECHANICAL ENGINEERING

in the

OFFICE OF GRADUATE STUDIES

of the

UNIVERSITY OF CALIFORNIA

DAVIS

Approved:

Bahram Ravani

Rida A.M.T. Farouki

Committee in Charge

2001

AKNOWLEDGEMENTS

First of all, I am grateful to the Mechanical and Aeronautical Department for giving me this great opportunity to study and work on my Masters degree at UC Davis.

I would like to express my gratitude to my advisor Prof. B. Ravani for his continuous assistance in the process of developing my thesis. Thank you, Prof. Ravani for making all that happen!

I would like to thank the California Department of Transportation (Caltrans) for the financial support of this work through the Automated Highway Maintenance and Construction Technology (AHMCT) Research Center at UC Davis.

I am sincerely indebted to Prof. S. Velinsky and Prof. R. Farouki for their time and consideration in reviewing my thesis.

I would like to gratefully acknowledge my lab-mates as well as my friends from the Ph.D. lab and also Colleen, for making the AHMCT Research Center a wonderful place for me. Thanks, guys, for keeping me smiling all the time - you are the best!

I wish to especially express my gratitude to Randy James whose friendship is invaluable for me. Thank you, Randy, for keeping the faith in me!

Mother, I am so proud of you! Thank you for always being there for me!

Most of all, I would like to thank and dedicate this thesis to my father, who enlightened the spirit of Robotics in my heart long, long time ago. Thank you daddy, for making me the person I am - you are the best thing in my life! I love you so much!

TABLE OF CONTENTS

LIST OF FIGURES

LIST OF TABLES

ABSTRACT

This thesis deals with kinematic analysis of a long reach robotic system developed at The University of California, Davis for painting of roadway markings. This robotic system is referred to as BASRS (Big Articulated Stenciling Robotic System) and has a kinematic structure consisting of two parallel linkages connected in series by a simple open loop linkage.

The direct and the inverse kinematics of the entire BASRS, as well as some special features of the robot end-effector are worked out and presented in this thesis.

A Partitioning Method is used for inverse kinematic analysis resulting in closed form solutions.

In addition a full kinematic analysis from the task space to the actuator space is presented.

1. INTRODUCTION

This thesis deals with kinematic analysis of the Big Articulated Stenciling Robotic System (BASRS), performing road-painting operation.

BASRS is a long reach robotic system developed at the Automated Highway Maintenance and Construction Technology (AHMCT) Research Center at UC Davis with funding from California Department of Transportation (Caltarns). This robot is to be used for painting operations of roadway markings.

The unique aspect of this thesis is that it includes the kinematics of the end-effector as well as the roadway-painting task in the overall kinematic model of the system. The results from this thesis can therefore be used for the direct kinematic control of BASRS.

1.1. Scope of the thesis

For more systematic formulation of the kinematic analysis, a brief description of the existing arm, as well as the main requirements for the painting operation are presented in Chap.1.

The direct and the inverse kinematics of the entire BASRS are subject of Chap.2. The kinematics of BASRS is discussed using a very convenient technique – so called Partitioning method.

Based on the already defined kinematics of the BASRS, Chap. 3 gives the relation between the road/task coordinate space and the manipulator actuator coordinate space.

Conclusions and some recommendations for future work are presented in Chap.4.

1.2. Basic Description of the Stenciling Robot

The stenciling robot is responsible for positioning the end-effector in the roadway x and y-axis positions (Fig.1.1). The robot has a pantograph type arm [1], which has been built to produce a large planar workspace using a simple actuation mechanism. It has been designed to orient the end-effector vertically with respect to the roadway surface at all times when painting.

The purpose of the end-effector of the Stenciling robot is to adjust the position and the orientation of the paint gun during the painting operation. While the end-effector is operating in its workspace (a horizontal plane), it rotates about a vertical axis in order to paint standard letters and shapes. By a vertical translation of the paint gun, the width of paint being applied to the ground can be altered as well as it can compensate for the non-flat road conditions. For a smooth paint distribution while painting tight curves, with the main idea of avoiding a build up of paint on the insides of the curves of the markings, the end-effector tilts the paint gun about a horizontal axis (which passes along the paint guns center of gravity). This type of motion reduces the paint build up in the insides of a curved marking, producing visually appealing markings on the roadway.

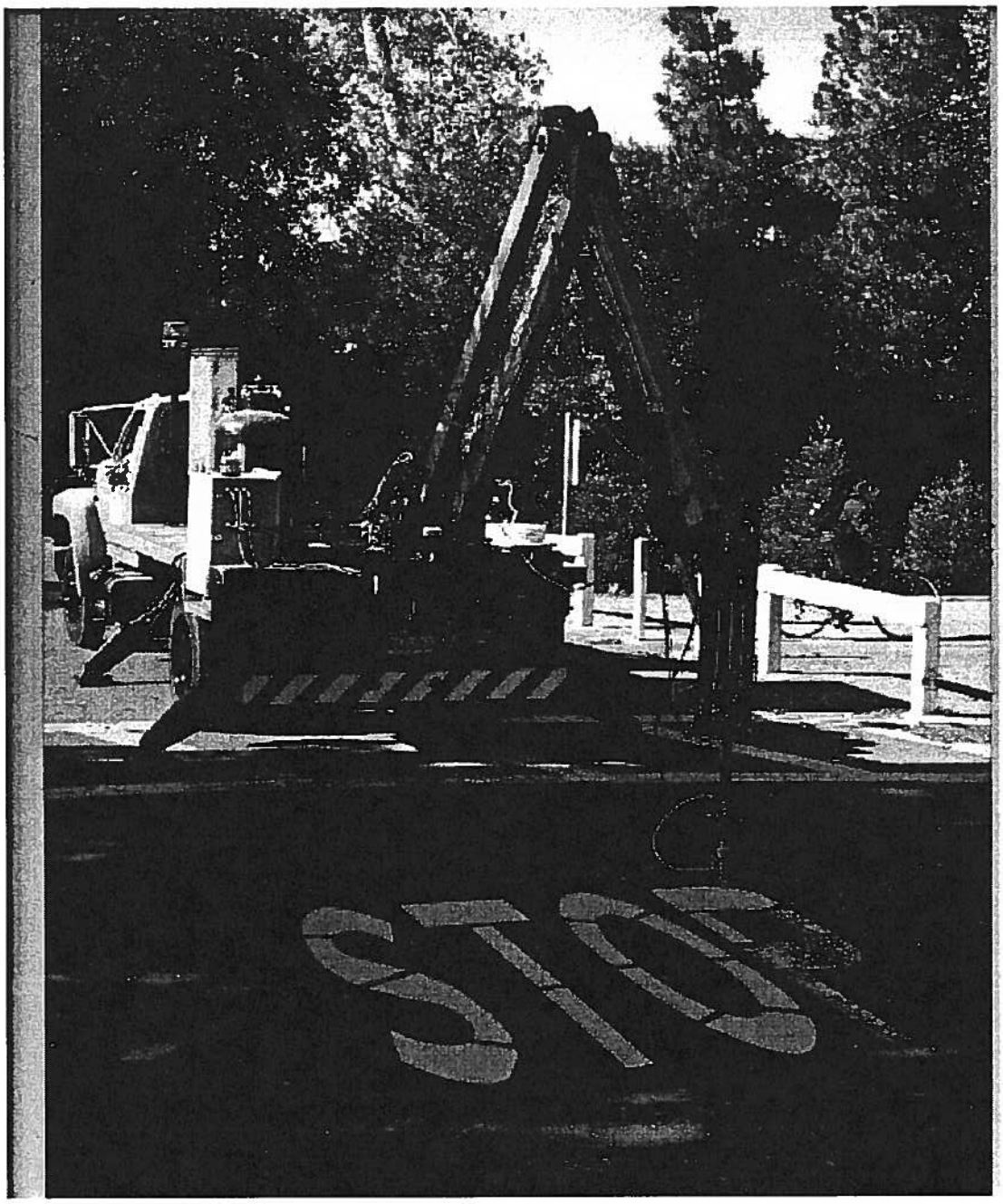

Fig.1.1. The Big Articulated Stenciling Robotic System (BASRS)

2. KINEMATIC ANALYSIS OF THE ENTIRE BASRS

2. 1. Hybrid Structures

Most industrial robot manipulators are designed with serial kinematic chains, which provide large workspaces. However, a robot with serial kinematic chain generally provides less rigidity and load-carrying capacity in comparison to a robot with closed kinematic chains. In general, the workspace volume of a robot arm with parallel kinematic chain is relatively small. Recently, there has been an increasing interest in the design of hybrid serial-and-parallel-driven robot manipulators [14]. The entire BASRS represents a combination of two parallel configurations (one in the arm and one in the end-effector), connected in a serial kinematic chain. This hybrid system consists of the first two joints in parallel drive, resulting in a translation of the end point of the arm (Fig. 2.1), and the last four joints, representing the end-effector (a four-bar linkage) in fully parallel configuration which combines good features of both the serial and the parallel kinematic chains.

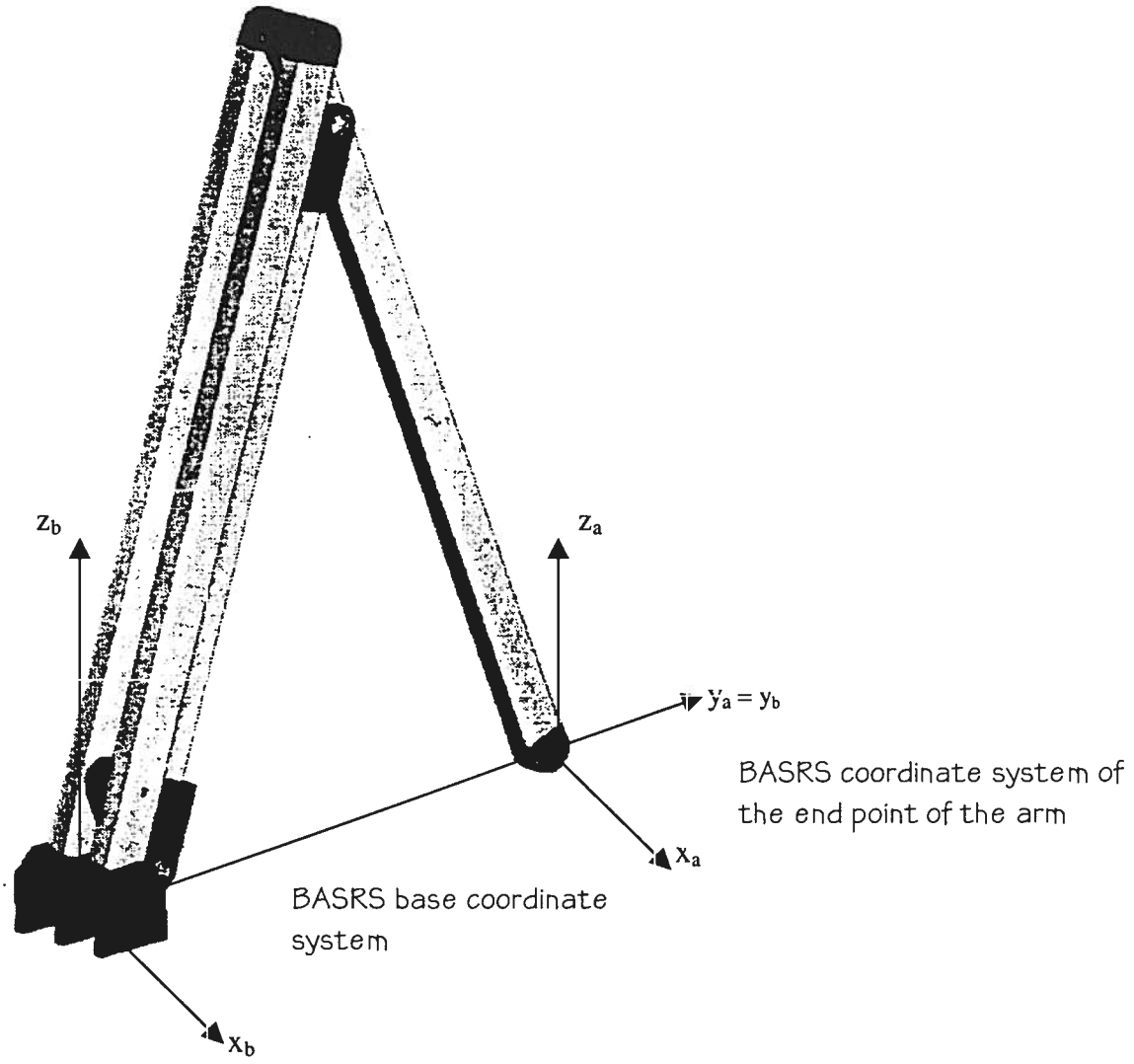

Fig. 2.1. BASRS Pantograph-type arm

2.2. Kinematic Equations for a Manipulator

Robot arm kinematics deals with an analytical study of the motion geometry of a robot arm with respect to a fixed reference coordinate system, without regard to the forces/moments that cause the motion [10]. It represents the analytical relationship between the joint-variable space and the position and orientation of the end effector of a robot arm [4, 11]. The solution set of kinematic equations can be obtained in direct or inverse form [5, 8]:

1.Direct Kinematics Problem

The solution of the direct kinematics problem for a manipulator involves finding the position and the orientation of the end-effector of the manipulator with respect to a reference coordinate system with given joint angles and geometric parameters of the robot. This is usually a simple problem which involves solving linear equations.

2.Inverse Kinematics Problem

The inverse kinematics solution involves solving for the joint variables given a desired position and orientation of the end-effector. The inverse kinematic solution usually involves solving nonlinear algebraic equations that can be transformed into polynomial equations.

In general, the inverse kinematic problem can be solved by several techniques, one of which, the Partitioning Method [13], will be the subject of interest of the following chapter. Other commonly used methods are iterative or computational approaches.

The homogeneous matrix T_i which specifies the location of the i-th coordinate frame with respect to the base coordinate system is the chain product of coordinate transformation matrices A_i and is expressed as:

$$T_i = A_1 \cdot A_2 \cdots\cdots A_i = \begin{bmatrix} x_i & y_i & z_i & d_i \\ 0 & 0 & 0 & 1 \end{bmatrix} = \begin{bmatrix} R_i & d_i \\ 0 & 1 \end{bmatrix} \tag{2.1}$$

where:

$$R_i = \begin{bmatrix} x_i & y_i & z_i \end{bmatrix} \tag{2.2}$$

is the orientation matrix of the i-th coordinate system established at i-th link with respect to the base (Appendix H);

d_i is the position vector of the hand, pointing from the origin of the base coordinate system to the origin of the hand coordinate system.

The transformation matrix A_i and its inverse, are expressed as:

$$A_i = \begin{bmatrix} \cos\theta_i & -\cos\alpha_i \sin\theta_i & \sin\alpha_i \sin\theta_i & a_i \cos\theta_i \\ \sin\theta_i & \cos\alpha_i \cos\theta_i & -\sin\alpha_i \cos\theta_i & a_i \sin\theta_i \\ 0 & \sin\alpha_i & \cos\alpha_i & d_i \\ 0 & 0 & 0 & 1 \end{bmatrix} \tag{2.3}$$

$$A_i^{-1} = \begin{bmatrix} \cos\theta_i & \sin\theta_i & 0 & -a_i \\ -\cos\alpha_i \sin\theta_i & \cos\alpha_i \cos\theta_i & \sin\alpha_i & -d_i \sin\alpha_i \\ \sin\alpha_i \sin\theta_i & -\sin\alpha_i \cos\theta_i & \cos\alpha_i & -d_i \cos\alpha_i \\ 0 & 0 & 0 & 1 \end{bmatrix} \tag{2.4}$$

where:

θ_i is the joint angle from x_{i-1} axis to the x_i axis about the z_{i-1} axis (using the right hand rule);

d_i- the distance from the origin of the (i-1)-th coordinate frame to the intersection of the z_{i-1} axis with the x_i axis along the z_{i-1} axis;

a_i - the offset distance from the intersection of the z_{i-1} axis with the x_i axis to the origin of the i-th frame along the x_i axis;

α_i - the offset angle from the z_{i-1} axis to the z_i axis about the x_i axis (using the right hand rule).

For a rotary joint d_i , a_i and α_i, are the joint parameters and remain constant for a robot, while θ_i is the joint variable that changes when link i rotates with respect to link i-1.

For a prismatic joint θ_i, a_i and α_i are the joint parameters and remain constant for a robot, while d_i is the joint variable.

The T_i matrix, which specifies the position and the orientation of the end point of the manipulator with respect to the base coordinate system, called "the hand matrix" can be expressed in the following form:

$$T_i = \begin{bmatrix} n_x & o_x & a_x & d_x \\ n_y & o_y & a_y & d_y \\ n_z & o_z & a_z & d_z \\ 0 & 0 & 0 & 1 \end{bmatrix} \qquad (2.5)$$

where:

n is the normal vector of the hand and is orthogonal to the fingers of the robot arm;

o is the sliding vector of the hand, which is pointing in the direction of the finger motion;

a is the approach vector of the hand, pointing in the direction normal to the palm of the hand;

d is the position vector of the hand, which was already mentioned.

2.3. Coordinate Systems for BASRS

In defining joint coordinate systems for BASRS, the kinematics of the robot is determined by the relative positions of its joint axis and the common normals between each pair of consecutive axes [6, 8, 13]. The relative position of two skew lines in space is expressed by two parameters: the distance and the twist angle between the two lines. For two consecutive joint axes of a robot, these two parameters are the link length and the link twist. For two consecutive common normals, these two parameters are the joint offset and the joint angle.

Having this in mind, an equivalent kinematic structure for the BASRS is presented in Fig. 2.1. In this structure the whole pantograph-type of the robot arm is configured as a single prismatic joint. The coordinate systems are defined, using the following set of rules:

- One coordinate system is attached to each joint axis of the robot.
- The z_i axis is attached to the i-th joint axis. The positive sign of z_i is chosen arbitrarily.
- The z_{i-1} axis lies along the axis of motion of the i-th joint.
- The x_i axis is normal to the z_{i-1} axis, and pointing away from it.
- The y_i axis completes the right-handed coordinate system as required.

Denavit-Hartenberg representation of a rigid link depends on four geometric parameters $(\theta_i, d_i, a_i, \alpha_i)$ associated with each link, which completely describe any revolute or prismatic joint. Referring to Fig. 2.2 these four parameters for BASRS are defined in Table 2.1.

Table 2.1

Joint i	θ	α	***a***	***d***
1.(base rotat.)	θ_1	*-90*	*0*	*0*
2.(arm translat.)	*0*	*90*	a_2	d_2
3.(e-eff. translat.)	*0*	*0*	*0*	d_3
4.(e-eff. rotat.)	θ_4	*0*	*0*	*0*

The tilt motion of the end-effector will be discussed in the end of this chapter and will be taken into consideration in the next chapter.

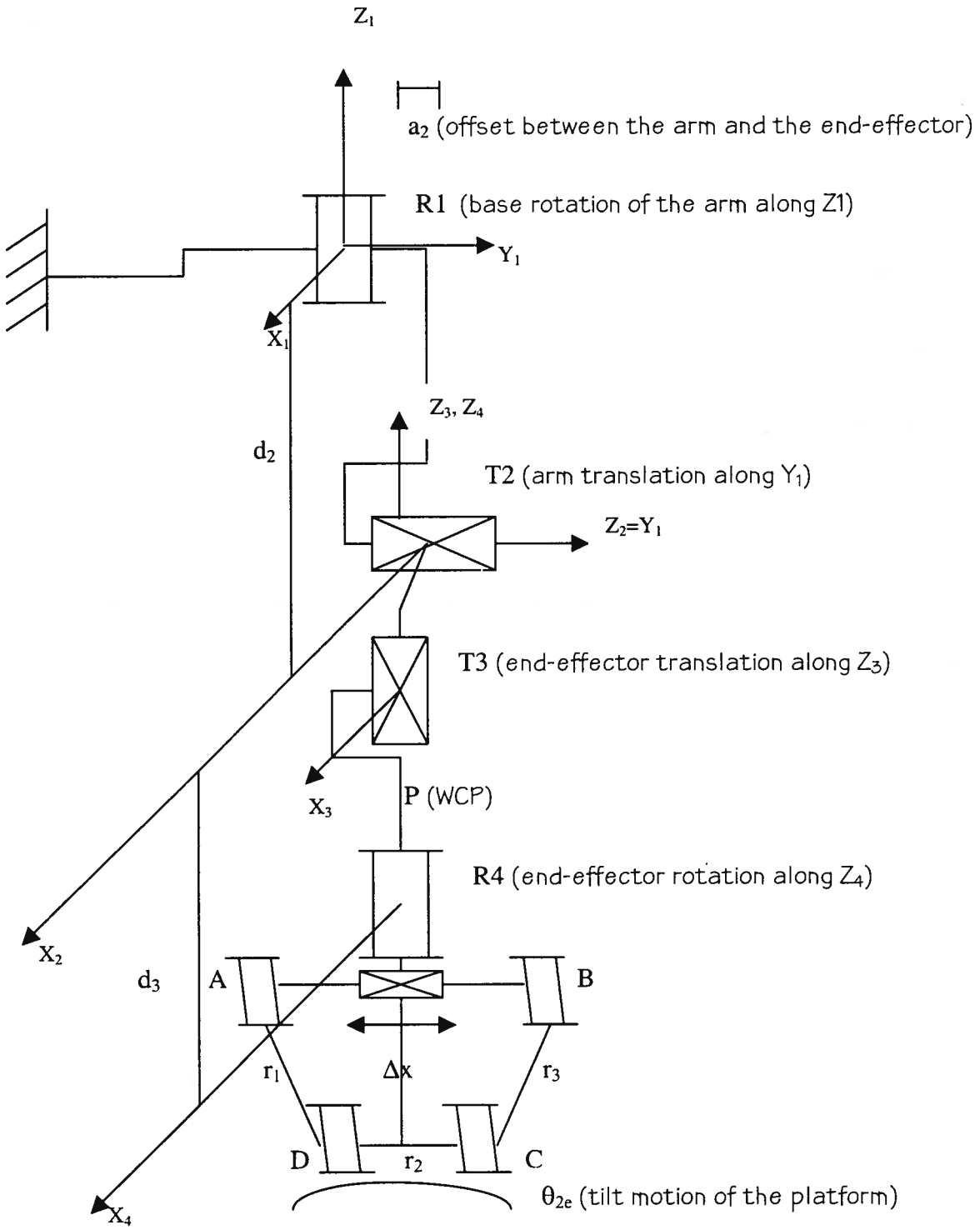

Fig. 2.2. A Kinematic Equivalent for BASRS with an Assigned Coordinate Frames

2.4. Denavit –Hartenberg Matrices for the BASRS

The homogeneous matrix T_i specifies the location (position and orientation) of the i-th coordinate frame with respect to the base coordinate system. In order to completely describe all revolute and prismatic joints of the BASRS, the Denavit-Hartenberg representation is used and the A_i transformation matrices and their inverse are expressed as follows:

$$A_1 = \begin{bmatrix} \cos\theta_1 & 0 & -\sin\theta_1 & 0 \\ \sin\theta_1 & 0 & \cos\theta_1 & 0 \\ 0 & -1 & 0 & 0 \\ 0 & 0 & 0 & 1 \end{bmatrix} \tag{2.6}$$

$$A_2 = \begin{bmatrix} 1 & 0 & 0 & a_2 \\ 0 & 0 & -1 & 0 \\ 0 & 1 & 0 & d_2 \\ 0 & 0 & 0 & 1 \end{bmatrix} \tag{2.7}$$

$$A_3 = \begin{bmatrix} 1 & 0 & 0 & 0 \\ 0 & 1 & 0 & 0 \\ 0 & 0 & 1 & d_3 \\ 0 & 0 & 0 & 1 \end{bmatrix} \tag{2.8}$$

$$A_4 = \begin{bmatrix} \cos\theta_4 & -\sin\theta_4 & 0 & 0 \\ \sin\theta_4 & \cos\theta_4 & 0 & 0 \\ 0 & 0 & 1 & 0 \\ 0 & 0 & 0 & 1 \end{bmatrix} \tag{2.9}$$

The inverse A_i^{-1} matrices, respectively, are:

$$A_1^{-1} = \begin{bmatrix} \cos\theta_1 & \sin\theta_1 & 0 & 0 \\ 0 & 0 & -1 & 0 \\ -\sin\theta_1 & \cos\theta_1 & 0 & 0 \\ 0 & 0 & 0 & 1 \end{bmatrix} \tag{2.10}$$

$$A_2^{-1} = \begin{bmatrix} 1 & 0 & 0 & -a_2 \\ 0 & 0 & 1 & -d_2 \\ 0 & -1 & 0 & 0 \\ 0 & 0 & 0 & 1 \end{bmatrix} \tag{2.11}$$

$$A_3^{-1} = \begin{bmatrix} 1 & 0 & 0 & 0 \\ 0 & 1 & 0 & 0 \\ 0 & 0 & 1 & -d_3 \\ 0 & 0 & 0 & 1 \end{bmatrix} \tag{2.12}$$

$$A_4^{-1} = \begin{bmatrix} \cos\theta_4 & \sin\theta_4 & 0 & 0 \\ -\sin\theta_4 & \cos\theta_4 & 0 & 0 \\ 0 & 0 & 1 & 0 \\ 0 & 0 & 0 & 1 \end{bmatrix} \tag{2.13}$$

2.5. The Partitioning Method for Describing the Kinematics of BASRS

The special feature for expressing the inverse kinematic problem for a robot using the Partitioning Method [2] is that the robot has a *partitioned geometry*, i.e. at least three of its axes have to be parallel to each other or to intersect. In such a case, the position of the end effector can be expressed *independently* from the orientation and the kinematic solutions can be easily derived by "hand" even for highly complicated structures.

Due to the fact that BASRS has a partitioned geometry and 5 DOF, the origin of the 3rd, 4th, 5th coordinate systems can be positioned at one point P, called the wrist center point (WCP), in Fig.2.2. In this fashion, determination of the location of the center of the 5th coordinate system with respect to the base coordinate system, only will require the location of the center of the 3rd coordinate system. This can be expressed as follows:

$$x_{p1}=A_1A_2A_3x_{p4} \tag{2.14}$$

where the vectors x_{pi} are the positions of the point P in the corresponding i-th coordinate system:

$$x_{p1}=[x_p\ y_p\ z_p\ 1]^T \tag{2.15}$$

$$x_{p4}=[0\ 0\ 0\ 1]^T \tag{2.16}$$

Taking into account the above mentioned, the direct kinematic problem for BASRS states: Given θ_1, d_2, d_3 (the first three generalized coordinates), find x_{p1} (the vector

describing the position of point P in the first coordinate system). Since x_{p4} is known, equation (2.14) can be solved for x_{p1}.

The *inverse kinematic solutions for the position and the orientation* can be determined from equation (2.14) and they are:

$$u_4=A_4u_5 \tag{2.17}$$

where u_i are the orientation unit vectors with respect to the corresponding i-th coordinate system:

$$u_4=[u_{4x}\ u_{4y}\ u_{4z}\ 0]^T \tag{2.18}$$

$$u_5=[1\quad 0\quad 0\quad 0]^T \tag{2.19}$$

Expressing θ_1, d_2, d_3, with given x_{p1}, is the task of the inverse kinematics.

2.5.1. Direct Kinematic Solutions for the Position of the End-effector

Taking into consideration eqns. (2.14), (2.15), (2.16) and the results from the first three transformation matrices for BASRS, eqns. (2.6), (2.7) and (2.8), the following matrix equation could be obtained:

$$\begin{bmatrix} x_p \\ y_p \\ z_p \\ 1 \end{bmatrix} = \begin{bmatrix} \cos\theta_1 & 0 & -\sin\theta_1 & 0 \\ \sin\theta_1 & 0 & \cos\theta_1 & 0 \\ 0 & -1 & 0 & 0 \\ 0 & 0 & 0 & 1 \end{bmatrix} \begin{bmatrix} 1 & 0 & 0 & a_2 \\ 0 & 0 & -1 & 0 \\ 0 & 1 & 0 & d_2 \\ 0 & 0 & 0 & 1 \end{bmatrix} \begin{bmatrix} 1 & 0 & 0 & 0 \\ 0 & 1 & 0 & 0 \\ 0 & 0 & 1 & d_3 \\ 0 & 0 & 0 & 1 \end{bmatrix} \begin{bmatrix} 0 \\ 0 \\ 0 \\ 1 \end{bmatrix} \tag{2.20}$$

Multiplication of the matrices on the right-hand side of eqn. (2.20) leads to:

$$\begin{bmatrix} x_p \\ y_p \\ z_p \\ 1 \end{bmatrix} = \begin{bmatrix} a_2\cos\theta_1 - d_2\sin\theta_1 \\ a_2\sin\theta_1 + d_2\cos\theta_1 \\ d_3 \\ 1 \end{bmatrix} \tag{2.21}$$

The matrix (2.21) represents a system of three equations for the position of the end-effector with respect to given joint parameters and geometric link parameters:

$$x_p = a_2\cos\theta_1 - d_2\sin\theta_1 \tag{2.22}$$

$$y_p = a_2\sin\theta_1 + d_2\cos\theta_1 \tag{2.23}$$

$$z_p = d_3 \tag{2.24}$$

Expressing $\sin\theta_1$ and $\cos\theta_1$ as tangents of half angles, yields to the following equations:

$$x_p = a_2\frac{1-\tan^2(\theta_1/2)}{1+\tan^2(\theta_1/2)} - d_2\frac{2\tan(\theta_1/2)}{1+\tan^2(\theta_1/2)} \tag{2.25}$$

$$y_p = a_2 \frac{2\tan(\theta_1/2)}{1+\tan^2(\theta_1/2)} - d_2 \frac{1-\tan^2(\theta_1/2)}{1+\tan^2(\theta_1/2)} \tag{2.26}$$

$$z_p = d_3 \tag{2.27}$$

Note: The translational motion along the z-axis, assumed to be constant here, will be considered in Chap.3.

MATLAB simulations (Appendix C) of the direct kinematic solution for the position are shown on Fig. 2.3 with the base rotational angle θ_1 in the range from 0 rad. to $\pi/2$ rad.

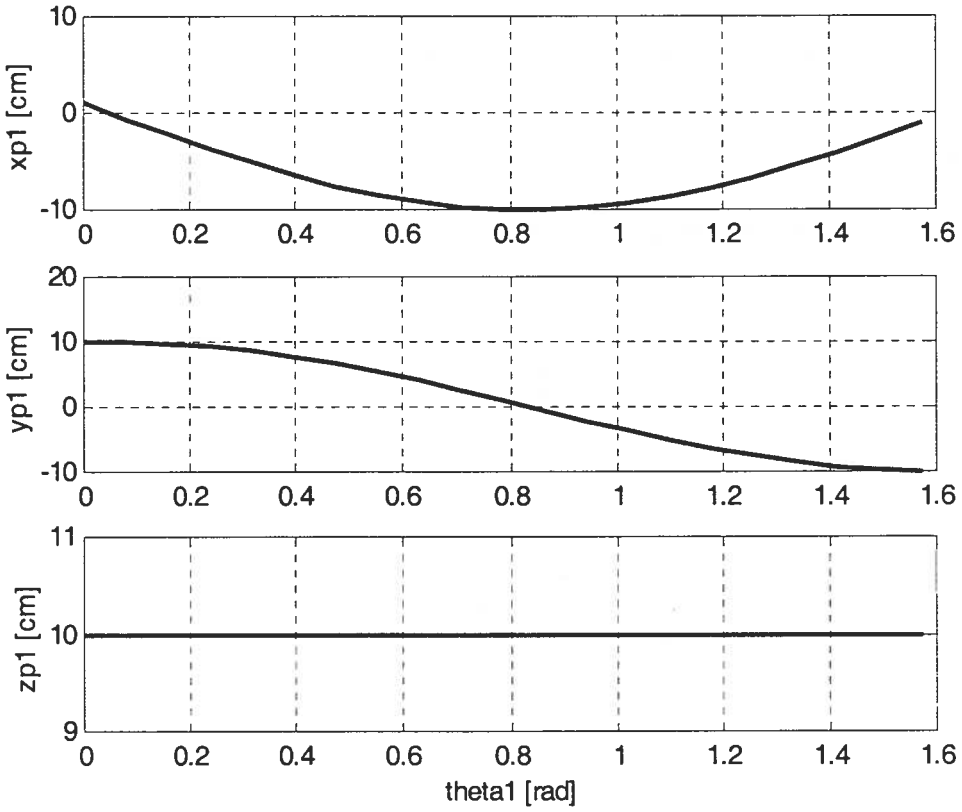

Fig.2.3. Direct Kinematic Solutions for the Position

2.5.2. Direct Kinematic Solutions for the Orientation of the End-effector

The direct solution for the orientation of the end-effector of BASRS can be easily expressed from the following matrix equation:

$$u_4=A_4u_5 \tag{2.28}$$

by accounting for the equations (2.9), (2.18) and (2.19):

$$\begin{bmatrix} u_{4x} \\ u_{4y} \\ u_{4z} \\ 0 \end{bmatrix} = \begin{bmatrix} \cos\theta_4 & -\sin\theta_1 & 0 & 0 \\ \sin\theta_4 & \cos\theta_1 & 0 & 0 \\ 0 & 0 & 1 & 0 \\ 0 & 0 & 0 & 1 \end{bmatrix} \begin{bmatrix} 1 \\ 0 \\ 0 \\ 0 \end{bmatrix}. \tag{2.29}$$

Multiplication of the right side of (2.29) yields to:

$$\begin{bmatrix} u_{4x} \\ u_{4y} \\ u_{4z} \\ 0 \end{bmatrix} = \begin{bmatrix} \cos\theta_4 \\ \sin\theta_4 \\ 0 \\ 0 \end{bmatrix} \tag{2.30}$$

The three equations, representing the orientation of the end-effector along x, y and z axes are:

$$u_{4x} = \cos\theta_4 \tag{2.31}$$

$$u_{4y} = \sin\theta_4 \tag{2.32}$$

$$u_{4z} = 0 \tag{2.33}$$

Expressing $\sin\theta_4$ and $\cos\theta_4$ as tangents of half angles, leads to the following equations:

$$u_{4x} = \frac{1-\tan^2(\theta_4/2)}{1+\tan^2(\theta_4/2)} \tag{2.34}$$

$$u_{4y} = \frac{2\tan(\theta_4/2)}{1+\tan^2(\theta_4/2)} \tag{2.35}$$

Note, that the tilt angle will be included in the kinematics of the BASRS in the next chapter.

Fig. 2.4 shows the MATLAB results (Appendix D) of the direct kinematic solution for the orientation of the end-effector for θ_4 in the range from 0 rad. to $\pi/2$ rad.

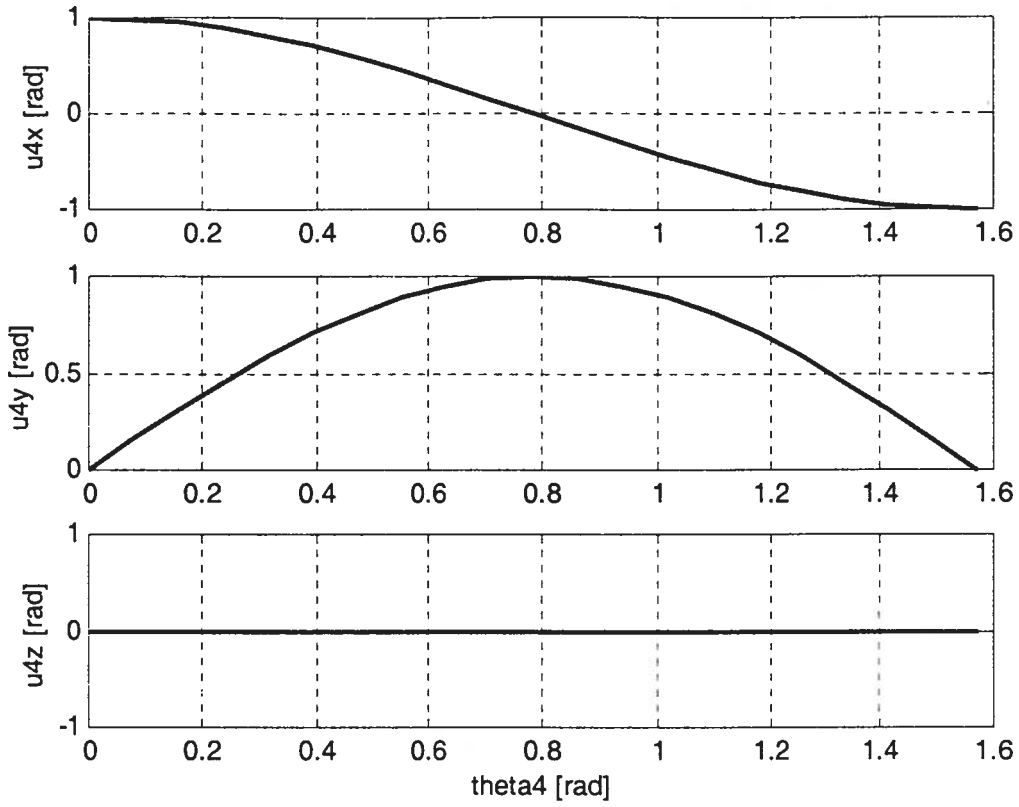

Fig.2.4. Direct Kinematic Solutions for the Orientation

2.5.3. Inverse Kinematic Solutions for the Position of the End-effector

Pre-multiplication of both sides of eq. (2.14) by $(A_1A_2)^{-1}$ yields the following equation:

$$A_2^{-1}A_1^{-1}x_{p1} = A_3x_{p4} \tag{2.36}$$

which can be solved for θ_1, d_2, d_3.

Eq. (2.36) leads to:

$$\begin{bmatrix} 1 & 0 & 0 & -a_2 \\ 0 & 0 & 1 & -d_2 \\ 0 & -1 & 0 & 0 \\ 0 & 0 & 0 & 1 \end{bmatrix} \begin{bmatrix} \cos\theta_1 & \sin\theta_1 & 0 & 0 \\ 0 & 0 & -1 & 0 \\ -\sin\theta_1 & \cos\theta_1 & 0 & 0 \\ 0 & 0 & 0 & 1 \end{bmatrix} \begin{bmatrix} x_p \\ y_p \\ z_p \\ 1 \end{bmatrix} = \begin{bmatrix} 1 & 0 & 0 & 0 \\ 0 & 1 & 0 & 0 \\ 0 & 0 & 1 & d_3 \\ 0 & 0 & 0 & 1 \end{bmatrix} \begin{bmatrix} 0 \\ 0 \\ 0 \\ 1 \end{bmatrix} \tag{2.37}$$

$$\begin{bmatrix} \cos\theta_1 & \sin\theta_1 & 0 & -a_2 \\ -\sin\theta_1 & \cos\theta_1 & 0 & -d_2 \\ 0 & 0 & 1 & 0 \\ 0 & 0 & 0 & 1 \end{bmatrix} \begin{bmatrix} x_p \\ y_p \\ z_p \\ 1 \end{bmatrix} = \begin{bmatrix} 0 \\ 0 \\ d_3 \\ 1 \end{bmatrix} \tag{2.38}$$

The following three equations describe the position of the end-effector:

$$\cos\theta_1 x_p + \sin\theta_1 y_p - a_2 = 0$$

$$-\sin\theta_1 x_p + \cos\theta_1 y_p - d_2 = 0 \tag{2.39}$$

$$z_{p1} = d_3$$

As in the previous two cases, $\sin\theta_1$ and $\cos\theta_1$ will be expressed as tangents of half angles.

Finally, the inverse kinematic solution for the position of the end-effector of the BASRS can be expressed as:

$$\theta_1 = 2\arctan\frac{y_p \pm \sqrt{[y_p^2 - (a_2^2 - x_p^2)}}{x_p + a_2} \tag{2.40}$$

$$d_2 = -\frac{2\tan(\theta_1/2)}{1+\tan^2(\theta_1/2)}x_p + \frac{1-\tan^2(\theta_1/2)}{1+\tan^2(\theta_1/2)}y_p \tag{2.41}$$

$$d_3 = z_p \tag{2.42}$$

The inverse kinematic solutions for the position of the end-effector, visualised in MATLAB (Appendix E), are shown in Fig.2.5.

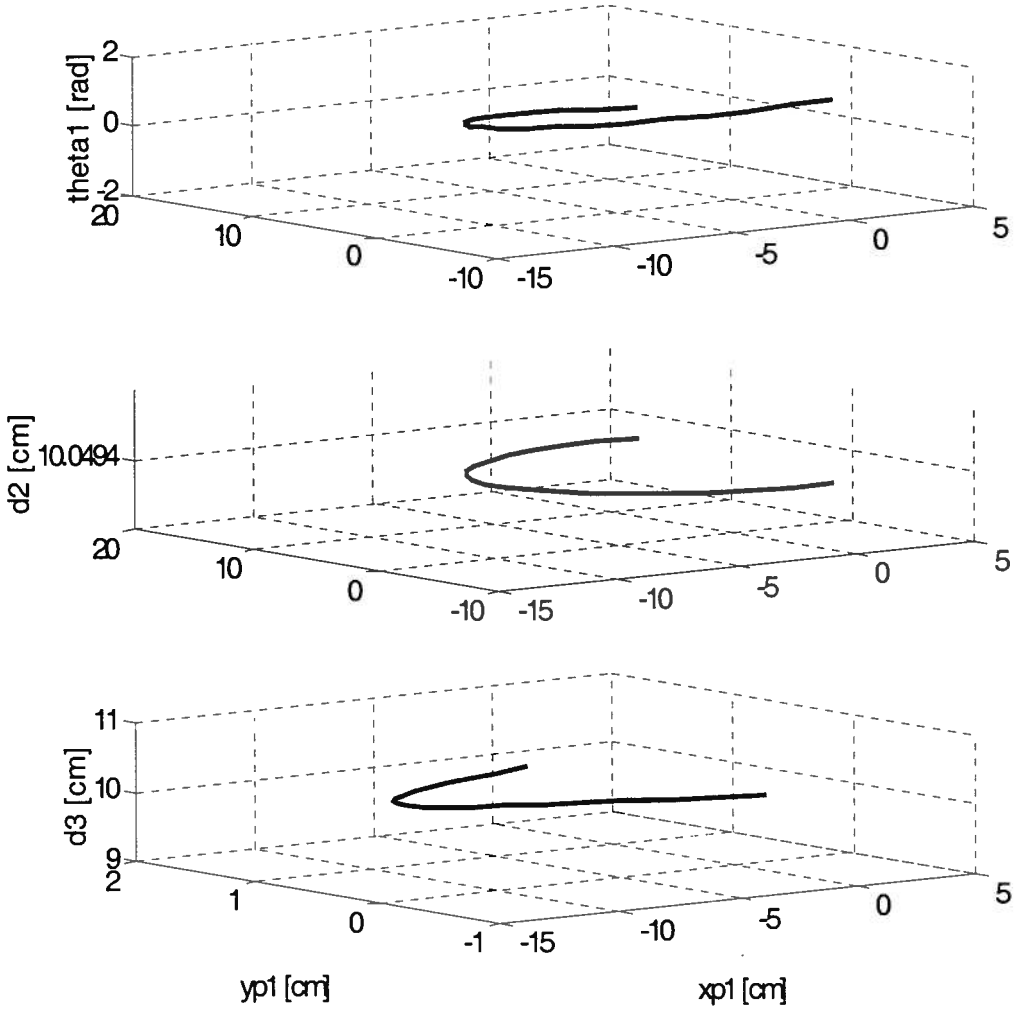

Fig.2.5. Inverse Kinematic Solutions for the Position

2.5.4. Inverse Kinematic Solutions for the Orientation of the End-effector

Following the logic of equation (2.16) and taking into account the fact, that the tilt motion will be considered in the kinematics of the BASRS in the next chapter, the orientation of the end-effector depends only on θ_4:

$$A_4^{-1} u_4 = u_5 \tag{2.43}$$

In matrix form, eqn. (2.43) can be expressed as:

$$\begin{bmatrix} \cos\theta_4 & \sin\theta_4 & 0 & 0 \\ -\sin\theta_4 & \cos\theta_4 & 0 & 0 \\ 0 & 0 & 1 & 0 \\ 0 & 0 & 0 & 1 \end{bmatrix} \begin{bmatrix} u_{4x} \\ u_{4y} \\ u_{4z} \\ 0 \end{bmatrix} = \begin{bmatrix} 1 \\ 0 \\ 0 \\ 0 \end{bmatrix} \tag{2.44}$$

The matrix eqn. (2.44) represents the following equations:

$$\begin{aligned} &\cos\theta_4 u_{4x} + \sin\theta_4 u_{4y} = 1 \\ &-\sin\theta_4 u_{4x} + \cos\theta_4 u_{4y} = 0 \\ &u_{4z} = 0 \end{aligned} \tag{2.45}$$

Expressing $\sin\theta_4$ and $\cos\theta_4$ as tangents of half angles, leads to the inverse kinematic solution for the orientation of the end-effector of BASRS:

$$\theta_4 = 2\arctan\frac{u_{4y} \pm \sqrt{[u_{4y}^2 + (u_{4x}^2 - 1)]}}{u_{4x} + 1} \tag{2.46}$$

The change of θ_4 with respect to given unit vector orientation coordinates, is shown on Fig.2.6. The code is attached in the corresponding Appendix D.

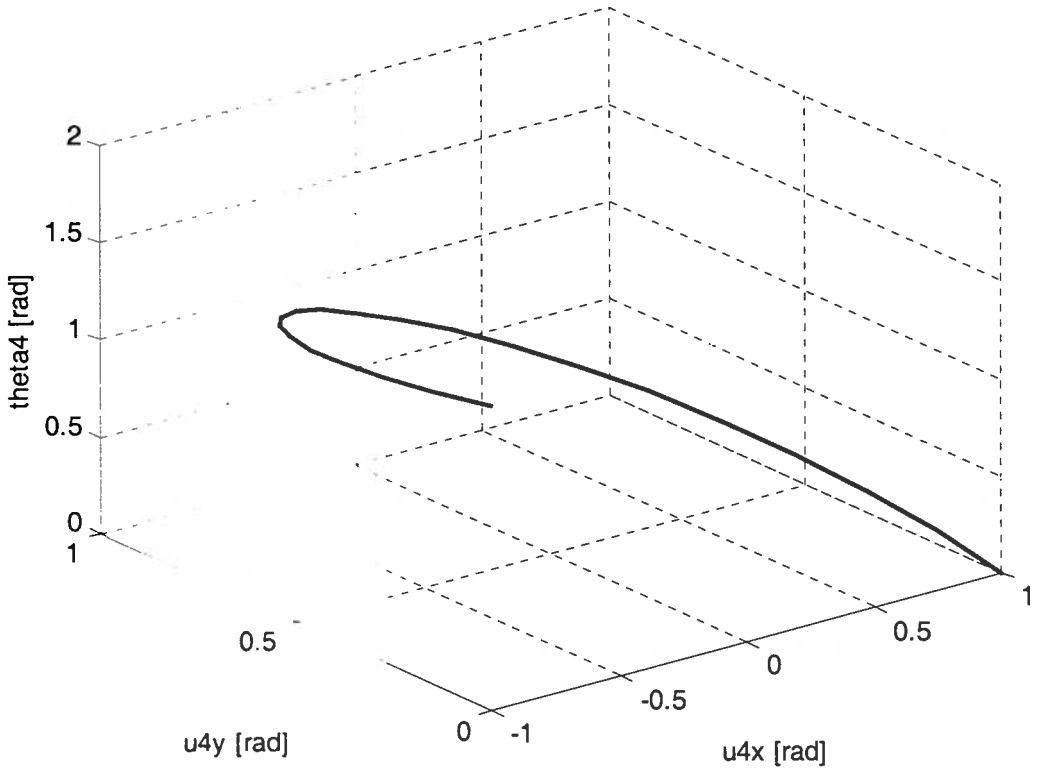

Fig.2.6. Inverse Kinematic Solutions for the Orientation

2.6. Kinematic Analysis of the BASRS End-effector Tilt Motion

The end-effector of the Stenciling robot utilizes a parallel structure (three-dimensional four bar linkage), with the main idea of increasing the rigidity of the painting gun while providing orientation control using a tilt motion.

For the four-bar linkage (Fig.2.7), the present work shall refer to the fixed link with the longest length as a base/input link r_4 and to the tilted link as a platform/output link r_2. Links r_1 and r_3 (r_1=r_3 and r_2=r_4/2) are considered to be the lengths of the intermediate/side links. In this case $r_1 + r_3 = r_2 + r_4$, i.e. the sum of shortest and longest links are equal to the sum of the other two links. The structure has been designed in a way that the triangle DPC = DP1C is equilateral. The advantage of this is the straight-line motion Δx (within a certain range), of the middle point P on the fixed base, while tilting the platform [7]. This structure allows the application of a very simple and convenient actuation system – a ball screw drive, embedded in the base of the four-bar linkage and rigidly connected to the tilting platform. The center of the tilt motion points always towards the center of the painted curvature, which leads to high accuracy of the painting process and simplifies the control strategy. By alternating the ratio of the height of the structure to its width, the accuracy of the tilt motion has been improved and that way, the uncontrolled translations in real x and y directions, apparent while tilting, can be minimized. The tilt angle is determined as θ_{2e}.

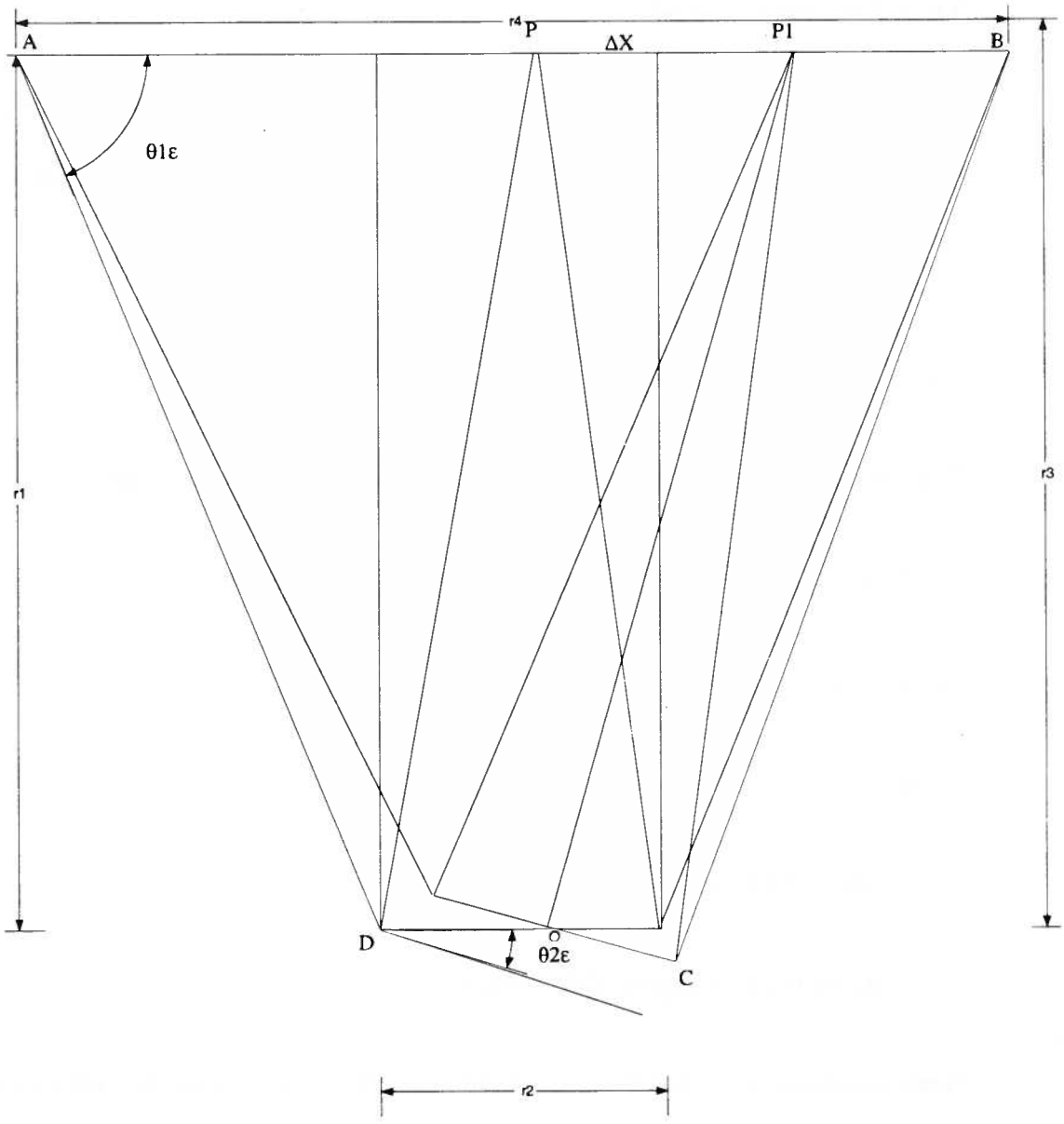

Fig.2.7. The Four-bar Linkage for the End-effector of BASRS in 2D

2.6.1. Special Plane Motion

A plane motion is in general determined if the paths of two points are prescribed [2, 3]. For the four-bar motion, the two given points A and B (Fig. 2.7) describe circles.

Since the vector sum of a closed polygon is zero it could be written:

$$\overline{AB} + \overline{BC} + \overline{CD} + \overline{DA} = 0 \tag{2.47}$$

This vector equation is equivalent to the system of two position loop equations:

$$r_1\cos\theta_{1e}+r_2\cos\theta_{2e}+r_3\cos\theta_{3e}-r_4=0 \tag{2.48}$$

$$r_1\sin\theta_{1e}+r_2\sin\theta_{2e}+r_3\sin\theta_{3e}-r_4=0,$$

where:

r_i (i=1,2,3,4) are the link lengths;

θ_{ie} are the four angles of the linkage.

These equations state that the sum of the x and y projections of the vectors in a closed vector polygon vanishes. For the particular case, link r_1 is the driving link. Therefore the angle θ_{1e} is known and the system of eqns. (2.48) provide two equations in the unknown variables θ_{2e} and θ_{3e}, which may be solved if the link lengths are specified using the Grashof's criteria [7] or if a prohibited angle for θ_{1e} is presented. That way the system of eqns. (2.48) can be solved for explicit algebraic expressions for θ_{2e} and θ_{3e}, as functions of θ_{1e}. The two loop equations provide sufficient information to define the configuration if one input (or driving variable) is defined. Thus the system has a single degree of

freedom.Simplifying, using some of the advantages of the proposed structure, such as equal side link lengths, the position equations (2.48) yield to the following system of complex vector equations:

$$r_1e^{j\theta 1e} + r_2e^{j\theta 2e} - r_4 = -r_3e^{j\theta 3e} \tag{2.49}$$

$$r_1e^{-j\theta 1e} + r_2e^{-j\theta 2e} - r_4 = -r_3e^{-j\theta 3e}$$

Multiplying the first equation in (2.3) by $r_3.e^{-j.\theta 3e}$, leads to:

$$r_3e^{-j\theta 3e}.(r_1e^{j\theta 1e} + r_2e^{j\theta 2e} - r_4) = -r_3^2 \tag{2.50}$$

Substituting for $r_3.e^{-j.\theta 3}$ (from the second equation in (2.49)) in eqn. (2.50):

$$(r_1e^{-j\theta 1e} + r_2e^{-j\theta 2e} - r_4).(r_1e^{j\theta 1e} + r_2e^{j\theta 2e} - r_4) = r_3^2 \tag{2.51}$$

Multiplying the terms and opening the brackets:

$$r_1^2 + r_2^2 + r_4^2 - r_3^2 + r_2r_1(e^{j(\theta 2e-\theta 1e)} + e^{j(\theta 1e-\theta 2e)}) - r_4r_2(e^{-j\theta 2e} + e^{j\theta 2e}) - r_4r_1(e^{-j\theta 1e} + e^{j\theta 1e}) = 0 \tag{2.52}$$

Presenting the complex terms as trigonometric functions:

$$r_1^2 + r_2^2 + r_4^2 - r_3^2 + 2r_2r_1(\cos(\theta_{2e} - \theta_{1e})) - 2r_4r_2\cos\theta_{2e} - 2r_4r_1\cos\theta_{1e} = 0 \tag{2.53}$$

Using the trigonometric equalities for tangent of a half of an angle leads to:

$$r_1^2 + r_2^2 + r_4^2 - r_3^2 - 2r_4r_2\cos\theta_{2e} + 2r_2r_1\cos\theta_{2e}(1 - \tan\theta_{1e}^2/(1 + \tan\theta_{1e}^2)) +$$

$$2r_2r_1\sin\theta_{2e}(2\tan\theta_{1e}/(1 + \tan\theta_{1e}^2)) - 2r_4r_1(1 - \tan\theta_{1e}^2/(1 + \tan\theta_{1e}^2)) = 0 \tag{2.54}$$

From equation (2.54), tan ($\theta_1/2$) can be directly expressed as:

$$\tan(\theta_{1e}/2)=(-b\pm\sqrt{b^2-4ac})/2a \tag{2.55}$$

where:

$$a= r_1^2+r_2^2+r_4^2-r_3^2-2r_4r_2\cos\theta_{2e} -2r_2r_1\cos\theta_{2e}+2r_4r_1$$

$$b= 4r_2r_1\sin\theta_{2e}$$

$$c= r_1^2+r_2^2+r_4^2-r_3^2-2r_4r_2\cos\theta_{2e} +2r_2r_1\cos\theta_{2e}-2r_4r_1$$

Finally, the equation for the output/tilt angle θ_{2e}, as a function of the input angle θ_{1e} is:

$$\theta_{1e}=\arctan[(-b\pm\sqrt{(b^2-4ac)}/a] \tag{2.56}$$

Note: θ_{1e} has real values if the following set of constraints is satisfied:

$$(4r_2r_1\sin\theta_{2e})^2-4[(r_1^2+r_2^2+r_4^2-r_3^2-2r_4r_2\cos\theta_{2e})^2-(2r_4r_1-2r_2r_1\cos\theta_{2e})^2]\geq 0 \tag{2.56a}$$

$$r_1^2+r_2^2+r_4^2-r_3^2-2r_4r_2\cos\theta_{2e} -2r_2r_1\cos\theta_{2e}+2r_4r_1 \neq 0 \tag{2.56b}$$

Knowing the range of θ_{2e} and the size of the links, the relation between the input and the output (Appendix A) of the proposed structure, visualized in Fig.2.8, can be completely defined.

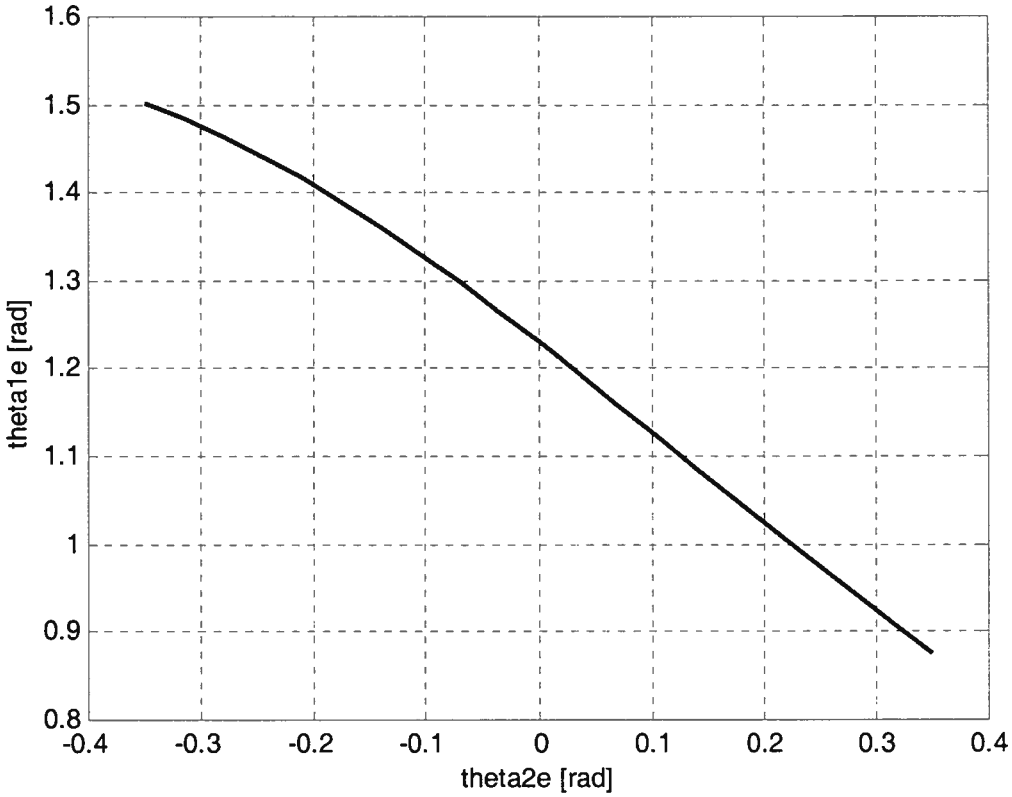

Fig.2.8. MATLAB Simulations of the Tilt Angle as a Function of the Input Angle

2.6.2. Straight-line Motion

As it was previously mentioned, the linear motion Δx (Fig.2.7) of the input link r_4, in the end-effector four-bar linkage is driven by a ball-screw. The relation between the tilt angle and the straight-line motion of the end-effector is given by eqn. (2.57) and can be seen in Fig.2.9. It is clear, from this figure, that for small values of θ_{2e}, this relationship is approximately linear.

$$\Delta x = r_4/2 - r_2\cos\theta_{2c} + r_2/2\cos\theta_{2c} + r_1\sin\theta_{1e}\tan\theta_{2e} - \mathrm{sqrt}[r_1^2 - (r_2\sin\theta_{2e} + r_1\sin\theta_{1e})^2] \qquad (2.57)$$

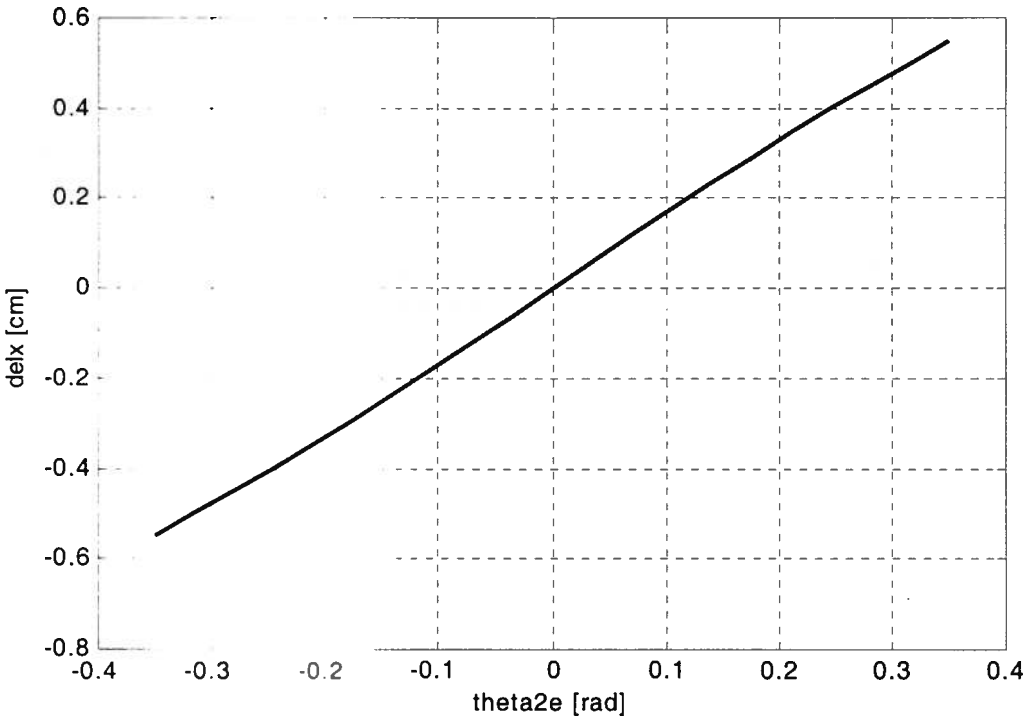

Fig.2.9. Relation between the Tilt Angle θ_{2e} and the Straight-line Motion Δx of the End-effector

At that stage of the thesis, the following could be outlined:

- The pantograph-type structure of the robot arm allows the end-effector to be positioned vertical to the road surface, making the task of painting roadway markings easier.

- A four-bar linkage is used as an end-effector of the BASRS, providing a tilt-type motion of the painting gun and that way improving the painting process.

- The direct and the inverse kinematic solutions for the BASRS had been obtained, without accounting for the tilt motion, which will be considered in the next chapter.

- The tilt motion is provided by the translatory motion of a ball screw, placed at the fixed base and rigidly connected to the moving platform. The relation between the tilt angle θ_{2e} and the straight-line motion of the end-effector had been obtained.

3. TASK ANALYSIS FOR ROADWAY PAINTING

3.1. Task Determination

A typical robot manipulator allows the user to input cartesian locations describing the end-effector position and orientation. The inverse kinematic solutions are then used to determine the joint variables for the purpose of programming a robot trajectory.

The task for the BASRS is usually described in terms of paint stripes on the roadway in the form of letters or signs. In previous work, a C-code has been written [1] to generate Cartesian locations for the end-effector of BASRS from the roadway markings. In addition, in order to produce certain visual quality, these roadway markings set specific restrictions, such as the tilt angle of the paint nozzle. These requirements are simplified and described [9, 12] by introducing three coordinate spaces - the cartesian coordinate space, the task coordinate space and the manipulator base coordinate space (Fig.3.1). The relation between the task coordinate space, which is assumed to be the known quantity, and the actuator space, which will be the solution of the inverse kinematics problem, are the subject of this chapter.

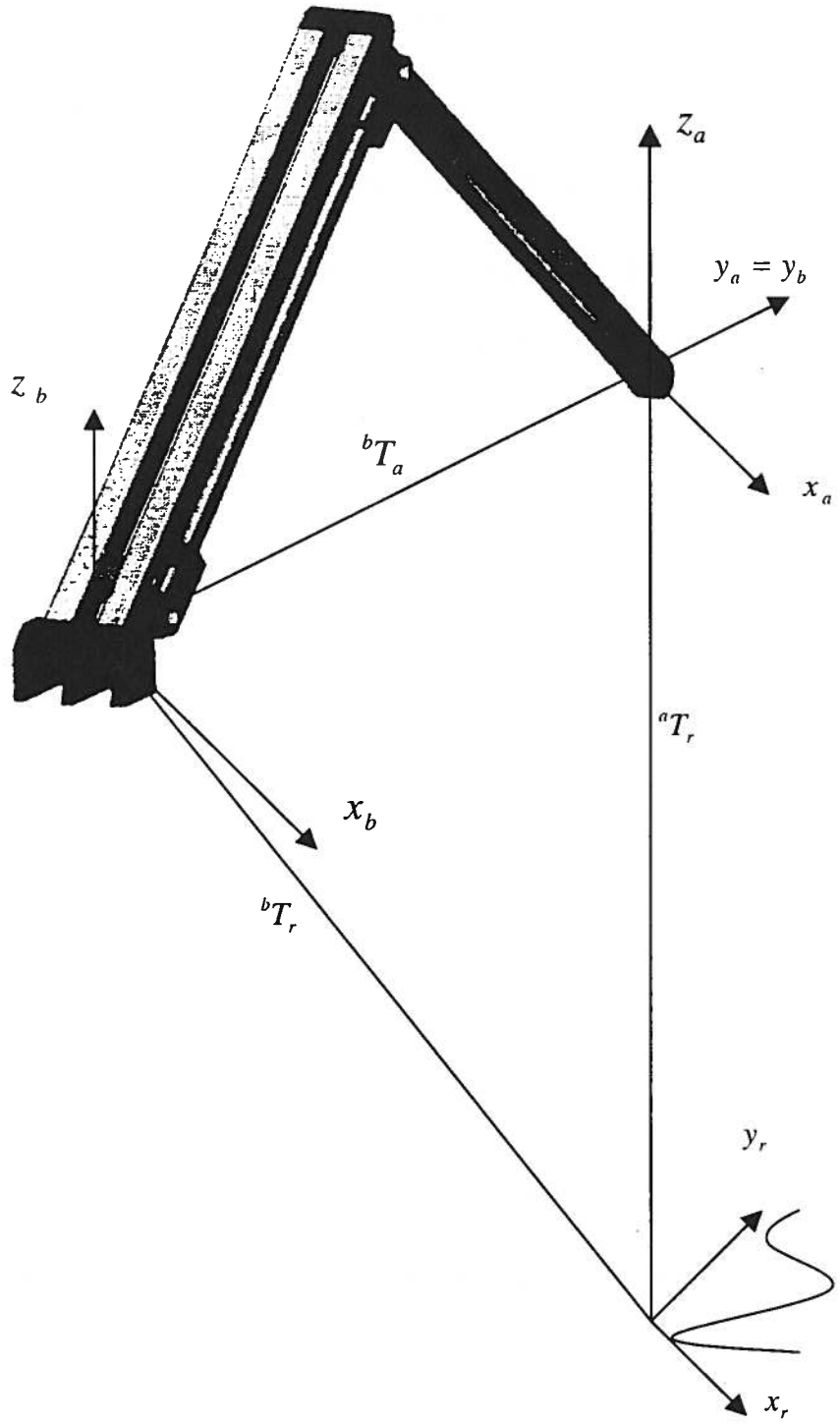

Fig.3.1. Relation between the Base Coordinate Space (x_b, y_b, z_b), the End-effector Coordinate Space (x_a, y_a, z_a) and the Task/Road Space (x_r, y_r)

3.2. Kinematic Equations for the Arm and the End-effector

Considering the standard form of the homogeneous transformation matrix T_i, the corresponding transformation matrices (Fig.3.1) ${}^{b}T_{r}$ (representing the relation between the road and the base coordinate systems) and ${}^{a}T_{r}$ (describing the road coordinate system with respect to the arm coordinate system), have the following form:

$$ {}^{b}T_{r} = \begin{bmatrix} 1 & 0 & 0 & {}^{b}p_{xr} \\ 0 & 1 & 0 & {}^{b}p_{yr} \\ 0 & 0 & 1 & {}^{b}p_{zr} \\ 0 & 0 & 0 & 1 \end{bmatrix} \tag{3.1} $$

$$ {}^{a}T_{r} = \begin{bmatrix} 1 & 0 & 0 & {}^{a}p_{xr} \\ 0 & 1 & 0 & {}^{a}p_{yr} \\ 0 & 0 & 1 & {}^{a}p_{zr} \\ 0 & 0 & 0 & 1 \end{bmatrix} \tag{3.2} $$

where ${}^{b}p_{xr}$, ${}^{b}p_{yr}$, ${}^{b}p_{zr}$ are the position vectors of the road coordinate system with respect to the base and ${}^{a}p_{xr}$, ${}^{a}p_{yr}$, ${}^{a}p_{zr}$ are the position vectors of the road coordinate system with respect to the end-effector coordinate system.

The homogeneous transformation matrix ${}^{b}T_{a}$ (representing the relation between the arm and the base coordinate system for BASRS) is equal to the product chain of the four coordinate transformation matrices A_i, derived in Chap.2:

$$ {}^{b}T_{a} = A_1 A_2 A_3 A_4 = \begin{bmatrix} \cos(\theta_1 + \theta_4) & \sin(\theta_1 + \theta_4) & 0 & a_2 \cos\theta_1 - d_2 \sin\theta_1 \\ -\sin(\theta_1 + \theta_4) & \cos(\theta_1 + \theta_4) & 0 & a_2 \sin\theta_1 + d_2 \cos\theta_1 \\ 0 & 0 & 1 & d_3 \\ 0 & 0 & 0 & 1 \end{bmatrix} \tag{3.3} $$

where (see Fig.2.1):

θ_1 is the rotation of the base of the robot-manipulator along z_1 axis;

a_2 is the offset between the arm and the end-effector;

d_2 is the arm/end-effector translation along y_a axis;

θ_4 is the end-effector rotation along z_a axis;

d_3 is the distance, between the end-effector and the road, which alternates in order to compensate for the tilt motion.

Note: The robot arm structure has been constructed as a pantograph mechanism, where the extension length is amplified 8.33 times the actuator movement.

The homogeneous transformation matrix ${}^{a}T_{r}$ is expressed as:

$$ {}^{a}T_{r} = ({}^{b}T_{a})^{-1}\,{}^{b}T_{r} \tag{3.4} $$

where:

$$({}^{b}T_{a})^{-1} = \begin{bmatrix} \cos(\theta_1+\theta_4) & \sin(\theta_1+\theta_4) & 0 & -a_2\cos\theta_4 - d_2\sin\theta_4 \\ -\sin(\theta_1+\theta_4) & \cos(\theta_1+\theta_4) & 0 & a_2\sin\theta_4 - d_2\cos\theta_4 \\ 0 & 0 & 1 & -d_3 \\ 0 & 0 & 0 & 1 \end{bmatrix} \tag{3.5}$$

Finally, the transformation matrix of the road coordinate system with respect to the arm coordinate system has the following form:

$${}^{a}T_{r} = ({}^{b}T_{a})^{-1}\,{}^{b}T_{r} = \tag{3.6}$$

$$\begin{bmatrix} \cos(\theta_1+\theta_4) & \sin(\theta_1+\theta_4) & 0 & {}^{b}p_{xr}\cos(\theta_1+\theta_4)+{}^{b}p_{yr}\sin(\theta_1+\theta_4) - d_2\sin\theta_4 - a_2\cos\theta_4 \\ -\sin(\theta_1+\theta_4) & \cos(\theta_1+\theta_4) & 0 & -{}^{b}p_{xr}\sin(\theta_1+\theta_4)+{}^{b}p_{yr}\cos(\theta_1+\theta_4) - d_2\cos\theta_4 + a_2\sin\theta_4 \\ 0 & 0 & 1 & {}^{b}p_{zr} - d_3 \\ 0 & 0 & 0 & 1 \end{bmatrix}$$

The two matrices (3.2) and (3.6) lead to the following system of kinematic equations:

$$\cos(\theta_1+\theta_4) = 1 \tag{3.7}$$

$$\sin(\theta_1+\theta_4) = 0 \tag{3.8}$$

$${}^{a}p_{xr} = {}^{b}p_{xr}\cos(\theta_1+\theta_4)+{}^{b}p_{yr}\sin(\theta_1+\theta_4) - d_2\sin\theta_4 - a_2\cos\theta_4 \tag{3.9}$$

$$ {}^{a}p_{yr} = -{}^{b}p_{xr}\sin(\theta_1+\theta_4)+{}^{b}p_{yr}\cos(\theta_1+\theta_4)-d_2\cos\theta_4+a_2\sin\theta_4 \tag{3.10} $$

$$ {}^{a}p_{zr}={}^{b}p_{zr}-d_3 \quad . \tag{3.11} $$

The spray distance ${}^{a}p_{zr}$ in eqn. (3.11) is a function of the width of the painted line w and the fan angle α (Fig. 3.2):

$$ {}^{a}p_{zr} = \frac{w}{2\tan\left(\frac{\alpha}{2}\right)} \tag{3.12} $$

The paint volume on a surface is equal to (Fig.3.2):

$$ V = \mu\sigma t \tag{3.13} $$

where:

μ is the flow rate on the nozzle;

σ is the paint transfer efficiency;

t is the spray time.

The average coating thickness δ (Fig.3.2) is a function of the paint volume V and the painted area A and can be expressed as follows:

$$ \delta = \frac{\mu\sigma t}{A} \tag{3.14} $$

The spray time t in eqn. (3.14) depends on the width of the sprayed area w, eqn. (3.12), and the velocity v of the nozzle along a defined trajectory as follows:

$$t = \frac{w}{v} = \frac{2\tan\left(\frac{\alpha}{2}\right)^{a} p_{zr}}{v} \tag{3.15}$$

The translational motion d_3 of the end-effector along its z-axis is a function of the length of the moving platform r_2 and the tilt angle θ_{2e}, written as:

$$d_3 = \frac{r_2}{2}\sin\theta_{2e} \tag{3.16}$$

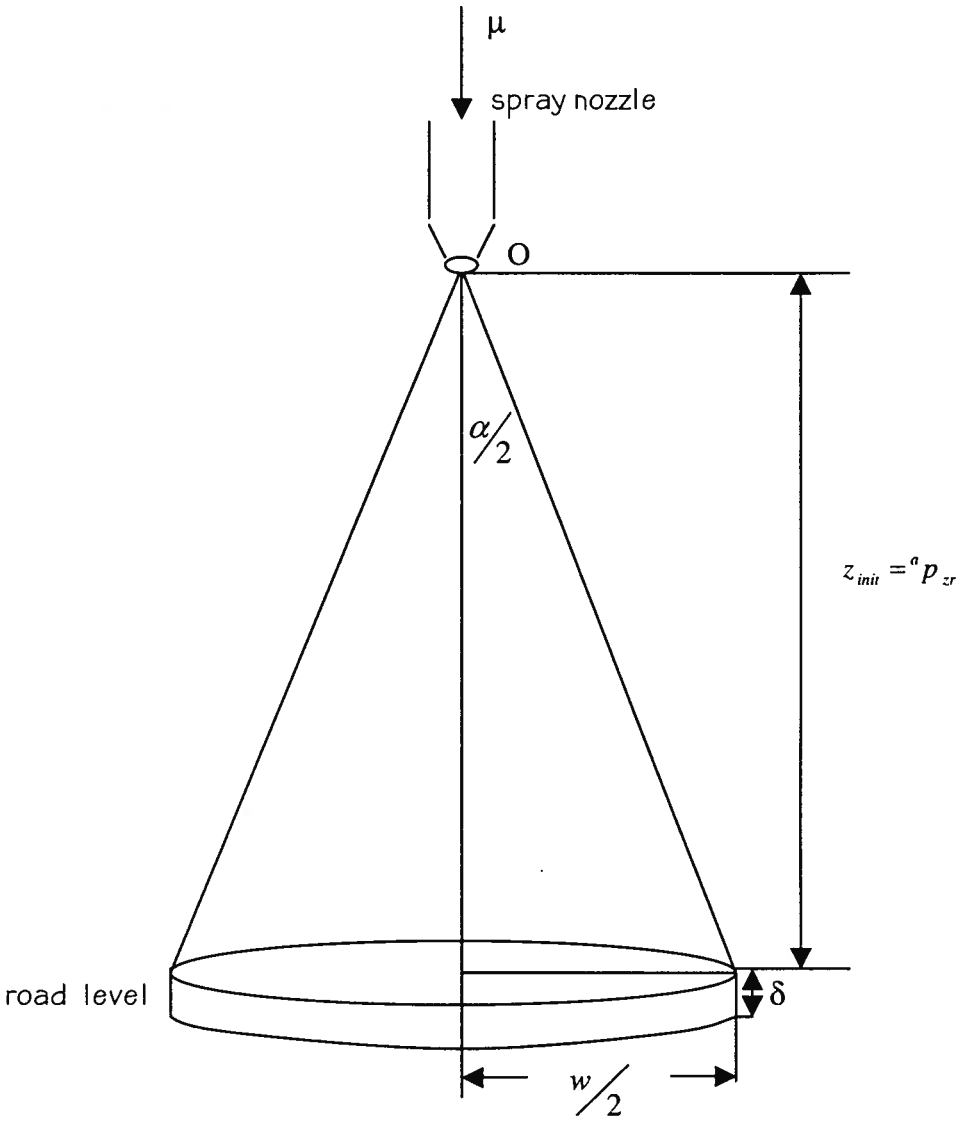

Fig.3.2. Geometry of the Spray Nozzle

Fig.3.3 presents the relations described in eqns. (3.12) and (3.16). The code can be found Appendix G. Note, that ${}^{a}p_{zr}$ is equal to Z_{init}, and that Z_{res} is the difference between Z_{init} and d_3.

The first plot presents the relation between the tilt angle and Z_{res}. The second plot shows the necessary vertical translation of the end-effector in order to compensate for the tilt motion, chosen to be in the range of (-0.4)rad and (+0.4)rad for this particular case.

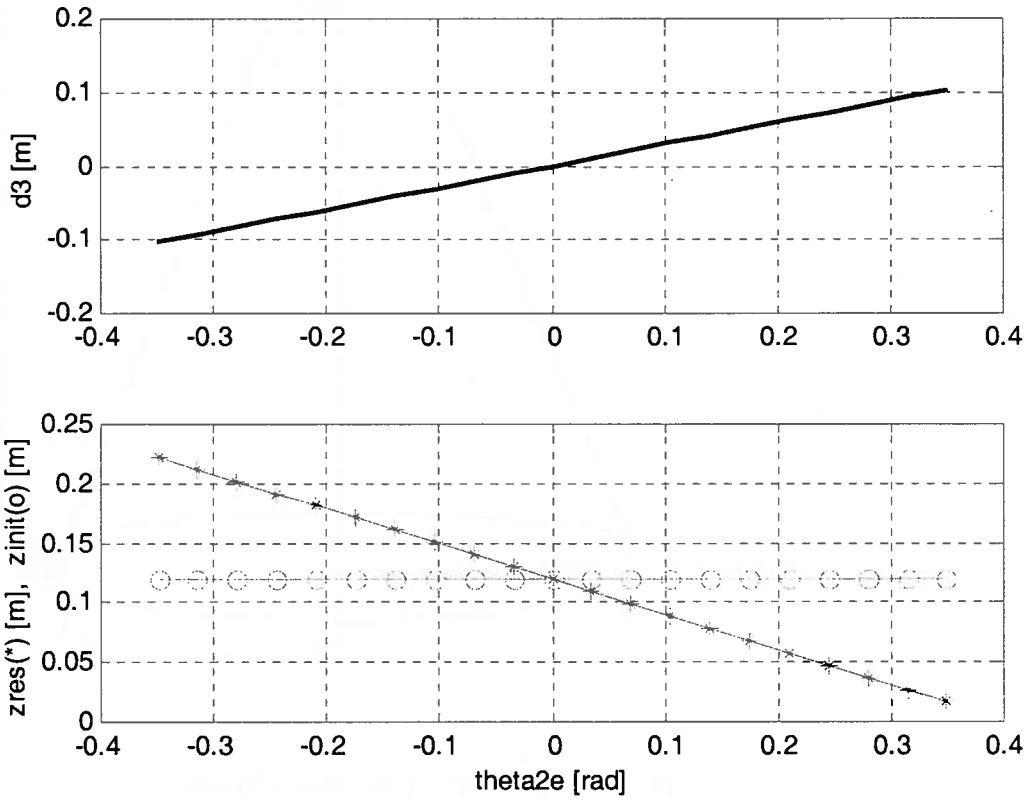

Fig.3.3. Relation between the Tilt Angle and the Vertical Translation for Compensating the Tilt Motion

3.3. Inverse Kinematic Solutions for the Roadway Painting Task

Considering the aforementioned, the equations describing the actuator space with respect to the task space, can be presented as a system of four equations with four unknown variables ($\theta_1, \theta_4, d_2, d_3$):

$$\theta_1 = -\theta_4 \tag{3.17}$$

$${}^{a}p_{xr} = {}^{b}p_{xr} - d_2 \sin\theta_4 - a_2 \cos\theta_4 \tag{3.18}$$

$${}^{a}p_{yr} = {}^{b}p_{yr} - d_2 \cos\theta_4 + a_2 \sin\theta_4 \tag{3.19}$$

$$d_3 = {}^{b}p_{zr} - {}^{a}p_{zr} \tag{3.20}$$

The unknown actuator space variables d_2 and θ_4 can be expressed from the following system of two nonlinear equations:

$$\tan^2\frac{\theta_4}{2}\left({}^{a}p_{xr} - {}^{b}p_{xr} - a_2\right) + 2d_2 \tan\frac{\theta_4}{2} + {}^{a}p_{xr} - {}^{b}p_{xr} + a_2 = 0 \tag{3.21}$$

$$\tan^2\frac{\theta_4}{2}\left({}^{a}p_{yr} - {}^{b}p_{yr} - d_2\right) - 2a_2 \tan\frac{\theta_4}{2} + {}^{a}p_{yr} - {}^{b}p_{yr} + d_2 = 0 \tag{3.22}$$

Factoring d_2 from eqn. (3.22) yields:

$$d_2 = \frac{T^2\,{}^{a}p_{yr} - T^2\,{}^{b}p_{yr} - 2a_2T + {}^{a}p_{yr} - {}^{b}p_{yr}}{8.33(T^2 - 1)} \tag{3.23}$$

where:

$$T = \tan\frac{\theta_4}{2} \tag{3.24}$$

Plugging the expression for d_2 into eqn. (3.21) leads to the following solutions for θ_4:

$$\theta_{41} = 2\arctan\left[\frac{({}^{a}p_{yr} - {}^{b}p_{yr}) + \sqrt{\left(({}^{b}p_{xr} - {}^{a}p_{xr})^2 + ({}^{b}p_{yr} - {}^{a}p_{yr})^2 + {a_2}^2\right)}}{({}^{b}p_{xr} - {}^{a}p_{xr} + a_2)}\right] \tag{3.25}$$

$$\theta_{42} = 2\arctan\left[\frac{({}^{a}p_{yr} - {}^{b}p_{yr}) - \sqrt{\left(({}^{b}p_{xr} - {}^{a}p_{xr})^2 + ({}^{b}p_{yr} - {}^{a}p_{yr})^2 + {a_2}^2\right)}}{({}^{b}p_{xr} - {}^{a}p_{xr} + a_2)}\right] \tag{3.26}$$

θ_4 has real values, if the following condition is satisfied:

$$({}^{b}p_{yr} - {}^{a}p_{yr})^2 + ({}^{b}p_{xr} - {}^{a}p_{xr})^2 + a_2^2 \geq 0 \tag{3.27}$$

The tilt angle θ_{2e} is derived from equations (3.11), (3.12), (3.16) and has the following form:

$$\theta_{2e1} = 2\arctan\left[\frac{-1 + \sqrt{\left(1 - 4({}^{a}p_{zr} - {}^{b}p_{zr})^2\right)}}{2({}^{a}p_{zr} - {}^{b}p_{zr})}\right] \tag{3.28}$$

$$\theta_{2e2} = 2\arctan\left[\frac{-1 - \sqrt{\left(1 - 4({}^{a}p_{zr} - {}^{b}p_{zr})^2\right)}}{2({}^{a}p_{zr} - {}^{b}p_{zr})}\right] \tag{3.29}$$

θ_{2e} has real values, if:

$$^{a}p_{zr} - {}^{b}p_{zr} \leq \frac{1}{2} \tag{3.30}$$

The relation between the tilt angle and the ball-screw drive motion (Δx) expressed in Chap.2, can now be written as:

$$\Delta x = \frac{r_4}{2} - \frac{r_2}{2}\left(\frac{1-\tan^2\frac{\theta_{2e1}}{2}}{1+\tan^2\frac{\theta_{2e1}}{2}}\right) + \frac{2r_1\tan\frac{\theta_{1e}}{2}\tan\theta_{2e1}}{1+\tan^2\frac{\theta_{1e}}{2}} \pm \sqrt{r_1^2 - \left(\frac{2r_2\tan\frac{\theta_{2e1}}{2}}{1+\tan^2\frac{\theta_{2e1}}{2}} + \frac{2r_1\tan\frac{\theta_{1e}}{2}}{1+\tan^2\frac{\theta_{1e}}{2}}\right)^2} \tag{3.31}$$

The relation between θ_{1e} and θ_{2e} is given in Chapter 2. The straight-line motion Δx has real values if:

$$r_1 \geq \frac{2r_2\tan\frac{\theta_{2e1}}{2}}{1+\tan^2\frac{\theta_{2e1}}{2}} + \frac{2r_1\tan\frac{\theta_{1e}}{2}}{1+\tan^2\frac{\theta_{1e}}{2}} \tag{3.32}$$

Finally, eqns. (3.17), (3.20), (3.23), (3.25), (3.26) and (3.31) completely present the relation between the robot manipulator actuator space variables and the task space variables.

Two practical examples of the application of the derived inverse kinematics solutions for the actuator space variables θ_1, θ_4 and d_2 is given in the next section. Particular values for the other two actuator space variables d_3 and Δx, with respect to the tilt angle, had been already shown in Chapter 2.

3.4. Expermental Results

The section describes the results for inverse kinematic solution for BASRS end-effector position, while painting the letter "S" of a "STOP" in a roadway marking. The letter "S" (Fig. 3.4) is chosen for the example provided here, since it has the most varying curvature as compared to other commonly used letters in roadway markings.

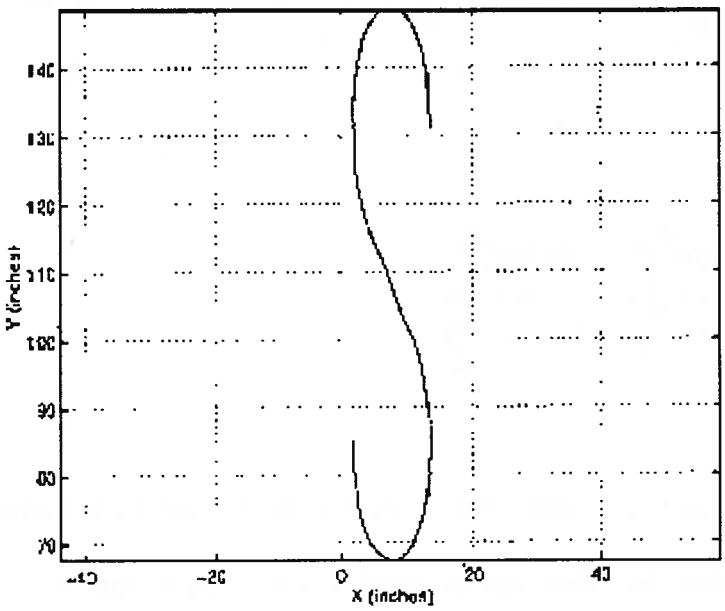

Fig. 3.4. Trajectory in X and Y coordinates

The roadway markings are specified by "Standard Alphabets for Highway Signs and Pavement Markings" printed by the U.S. Department of Transportation. The letters are in the two dimensional space of the road and are required to be applied at heights not shorter than 2.44m (8 feet). This allows a roadway marking to be read clearly by the drivers from sharp angles. As it was mentioned, a sample of the standard letter "S" in proper coordinates is shown in Fig. 3.4. The robot end-effector has to trace this letter, which means that the coordinates of every point of "S" should be used in describing the Cartesian location of the robot end-effector. The coordinates of fifteen points (p_{xra}, p_{yrb}) of the letter "S" are generated and substituted in equations (3.17), (3.23), (3.24), (3.25), (3.26). Data for two examples are provided in Appendix I.

4. CONCLUSIONS

The present work dealt with a kinematic study of the Big Articulated Stenciling Robotic System (BASRS) from the roadway-painting task to the joint actuators of the robot.

For more systematic formulation of the analysis and synthesis of the stenciling robot, special attention had been paid to the tilt motion of the end-effector. Some important features of the four bar linkage – its special plane motion and straight-line motion, have been discussed. The incorporation of the tilt motion, along with the vertical translation for its compensation in the entire kinematics of BASRS, will introduce a consistent paint thickness in painting roadway markings.

The overall kinematic analysis of the system, from the roadway painting task to the actuator motion, has been presented facilitating the future control algorithms. The obtained results can be used for a kinematic control and can provide the basis for further work on Trajectory generation and smoothing methods that can enhance the performance of BASRS in painting roadway markings.

REFERENCES

1. Blank R. (1998) *Algorithms for Robotic Hardware Improvements for Painting of Roadway Markings*, AHMCT Research Report, UCD-ARR-98-01-15-01, 1998.

2. Bottema O. and B. Roth (1979) *Theoretical Kinematics*, Dover Publications, Inc., New York.

3. Burton P. (1979) *Kinematics and Dynamics of Planar Machinery*, Prentice-Hall,Inc., Englewood Cliffs, New Jersey.

4. Chernoushko F., N. Bolotnik and V. Gradetsky (1994) *Manipulation Robots: dynamics, control and optimization*, Boca Raton: CRC Press.

5. Craig J. (1989) *Introduction to Robotics, Mechanics and Control*, Addison-Wesley Publishing Company, Inc.

6. Crane C. and Joseph Duffy (1998) *Kinematic Analysis of Robot Manipulators*, Cambridge University Press.

7. Erdman A. and G. Sandor (1991) *Mechanism Design*, Prentice-Hall, Englewood Cliffs, New Jersey.

8. Fu K. S., R. C. Gonzalez and C. S. G. Lee (1987) *Robotics Control, Sensing, Vision and Intelligence*, McGraw-Hill, Inc.

9. Klafter R., T. Chmielewski and M. Negin (1989) *Robotic Engineering – an Integrated Approach*, Prentice-Hall, Englewood Cliffs, New Jersey.

10. Lenarcic J. and V. Parenti-Castelli (1996) *Recent Advances in Robot Kinematics*, Kluwer Academic Publishers, Boston.

11. Mason S. (1985) *Robot Hands and the Mechanics of Manipulation*, MIT Press.

12. Parkin R. (1991) *Applied Robotic Analysis*, Prentice-Hall, Englewood Cliffs, New Jersey.

13. Ravani B. (2000) *Lecture Notes on Spatial Kinematics*, Spring'2000.

14. Tsai L. (1999) *The Mechanics of Serial and Parallel Manipulators*, John Wiley & Sons, Inc., New York.

Appendix A

MATLAB Program for θ_{1e} Calculation as a Function of θ_{2e}

This appendix includes calculation of the input angle θ_{1e}, for the four bar linkage of the end-effector of BASRS, with respect to the tilt motion θ_{2e}. The links of the four bar linkage are marked as r_1, r_2, r_3 and r_4 and their size is given in meters. Alpha is the angle of the spray nozzle and is given in radians. The MATLAB program for the calculations and the results are as follows:

```
global theta2e theta1e1 a b c


r1=0.9
r2=0.6
r3=0.9
r4=1.2


alpha=8*pi/18

reszz=zeros(21,2);
i=1;

for theta2e=-pi/9:pi/90:pi/9

a=(r1)^2+(r2)^2+(r4)^2-(r3)^2-2*r4*r2*cos(theta2e)-
2*r2*r1*cos(theta2e)+2*r4*r1;
b=4*r2*r1*sin(theta2e);
c=(r1)^2+(r2)^2+(r4)^2-(r3)^2-
2*r4*r2*cos(theta2e)+2*r2*r1*cos(theta2e)-2*r4*r1;

theta1e=2*atan((-b+sqrt((b^2)-4*a*c))/(2*a));

reszz(i,:)=[theta2e theta1e];
i=i+1;
end


reszz

plot(reszz(:,1),reszz(:,2),'*')
xlabel('theta2e')
ylabel('theta1e')
grid
```

Results (Appendix A)

r1 =

0.9

r2 =

0.6

r3 =

0.9

r4 =

1.2

alpha =

1.3963

reszz =

θ_{2e}	θ_{1e}
-0.34907	1.5023
-0.31416	1.4842
-0.27925	1.4638
-0.24435	1.4412
-0.20944	1.4165
-0.17453	1.3898
-0.13963	1.3611
-0.10472	1.3307
-0.069813	1.2987
-0.034907	1.2654
0	1.231
0.034907	1.1957
0.069813	1.1598
0.10472	1.1235
0.13963	1.0872
0.17453	1.0509
0.20944	1.0151
0.24435	0.97971
0.27925	0.94505
0.31416	0.9112
0.34907	0.87828

Appendix B

MATLAB Program for Δx Calculation as a Function of θ_{2e}

This appendix includes calculations of the tilt motion θ_{2e} with respect to the straight-line motion Δx of the four-bar linkage, which represents the end-effector of BASRS. The links of the four bar linkage are marked as r_1, r_2, r_3 and r_4 and their size is given in meters. The MATLAB program and the results are given below:

```
global theta2e a b c theta1e delx

r1=0.9
r2=0.6
r3=0.9
r4=1.2
reszz=zeros(21,3);
i=1;

for theta2e=-pi/9:pi/90:pi/9

a=(r1)^2+(r2)^2+(r4)^2-(r3)^2-2*r4*r2*cos(theta2e)-...
2*r2*r1*cos(theta2e)+2*r4*r1;

b=4*r2*r1*sin(theta2e);

c=(r1)^2+(r2)^2+(r4)^2-(r3)^2-2*r4*r2*cos(theta2e)+...
2*r2*r1*cos(theta2e)-2*r4*r1;

theta1e=2*atan((-b+sqrt((b^2)-4*a*c))/(2*a));

delx=r4/2-r2*cos(theta2e)+r2/(2*cos(theta2e))+...
r1*sin(theta1e)*tan(theta2e)-...
sqrt((r1)^2-(r2*sin(theta2e)+r1*sin(theta1e))^2);

reszz(i,:)=[theta2e theta1e delx];

i=i+1;
end

reszz

plot(reszz(:,1),reszz(:,3),'*')
xlabel('theta2e')
ylabel('delx')
grid
```

Results (Appendix B)

r1 =

0.9

r2 =

0.6

r3 =

0.9

r4 =

1.2

reszz =

θ_{2e}	θ_{1e}	Δx
-0.34907	1.5023	-0.54599
-0.31416	1.4842	-0.49804
-0.27925	1.4638	-0.4484
-0.24435	1.4412	-0.39704
-0.20944	1.4165	-0.34402
-0.17453	1.3898	-0.28943
-0.13963	1.3611	-0.23342
-0.10472	1.3307	-0.1762
-0.069813	1.2987	-0.11802
-0.034907	1.2654	-0.059181
0	1.231	2.2204e-016
0.034907	1.1957	0.059181
0.069813	1.1598	0.11802
0.10472	1.1235	0.1762
0.13963	1.0872	0.23342
0.17453	1.0509	0.28943
0.20944	1.0151	0.34402
0.24435	0.97971	0.39704
0.27925	0.94505	0.4484
0.31416	0.9112	0.49804
0.34907	0.87828	0.54599

Appendix C

MATLAB Program for the Direct Kinematics Solution for the Position

This appendix includes the direct kinematic solutions for the position (xp1, yp1, zp1) of the end-effector of BASRS. The base rotation angle is θ_1.The offset between the arm and the end-effector is a2 and its value is given in cm. The arm extension length d_2 and the translation of the end-effector along its z-axis d_3, are also given in cm. The MATLAB program and the results are provided below:

```
global theta1 xp1 yp1 zp1

a2=1
d2=10
d3=10

zp1=d3;
resdp=zeros (21,4);
i=1

for theta1=0.0:pi/40:pi/2

xp1=a2.*(1-(tan(theta1)).^2)/(1+(tan(theta1)).^2)-
d2.*(2.*tan(theta1))/(1+(tan(theta1)).^2);
yp1=a2.*(2.*tan(theta1))/(1+(tan(theta1)).^2)+d2.*(1-
(tan(theta1)).^2)/(1+(tan(theta1)).^2);

resdp (i,:)=[theta1 xp1 yp1 zp1];
i=i+1;
end

resdp

subplot (3,1,1),plot (resdp(:,1),resdp(:,2),'*')
title ('Direct solutions for the position')
ylabel ('xp1')
grid

subplot (3,1,2),plot (resdp (:,1),resdp (:,3),'*')
ylabel ('yp1')
grid

subplot (3,1,3),plot (resdp(:,1),resdp(:,4),'*')
xlabel ('theta1')
ylabel ('zp1')
grid
```

a2 =

1

d2 =

10

d3 =

10

i =

1

resdp =

θ_1	xp1	yp1	zp1
0	1	10	10
0.07854	-0.57666	10.033	10
0.15708	-2.1391	9.8196	10
0.23562	-3.6489	9.3641	10
0.31416	-5.0688	8.678	10
0.3927	-6.364	7.7782	10
0.47124	-7.5024	6.6869	10
0.54978	-8.4561	5.4309	10
0.62832	-9.2015	4.0412	10
0.70686	-9.7204	2.552	10
0.7854	-10	1	10
0.86394	-10.033	-0.57666	10
0.94248	-9.8196	-2.1391	10
1.021	-9.3641	-3.6489	10
1.0996	-8.678	-5.0688	10
1.1781	-7.7782	-6.364	10
1.2566	-6.6869	-7.5024	10
1.3352	-5.4309	-8.4561	10
1.4137	-4.0412	-9.2015	10
1.4923	-2.552	-9.7204	10
1.5708	-1	-10	10

Appendix D

MATLAB Program for the Direct Kinematics Solution for the Orientation

This appendix includes the direct kinematic solutions for the orientation (u4x, u4y, u4z) of the end-effector of BASRS. The angle of rotation of the end-effector around its z-axis is θ_4. The mATLAB program and the results are given below:

```
global u4x u4y u4z theta4

u4z=0;

resdo=zeros (21,4);
i=1;

for theta4=0.0:pi/40:pi/2
u4x=(1-(tan(theta4)).^2)/(1+(tan(theta4)).^2);
u4y=(2.*tan(theta4))/(1+(tan(theta4)).^2);

resdo(i,:)=[theta4 u4x u4y u4z];
i=i+1;
end

resdo

subplot (3,1,1),plot (resdo(:,1),resdo(:,2),'*')
title ('Direct solutions for the orientation')
ylabel ('u4x')
grid

subplot (3,1,2),plot (resdo (:,1),resdo (:,3),'*')
ylabel ('u4y')
grid

subplot (3,1,3),plot (resdo(:,1),resdo(:,4),'*')
xlabel ('theta4')
ylabel ('u4z')
grid
```

Results (Appendix D)

resdo =

θ_4	u4x	u4y	u4z
0	1	0	0
0.07854	0.98769	0.15643	0
0.15708	0.95106	0.30902	0
0.23562	0.89101	0.45399	0
0.31416	0.80902	0.58779	0
0.3927	0.70711	0.70711	0
0.47124	0.58779	0.80902	0
0.54978	0.45399	0.89101	0
0.62832	0.30902	0.95106	0
0.70686	0.15643	0.98769	0
0.7854	1.1102e-016	1	0
0.86394	-0.15643	0.98769	0
0.94248	-0.30902	0.95106	0
1.021	-0.45399	0.89101	0
1.0996	-0.58779	0.80902	0
1.1781	-0.70711	0.70711	0
1.2566	-0.80902	0.58779	0
1.3352	-0.89101	0.45399	0
1.4137	-0.95106	0.30902	0
1.4923	-0.98769	0.15643	0
1.5708	-1	1.2246e-016	0

Appendix E

MATLAB Program for the Inverse Kinematics Solution for the Position

This appendix includes the inverse kinematic solutions for the position (xp1, yp1, zp1) of the end-effector of BASRS. The angle of rotation of the base of the arm is θ_1, d_2 is the extension length of the arm and a_2 is the offset between the arm and the end-effector. The MATLAB program and the results are given below:

```
global resdp resip xp1 yp1 zp1 theta1 d2 d3 broi a2

a2=0.1
xp1=resdp(:,2);
yp1=resdp(:,3);
zp1=resdp(:,4);
d3=zp1;
broi=length(xp1);
resip=zeros(broi,6);

for j=1:broi
theta1(j)=atan((yp1(j)-sqrt((yp1(j)).^2-((a2).^2-
xp1(j).^2)))/(xp1(j)+a2));
d2(j)=-(2.*tan(theta1(j)).*xp1(j))/(1+(tan(theta1(j))).^2)+(1-
(tan(theta1(j))).^2).*yp1(j)/(1+(tan(theta1(j))).^2);
resip(j,:)=[xp1(j) yp1(j) zp1(j) theta1(j) d2(j) d3(j)];

end

resip

subplot(3,1,1),plot3 (resip (:,1),resip (:,2),resip (:,4),'*')
title ('Inverse solutions for the position')
%xlabel ('xp1')
%ylabel ('yp1')
zlabel ('theta1')
grid
subplot(3,1,2),plot3 (resip(:,1),resip (:,2),resip (:,5),'*')
%xlabel ('xp1')
%ylabel ('yp1')
zlabel ('d2')
grid
subplot(3,1,3),plot3 (resip (:,1),resip (:,4),resip (:,6),'*')
xlabel ('xp1')
ylabel ('yp1')
zlabel ('d3')
grid
```

a2 =

1

resip =

xp1	yp1	zp1	θ_1	d_2	d_3
1	10	10	0	10	10
-0.57666	10.033	10	0.07854	10	10
-2.1391	9.8196	10	0.15708	10	10
-3.6489	9.3641	10	0.23562	10	10
-5.0688	8.678	10	0.31416	10	10
-6.364	7.7782	10	0.3927	10	10
-7.5024	6.6869	10	0.47124	10	10
-8.4561	5.4309	10	0.54978	10	10
-9.2015	4.0412	10	0.62832	10	10
-9.7204	2.552	10	0.70686	10	10
-10	1	10	0.7854	10	10
-10.033	-0.57666	10	0.86394	10	10
-9.8196	-2.1391	10	0.94248	10	10
-9.3641	-3.6489	10	1.021	10	10
-8.678	-5.0688	10	1.0996	10	10
-7.7782	-6.364	10	1.1781	10	10
-6.6869	-7.5024	10	1.2566	10	10
-5.4309	-8.4561	10	1.3352	10	10
-4.0412	-9.2015	10	1.4137	10	10
-2.552	-9.7204	10	1.4923	10	10
-1	-10	10	1.5708	10	10

Appendix F

MATLAB Program for the Inverse Kinematics Solution for the Orientation

This appendix includes the inverse kinematic solutions (u4x, u4y, u4z) for the end-effector of BASRS, where θ_4 is the angle of rotation of the end-effector around its z-axis.

The MATLAB program and the results are given below:

```
global  resdo resio u4x u4y u4z theta4 broi

u4x=resdo(:,2);
u4y=resdo(:,3);
u4z=resdo(:,4);

broi=length(u4x);

resio=zeros(broi,4);

for j=1:broi

theta4(j)=atan(u4y(j)/(u4x(j)+1));

resio(j,:)=[u4x(j) u4y(j) u4z(j) theta4(j)];

end

resio

plot3(resio(:,1),resio(:,2),resio(:,4),'*')
title('Inverse solutions for the orientation')
xlabel('u4x')
ylabel('u4y')
zlabel('theta4')
grid
```

Results (Appendix F)

resio =

u4x	u4y	u4z	θ_4
1	0	0	0
0.98769	0.15643	0	0.07854
0.95106	0.30902	0	0.15708
0.89101	0.45399	0	0.23562
0.80902	0.58779	0	0.31416
0.70711	0.70711	0	0.3927
0.58779	0.80902	0	0.47124
0.45399	0.89101	0	0.54978
0.30902	0.95106	0	0.62832
0.15643	0.98769	0	0.70686
1.1102e-016	1	0	0.7854
-0.15643	0.98769	0	0.86394
-0.30902	0.95106	0	0.94248
-0.45399	0.89101	0	1.021
-0.58779	0.80902	0	1.0996
-0.70711	0.70711	0	1.1781
-0.80902	0.58779	0	1.2566
-0.89101	0.45399	0	1.3352
-0.95106	0.30902	0	1.4137
-0.98769	0.15643	0	1.4923
-1	1.2246e-016	0	1.5708

Appendix G

MATLAB Program Giving the Relation between the Task Coordinates and the Robot-manipulator Actuator Space Variables

This appendix includes calculations of the end-effector translation along its z-axis (zres), for compensating the tilt motion θ_{2e}. The width of the painted line, w, is given in cm. The size of the second bar of the four-bar linkage of the end-effector of BASRS is r2 and is given in cm. The initial length, between the road and the painting nozzle, which is rigidly connected to the end-effector, is zinit, given also .in cm. Alpha is the spray angle and is measured in radians. The MATLAB program and the results are given below:

```
global theta2e zres zinit d3

r2=0.6
w=0.2

alpha=8*pi/18
zinit=w/(2*tan(alpha/2))
reszz=zeros(21,4);
i=1;

for theta2e=-pi/9:pi/90:pi/9

d3=(r2/2)*sin(theta2e);
zres=zinit-d3;

reszz(i,:)=[theta2e zinit d3 zres];
i=i+1;
end

reszz

subplot(2,1,1),plot(reszz(:,1),reszz(:,3),'*')
ylabel('d3(*)')
grid


subplot(2,1,2),plot(reszz(:,1),reszz(:,4),'*',reszz(:,1),reszz(:,2),'o'
)
xlabel('theta2e')
ylabel('zres(*) zinit(o)')
grid
```

r2 =

0.6000

w =

0.2000

alpha =

1.3963

zinit =

0.1192

reszz =

θ_{2e}	zinit	d_3	zres
-0.3491	0.1192	-0.1026	0.2218
-0.3142	0.1192	-0.0927	0.2119
-0.2793	0.1192	-0.0827	0.2019
-0.2443	0.1192	-0.0726	0.1918
-0.2094	0.1192	-0.0624	0.1815
-0.1745	0.1192	-0.0521	0.1713
-0.1396	0.1192	-0.0418	0.1609
-0.1047	0.1192	-0.0314	0.1505
-0.0698	0.1192	-0.0209	0.1401
-0.0349	0.1192	-0.0105	0.1296
0	0.1192	0	0.1192
0.0349	0.1192	0.0105	0.1087
0.0698	0.1192	0.0209	0.0982
0.1047	0.1192	0.0314	0.0878
0.1396	0.1192	0.0418	0.0774
0.1745	0.1192	0.0521	0.0671
0.2094	0.1192	0.0624	0.0568
0.2443	0.1192	0.0726	0.0466
0.2793	0.1192	0.0827	0.0365
0.3142	0.1192	0.0927	0.0265
0.3491	0.1192	0.1026	0.0166

Appendix H

Link Coordinate System and its Parameters

This appendix presents a general description of a link coordinate system and its parameters.

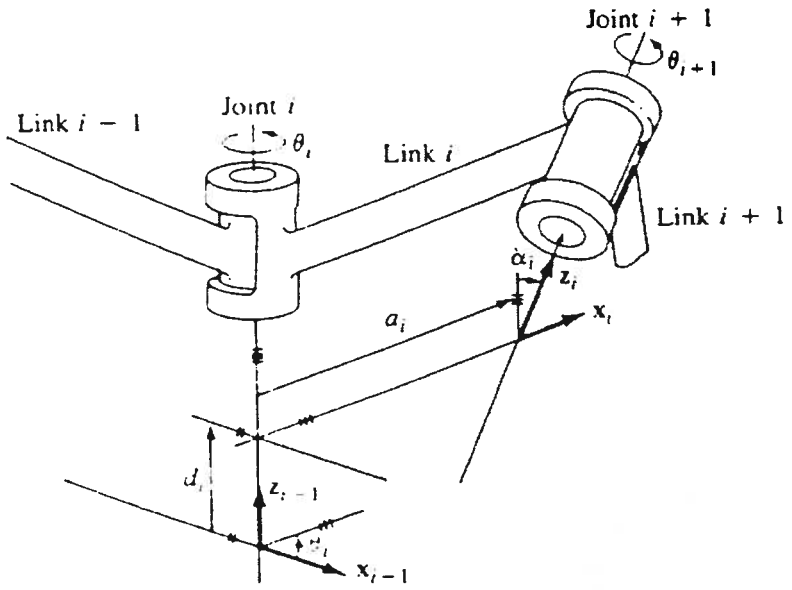

Link coordinate system and its parameters.

The Denavit-Hartenberg representation of a rigid link depends on:

θ_i - joint angle from x_{i-1} axis to the x_i axis about the z_{i-1} axis;

d_i- distance from the origin of the (i-1)-th coordinate frame to the intersection of the z_{i-1} axis with the x_i axis along the z_{i-1} axis;

a_i - the offset distance from the intersection of the z_{i-1} axis with the x_i axis to the origin of the i-th frame along the x_i axis;

α_i - the offset angle from the z_{i-1} axis to the z_i axis about the x_i axis (using the right hand rule).

Appendix I

Examples of the Inverse Kinematics Solutions for Markings of the Letter "S"

In this appendix, data for two different examples, outlining the changes in location of the end-effector, while painting the letter "S" are provided. The input of each case in these two examples are the coordinates of a particular point of the letter "S" (p_{xra}, p_{yra}), as well as the position of the base of the arm, which remains constant throughout the painting process of the letter. The Mathcad simulations, shown in this appendix, calculate the respective values for the end-effector location (base angle and extension length) for each of these points.

In the first example the position of the base of the arm with respect to the road coordinate system (Fig. 3.4) is chosen to be p_{xrb} = 0.1905m (8 inches), p_{yrb} = 0m and, as mentioned, remains constant throughout the whole painting process of the letter. In that case the base angle changes its sign two times due to the correlation between the chosen arm base coordinates and the varying curvature of the letter.

The second example describes a different position of the arm base (-1, 0.762) meters, which is equal to (-40, 30) feet. That means, that the arm base has been positioned further away on the left of the letter coordinate space. That is the reason why the results for the base angle show much higher values. In this example the base angle does not change sign, due to the chosen position of the arm.

Both examples show also the arm extension length for each point with respect to the already calculated base angle. All angles have two values, which represent one and the same angle in both first and second quadrant. The same holds true for the lengths of the arm extension, which are directly calculated from the respective base angles.

Note that all the calculations, as well as the experimental results concerning the tilt motion of the end-effector are shown in Chapter 2.

FIRST EXAMPLE

CASE 1:

Coordinates of the first point of the letter "S":

$p_{xra} := 0.3175m$

$p_{yra} := 3.3528m$

Coordinates of the truck wrt the road:

$p_{xrb} := 0.1905m$

$p_{yrb} := 0m$

Offset value between the arm and the end-effector:

$a_2 := 0.01m$

The rotation of the end-effector around z-axis (see Fig.2.1):

$$\theta_{4,1} := 2\cdot\operatorname{atan}\left[\frac{1}{\left[2\cdot\left(-p_{xra}+p_{xrb}+a_2\right)\right]}\cdot\left[-2\cdot p_{yrb}+2\cdot p_{yra}+2\cdot\left[\left(p_{xrb}-p_{xra}\right)^2+\left(-p_{yra}+p_{yrb}\right)^2-a_2^2\right]^{\left(\frac{1}{2}\right)}\right]\right]$$

$$\theta_{4,2} := 2\cdot\operatorname{atan}\left[\frac{1}{\left[2\cdot\left(-p_{xra}+p_{xrb}+a_2\right)\right]}\cdot\left[-2\cdot p_{yrb}+2\cdot p_{yra}-2\cdot\left[\left(p_{xrb}-p_{xra}\right)^2+\left(-p_{yra}+p_{yrb}\right)^2-a_2^2\right]^{\left(\frac{1}{2}\right)}\right]\right]$$

$\theta_{4,1} = -178.002\,\text{deg}$ $\theta_{4,2} = 2.34\,\text{deg}$ see eqns (3.25) and (3.26)

The base rotation of the arm:

$$T_n := \tan\left(\frac{\theta_{4,n}}{2}\right) \qquad n := 1..2$$

$\theta_{1,1} := 178.002\text{deg}$ $\theta_{1,2} := -2.34\text{deg}$ see eqn. (3.17)

$$T = \begin{pmatrix} 0 \\ -3.285\times 10^{3} \\ 1.17 \end{pmatrix}\text{deg}$$

The translation of the arm along y-axis (see Fig.2.1):

$$d_{2,n} := \frac{-\left[-\left(T_n\right)^2\cdot p_{yra}+\left(T_n\right)^2\cdot p_{yrb}+2\cdot a_2\cdot T_n-p_{yra}+p_{yrb}\right]}{8.33\cdot\left[\left(T_n\right)^2-1\right]}$$

$d_{2,1} = 0.403\,m$ $d_{2,2} = -0.403\,m$ see eqn. (3.23)

Note, that the relation between the tilt motion θ_{2e} and the ball-screw drive Δx as well as the compensation for the tilt, Zres, are given in Chap.2.

All the angles and lengths are presented in degrees and in meters, respectively.

CASE 2:

$p_{xra} := 0.3048m$ $p_{xrb} := 0.1905m$

$p_{yra} := 3.556m$ $p_{yrb} := 0m$

$a_2 := 0.01m$

$$\theta_{4,1} := 2\cdot\operatorname{atan}\left[\frac{1}{\left[2\cdot\left(-p_{xra}+p_{xrb}+a_2\right)\right]}\cdot\left[-2\cdot p_{yrb}+2\cdot p_{yra}+2\cdot\left[\left(p_{xrb}-p_{xra}\right)^2+\left(-p_{yra}+p_{yrb}\right)^2-a_2^2\right]^{\left(\frac{1}{2}\right)}\right]\right]$$

$$\theta_{4,2} := 2\cdot\operatorname{atan}\left[\frac{1}{\left[2\cdot\left(-p_{xra}+p_{xrb}+a_2\right)\right]}\cdot\left[-2\cdot p_{yrb}+2\cdot p_{yra}-2\cdot\left[\left(p_{xrb}-p_{xra}\right)^2+\left(-p_{yra}+p_{yrb}\right)^2-a_2^2\right]^{\left(\frac{1}{2}\right)}\right]\right]$$

$\theta_{4,1} = -178.32\,deg$ $\theta_{4,2} = 2.002\,deg$

$\theta_{1,1} := 178.32deg$ $\theta_{1,2} := -2.002deg$

$$T_n := \tan\left(\frac{\theta_{4,n}}{2}\right) \qquad n := 1..2$$

$$T = \begin{pmatrix} 0 \\ -3.908\times 10^{3} \\ 1.001 \end{pmatrix} deg$$

$$d_{2,n} := \frac{-\left[-\left(T_n\right)^2\cdot p_{yra}+\left(T_n\right)^2\cdot p_{yrb}+2\cdot a_2\cdot T_n-p_{yra}+p_{yrb}\right]}{8.33\cdot\left[\left(T_n\right)^2-1\right]}$$

$d_{2,1} = 0.427\,m$ $d_{2,2} = -0.427\,m$

CASE 3:

$p_{xra} := 0.1905m$ $p_{xrb} := 0.1905m$

$p_{yra} := 3.81m$ $p_{yrb} := 0m$

$a_2 := 0.01m$

$$\theta_{4,1} := 2\cdot\operatorname{atan}\left[\frac{1}{\left[2\cdot\left(-p_{xra}+p_{xrb}+a_2\right)\right]}\cdot\left[-2\cdot p_{yrb}+2\cdot p_{yra}+2\cdot\left[\left(p_{xrb}-p_{xra}\right)^2+\left(-p_{yra}+p_{yrb}\right)^2-a_2^2\right]^{\left(\frac{1}{2}\right)}\right]\right]$$

$$\theta_{4,2} := 2\cdot\operatorname{atan}\left[\frac{1}{\left[2\cdot\left(-p_{xra}+p_{xrb}+a_2\right)\right]}\cdot\left[-2\cdot p_{yrb}+2\cdot p_{yra}-2\cdot\left[\left(p_{xrb}-p_{xra}\right)^2+\left(-p_{yra}+p_{yrb}\right)^2-a_2^2\right]^{\left(\frac{1}{2}\right)}\right]\right]$$

$\theta_{4,1} = 179.85\,deg$ $\theta_{4,2} = 0.15\,deg$

$\theta_{1,1} := -179.85deg$ $\theta_{1,2} := -0.15deg$

$$T_n := \tan\left(\frac{\theta_{4,n}}{2}\right) \qquad n := 1..2$$

$$T = \begin{pmatrix} 0 \\ 4.366\times 10^4 \\ 0.075 \end{pmatrix} deg$$

$$d_{2,n} := \frac{-\left[-\left(T_n\right)^2\cdot p_{yra}+\left(T_n\right)^2\cdot p_{yrb}+2\cdot a_2\cdot T_n-p_{yra}+p_{yrb}\right]}{8.33\cdot\left[\left(T_n\right)^2-1\right]}$$

$d_{2,1} = 0.457\,m$ $d_{2,2} = -0.457\,m$

CASE 4:

$p_{xra} := 0.0508m$ $\quad p_{xrb} := 0.1905m$

$p_{yra} := 3.556m$ $\quad p_{yrb} := 0m$

$a_2 := 0.01m$

$$\theta_{4,1} := 2\cdot\operatorname{atan}\left[\frac{1}{\left[2\cdot\left(-p_{xra}+p_{xrb}+a_2\right)\right]}\cdot\left[-2\cdot p_{yrb}+2\cdot p_{yra}+2\cdot\left[\left(p_{xrb}-p_{xra}\right)^2+\left(-p_{yra}+p_{yrb}\right)^2-a_2^2\right]^{\left(\frac{1}{2}\right)}\right]\right]$$

$$\theta_{4,2} := 2\cdot\operatorname{atan}\left[\frac{1}{\left[2\cdot\left(-p_{xra}+p_{xrb}+a_2\right)\right]}\cdot\left[-2\cdot p_{yrb}+2\cdot p_{yra}-2\cdot\left[\left(p_{xrb}-p_{xra}\right)^2+\left(-p_{yra}+p_{yrb}\right)^2-a_2^2\right]^{\left(\frac{1}{2}\right)}\right]\right]$$

$$T_n := \tan\left(\frac{\theta_{4,n}}{2}\right)$$

$\theta_{4,1} = 177.589\,deg$ $\quad \theta_{4,2} = -2.089\,deg$

$n := 1..2$

$\theta_{1,1} := -177.589deg$ $\quad \theta_{1,2} := 2.089deg$

$$T = \begin{pmatrix} 0 \\ 2.723\times 10^3 \\ -1.044 \end{pmatrix} deg$$

$$d_{2,n} := \frac{-\left[-\left(T_n\right)^2\cdot p_{yra}+\left(T_n\right)^2\cdot p_{yrb}+2\cdot a_2\cdot T_n-p_{yra}+p_{yrb}\right]}{8.33\cdot\left[\left(T_n\right)^2-1\right]}$$

$d_{2,1} = 0.427\,m$ $\quad d_{2,2} = -0.427\,m$

CASE 5:

$p_{xra} := 0.0381m$ $\quad p_{xrb} := 0.1905m$

$p_{yra} := 3.302m$ $\quad p_{yrb} := 0m$

$a_2 := 0.01m$

$$\theta_{4,1} := 2\cdot\operatorname{atan}\left[\frac{1}{\left[2\cdot\left(-p_{xra}+p_{xrb}+a_2\right)\right]}\cdot\left[-2\cdot p_{yrb}+2\cdot p_{yra}+2\cdot\left[\left(p_{xrb}-p_{xra}\right)^2+\left(-p_{yra}+p_{yrb}\right)^2-a_2^2\right]^{\left(\frac{1}{2}\right)}\right]\right]$$

$$\theta_{4,2} := 2\cdot\operatorname{atan}\left[\frac{1}{\left[2\cdot\left(-p_{xra}+p_{xrb}+a_2\right)\right]}\cdot\left[-2\cdot p_{yrb}+2\cdot p_{yra}-2\cdot\left[\left(p_{xrb}-p_{xra}\right)^2+\left(-p_{yra}+p_{yrb}\right)^2-a_2^2\right]^{\left(\frac{1}{2}\right)}\right]\right]$$

$\theta_{4,1} = 177.184\,deg$ $\quad \theta_{4,2} = -2.469\,deg$ $\quad T_n := \tan\left(\frac{\theta_{4,n}}{2}\right)$

$\theta_{1,1} := -177.184deg$ $\quad \theta_{1,2} := 2.469deg$

$n := 1..2$

$$T = \begin{pmatrix} 0 \\ 2.331\times 10^{3} \\ -1.235 \end{pmatrix} deg$$

$$d_{2,n} := \frac{-\left[-\left(T_n\right)^2\cdot p_{yra}+\left(T_n\right)^2\cdot p_{yrb}+2\cdot a_2\cdot T_n-p_{yra}+p_{yrb}\right]}{8.33\cdot\left[\left(T_n\right)^2-1\right]}$$

$d_{2,1} = 0.397\,m$ $\quad d_{2,2} = -0.397\,m$

CASE 6:

$p_{xra} := 0.0508m$ $p_{xrb} := 0.1905m$

$p_{yra} := 3m$ $p_{yrb} := 0m$

$a_2 := 0.01m$

$$\theta_{4,1} := 2\cdot\operatorname{atan}\left[\frac{1}{\left[2\cdot\left(-p_{xra}+p_{xrb}+a_2\right)\right]}\cdot\left[-2\cdot p_{yrb}+2\cdot p_{yra}+2\cdot\left[\left(p_{xrb}-p_{xra}\right)^2+\left(-p_{yra}+p_{yrb}\right)^2-a_2^2\right]^{\left(\frac{1}{2}\right)}\right]\right]$$

$$\theta_{4,2} := 2\cdot\operatorname{atan}\left[\frac{1}{\left[2\cdot\left(-p_{xra}+p_{xrb}+a_2\right)\right]}\cdot\left[-2\cdot p_{yrb}+2\cdot p_{yra}-2\cdot\left[\left(p_{xrb}-p_{xra}\right)^2+\left(-p_{yra}+p_{yrb}\right)^2-a_2^2\right]^{\left(\frac{1}{2}\right)}\right]\right]$$

$\theta_{4,1} = 177.143\,deg$ $\theta_{4,2} = -2.475\,deg$

$\theta_{1,1} := 179.168deg$ $\theta_{1,2} := -1.24deg$

$$T_n := \tan\left(\frac{\theta_{4,n}}{2}\right) \qquad n := 1..2$$

$$T = \begin{pmatrix} 0 \\ 2.298\times 10^3 \\ -1.238 \end{pmatrix} deg$$

$$d_{2,n} := \frac{-\left[-\left(T_n\right)^2\cdot p_{yra}+\left(T_n\right)^2\cdot p_{yrb}+2\cdot a_2\cdot T_n-p_{yra}+p_{yrb}\right]}{8.33\cdot\left[\left(T_n\right)^2-1\right]}$$

$d_{2,1} = 0.361\,m$ $d_{2,2} = -0.361\,m$

CASE 7:

$p_{xra} := 0.1905m$

$p_{yra} := 2.794m$

$a_2 := 0.01m$

$p_{xrb} := 0.1905m$

$p_{yrb} := 0m$

$$\theta_{4,1} := 2\cdot\operatorname{atan}\left[\frac{1}{\left[2\cdot\left(-p_{xra}+p_{xrb}+a_2\right)\right]}\cdot\left[-2\cdot p_{yrb}+2\cdot p_{yra}+2\cdot\left[\left(p_{xrb}-p_{xra}\right)^2+\left(-p_{yra}+p_{yrb}\right)^2-a_2^{\,2}\right]^{\left(\frac{1}{2}\right)}\right]\right]$$

$$\theta_{4,2} := 2\cdot\operatorname{atan}\left[\frac{1}{\left[2\cdot\left(-p_{xra}+p_{xrb}+a_2\right)\right]}\cdot\left[-2\cdot p_{yrb}+2\cdot p_{yra}-2\cdot\left[\left(p_{xrb}-p_{xra}\right)^2+\left(-p_{yra}+p_{yrb}\right)^2-a_2^{\,2}\right]^{\left(\frac{1}{2}\right)}\right]\right]$$

$\theta_{4,1} = 179.795\,deg$ $\theta_{4,2} = 0.205\,deg$

$\theta_{1,1} := -179.637deg$ $\theta_{1,2} := -0.047deg$

$$T_n := \tan\left(\frac{\theta_{4,n}}{2}\right) \qquad n := 1..2$$

$$T = \begin{pmatrix} 0 \\ 3.202\times 10^4 \\ 0.103 \end{pmatrix} deg$$

$$d_{2,n} := \frac{-\left[-\left(T_n\right)^2\cdot p_{yra}+\left(T_n\right)^2\cdot p_{yrb}+2\cdot a_2\cdot T_n-p_{yra}+p_{yrb}\right]}{8.33\cdot\left[\left(T_n\right)^2-1\right]}$$

$d_{2,1} = 0.335\,m$ $d_{2,2} = -0.335\,m$

CASE 8:

$p_{xrb} := 0.1905m$

$p_{xra} := 0.254m$ $\quad p_{yrb} := 0m$

$p_{yra} := 2.54m$

$a_2 := 0.01m$

$$\theta_{4,1} := 2\cdot\operatorname{atan}\left[\frac{1}{\left[2\cdot\left(-p_{xra}+p_{xrb}+a_2\right)\right]}\cdot\left[-2\cdot p_{yrb}+2\cdot p_{yra}+2\cdot\left[\left(p_{xrb}-p_{xra}\right)^2+\left(-p_{yra}+p_{yrb}\right)^2-a_2^2\right]^{\left(\frac{1}{2}\right)}\right]\right]$$

$$\theta_{4,2} := 2\cdot\operatorname{atan}\left[\frac{1}{\left[2\cdot\left(-p_{xra}+p_{xrb}+a_2\right)\right]}\cdot\left[-2\cdot p_{yrb}+2\cdot p_{yra}-2\cdot\left[\left(p_{xrb}-p_{xra}\right)^2+\left(-p_{yra}+p_{yrb}\right)^2-a_2^2\right]^{\left(\frac{1}{2}\right)}\right]\right]$$

$\theta_{4,1} = -178.793\,\text{deg}$ $\quad \theta_{4,2} = 1.658\,\text{deg}$ $\quad T_n := \tan\left(\frac{\theta_{4,n}}{2}\right)$ $\quad n := 1..2$

$\theta_{1,1} := 178.793\text{deg}$ $\quad \theta_{1,2} := -1.658\text{deg}$ $\quad T = \begin{pmatrix} 0 \\ -5.441\times 10^{3} \\ 0.829 \end{pmatrix}\text{deg}$

$$d_{2,n} := \frac{-\left[-\left(T_n\right)^2\cdot p_{yra}+\left(T_n\right)^2\cdot p_{yrb}+2\cdot a_2\cdot T_n-p_{yra}+p_{yrb}\right]}{8.33\cdot\left[\left(T_n\right)^2-1\right]}$$

$d_{2,1} = 0.305\,\text{m}$ $\quad d_{2,2} = -0.305\,\text{m}$

CASE 9:

$p_{xra} := 0.3048m$ $p_{xrb} := 0.1905m$

$p_{yra} := 2.286m$ $p_{yrb} := 0m$

$a_2 := 0.01m$

$$\theta_{4,1} := 2\cdot\operatorname{atan}\left[\frac{1}{\left[2\cdot\left(-p_{xra}+p_{xrb}+a_2\right)\right]}\cdot\left[-2\cdot p_{yrb}+2\cdot p_{yra}+2\cdot\left[\left(p_{xrb}-p_{xra}\right)^2+\left(-p_{yra}+p_{yrb}\right)^2-a_2^{\,2}\right]^{\left(\frac{1}{2}\right)}\right]\right]$$

$$\theta_{4,2} := 2\cdot\operatorname{atan}\left[\frac{1}{\left[2\cdot\left(-p_{xra}+p_{xrb}+a_2\right)\right]}\cdot\left[-2\cdot p_{yrb}+2\cdot p_{yra}-2\cdot\left[\left(p_{xrb}-p_{xra}\right)^2+\left(-p_{yra}+p_{yrb}\right)^2-a_2^{\,2}\right]^{\left(\frac{1}{2}\right)}\right]\right]$$

$\theta_{4,1} = -177.388\,deg$ $\theta_{4,2} = 3.113\,deg$

$\theta_{1,1} := 177.388deg$ $\theta_{1,2} := -3.113deg$

$$T_n := \tan\left(\frac{\theta_{4,n}}{2}\right)$$

$n := 1..2$

$$T = \begin{pmatrix} 0 \\ -2.513\times 10^{3} \\ 1.557 \end{pmatrix} deg$$

$$d_{2,n} := \frac{-\left[-\left(T_n\right)^2\cdot p_{yra}+\left(T_n\right)^2\cdot p_{yrb}+2\cdot a_2\cdot T_n-p_{yra}+p_{yrb}\right]}{8.33\cdot\left[\left(T_n\right)^2-1\right]}$$

$d_{2,1} = 0.275\,m$ $d_{2,2} = -0.275\,m$

CASE 10:

$p_{xra} := 0.3175m$ $p_{xrb} := 0.1905m$

$p_{yra} := 2.032m$ $p_{yrb} := 0m$

$a_2 := 0.01m$

$$\theta_{4,1} := 2\cdot\operatorname{atan}\left[\frac{1}{\left[2\cdot\left(-p_{xra}+p_{xrb}+a_2\right)\right]}\cdot\left[-2\cdot p_{yrb}+2\cdot p_{yra}+2\cdot\left[\left(p_{xrb}-p_{xra}\right)^2+\left(-p_{yra}+p_{yrb}\right)^2-a_2^2\right]^{\left(\frac{1}{2}\right)}\right]\right]$$

$$\theta_{4,2} := 2\cdot\operatorname{atan}\left[\frac{1}{\left[2\cdot\left(-p_{xra}+p_{xrb}+a_2\right)\right]}\cdot\left[-2\cdot p_{yrb}+2\cdot p_{yra}-2\cdot\left[\left(p_{xrb}-p_{xra}\right)^2+\left(-p_{yra}+p_{yrb}\right)^2-a_2^2\right]^{\left(\frac{1}{2}\right)}\right]\right]$$

$\theta_{4,1} = -176.705\,\text{deg}$ $\theta_{4,2} = 3.858\,\text{deg}$

$$T_n := \tan\left(\frac{\theta_{4,n}}{2}\right)$$

$\theta_{1,1} := 176.705\text{deg}$ $\theta_{1,2} := -3.858\text{deg}$

$n := 1..2$

$$T = \begin{pmatrix} 0 \\ -1.992\times 10^3 \\ 1.93 \end{pmatrix}\text{deg}$$

$$d_{2,n} := \frac{-\left[-\left(T_n\right)^2\cdot p_{yra}+\left(T_n\right)^2\cdot p_{yrb}+2\cdot a_2\cdot T_n-p_{yra}+p_{yrb}\right]}{8.33\cdot\left[\left(T_n\right)^2-1\right]}$$

$d_{2,1} = 0.244\,m$ $d_{2,2} = -0.244\,m$

CASE 11:

$p_{xrb} := 0.1905m$

$p_{xra} := 0.254m$

$p_{yrb} := 0m$

$p_{yra} := 1.778m$

$a_2 := 0.01m$

$$\theta_{4,1} := 2\cdot\operatorname{atan}\left[\frac{1}{\left[2\cdot\left(-p_{xra}+p_{xrb}+a_2\right)\right]}\cdot\left[-2\cdot p_{yrb}+2\cdot p_{yra}+2\cdot\left[\left(p_{xrb}-p_{xra}\right)^2+\left(-p_{yra}+p_{yrb}\right)^2-a_2^{\,2}\right]^{\left(\frac{1}{2}\right)}\right]\right]$$

$$\theta_{4,2} := 2\cdot\operatorname{atan}\left[\frac{1}{\left[2\cdot\left(-p_{xra}+p_{xrb}+a_2\right)\right]}\cdot\left[-2\cdot p_{yrb}+2\cdot p_{yra}-2\cdot\left[\left(p_{xrb}-p_{xra}\right)^2+\left(-p_{yra}+p_{yrb}\right)^2-a_2^{\,2}\right]^{\left(\frac{1}{2}\right)}\right]\right]$$

$\theta_{4,1} = -178.277\,\text{deg}$ $\theta_{4,2} = 2.367\,\text{deg}$

$\theta_{1,1} := 178.277\text{deg}$ $\theta_{1,2} := -2.367\text{deg}$

$T_n := \tan\left(\frac{\theta_{4,n}}{2}\right)$

$n := 1..2$

$$T = \begin{pmatrix} 0 \\ -3.809\times 10^{3} \\ 1.184 \end{pmatrix}\text{deg}$$

$$d_{2,n} := \frac{-\left[-\left(T_n\right)^2\cdot p_{yra}+\left(T_n\right)^2\cdot p_{yrb}+2\cdot a_2\cdot T_n-p_{yra}+p_{yrb}\right]}{8.33\cdot\left[\left(T_n\right)^2-1\right]}$$

$d_{2,1} = 0.214\,m$ $d_{2,2} = -0.214\,m$

CASE 12:

$p_{xra} := 0.1905m$ $p_{xrb} := 0.1905m$

$p_{yra} := 1.7272m$ $p_{yrb} := 0m$

$a_2 := 0.01m$

$$\theta_{4,1} := 2\cdot\operatorname{atan}\left[\frac{1}{\left[2\cdot\left(-p_{xra}+p_{xrb}+a_2\right)\right]}\cdot\left[-2\cdot p_{yrb}+2\cdot p_{yra}+2\cdot\left[\left(p_{xrb}-p_{xra}\right)^2+\left(-p_{yra}+p_{yrb}\right)^2-a_2^2\right]^{\left(\frac{1}{2}\right)}\right]\right]$$

$$\theta_{4,2} := 2\cdot\operatorname{atan}\left[\frac{1}{\left[2\cdot\left(-p_{xra}+p_{xrb}+a_2\right)\right]}\cdot\left[-2\cdot p_{yrb}+2\cdot p_{yra}-2\cdot\left[\left(p_{xrb}-p_{xra}\right)^2+\left(-p_{yra}+p_{yrb}\right)^2-a_2^2\right]^{\left(\frac{1}{2}\right)}\right]\right]$$

$\theta_{4,1} = 179.668\,deg$ $\theta_{4,2} = 0.332\,deg$ $n := 1..2$ $T_n := \tan\left(\frac{\theta_{4,n}}{2}\right)$

$\theta_{1,1} := -179.668deg$ $\theta_{1,2} := -0.332deg$

$$T = \begin{pmatrix} 0 \\ 1.979\times 10^4 \\ 0.166 \end{pmatrix} deg$$

$$d_{2,n} := \frac{-\left[-\left(T_n\right)^2\cdot p_{yra}+\left(T_n\right)^2\cdot p_{yrb}+2\cdot a_2\cdot T_n-p_{yra}+p_{yrb}\right]}{8.33\cdot\left[\left(T_n\right)^2-1\right]}$$

$d_{2,1} = 0.207\,m$ $d_{2,2} = -0.207\,m$

CASE 13:

$p_{xra} := 0.0762m$

$p_{yra} := 1.778m$

$a_2 := 0.01m$

$p_{xrb} := 0.1905m$

$p_{yrb} := 0m$

$$\theta_{4,1} := 2\cdot\operatorname{atan}\left[\frac{1}{\left[2\cdot\left(-p_{xra}+p_{xrb}+a_2\right)\right]}\cdot\left[-2\cdot p_{yrb}+2\cdot p_{yra}+2\cdot\left[\left(p_{xrb}-p_{xra}\right)^2+\left(-p_{yra}+p_{yrb}\right)^2-a_2^2\right]^{\left(\frac{1}{2}\right)}\right]\right]$$

$$\theta_{4,2} := 2\cdot\operatorname{atan}\left[\frac{1}{\left[2\cdot\left(-p_{xra}+p_{xrb}+a_2\right)\right]}\cdot\left[-2\cdot p_{yrb}+2\cdot p_{yra}-2\cdot\left[\left(p_{xrb}-p_{xra}\right)^2+\left(-p_{yra}+p_{yrb}\right)^2-a_2^2\right]^{\left(\frac{1}{2}\right)}\right]\right]$$

$\theta_{4,1} = 176\,deg$ $\theta_{4,2} = -3.357\,deg$

$\theta_{1,1} := -176deg$ $\theta_{1,2} := 3.357deg$

$$T_n := \tan\left(\frac{\theta_{4,n}}{2}\right) \qquad n := 1..2$$

$$T = \begin{pmatrix} 0 \\ 1.641\times 10^3 \\ -1.679 \end{pmatrix} deg$$

$$d_{2,n} := \frac{-\left[-\left(T_n\right)^2\cdot p_{xra}+\left(T_n\right)^2\cdot p_{yrb}+2\cdot a_2\cdot T_n-p_{yra}+p_{yrb}\right]}{8.33\cdot\left[\left(T_n\right)^2-1\right]}$$

$d_{2,1} = 0.214\,m$ $d_{2,2} = -0.214\,m$

CASE14 :

$p_{xrb} := 0.1905m$

$p_{xra} := 0.036m$

$p_{yrb} := 0m$

$p_{yra} := 2.032m$

$a_2 := 0.01m$

$$\theta_{4,1} := 2\cdot\operatorname{atan}\left[\frac{1}{\left[2\cdot\left(-p_{xra}+p_{xrb}+a_2\right)\right]}\cdot\left[-2\cdot p_{yrb}+2\cdot p_{yra}+2\cdot\left[\left(p_{xrb}-p_{xra}\right)^2+\left(-p_{yra}+p_{yrb}\right)^2-a_2^{\,2}\right]^{\left(\frac{1}{2}\right)}\right]\right]$$

$$\theta_{4,2} := 2\cdot\operatorname{atan}\left[\frac{1}{\left[2\cdot\left(-p_{xra}+p_{xrb}+a_2\right)\right]}\cdot\left[-2\cdot p_{yrb}+2\cdot p_{yra}-2\cdot\left[\left(p_{xrb}-p_{xra}\right)^2+\left(-p_{yra}+p_{yrb}\right)^2-a_2^{\,2}\right]^{\left(\frac{1}{2}\right)}\right]\right]$$

$\theta_{4,1} = 175.371\,\text{deg}$ $\theta_{4,2} = -4.067\,\text{deg}$ $T_n := \tan\left(\frac{\theta_{4,n}}{2}\right)$ $n := 1..2$

$\theta_{1,1} := -175.371\text{deg}$ $\theta_{1,2} := 4.067\text{deg}$ $T = \begin{pmatrix} 0 \\ 1.418\times 10^3 \\ -2.034 \end{pmatrix}\text{deg}$

$$d_{2,n} := \frac{-\left[-\left(T_n\right)^2\cdot p_{yra}+\left(T_n\right)^2\cdot p_{yrb}+2\cdot a_2\cdot T_n-p_{yra}+p_{yrb}\right]}{8.33\cdot\left[\left(T_n\right)^2-1\right]}$$

$d_{2,1} = 0.245\,m$ $d_{2,2} = -0.245\,m$

CASE 15:

$p_{xra} := 0.036m$ $\quad p_{xrb} := 0.1905m$

$p_{yra} := 2.159m$ $\quad p_{yrb} := 0m$

$a_2 := 0.01m$

$$\theta_{4,1} := 2\cdot\operatorname{atan}\left[\frac{1}{\left[2\cdot\left(-p_{xra}+p_{xrb}+a_2\right)\right]}\cdot\left[-2\cdot p_{yrb}+2\cdot p_{yra}+2\cdot\left[\left(p_{xrb}-p_{xra}\right)^2+\left(-p_{yra}+p_{yrb}\right)^2-a_2^2\right]^{\left(\frac{1}{2}\right)}\right]\right]$$

$$\theta_{4,2} := 2\cdot\operatorname{atan}\left[\frac{1}{\left[2\cdot\left(-p_{xra}+p_{xrb}+a_2\right)\right]}\cdot\left[-2\cdot p_{yrb}+2\cdot p_{yra}-2\cdot\left[\left(p_{xrb}-p_{xra}\right)^2+\left(-p_{yra}+p_{yrb}\right)^2-a_2^2\right]^{\left(\frac{1}{2}\right)}\right]\right]$$

$$T_n := \tan\left(\frac{\theta_{4,n}}{2}\right)$$

$\theta_{4,1} = 175.642\,deg$ $\quad \theta_{4,2} = -3.828\,deg$

$n := 1..2$

$\theta_{1,1} := -175.642deg$ $\quad \theta_{1,2} := 3.828deg$

$$T = \begin{pmatrix} 0 \\ 1.506\times 10^3 \\ -1.915 \end{pmatrix} deg$$

$$d_{2,n} := \frac{-\left[-\left(T_n\right)^2\cdot p_{yra}+\left(T_n\right)^2\cdot p_{yrb}+2\cdot a_2\cdot T_n-p_{yra}+p_{yrb}\right]}{8.33\cdot\left[\left(T_n\right)^2-1\right]}$$

$d_{2,1} = 0.26\,m$ $\quad d_{2,2} = -0.26\,m$

SECOND EXAMPLE

CASE 1:

Coordinates of the first point of the letter "S":

$p_{xra} := 0.3175m$

$p_{yra} := 3.3528m$

Coordinates of the truck wrt the road:

$p_{xrb} := -1m$

$p_{yrb} := 0.762m$

Offset value between the arm and the end-effector:

$a_2 := 0.01m$

The rotation of the end-effector around z-axis (see Fig.2.1):

$$\theta_{4,1} := 2\cdot\operatorname{atan}\left[\frac{1}{\left[2\cdot\left(-p_{xra}+p_{xrb}+a_2\right)\right]}\cdot\left[-2\cdot p_{yrb}+2\cdot p_{yra}+2\cdot\left[\left(p_{xrb}-p_{xra}\right)^2+\left(-p_{yra}+p_{yrb}\right)^2-a_2^2\right]^{\left(\frac{1}{2}\right)}\right]\right]$$

$$\theta_{4,2} := 2\cdot\operatorname{atan}\left[\frac{1}{\left[2\cdot\left(-p_{xra}+p_{xrb}+a_2\right)\right]}\cdot\left[-2\cdot p_{yrb}+2\cdot p_{yra}-2\cdot\left[\left(p_{xrb}-p_{xra}\right)^2+\left(-p_{yra}+p_{yrb}\right)^2-a_2^2\right]^{\left(\frac{1}{2}\right)}\right]\right]$$

$\theta_{4,1} = -153.242\,deg$ $\theta_{4,2} = 27.152\,deg$ see eqns (3.25) and (3.26)

The base rotation of the arm:

$$T_n := \tan\left(\frac{\theta_{4,n}}{2}\right) \qquad n := 1..2$$

$$T = \begin{pmatrix} 0 \\ -240.898 \\ 13.836 \end{pmatrix} deg$$

$\theta_{1,1} := 153.242deg$ $\theta_{1,2} := -27.152deg$ see eqn. (3.17)

The translation of the arm along y-axis (see Fig.2.1):

$$d_{2,n} := \frac{-\left[-\left(T_n\right)^2\cdot p_{yra}+\left(T_n\right)^2\cdot p_{yrb}+2\cdot a_2\cdot T_n-p_{yra}+p_{yrb}\right]}{8.33\cdot\left[\left(T_n\right)^2-1\right]}$$

see eqn. (3.23)

$d_{2,1} = 0.349\,m$ $d_{2,2} = -0.349\,m$

Note, that the relation between the tilt motion θ_{2e} and the ball-screw drive Δx as well as the compensation for the tilt, Zres, are given in Chap.3.

All the angles and lengths are presented in degrees and in meters, respectively.

CASE 2:

$p_{xra} := 0.3048m$ $\quad p_{xrb} := -1m$

$p_{yra} := 3.556m$ $\quad p_{yrb} := 0.762m$

$a_2 := 0.01m$

$$\theta_{4,1} := 2\cdot\operatorname{atan}\left[\frac{1}{\left[2\cdot\left(-p_{xra}+p_{xrb}+a_2\right)\right]}\cdot\left[-2\cdot p_{yrb}+2\cdot p_{yra}+2\cdot\left[\left(p_{xrb}-p_{xra}\right)^2+\left(-p_{yra}+p_{yrb}\right)^2-a_2^2\right]^{\left(\frac{1}{2}\right)}\right]\right]$$

$$\theta_{4,2} := 2\cdot\operatorname{atan}\left[\frac{1}{\left[2\cdot\left(-p_{xra}+p_{xrb}+a_2\right)\right]}\cdot\left[-2\cdot p_{yrb}+2\cdot p_{yra}-2\cdot\left[\left(p_{xrb}-p_{xra}\right)^2+\left(-p_{yra}+p_{yrb}\right)^2-a_2^2\right]^{\left(\frac{1}{2}\right)}\right]\right]$$

$\theta_{4,1} = -155.153\,\text{deg}$ $\quad \theta_{4,2} = 25.218\,\text{deg}$

$\theta_{1,1} := 155.153\text{deg}$ $\quad \theta_{1,2} := -25.218\text{deg}$

$$T_n := \tan\left(\frac{\theta_{4,n}}{2}\right) \qquad n := 1..2$$

$$T = \begin{pmatrix} 0 \\ -260.09 \\ 12.817 \end{pmatrix}\text{deg}$$

$$d_{2,n} := \frac{-\left[-\left(T_n\right)^2\cdot p_{yra}+\left(T_n\right)^2\cdot p_{yrb}+2\cdot a_2\cdot T_n-p_{yra}+p_{yrb}\right]}{8.33\cdot\left[\left(T_n\right)^2-1\right]}$$

$d_{2,1} = 0.37\,\text{m}$ $\quad d_{2,2} = -0.37\,\text{m}$

CASE 3:

$p_{xra} := 0.1905m$ $\quad p_{xrb} := -1m$

$p_{yra} := 3.81m$ $\quad p_{yrb} := 0.762m$

$a_2 := 0.01m$

$$\theta_{4,1} := 2\cdot\operatorname{atan}\left[\frac{1}{\left[2\cdot\left(-p_{xra}+p_{xrb}+a_2\right)\right]}\cdot\left[-2\cdot p_{yrb}+2\cdot p_{yra}+2\cdot\left[\left(p_{xrb}-p_{xra}\right)^2+\left(-p_{yra}+p_{yrb}\right)^2-a_2^2\right]^{\left(\frac{1}{2}\right)}\right]\right]$$

$$\theta_{4,2} := 2\cdot\operatorname{atan}\left[\frac{1}{\left[2\cdot\left(-p_{xra}+p_{xrb}+a_2\right)\right]}\cdot\left[-2\cdot p_{yrb}+2\cdot p_{yra}-2\cdot\left[\left(p_{xrb}-p_{xra}\right)^2+\left(-p_{yra}+p_{yrb}\right)^2-a_2^2\right]^{\left(\frac{1}{2}\right)}\right]\right]$$

$\theta_{4,1} = -158.84\,deg$ $\quad \theta_{4,2} = 21.51\,deg$ $\quad T_n := \tan\left(\frac{\theta_{4,n}}{2}\right)$ $\quad n := 1..2$

$\theta_{1,1} := 158.84deg$ $\quad \theta_{1,2} := -21.51deg$ $\quad T = \begin{pmatrix} 0 \\ -306.754 \\ 10.883 \end{pmatrix} deg$

$$d_{2,n} := \frac{-\left[-\left(T_n\right)^2\cdot p_{yra}+\left(T_n\right)^2\cdot p_{yrb}+2\cdot a_2\cdot T_n-p_{yra}+p_{yrb}\right]}{8.33\cdot\left[\left(T_n\right)^2-1\right]}$$

$d_{2,1} = 0.393\,m$ $\quad d_{2,2} = -0.393\,m$

CASE 4:

$p_{xra} := 0.0508m$ $\quad p_{xrb} := -1m$

$p_{yra} := 3.556m$ $\quad p_{yrb} := 0.762m$

$a_2 := 0.01m$

$$\theta_{4,1} := 2\cdot\operatorname{atan}\left[\frac{1}{\left[2\cdot\left(-p_{xra}+p_{xrb}+a_2\right)\right]}\cdot\left[-2\cdot p_{yrb}+2\cdot p_{yra}+2\cdot\left[\left(p_{xrb}-p_{xra}\right)^2+\left(-p_{yra}+p_{yrb}\right)^2-a_2^2\right]^{\left(\frac{1}{2}\right)}\right]\right]$$

$$\theta_{4,2} := 2\cdot\operatorname{atan}\left[\frac{1}{\left[2\cdot\left(-p_{xra}+p_{xrb}+a_2\right)\right]}\cdot\left[-2\cdot p_{yrb}+2\cdot p_{yra}-2\cdot\left[\left(p_{xrb}-p_{xra}\right)^2+\left(-p_{yra}+p_{yrb}\right)^2-a_2^2\right]^{\left(\frac{1}{2}\right)}\right]\right]$$

$\theta_{4,1} = -159.581\,\text{deg}$ $\quad \theta_{4,2} = 20.803\,\text{deg}$

$\theta_{1,1} := 159.581\text{deg}$ $\quad \theta_{1,2} := -20.803\text{deg}$

$$T_n := \tan\left(\frac{\theta_{4,n}}{2}\right)$$

$n := 1..2$

$$T = \begin{pmatrix} 0 \\ -318.135 \\ 10.517 \end{pmatrix}\text{deg}$$

$$d_{2,n} := \frac{-\left[-\left(T_n\right)^2\cdot p_{yra}+\left(T_n\right)^2\cdot p_{yrb}+2\cdot a_2\cdot T_n-p_{yra}+p_{yrb}\right]}{8.33\cdot\left[\left(T_n\right)^2-1\right]}$$

$d_{2,1} = 0.358\,m$ $\quad d_{2,2} = -0.358\,m$

CASE 5:

$p_{xra} := 0.0381\text{m}$ $\quad p_{xrb} := -1\text{m}$

$p_{yra} := 3.302\text{m}$ $\quad p_{yrb} := 0.762\text{m}$

$a_2 := 0.01\text{m}$

$$\theta_{4,1} := 2\cdot\text{atan}\left[\frac{1}{\left[2\cdot\left(-p_{xra}+p_{xrb}+a_2\right)\right]}\cdot\left[-2\cdot p_{yrb}+2\cdot p_{yra}+2\cdot\left[\left(p_{xrb}-p_{xra}\right)^2+\left(-p_{yra}+p_{yrb}\right)^2-a_2^2\right]^{\left(\frac{1}{2}\right)}\right]\right]$$

$$\theta_{4,2} := 2\cdot\text{atan}\left[\frac{1}{\left[2\cdot\left(-p_{xra}+p_{xrb}+a_2\right)\right]}\cdot\left[-2\cdot p_{yrb}+2\cdot p_{yra}-2\cdot\left[\left(p_{xrb}-p_{xra}\right)^2+\left(-p_{yra}+p_{yrb}\right)^2-a_2^2\right]^{\left(\frac{1}{2}\right)}\right]\right]$$

$\theta_{4,1} = -157.979\,\text{deg}$ $\quad \theta_{4,2} = 22.439\,\text{deg}$

$$T_n := \tan\left(\frac{\theta_{4,n}}{2}\right)$$

$\theta_{1,1} := -177.184\text{deg}$ $\quad \theta_{1,2} := 2.469\text{deg}$

$n := 1..2$

$$T = \begin{pmatrix} 0 \\ -294.472 \\ 11.365 \end{pmatrix}\text{deg}$$

$$d_{2,n} := \frac{-\left[-\left(T_n\right)^2\cdot p_{yra}+\left(T_n\right)^2\cdot p_{yrb}+2\cdot a_2\cdot T_n-p_{yra}+p_{yrb}\right]}{8.33\cdot\left[\left(T_n\right)^2-1\right]}$$

$d_{2,1} = 0.329\,\text{m}$ $\quad d_{2,2} = -0.329\,\text{m}$

CASE 6:

$p_{xra} := 0.0508m$ $\quad p_{xrb} := -1m$

$p_{yra} := 3m$ $\quad p_{yrb} := 0.762m$

$a_2 := 0.01m$

$$\theta_{4,1} := 2\cdot\operatorname{atan}\left[\frac{1}{\left[2\cdot\left(-p_{xra}+p_{xrb}+a_2\right)\right]}\cdot\left[-2\cdot p_{yrb}+2\cdot p_{yra}+2\cdot\left[\left(p_{xrb}-p_{xra}\right)^2+\left(-p_{yra}+p_{yrb}\right)^2-a_2^2\right]^{\left(\frac{1}{2}\right)}\right]\right]$$

$$\theta_{4,2} := 2\cdot\operatorname{atan}\left[\frac{1}{\left[2\cdot\left(-p_{xra}+p_{xrb}+a_2\right)\right]}\cdot\left[-2\cdot p_{yrb}+2\cdot p_{yra}-2\cdot\left[\left(p_{xrb}-p_{xra}\right)^2+\left(-p_{yra}+p_{yrb}\right)^2-a_2^2\right]^{\left(\frac{1}{2}\right)}\right]\right]$$

$\theta_{4,1} = -155.08\,\text{deg}$ $\quad \theta_{4,2} = 25.383\,\text{deg}$ $\quad T_n := \tan\left(\frac{\theta_{4,n}}{2}\right)$ $\quad n := 1..2$

$\theta_{1,1} := 155.08\text{deg}$ $\quad \theta_{1,2} := -25.383\text{deg}$

$$T = \begin{pmatrix} 0 \\ -259.306 \\ 12.903 \end{pmatrix}\text{deg}$$

$$d_{2,n} := \frac{-\left[-\left(T_n\right)^2\cdot p_{yra}+\left(T_n\right)^2\cdot p_{yrb}+2\cdot a_2\cdot T_n-p_{yra}+p_{yrb}\right]}{8.33\cdot\left[\left(T_n\right)^2-1\right]}$$

$d_{2,1} = 0.297\,m$ $\quad d_{2,2} = -0.297\,m$

CASE 7:

$p_{xra} := 0.1828m$

$p_{yra} := 2.794m$

$a_2 := 0.01m$

$p_{xrb} := -1m$

$p_{yrb} := 0.762m$

$$\theta_{4,1} := 2\cdot\operatorname{atan}\left[\frac{1}{\left[2\cdot\left(-p_{xra}+p_{xrb}+a_2\right)\right]}\cdot\left[-2\cdot p_{yrb}+2\cdot p_{yra}+2\cdot\left[\left(p_{xrb}-p_{xra}\right)^2+\left(-p_{yra}+p_{yrb}\right)^2-a_2^2\right]^{\left(\frac{1}{2}\right)}\right]\right]$$

$$\theta_{4,2} := 2\cdot\operatorname{atan}\left[\frac{1}{\left[2\cdot\left(-p_{xra}+p_{xrb}+a_2\right)\right]}\cdot\left[-2\cdot p_{yrb}+2\cdot p_{yra}-2\cdot\left[\left(p_{xrb}-p_{xra}\right)^2+\left(-p_{yra}+p_{yrb}\right)^2-a_2^2\right]^{\left(\frac{1}{2}\right)}\right]\right]$$

$\theta_{4,1} = -150.041\,\text{deg}$ $\theta_{4,2} = 30.447\,\text{deg}$

$\theta_{1,1} := 150.041\text{deg}$ $\theta_{1,2} := -30.447\text{deg}$

$$T_n := \tan\left(\frac{\theta_{4,n}}{2}\right) \qquad n := 1..2$$

$$T = \begin{pmatrix} 0 \\ -214.134 \\ 15.592 \end{pmatrix}\text{deg}$$

$$d_{2,n} := \frac{-\left[-\left(T_n\right)^2\cdot p_{yra}+\left(T_n\right)^2\cdot p_{yrb}+2\cdot a_2\cdot T_n-p_{yra}+p_{yrb}\right]}{8.33\cdot\left[\left(T_n\right)^2-1\right]}$$

$d_{2,1} = 0.282\,m$ $d_{2,2} = -0.282\,m$

CASE 8:

$p_{xra} := 0.254m$ $\quad p_{xrb} := -1m$

$p_{yra} := 2.54m$ $\quad p_{yrb} := 0.762m$

$a_2 := 0.01m$

$$\theta_{4,1} := 2\cdot\operatorname{atan}\left[\frac{1}{\left[2\cdot\left(-p_{xra}+p_{xrb}+a_2\right)\right]}\cdot\left[-2\cdot p_{yrb}+2\cdot p_{yra}+2\cdot\left[\left(p_{xrb}-p_{xra}\right)^2+\left(-p_{yra}+p_{yrb}\right)^2-a_2^2\right]^{\left(\frac{1}{2}\right)}\right]\right]$$

$$\theta_{4,2} := 2\cdot\operatorname{atan}\left[\frac{1}{\left[2\cdot\left(-p_{xra}+p_{xrb}+a_2\right)\right]}\cdot\left[-2\cdot p_{yrb}+2\cdot p_{yra}-2\cdot\left[\left(p_{xrb}-p_{xra}\right)^2+\left(-p_{yra}+p_{yrb}\right)^2-a_2^2\right]^{\left(\frac{1}{2}\right)}\right]\right]$$

$\theta_{4,1} = -145.069\,\text{deg}$ $\quad \theta_{4,2} = 35.458\,\text{deg}$ $\quad T_n := \tan\left(\frac{\theta_{4,n}}{2}\right)$ $\quad n := 1..2$

$\theta_{1,1} := 145.69\text{deg}$ $\quad \theta_{1,2} := -35.458\text{deg}$ $\quad T = \begin{pmatrix} 0 \\ -182.099 \\ 18.317 \end{pmatrix}\text{deg}$

$$d_{2,n} := \frac{-\left[-\left(T_n\right)^2\cdot p_{yra}+\left(T_n\right)^2\cdot p_{yrb}+2\cdot a_2\cdot T_n-p_{yra}+p_{yrb}\right]}{8.33\cdot\left[\left(T_n\right)^2-1\right]}$$

$d_{2,1} = 0.261\,m$ $\quad d_{2,2} = -0.261\,m$

CASE 9:

$p_{xra} := 0.3048m$ $p_{xrb} := -1m$

$p_{yra} := 2.286m$ $p_{yrb} := 0.762m$

$a_2 := 0.01m$

$$\theta_{4,1} := 2\cdot\operatorname{atan}\left[\frac{1}{\left[2\cdot\left(-p_{xra}+p_{xrb}+a_2\right)\right]}\cdot\left[-2\cdot p_{yrb}+2\cdot p_{yra}+2\cdot\left[\left(p_{xrb}-p_{xra}\right)^2+\left(-p_{yra}+p_{yrb}\right)^2-a_2^2\right]^{\left(\frac{1}{2}\right)}\right]\right]$$

$$\theta_{4,2} := 2\cdot\operatorname{atan}\left[\frac{1}{\left[2\cdot\left(-p_{xra}+p_{xrb}+a_2\right)\right]}\cdot\left[-2\cdot p_{yrb}+2\cdot p_{yra}-2\cdot\left[\left(p_{xrb}-p_{xra}\right)^2+\left(-p_{yra}+p_{yrb}\right)^2-a_2^2\right]^{\left(\frac{1}{2}\right)}\right]\right]$$

$\theta_{4,1} = -139.717\,deg$ $\theta_{4,2} = 40.855\,deg$

$\theta_{1,1} := 139.717deg$ $\theta_{1,2} := -40.855deg$

$$T_n := \tan\left(\frac{\theta_{4,n}}{2}\right) \qquad n := 1..2$$

$$T = \begin{pmatrix} 0 \\ -156.215 \\ 21.339 \end{pmatrix} deg$$

$$d_{2,n} := \frac{-\left[-\left(T_n\right)^2\cdot p_{yra}+\left(T_n\right)^2\cdot p_{yrb}+2\cdot a_2\cdot T_n-p_{yra}+p_{yrb}\right]}{8.33\cdot\left[\left(T_n\right)^2-1\right]}$$

$d_{2,1} = 0.241\,m$ $d_{2,2} = -0.241\,m$

CASE 10:

$p_{xra} := 0.3175m$ $\quad p_{xrb} := -1m$

$p_{yra} := 2.032m$ $\quad p_{yrb} := 0.762m$

$a_2 := 0.01m$

$$\theta_{4,1} := 2\cdot\operatorname{atan}\left[\frac{1}{\left[2\cdot\left(-p_{xra}+p_{xrb}+a_2\right)\right]}\cdot\left[-2\cdot p_{yrb}+2\cdot p_{yra}+2\cdot\left[\left(p_{xrb}-p_{xra}\right)^2+\left(-p_{yra}+p_{yrb}\right)^2-a_2^{\,2}\right]^{\left(\frac{1}{2}\right)}\right]\right]$$

$$\theta_{4,2} := 2\cdot\operatorname{atan}\left[\frac{1}{\left[2\cdot\left(-p_{xra}+p_{xrb}+a_2\right)\right]}\cdot\left[-2\cdot p_{yrb}+2\cdot p_{yra}-2\cdot\left[\left(p_{xrb}-p_{xra}\right)^2+\left(-p_{yra}+p_{yrb}\right)^2-a_2^{\,2}\right]^{\left(\frac{1}{2}\right)}\right]\right]$$

$\theta_{4,1} = -134.261\,\text{deg}$ $\quad \theta_{4,2} = 46.365\,\text{deg}$ $\quad T_n := \tan\left(\frac{\theta_{4,n}}{2}\right)$

$\theta_{1,1} := 134.261\text{deg}$ $\quad \theta_{1,2} := -46.365\text{deg}$ $\quad n := 1..2$

$$T = \begin{pmatrix} 0 \\ -135.841 \\ 24.536 \end{pmatrix}\text{deg}$$

$$d_{2,n} := \frac{-\left[-\left(T_n\right)^2\cdot p_{yra}+\left(T_n\right)^2\cdot p_{yrb}+2\cdot a_2\cdot T_n-p_{yra}+p_{yrb}\right]}{8.33\cdot\left[\left(T_n\right)^2-1\right]}$$

$d_{2,1} = 0.22\,\text{m}$ $\quad d_{2,2} = -0.22\,\text{m}$

CASE 11:

$p_{xra} := 0.254m$ $p_{xrb} := -1m$

$p_{yra} := 1.778m$ $p_{yrb} := 0.762m$

$a_2 := 0.01m$

$$\theta_{4,1} := 2\cdot\operatorname{atan}\left[\frac{1}{\left[2\cdot\left(-p_{xra}+p_{xrb}+a_2\right)\right]}\cdot\left[-2\cdot p_{yrb}+2\cdot p_{yra}+2\cdot\left[\left(p_{xrb}-p_{xra}\right)^2+\left(-p_{yra}+p_{yrb}\right)^2-a_2^2\right]^{\left(\frac{1}{2}\right)}\right]\right]$$

$$\theta_{4,2} := 2\cdot\operatorname{atan}\left[\frac{1}{\left[2\cdot\left(-p_{xra}+p_{xrb}+a_2\right)\right]}\cdot\left[-2\cdot p_{yrb}+2\cdot p_{yra}-2\cdot\left[\left(p_{xrb}-p_{xra}\right)^2+\left(-p_{yra}+p_{yrb}\right)^2-a_2^2\right]^{\left(\frac{1}{2}\right)}\right]\right]$$

$\theta_{4,1} = -129.37\,deg$ $\theta_{4,2} = 51.34\,deg$

$\theta_{1,1} := 129.37deg$ $\theta_{1,2} := -51.34deg$

$$T_n := \tan\left(\frac{\theta_{4,n}}{2}\right)$$

$n := 1..2$

$$T = \begin{pmatrix} 0 \\ -121.127 \\ 27.538 \end{pmatrix} deg$$

$$d_{2,n} := \frac{-\left[-\left(T_n\right)^2\cdot p_{yra}+\left(T_n\right)^2\cdot p_{yrb}+2\cdot a_2\cdot T_n-p_{yra}+p_{yrb}\right]}{8.33\cdot\left[\left(T_n\right)^2-1\right]}$$

$d_{2,1} = 0.194\,m$ $d_{2,2} = -0.194\,m$

CASE 12:

$p_{xra} := 0.1905m$ $\quad p_{xrb} := -1m$

$p_{yra} := 1.7272m$ $\quad p_{yrb} := 0.762m$

$a_2 := 0.01m$

$$\theta_{4,1} := 2\cdot\operatorname{atan}\left[\frac{1}{\left[2\cdot\left(-p_{xra}+p_{xrb}+a_2\right)\right]}\cdot\left[-2\cdot p_{yrb}+2\cdot p_{yra}+2\cdot\left[\left(p_{xrb}-p_{xra}\right)^2+\left(-p_{yra}+p_{yrb}\right)^2-a_2^2\right]^{\left(\frac{1}{2}\right)}\right]\right]$$

$$\theta_{4,2} := 2\cdot\operatorname{atan}\left[\frac{1}{\left[2\cdot\left(-p_{xra}+p_{xrb}+a_2\right)\right]}\cdot\left[-2\cdot p_{yrb}+2\cdot p_{yra}-2\cdot\left[\left(p_{xrb}-p_{xra}\right)^2+\left(-p_{yra}+p_{yrb}\right)^2-a_2^2\right]^{\left(\frac{1}{2}\right)}\right]\right]$$

$\theta_{4,1} = -129.407\,deg$ $\quad \theta_{4,2} = 51.34\,deg$ $\quad n := 1..2$ $\quad T_n := \tan\left(\frac{\theta_{4,n}}{2}\right)$

$\theta_{1,1} := 129.407deg$ $\quad \theta_{1,2} := -51.34deg$

$$T = \begin{pmatrix} 0 \\ -121.23 \\ 27.538 \end{pmatrix} deg$$

$$d_{2,n} := \frac{-\left[-\left(T_n\right)^2\cdot p_{yra}+\left(T_n\right)^2\cdot p_{yrb}+2\cdot a_2\cdot T_n-p_{yra}+p_{yrb}\right]}{8.33\cdot\left[\left(T_n\right)^2-1\right]}$$

$d_{2,1} = 0.184\,m$ $\quad d_{2,2} = -0.184\,m$

CASE 13:

$p_{xra} := 0.0762m$ $\quad p_{xrb} := -1m$

$p_{yra} := 1.778m$ $\quad p_{yrb} := 0.762m$

$a_2 := 0.01m$

$$\theta_{4,1} := 2\cdot\operatorname{atan}\left[\frac{1}{\left[2\cdot\left(-p_{xra}+p_{xrb}+a_2\right)\right]}\cdot\left[-2\cdot p_{yrb}+2\cdot p_{yra}+2\cdot\left[\left(p_{xrb}-p_{xra}\right)^2+\left(-p_{yra}+p_{yrb}\right)^2-a_2^2\right]^{\left(\frac{1}{2}\right)}\right]\right]$$

$$\theta_{4,2} := 2\cdot\operatorname{atan}\left[\frac{1}{\left[2\cdot\left(-p_{xra}+p_{xrb}+a_2\right)\right]}\cdot\left[-2\cdot p_{yrb}+2\cdot p_{yra}-2\cdot\left[\left(p_{xrb}-p_{xra}\right)^2+\left(-p_{yra}+p_{yrb}\right)^2-a_2^2\right]^{\left(\frac{1}{2}\right)}\right]\right]$$

$\theta_{4,1} = -133.739\,deg$ $\quad \theta_{4,2} = 47.035\,deg$

$\theta_{1,1} := 133.739deg$ $\quad \theta_{1,2} := -47.035deg$

$$T_n := \tan\left(\frac{\theta_{4,n}}{2}\right) \qquad n := 1..2$$

$$T = \begin{pmatrix} 0 \\ -134.13 \\ 24.934 \end{pmatrix} deg$$

$$d_{2,n} := \frac{-\left[-\left(T_n\right)^2\cdot p_{yra}+\left(T_n\right)^2\cdot p_{yrb}+2\cdot a_2\cdot T_n-p_{yra}+p_{yrb}\right]}{8.33\cdot\left[\left(T_n\right)^2-1\right]}$$

$d_{2,1} = 0.178\,m$ $\quad d_{2,2} = -0.178\,m$

CASE14 :

$p_{xrb} := -1\,m$

$p_{xra} := 0.036\,m$

$p_{yrb} := 0.762\,m$

$p_{yra} := 2.032\,m$

$a_2 := 0.01\,m$

$$\theta_{4,1} := 2\cdot\operatorname{atan}\left[\frac{1}{\left[2\cdot\left(-p_{xra}+p_{xrb}+a_2\right)\right]}\cdot\left[-2\cdot p_{yrb}+2\cdot p_{yra}+2\cdot\left[\left(p_{xrb}-p_{xra}\right)^2+\left(-p_{yra}+p_{yrb}\right)^2-a_2^2\right]^{\left(\frac{1}{2}\right)}\right]\right]$$

$$\theta_{4,2} := 2\cdot\operatorname{atan}\left[\frac{1}{\left[2\cdot\left(-p_{xra}+p_{xrb}+a_2\right)\right]}\cdot\left[-2\cdot p_{yrb}+2\cdot p_{yra}-2\cdot\left[\left(p_{xrb}-p_{xra}\right)^2+\left(-p_{yra}+p_{yrb}\right)^2-a_2^2\right]^{\left(\frac{1}{2}\right)}\right]\right]$$

$\theta_{4,1} = -141.144\,deg$ $\theta_{4,2} = 39.555\,deg$ $T_n := \tan\left(\frac{\theta_{4,n}}{2}\right)$ $n := 1..2$

$\theta_{1,1} := 141.144deg$ $\theta_{1,2} := -39.555deg$ $T = \begin{pmatrix} 0 \\ -162.446 \\ 20.603 \end{pmatrix} deg$

$$d_{2,n} := \frac{-\left[-\left(T_n\right)^2\cdot p_{yra}+\left(T_n\right)^2\cdot p_{yrb}+2\cdot a_2\cdot T_n-p_{yra}+p_{yrb}\right]}{8.33\cdot\left[\left(T_n\right)^2-1\right]}$$

$d_{2,1} = 0.197\,m$ $d_{2,2} = -0.197\,m$

CASE 15:

$p_{xra} := 0.036m$ $\quad p_{xrb} := -1m$

$p_{yra} := 2.159m$ $\quad p_{yrb} := 0.762m$

$a_2 := 0.01m$

$$\theta_{4,1} := 2\cdot\operatorname{atan}\left[\frac{1}{\left[2\cdot\left(-p_{xra}+p_{xrb}+a_2\right)\right]}\cdot\left[-2\cdot p_{yrb}+2\cdot p_{yra}+2\cdot\left[\left(p_{xrb}-p_{xra}\right)^2+\left(-p_{yra}+p_{yrb}\right)^2-a_2^2\right]^{\left(\frac{1}{2}\right)}\right]\right]$$

$$\theta_{4,2} := 2\cdot\operatorname{atan}\left[\frac{1}{\left[2\cdot\left(-p_{xra}+p_{xrb}+a_2\right)\right]}\cdot\left[-2\cdot p_{yrb}+2\cdot p_{yra}-2\cdot\left[\left(p_{xrb}-p_{xra}\right)^2+\left(-p_{yra}+p_{yrb}\right)^2-a_2^2\right]^{\left(\frac{1}{2}\right)}\right]\right]$$

$$T_n := \tan\left(\frac{\theta_{4,n}}{2}\right) \qquad n := 1..2$$

$\theta_{4,1} = -143.769\,\text{deg}$ $\quad \theta_{4,2} = 36.89\,\text{deg}$

$\theta_{1,1} := 143.769\text{deg}$ $\quad \theta_{1,2} := -36.89\text{deg}$

$$T = \begin{pmatrix} 0 \\ -175.137 \\ 19.11 \end{pmatrix}\text{deg}$$

$$d_{2,n} := \frac{-\left[-\left(T_n\right)^2\cdot p_{yra}+\left(T_n\right)^2\cdot p_{yrb}+2\cdot a_2\cdot T_n-p_{yra}+p_{yrb}\right]}{8.33\cdot\left[\left(T_n\right)^2-1\right]}$$

$d_{2,1} = 0.209\,\text{m}$ $\quad d_{2,2} = -0.209\,\text{m}$

Section IV:

Appendix C

Mechanical Redesign of Big Articulating Stenciling Robot End Effecter Employing a Novel Mechanism for Paint Spray Gun Orientation Control

MECHANICAL REDESIGN OF BIG ARTICULATING STENCILING ROBOT END EFFECTER EMPLOYING A NOVEL MECHANISM FOR PAINT SPRAY GUN ORIENTATION CONTROL

BY

SEAN PATRICK STEFFENSEN

B.S. (University of California, Davis) 1999

THESIS

Submitted in partial satisfaction of the requirements for the degree of

Master of Science

in

Mechanical Engineering

in the

OFFICE OF GRADUATE STUDIES

of the

UNIVERSITY OF CALIFORNIA

DAVIS

Approved:

Bahram Ravani

Ridha A.M.T. Farouki

Committee in Charge

2001

TABLE OF CONTENTS

LIST OF FIGURES

CHAPTER 1: INTRODUCTION

The need to improve the safety and efficiency of highway maintenance motivated the work performed by the Advanced Highway Maintenance and Construction Technology Research Center (AHMCT) to develop the Big Articulating Stenciling Robot (BASR). Each year highway maintenance workers suffer injuries caused by accidents with passing motor vehicles. Automation of roadway marking operations will reduce the possibility of injury by removing the maintenance worker from hazardous roadside situations and placing the worker within the security of a maintenance vehicle. Section 1.1 describes the technique presently employed by state highway maintenance workers to create roadway markings on state highways. Section 1.2 presents the results of a search for current automated roadway marking systems. Section 1.3 describes the approach taken by the AHMCT to design an automated roadway marking system.

Much of the work presented in this master thesis is a continuation of the work performed in [1].

1.1 Description of Current Methods of Roadway Marking

Presently, the highway maintenance worker is required to perform roadside work to create roadway markings. The maintenance worker uses a set of large wood, plastic or metal stencils to mask patterns on the roadway in the shape of letters in preparation for painting. The maintenance worker pushes a cart equipped with paint spraying equipment over the stencils to mark each letter. After the painting is completed, the maintenance worker loads the stencils and painting equipment onto a truck to be transported to the next work site. The labor-intensive method of roadway marking exposes the worker to injuries due to the strenuous nature of the work and from accidents involving high-speed vehicular traffic.

1.2 Description of Current Methods of Robotic Roadway Marking

A search of literature yielded three approaches to automated roadway marking currently developed to paint roadway symbols. Additional automated roadway marking systems exist for the marking of dividing lines and limit lines on roadways. The simplicity of these line-marking systems limits their relevancy to the design problems encountered in the robotic painting of complex roadway symbols and therefore this section will only discuss those systems that create roadway symbols. Section 1.2.1 features a description of a gantry robot used to create aerial survey markings for state highways. Section 1.2.2 describes the efforts to produce a low cost marking system capable of being mounted to a telerobotic vehicle or an automobile. Section 1.2.3 describes the previous BASR design.

1.2.1 Stenciling Robot for Aerial Surveying Premarks

Markings such as the one shown in Figure 1.1 are employed to aid in the aerial surveying of state highway systems. A gantry style robot was constructed by AHMCT to make these markings using a standard paint gun spraying system. The gantry robot consists of two linear robotic actuators orientated perpendicularly. Each actuator controls the position of the spray gun in one direction. The entire robotic system is entirely contained within a trailer that can be towed behind a highway maintenance vehicle. A maintenance worker positions the gantry robotic system over the marking area. The gantry system then guides the spray nozzle to form the appropriate roadway marking. Since the size of the trailer limits the available painting workspace, the workspace cannot exceed more than one highway lane width due to limitations on trailer size imposed by California vehicle code.

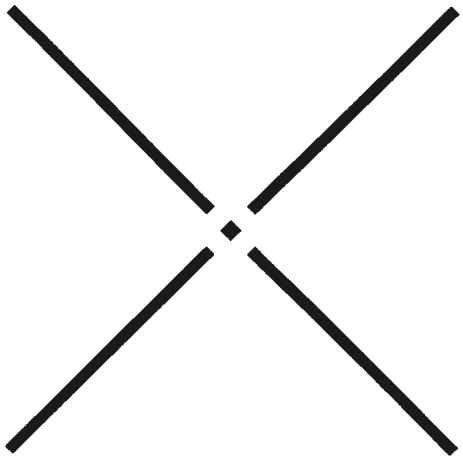

Figure 1.1 - Aerial Surveying Premark

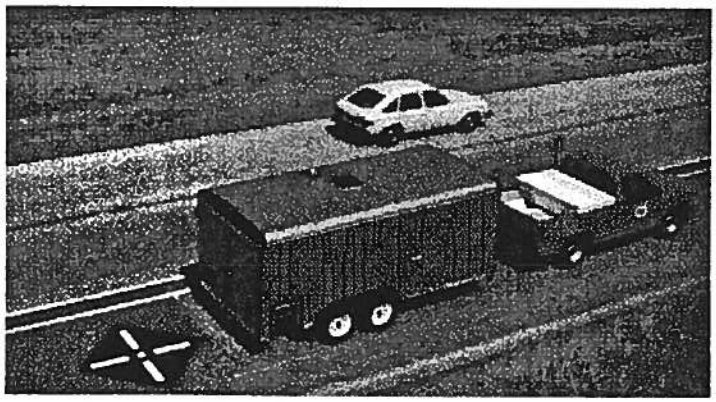

Figure 1.2 - Stenciling Robot for Aerial Premarks [2]

1.2.2 Telerobotic Graffiti Writer

The telerobotic Graffiti Writer vehicle was designed and built by the Institute for Applied Autonomy (IAA). The IAA designers incorporated common hobbyist remote control vehicle technology to create a moving platform to carry a linear array of standard paint spray cans. Each paint spray can was controlled individually by a solenoid that received commands from a microcontroller located on board the vehicle. The operator guided the vehicle to the targeted marking location by remote control and as the robot passed over the targeted location, the operator triggered the painting operation. A microcontroller

controlled the firing of the solenoids to allow individual spray cans to paint for a specific period of time to form letters. The choice of spray cans and duration of painting determines the shape of each letter. The robot's method of marking is similar in function to a dot matrix printer. The demonstration vehicle was capable of creating letters using a five dot tall dot matrix with each letter three dots wide. This technology has been successfully demonstrated to spray paint messages with two-foot tall letters as the vehicle moves at a rate of 15 kph. Encoder feedback allows the microcontroller to adjust the spray paint triggering pattern to account for the speed of the vehicle. A larger version of the this roadway marking technology was scheduled to be implemented on a standard automobile by July of 2000 to produce the letters with a height equal to the width of a car [3].

1.3 Description of Proposed Robotic Roadway Marking System

The design of the BASR employed a five-degree of freedom serial manipulator robotic arm to control the position and orientation of a standard spray gun similar to those used currently in stenciling operations. Mounted to the bed of a Caltrans maintenance truck, the arm could be easily transported to and from each worksite. From the safety of the cab, the operator would position the back of the truck in front of the stenciling area. The operator would issue commands specifying the types and scale of the roadway markings. From these commands, the robot would reference a preprogrammed trajectory for the spray gun to follow to paint each marking. The markings would be painted without the aid of a stencil since the orientation and position of the gun determine the width of the painted line as well as the paint distribution. By following these programmed descriptions the robot would paint each letter onto the roadway in a single pass.

Placing all of the required duties of the operator inside the truck would better protect the highway maintenance worker from the hazards of working in a high-speed traffic environment. The versatility of the robotic arm would also eliminate the need to carry stencils. Finally, the automating of the painting process reduces the physical demands placed upon the operator.

This thesis will detail the redesign of the BASR end effecter to incorporate a novel four bar mechanism for orientation control of the paint spray gun. Additional design modifications were made to the rotary joint and vertical extension joint to accommodate changes in design parameters created by addition of the four bar mechanism. Chapter 2 describes the design method followed to create the four bar mechanism. Chapter 3 details the rotary joint design while chapter 4 details the vertical extension joint design.

CHAPTER 2: SPRAY GUN ORIENTATION MECHANISM DESIGN

The design of the spray gun orientation mechanism of the BASR end effecter progressed through three phases. Section 2.1 describes a search for ideas to create a simply actuated tilt motion. With the selection of a four bar mechanism, the mechanism was sized to fit functional requirements such as tilt rotation range and nozzle tip translation. Section 2.2 details how components were selected to meet specifications developed during the mechanism sizing phase. In Section 2.3, the structure of each of the mechanism links was designed to accommodate the chosen components.

2.1 Four Bar Mechanism Concept Design

This section describes the work undertaken to develop a four bar mechanism concept designed to provide tilt motion to the robotic system.

2.1.1 Spray Gun Orientation Mechanism Subsystem Requirements

The robot system design specifications required that the tilt system be mechanically simple to improve reliability and decrease cost. Additionally, to minimize the control system complexity, the spray gun orientation mechanism should employ one actuator to control a one-degree of freedom tilt motion. A simple revolute joint was initially designed to provide tilt motion. To meet these specifications a four bar mechanism was chosen to provide the tilt motion for the robot system.

2.1.2 Use of Four Bar Mechanism Within BASR End Effecter

A four bar mechanism is commonly used to simulate the motion of a revolute joint when the point of rotation of the revolute joint is located in an inconvenient spot for the design [4]. The motion of the coupler created the tilting motion of the paint spray gun as the

coupler tilts. Nina Patarinska performed this initial design work. Figure 2.1 shows the initial concept for using the four bar linkage with the paint spray system.

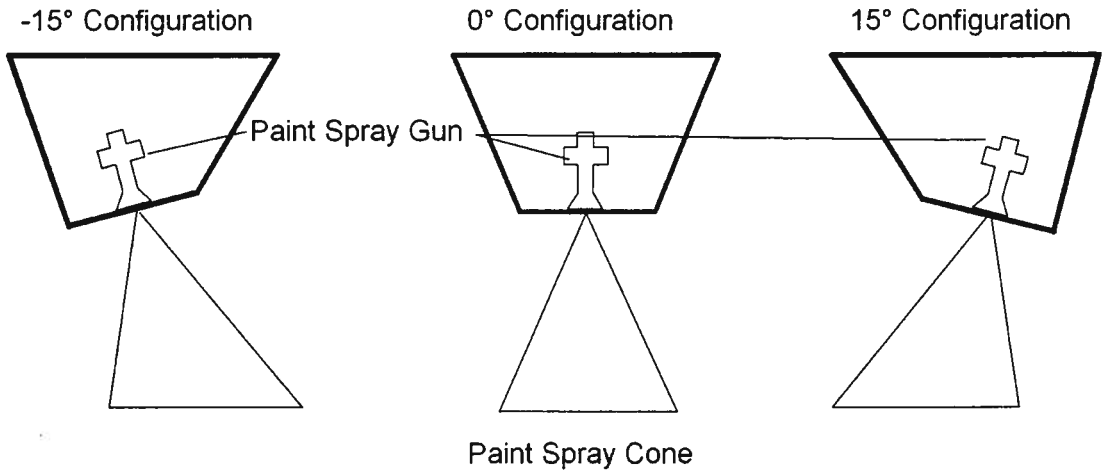

Figure 2.1- 3 Tilt Configurations

2.1.3 Description of Configuration of Four Bar Mechanism

A four bar mechanism consists of four links connected by simple revolute joints. The links are given names based upon their motion. The ground link is stationary and forms the base of the mechanism. The rocker links pivot about the joints they share with the ground link. The two rocker links support the coupler link. The coupler link follows the motion of the two rocker links. The four bar mechanism has a single degree of freedom motion. A four bar mechanism is shown in Figure 2.2.

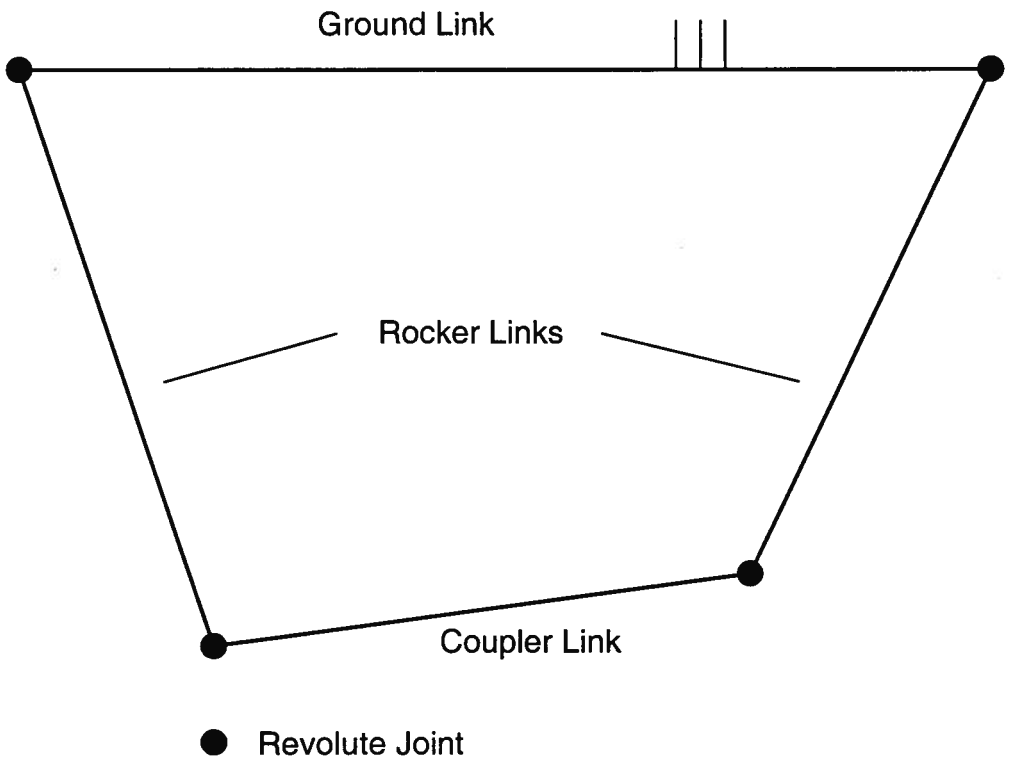

Figure 2.2 - Four Bar Mechanism Configuration

2.1.4 Configuration Equation for a Four Bar Mechanism

Equations (2.1) and (2.2) were used to analyze the motion of the nozzle tip and the motion of the connection point of the coupler. The equations describe the configuration of

the four bar mechanism and its geometric inversion. Figure 2.3 shows the definitions of the link lengths and angles used in the derivation of the configuration equation.

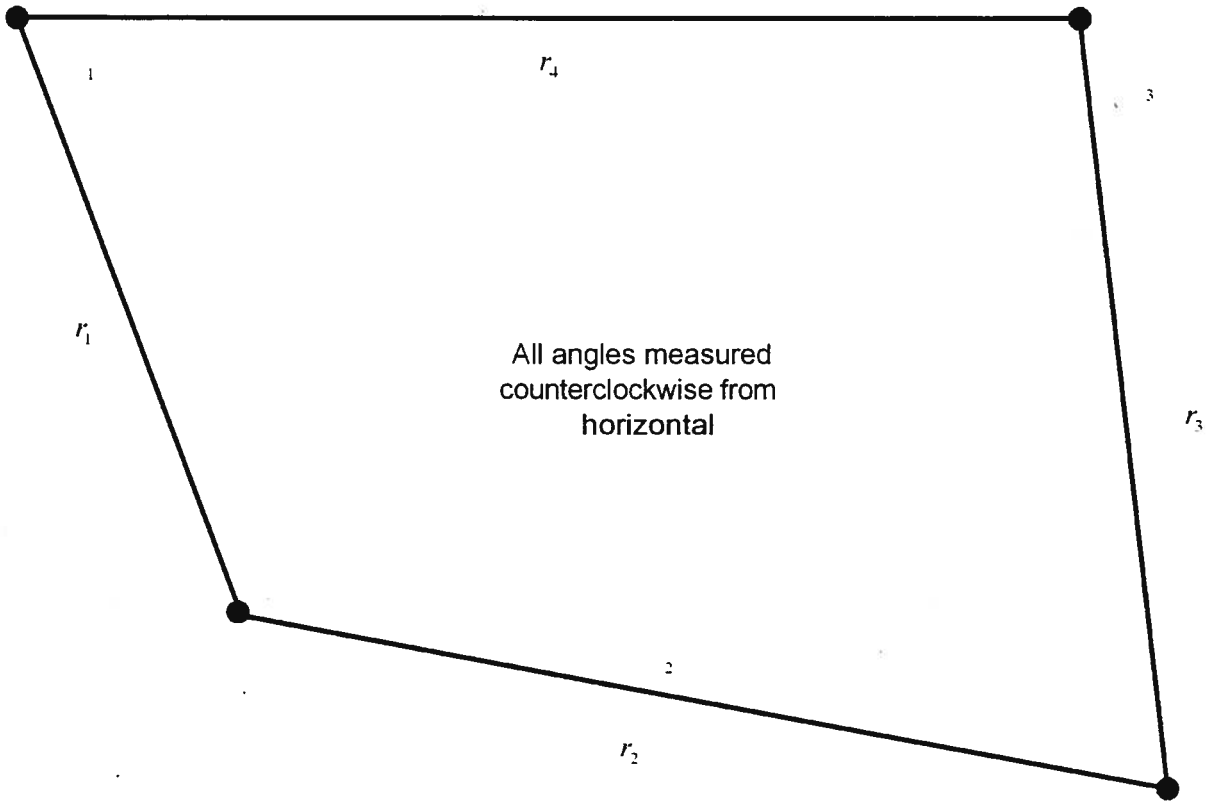

Figure 2.3 - Link Length Labels and Angle Labels

Configuration Equations

$$r_1 e^{i\theta_1} + r_2 e^{i\theta_2} - r_4 = r_3 e^{i\theta_3} \tag{2.1}$$

$$r_1 e^{-i\theta_1} + r_2 e^{-i\theta_2} - r_4 = r_3 e^{-i\theta_3} \tag{2.2}$$

From (2.1) and (2.2), Equation 2.3 was derived to find the angular position of one of the rocker links given the angular position of the coupler link.

Angular Position of Rocker Link Equation

$$\theta_1 = 2\tan^{-1}\{\frac{-b-\sqrt{b^2-4ac}}{2a}\} \tag{2.3}$$

where

$$a = r_1^{\,2} + r_2^{\,2} - r_3^{\,2} + r_4^2 - 2r_4 r_2 \cos\theta_2 - 2r_2 r_1 \cos\theta_2 + 2r_4 r_1$$

$$b = 4r_2 r_1 \sin\theta_2$$

$$c = r_1^2 + r_2^2 - r_3^2 + r_4^2 - 2r_4 r_2 \cos\theta_2 + 2r_2 r_1 \cos\theta_2 - 2r_4 r_1$$

$$c = r_1^2 + r_2^2 - r_3^2 + r_4^2 - 2r_4 r_2 \cos\theta_2 + 2r_2 r_1 \cos\theta_2 - 2r_4 r_1$$

2.1.5 Concept Generation of Actuation Methods for Four Bar Mechanism

Concept generation yielded two approaches to actuate the motion of the four bar linkage that differed depending upon whether the actuator drove one of the rocker links or if the actuator drove the coupler link.

Driving the rocker link with an actuator is the most common method of actuating a four bar mechanism especially if the motion of the linkage is continuous. The actuator would control the rotation of the rocker link and through this motion would cause the coupler to rotate. Analysis of the configuration equation indicated that the amount of rotation of the rocker link was of the same magnitude as the rotation of the coupler link. Because path planning requirements required only 30° of rotation of the coupler, this implied fine control would have to be exerted upon the motion of the actuator to assure the required precision of positioning the spray nozzle.

Driving the motion of the coupler link was another possibility for actuating the spray gun orientation mechanism. An actuator mounted to the ground link would provide the power to move the coupler. Use of a straight-line mechanism would simplify design considerations though utilization of the straight-line motion of its coupler link. Directly driving the coupler would allow for easier precise motion of the coupler.

2.1.6 Review of Straight-line Mechanisms

A review of literature resulted in the consideration of the Level Lofting Crane [5], Watt's Mechanism [4], Robert's Mechanism [5], Evan's Mechanism [4] and Hoeken's Mechanism [4]. Figure 2.4 shows the configuration of the links of each mechanism and the regions where approximate straight-line motion occurs. Robert's Mechanism was chosen because of its compact configuration of linkages and its symmetry of motion whether the coupler was tilting to one side or to the other. Robert's Mechanism was also favored due to the relative location of the straight-line motion zone to the location of the coupler.

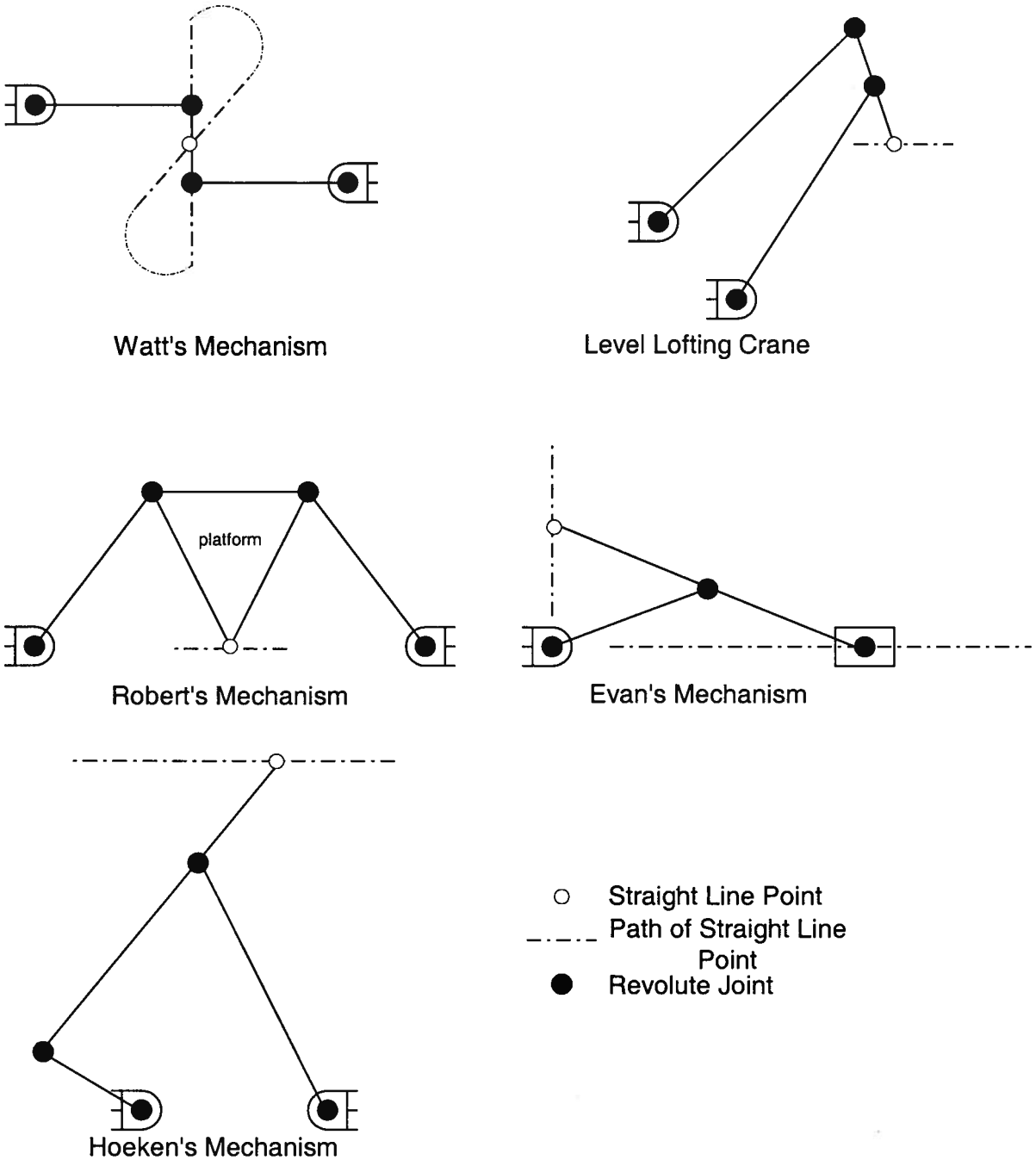

Figure 2.4 - Examples of Straight-line Mechanisms

2.1.7 Robert's Mechanism

Robert's Mechanism is a four bar mechanism that exhibits an approximate straight-line motion for a particular point located on the coupler. Figure 2.5 shows the relationships

between the link lengths required to achieve the approximate straight-line motion. Robert's Mechanism requires that the ground link be twice the length of the coupler link. This choice of link lengths forms two identical isosceles triangles, ABP and CDP. Point P represents the region on the coupler that exhibits approximate straight-line motion.

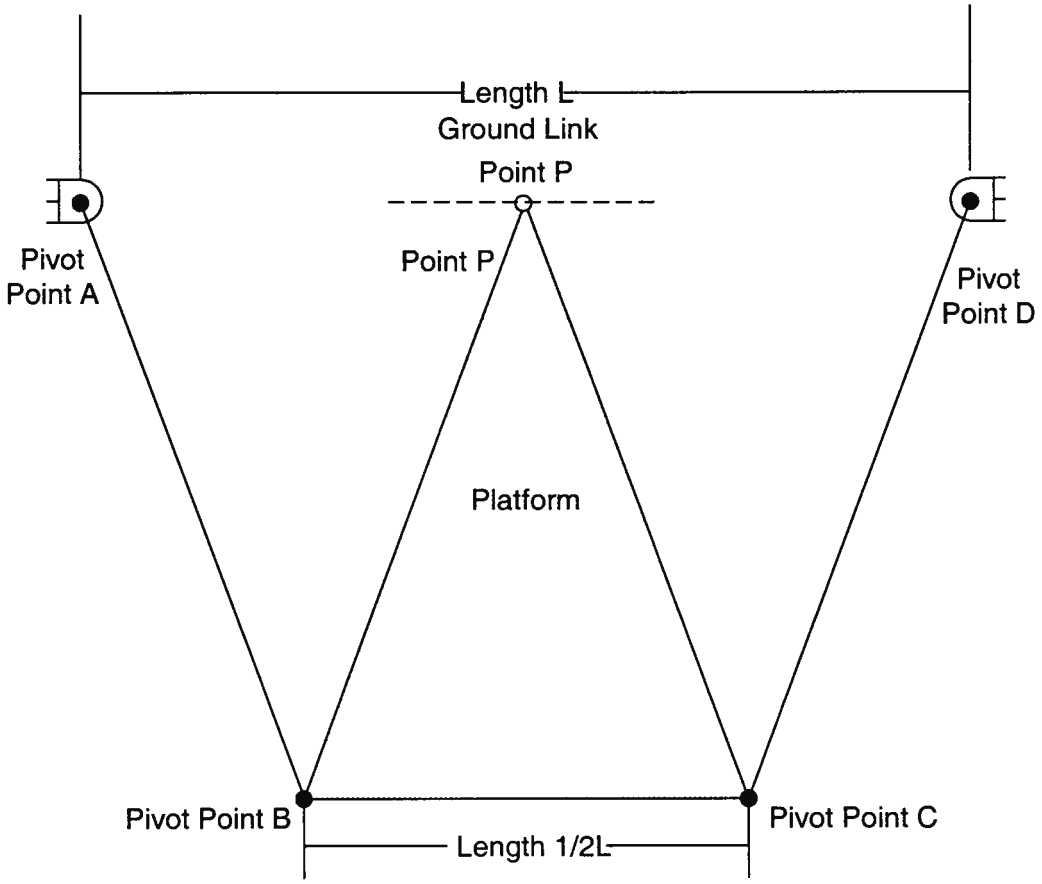

Figure 2.5 - Robert's Mechanism

2.1.8 Derivation of Position Equations for the Straight-line Motion Point on Coupler

Figure 2.6 shows a diagram used to derive the position equations of the approximate straight-line motion point P as a function of tilt angle. Equation (2.4) and Equation (2.5) describe the position of point P given the lengths and orientations of the links of the four bar mechanism. The distance h is the distance from the midpoint of the coupler to the point P.

The angle γ is formed from the tangent of the distance h and the distance equal to half the length of the coupler.

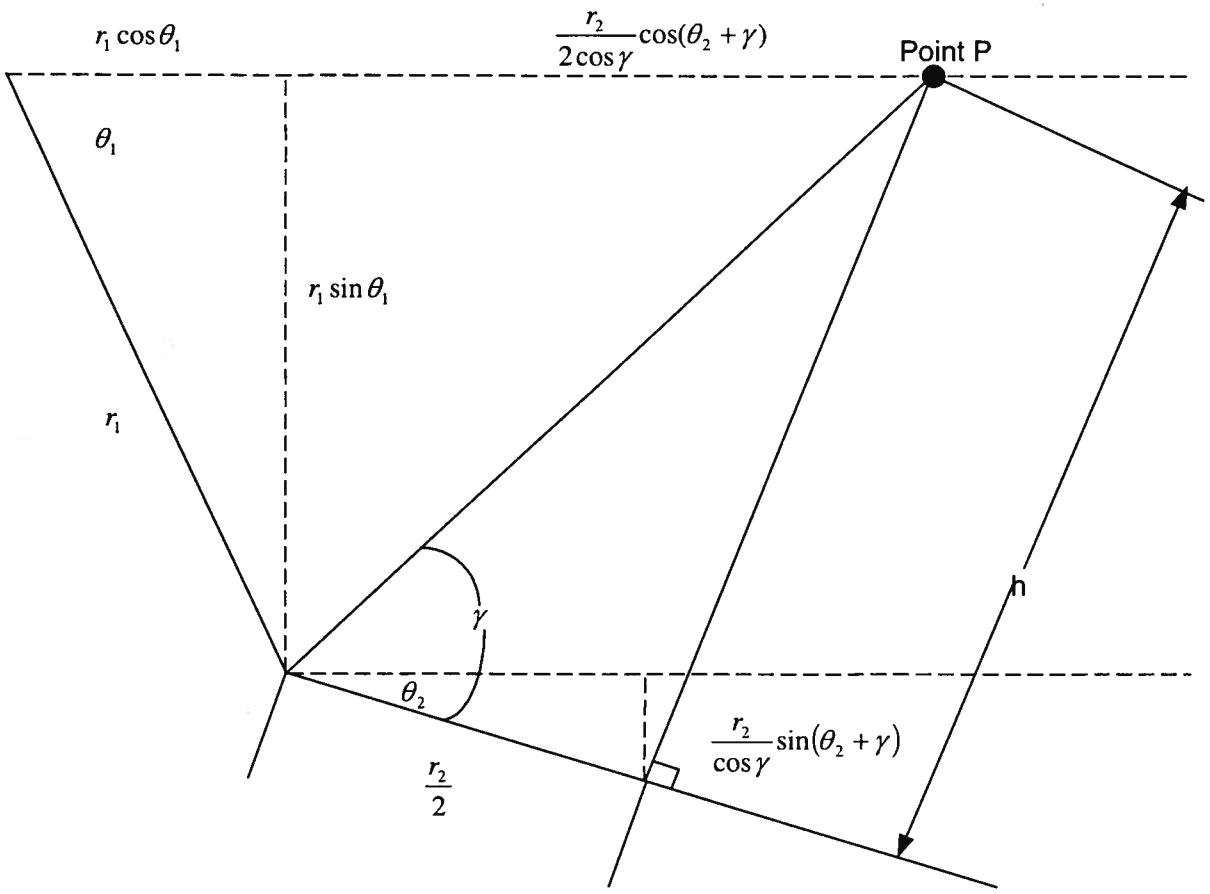

Figure 2.6 - Calculation of Position of Point P

Horizontal Position of Point P Equation

$$p_x = r_1 \cos(\theta_1) + \frac{r_2}{2\cos\gamma}\cos(\theta_2+\gamma) \qquad (2.4)$$

Vertical Position of Point P Equation

$$p_y = r_1 \sin(\theta_1) + \frac{r_2}{2\cos\gamma}\sin(\theta_2+\gamma) \qquad (2.5)$$

Figure 2.7 shows the relationship between the motion of point P and the angular tilt motion of the coupler and spray gun. The relationship between the linear displacement of P along the x-axis and the angular tilt motion of the coupler is nearly linear. A linear

relationship helps to eliminate problems that may occur due to calibration errors in the tilt positioning of the spray gun. The rotation rate of the coupler versus linear displacement of point P is nearly constant throughout the designed range of motion of the mechanism. Therefore, any angular calibration error will remain constant independent of the tilt motion. Equation (2.6) shows the results of a linear regression performed on the four bar motion over the ± 15° range of the coupler link.

Linear Regression and R Squared Value Equation

$$P_x(m) = -0.0073\theta_2(°) + 0.0005$$
$$R^2 = 0.9998 \qquad (2.6)$$

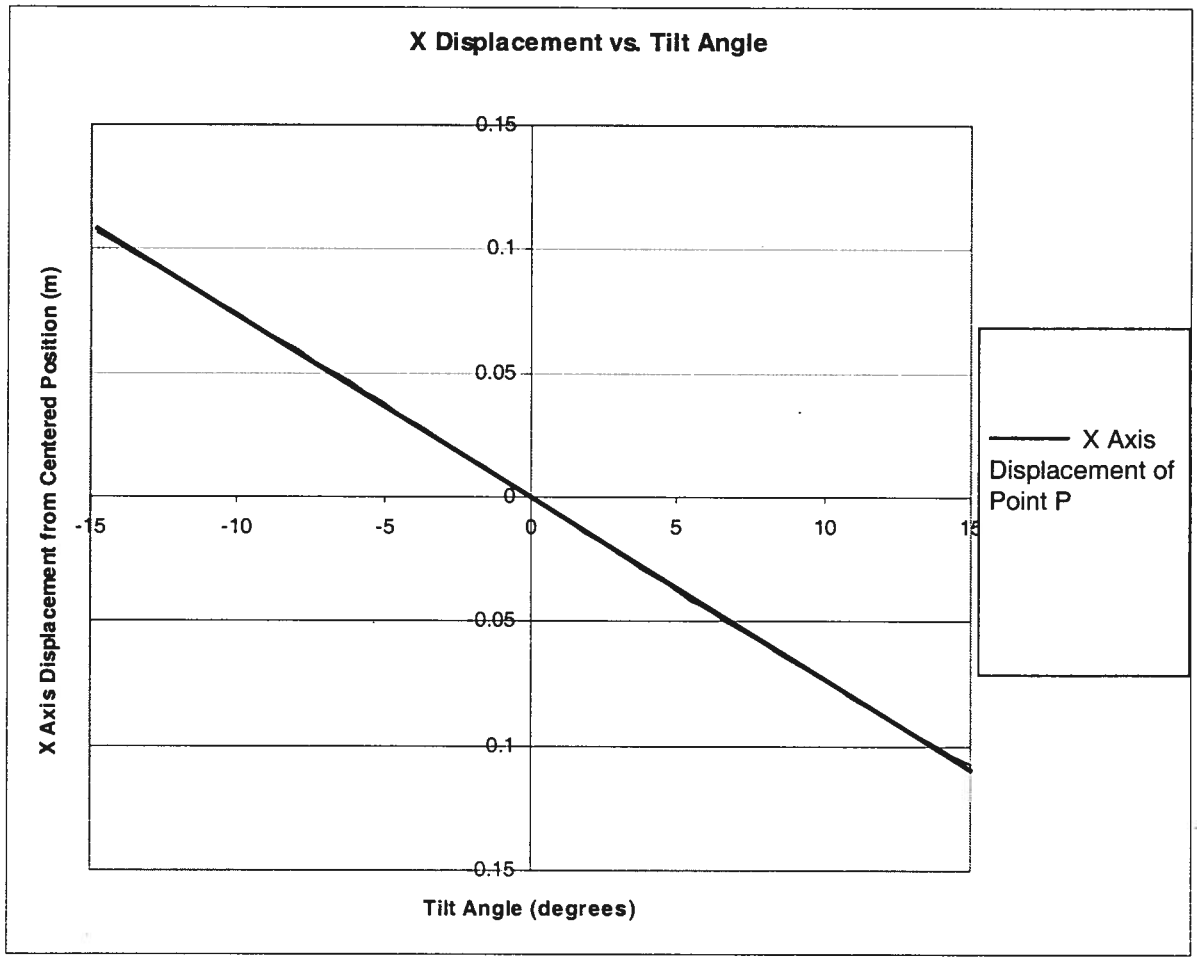

Figure 2.7 - Displacement of Connection Point vs. Tilt Angle

2.1.9 Selection of Rocker Link Lengths

The rocker, coupler and ground lengths were varied subject to the restrictions set by the Robert's Mechanism's criterion to determine the approximate ratios of the rocker link lengths to ground link and coupler link lengths. Both rocker link lengths were kept equal to produce a symmetrical motion whether the spray gun was tilted to one side or the other. The ratio between the ground link length and the rocker link length was varied to determine values that would produce the greatest tilt rotation with a minimum translation of both the nozzle tip and the coupler connection point. Reducing the translation of the nozzle tip in the end effecter minimized the motion requirements that the robotic arm would have to compensate for to maintain the nozzle tip path. Minimizing the translation of the coupler connection point would reduce the drive requirements of the tilt actuation system by reducing the required speeds and accelerations required by the tilt actuator. Additionally, consideration was made regarding the magnitude of the vertical translation of point P since a large vertical translation during the tilt motion would increase the difficulty of designing a suitable actuation method for the four bar mechanism.

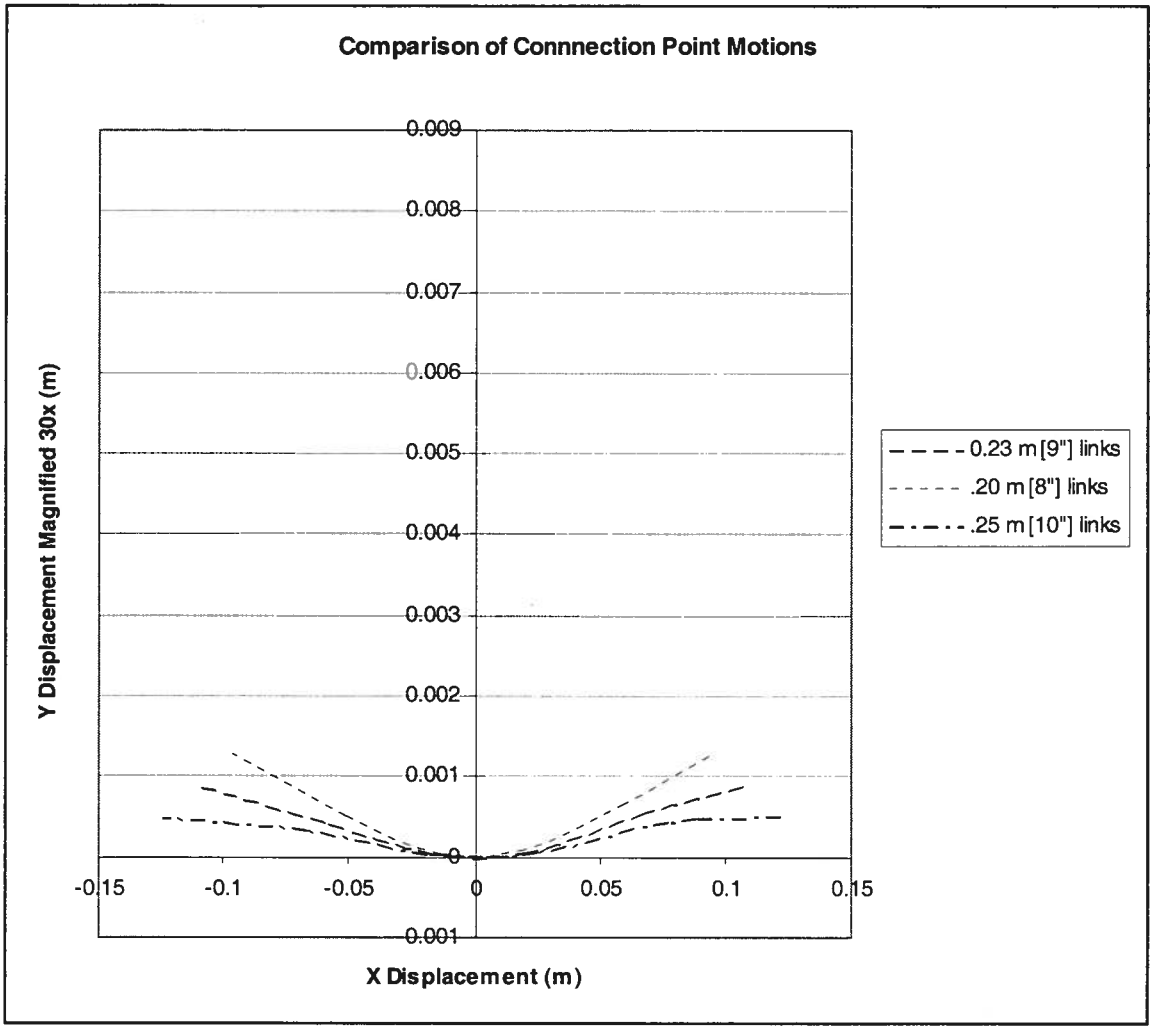

Figure 2.8 - Comparison of Connection Point Motion

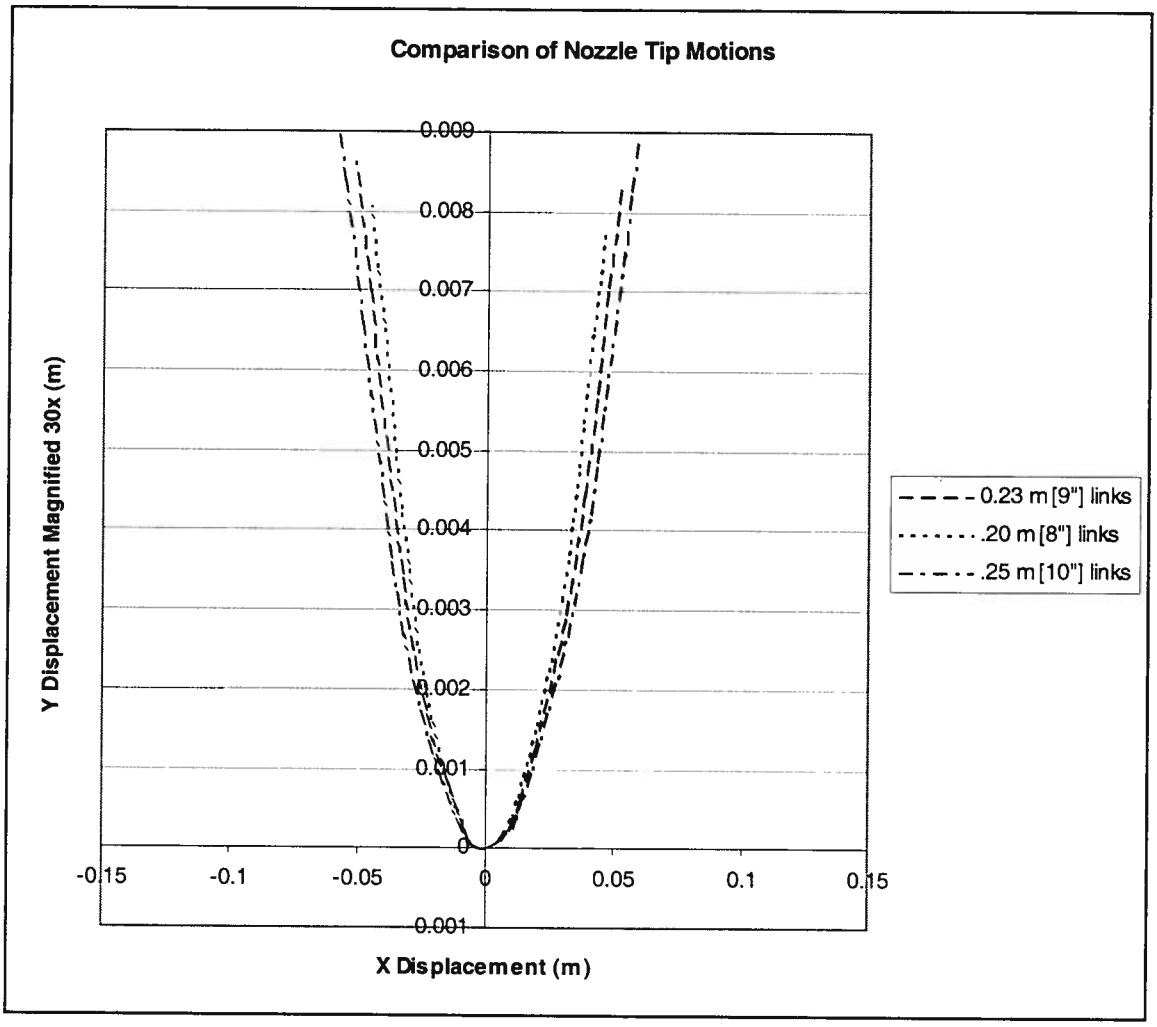

Figure 2.9 - Comparison of Nozzle Tip Motion

Examination of Figure 2.8 and Figure 2.9 shows the tradeoff between straight-line motion of the connection point and the translation of the nozzle tip. While shortening the rocker links will decrease the translation of the nozzle tip during the tilt motion, the shorter links create more vertical translation of the connection point. A trade must be made to determine the optimum length of the rocker links while also considering other factors in the trade decision such as size of the spray nozzle that must fit within the four bar mechanism.

0.23 m [9"] rocker links provided the best compromise of minimum nozzle tip and connection point motion.

2.1.10 Grahof's Range of Motion Criterion for a Four Bar Mechanism

Grashof's criterion specifies the range of motion of a four bar mechanism for a given set of link lengths [5]. Grashof's criterion is shown in Equation (2.7). θ_1 represents the angular limit of motion of the rocker link as defined in Figure 2.3. This criterion was examined to determine if the proposed mechanism design had an adequate range of motion. Figure 2.10 and Figure 2.11 show plots of the range of motion. Areas toward the limits of range of motion exhibit undesirable behavior. In these regions, the relationship between the angular tilt motion and the translation of the connection point becomes nonlinear and the straight-line motion of the mechanism is lost defeating the purpose of choosing Robert's Mechanism. Therefore, during the design of the mechanism all required motion of the spray gun orientation mechanism's connection point was kept within the approximate straight-line motion zone of the four bar mechanism.

Grashof's Criterion Equation

$$\cos\theta_1 = \frac{r_4^{\,2} + r_1^2 - (r_3 + r_2)^2}{2r_4 r_1} \quad \text{if } r_1 + r_4 > r_3 + r_2 \tag{2.7}$$

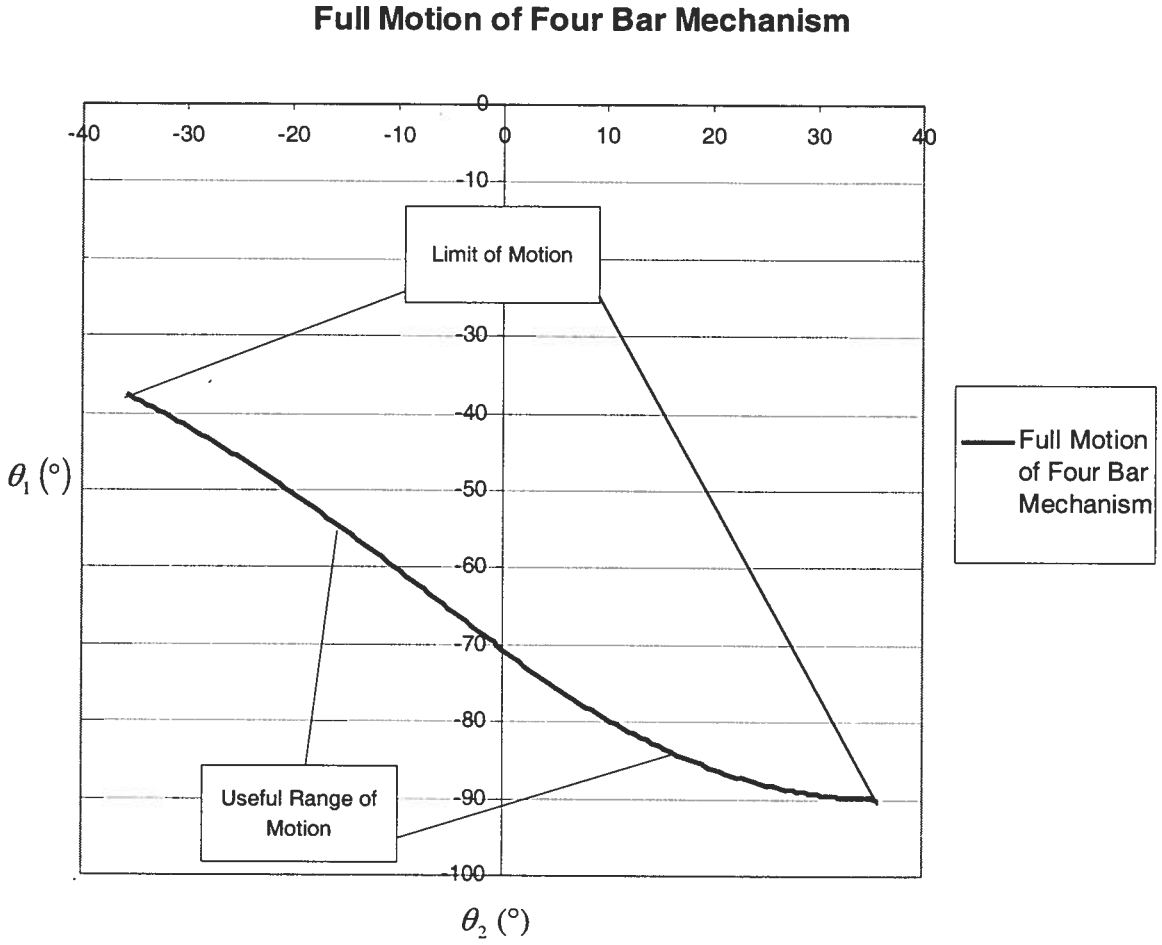

Figure 2.10 - Full Motion of Four Bar Mechanism

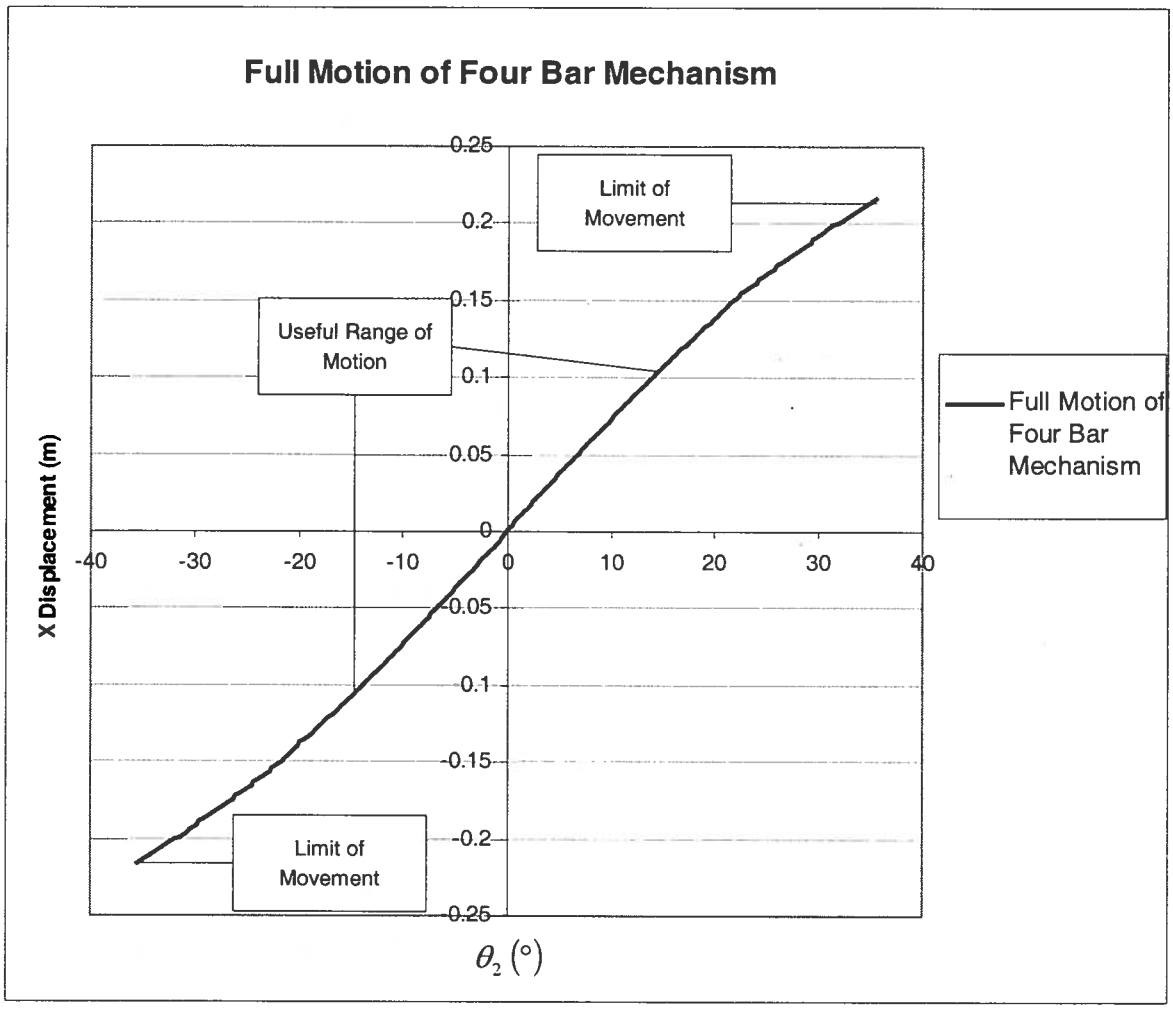

Figure 2.11 - Full Motion of Four Bar Mechanism

2.2 Spray Gun Orientation Mechanism Linear Actuation Specifications for Components

Component selection began the next stage of the spray gun orientation mechanism design. At this point the design included only the lengths of the four bar mechanism lengths and the location of the paint spray nozzle tip. Determining the type, size and orientation of the individual components such as the spray gun, the ball screw and servomotor would allow for the completion of the structural design of the four bar mechanism's links.

2.2.1 Creation of Technical Specifications for Spray Gun Orientation Mechanism Actuation

The choice of link lengths of the spray gun orientation mechanism required that the actuator provide a minimum stroke of 0.22m [8.5"] to allow for a ± 15° tilt motion as required by the paint path planning requirements.

Other requirements included minimal weight, ease of providing position and velocity feedback and precise movement. The methods investigated included a belt and pulley system, a ball screw system, and a rack and pinion system.

2.2.2 Comparison of Spray Gun Orientation Mechanism Actuation Methods

The use of an approximate straight-line mechanism necessitated a linear actuation method to drive the coupler's tilt motion. The evaluation of several linear actuation methods determined the most suitable method to actuate the spray gun orientation mechanism design.

Figure 2.12 shows a sketch of a proposed belt and pulley system used to control the position of the straight-line point on the coupler. The belt and pulley system is capable of meeting the requirements for speed and stroke length. Other advantages include flexibility in placement of drive components and simplicity in its mechanical design. Positional feedback of the linear translation could also be easily accomplished through an encoder attached to motor shaft. The belt pulley system also offered a solid connection to the coupler because of the elastic nature of the belt. Disadvantages included a need to preload the belt and compliance due to the elastic nature of the belt that could reduce the positional accuracy of the paint nozzle.

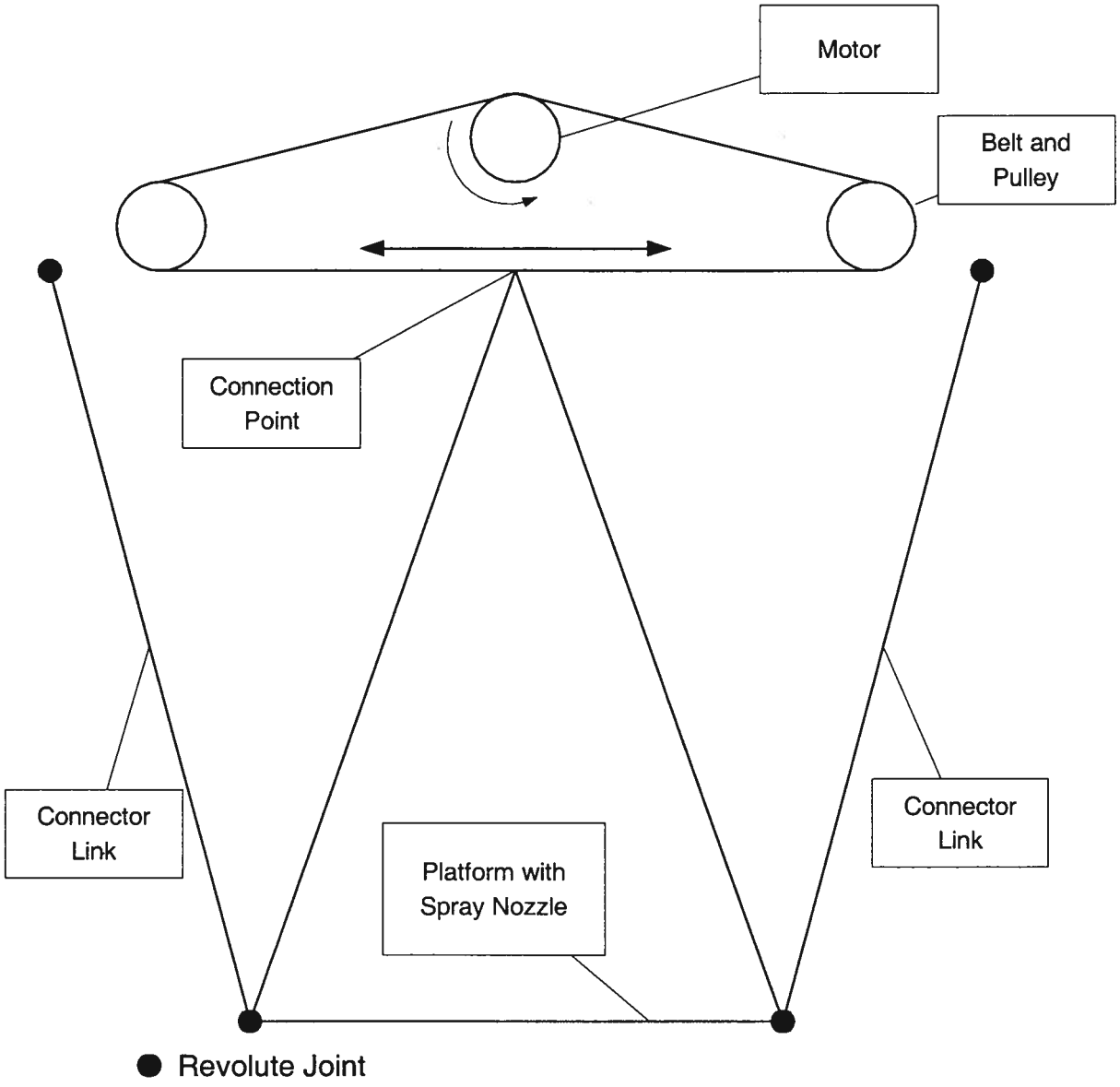

Figure 2.12 - Belt and Pulley Actuation System

Figure 2.13 shows a sketch of a proposed rack and pinion system used to drive the coupler and create tilt motion. The rack is rigidly mounted to the ground link while the pinion and motor would be mounted to the coupler. The rack and pinion system would provide a more rigid connection between the coupler link and ground link than the belt and pulley system. Analysis of the design revealed several disadvantages. The rack and pinion

system would require a larger motor drive due to the increased inertia of the coupler because the motor would be moving with the coupler. The increased moving mass would also create unwanted vibrations that would degrade the accuracy of the nozzle aiming. Backlash within the rack and pinion gears would also be a problem because of the approximate straight-line motion of the mechanism. Backlash depends upon the spacing between the center of the pinion and the rack. Some backlash would be present if a straight rack were used because the pinion would follow an approximate straight-line motion and could not maintain a constant spacing between the rack and pinion.

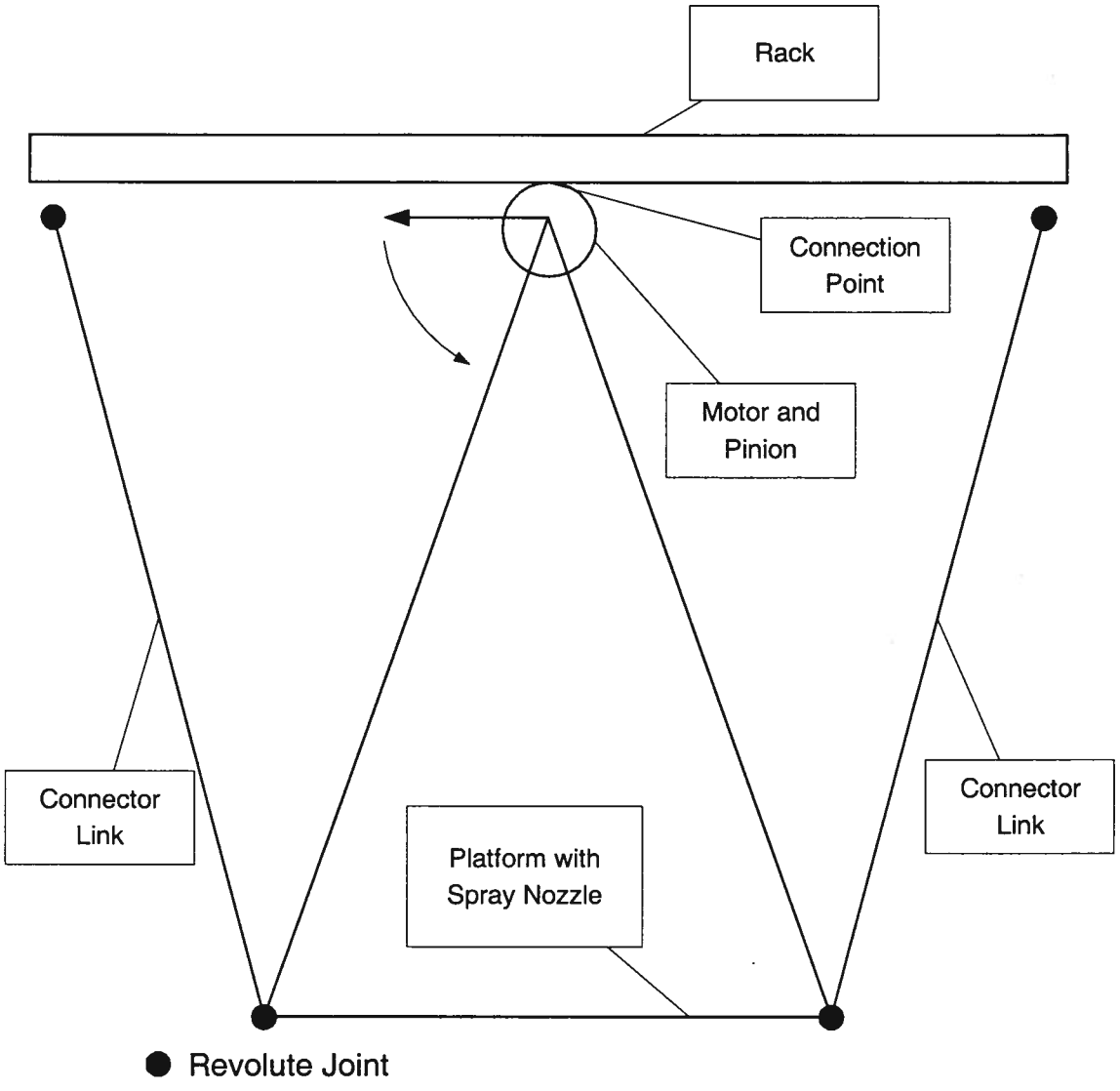

Figure 2.13 - Rack and Pinion Actuation System

Figure 2.14 shows a sketch of the ball screw used to actuate the spray gun orientation mechanism. The spinning of the ball screw would cause the ball nut to translate. The ball nut mates with a specially designed yoke mounted to the coupler to control the coupler's tilt angle. The ball nut can also be configured to provide almost zero backlash. Use of a ball screw would provide an attractive method of actuating the spray gun orientation mechanism.

Use of a ball end joint to connect the coupler to the ball screw would allow for the slight vertical translation inherent in the approximate straight-line motion.

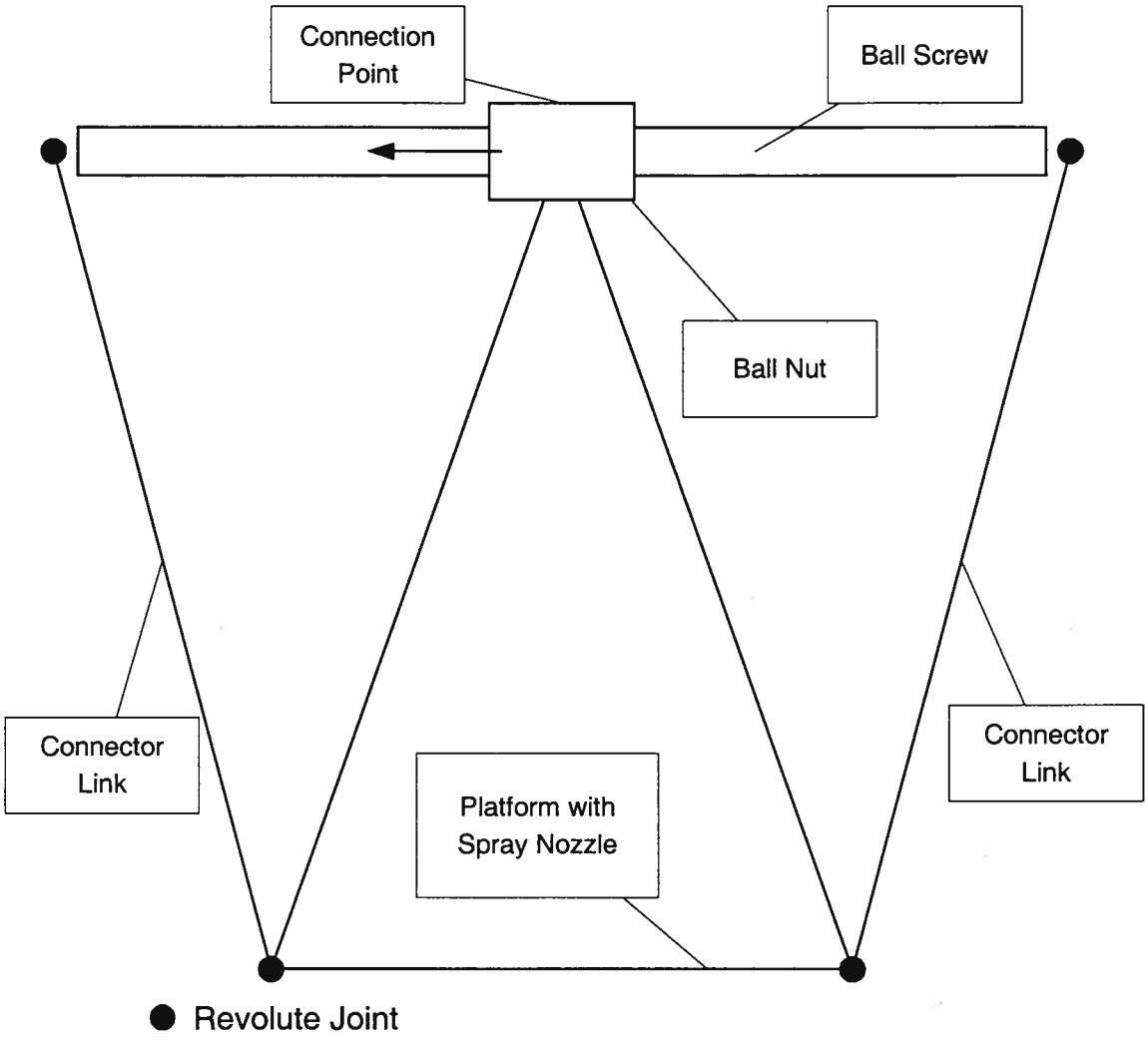

Figure 2.14 - Ball Screw Actuation System

2.2.3 Ball Screw Specifications

The selection of a ball screw depends upon a combination of linear speed, load, and stroke length requirements for the application. In addition, the rated speeds of the bearings used to support the ball screw must be considered in the design to ensure that these speeds are not exceeded. The manufacturers of ball screws provide tables for load and length

calculations [6]. Because of the light loads a small diameter ball screw would provide adequate strength to withstand axial loading. Minimizing the ball screw diameter also would minimize the torque requirements upon the motor drive. Based upon these tables, a 0.0095 m [3/8"] dia. ball screw was selected. Equation (2.8) calculates the maximum linear velocity of the ball nut given the stroke distance and the times of acceleration and deceleration. A trapezoidal motion profile was assumed in the velocity calculations. Equation (2.9) was used to calculate the ball screw angular velocity given the ball screw's pitch and linear velocity of the ball nut. Calculations revealed that a ball screw with a pitch of 0.0032 m [1/8"] could provide the needed linear translation speed while not exceeding the maximum rated angular speed of 2500 rpm of the bearings holding the ball screw.

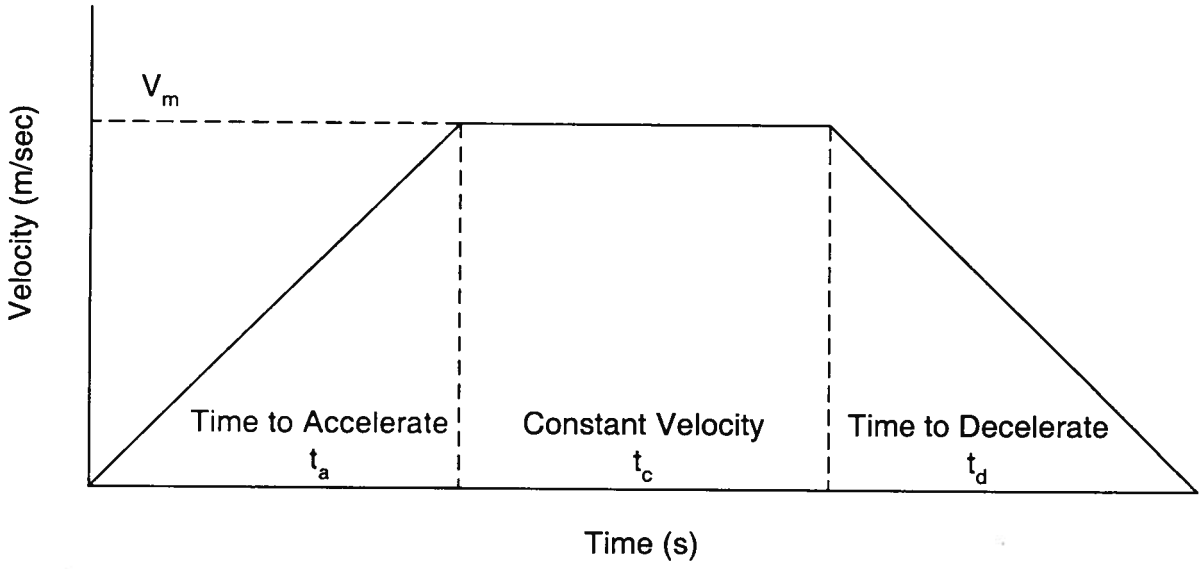

Figure 2.15 - Trapezoidal Motion Profile

Maximum Velocity Equation

$$V_m = \frac{2 \cdot Stroke}{t_a + t_d + 2 \cdot t_c} = 0.110 \text{ m/s} \qquad (2.8)$$

where t_a and $t_d = 1/50^{th}\, s$ and $t_c = 24/25^{th}\, s$ and stroke = 0.108 m [4.25"]

Maximum Angular Velocity of Ball Screw Equation

$$\omega_{max} \doteq \frac{V_{max}}{Ball\ Screw's\ Pitch} = 2080\ rpm \qquad (2.9)$$

where $V_{max} = 0.110\ m/s$

and $Ball\ Screw\ Pitch = 0.0032\ m/rev$

The ball screw will also provide precise tilt position of the robotic end effecter. 1 revolution of the ball screw will create about .5° of end effecter tilt. Equation (2.10) shows the relation between ball screw turns and tilt motion.

Degrees of Tilt per Revolution of Ball Screw Equation

$$\text{degrees/revolution} = 137\ \text{degrees/m} \cdot \text{Ball Screw Pitch} = .5\ \text{deg/rev} \qquad (2.10)$$

137 degrees/m was derived from the linear regression of the slope of the motion found in Figure 2.7. Appendix A details these calculations.

The length of the ball screw includes the required stroke length with an additional length to provide clearance for the ball nut.

In addition, the ball screw was designed with an end protruding outside the spray gun orientation mechanism enclosure to allow hand positioning of the spray gun orientation mechanism during diagnostic work.

2.2.4 Torque Transmission for Tilt Motion Specifications

The actuation method employing a ball screw required a motor to drive the ball screw. Usually, an inline configuration of the motor and ball screw is used where the motor shaft is directly attached to the ball screw by means of a shaft coupler. This inline configuration would add an additional undesired length to the spray gun orientation

mechanism. To reduce the overall length of the spray gun orientation mechanism and reduce the end effecter's weight and inertia, a side-by-side configuration of the servomotor and ball screw was used. Figure 2.16 shows a comparison of the side-by-side and inline configurations. A belt and pulley system and a gear system were analyzed to determine which system would provide better drive capabilities. The systems are displayed in Figure 2.17. The belt system was rejected because of previous experience with an elastic belt introducing too much compliance into the system. This compliance would lead to errors in positioning and sluggish system response. Transmitting the torque through a set of gears would create a much more responsive system because the compliance would be smaller. Therefore a gear train was chosen to provide the torque transmission from the motor to the ball screw.

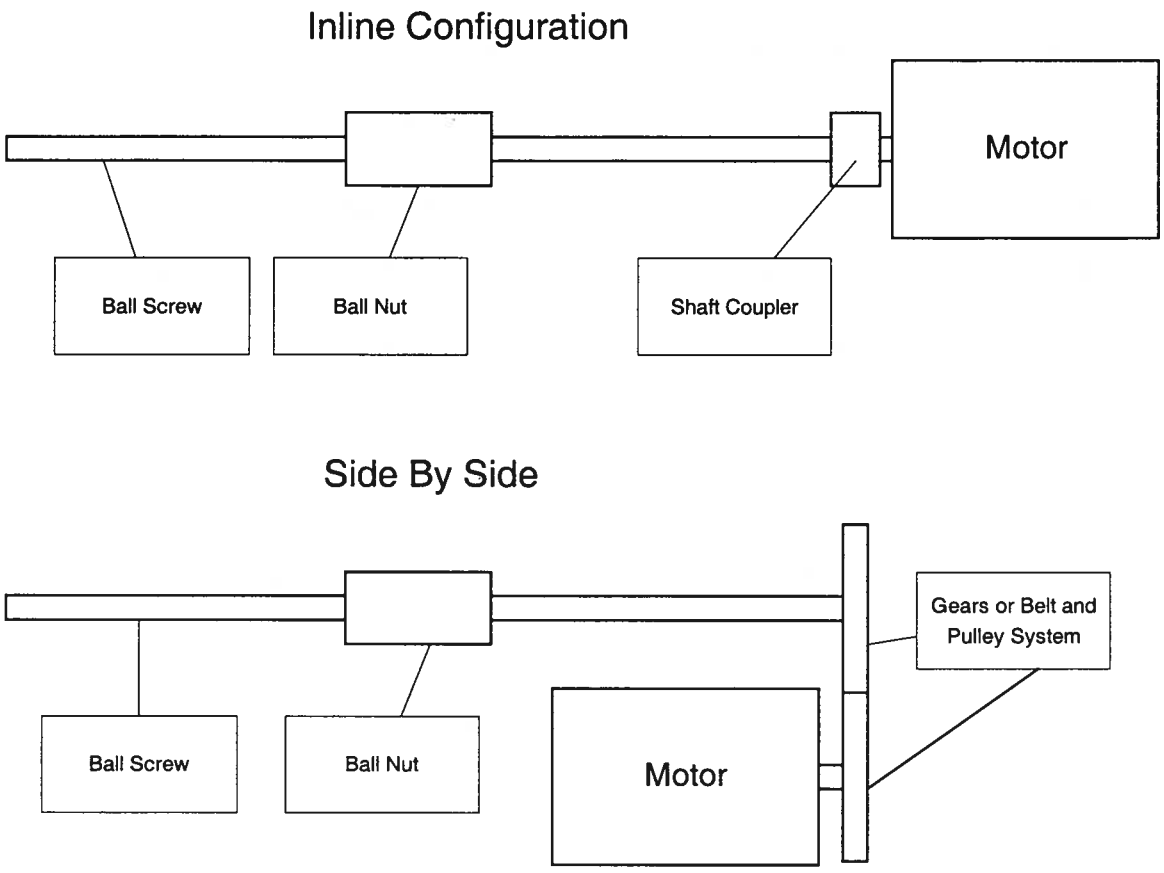

Figure 2.16 - Comparison of Motor And Ball Screw Configurations

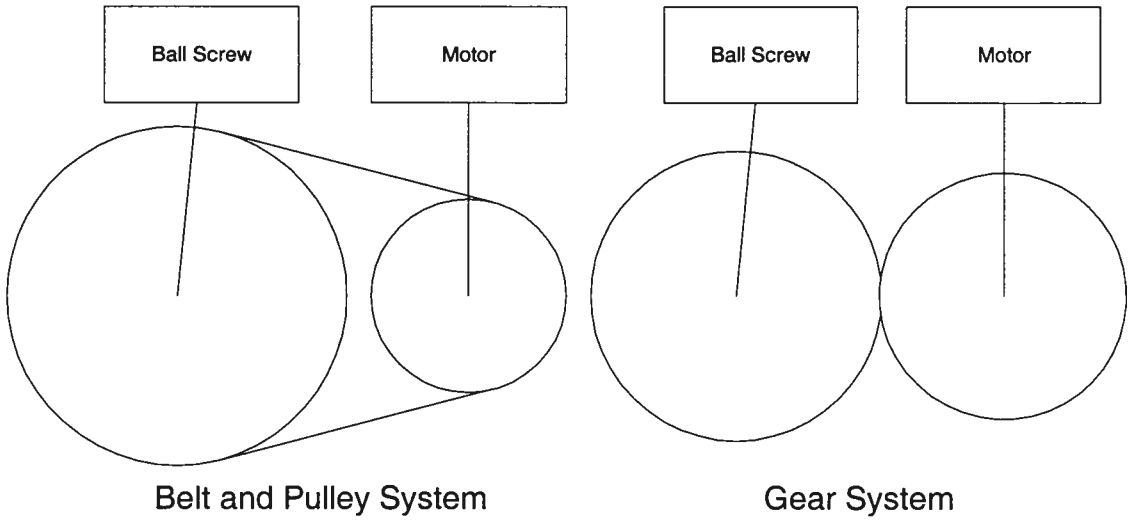

Figure 2.17 - Comparison of Belt and Pulley System and Gear System

2.2.5 Ball Screw Gear Specifications

Mechanical strength and fatigue calculations were performed to select the proper gear material and pitch. Gear tooth bending and surface stresses were considered in the selection of gear material and pitch. Results from the calculations indicated steel gears with a diametrical pitch of 32 would be appropriate to this application. To prevent the gear teeth from pairing with each other and reducing the gear train life, the gears were chosen so that the gear ratio was a non-integer value. Other design factors, such as the spacing required between the ball screw and the motor and the size of the enclosure constrained the individual gear choices to roughly equal sized gears. A gear ratio of 1.1:1 provides a slight mechanical advantage for the motor. To reduce backlash in the gear train, the largest gear pitch that could withstand the expected forces was chosen while maintaining a contact ratio of 1.85. Appendix A shows calculations for the determination of the gear parameters.

2.2.6 Tilt Servo Motor Specifications

The design of the spray gun orientation mechanism assigned the torque, speed and required precision of positioning. To find the torque required to create 15°/s of tilt, the spray gun orientation mechanism was approximated as a 15 kg mass pushed linearly by a ball screw a distance of 0.108m [4.25"] in 1 second. The mass was used to simulate the loadings both from mass of the moving coupler and rocker links and forces due to friction and cabling. Angular kinetic energy of the coupler and rocker links was ignored due to the low angular speeds of the coupler and rocker links.

A trapezoidal velocity profile was assumed with an acceleration period of $1/50^{th}$s. Equation (2.11) shows how the required torque was calculated for sizing the motor. With these assumptions the required motor torque was calculated to be 0.32Nm [45oz-in]. Factory

specifications indicated that a Compumotor SM231 AE servomotor would provide the necessary torque. With a continuous torque rating of 0.43Nm [61oz-in] and peak torque rating of 1.28Nm [181oz-in] the servomotor should provide enough torque to position the spray gun orientation mechanism.

Tilt Motor Torque Calculation Equation

$$T_{acc} = \frac{[\frac{J_{load}}{e} + J_{screw} + J_{motor}] \cdot \frac{\varpi_{screw}}{m_G}}{t_a} \tag{2.11}$$

where

$$J_{load} = \frac{M_{load} \cdot p_{screw}^2 \cdot m_G^2}{2\pi^2}$$

$$J_{screw} = \frac{\pi \cdot l \cdot \rho \cdot r^4 \cdot m_G^2}{2}$$

m_G = Gear Ratio
l = length of ball screw
r = radius of ball screw
ρ = density of ball screw
p_{screw} = pitch of ball screw

An encoder mounted to the servomotor shaft will provide position feedback. At 1000 points per revolution, the encoder will provide adequately sensitivity to position the nozzle tip of the end effecter. Although theoretically the encoder feedback could give a nozzle tilt position resolution of about ± .005°, the precision of the design is limited because of other design limitations involving the backlash in the ball screw. Appendix A shows calculations for determination of these servo motor parameters.

A Gemini GV-L3E servo drive provided the power to the servomotor and received encoder feedback. The servo drive received commands from an Intel Celeron PC on board the BASR truck.

The servomotor was configured with an electrically activated brake to help the motor maintain position during periods of inactivity. The brake will receive commands from the servo drive.

2.3 Structural Design of Spray Gun Orientation Mechanism Links

This section details the design of the structural parts used to mount the components and create the four bar mechanism. Their design emphasized ease of manufacture and lightness while meeting all required functions of the spray gun orientation mechanism design. Because loading on these parts was expected to be small, no strength calculations were performed. Each of the subsections explains the major features of the individual parts. The subsections are broken into parts that roughly divide along the individual links of the four bar mechanism.

2.3.1 Ground Link

The ground link design incorporates the needs of providing a connection to the rotary joint of the end effecter of the robot, supporting the servo motor and ball screw, protecting the ball screw, gears and servo motor from environmental contamination and supporting the joints of ground link of the four bar mechanism.

A rectangular box provided the simplest geometry to incorporate the spray gun orientation mechanism's functions. The thicknesses of the sides of the box were sized according to the anticipated loading that each side would take. All parts of the box were

designed for ease of manufacture. The enclosure size was then minimized to reduce the weight of the spray gun orientation mechanism.

The ground link enclosure provided support and protection to the ball screw. Two elbow brackets provided support for the ball screw. To allow for the ball screw to turn a Conrad style ball bearing was press fit into each elbow bracket. The ball bearings had a maximum rated speed of 2500 rpm. Socket cap screws were used to affix the brackets to the roof of the ground link enclosure.

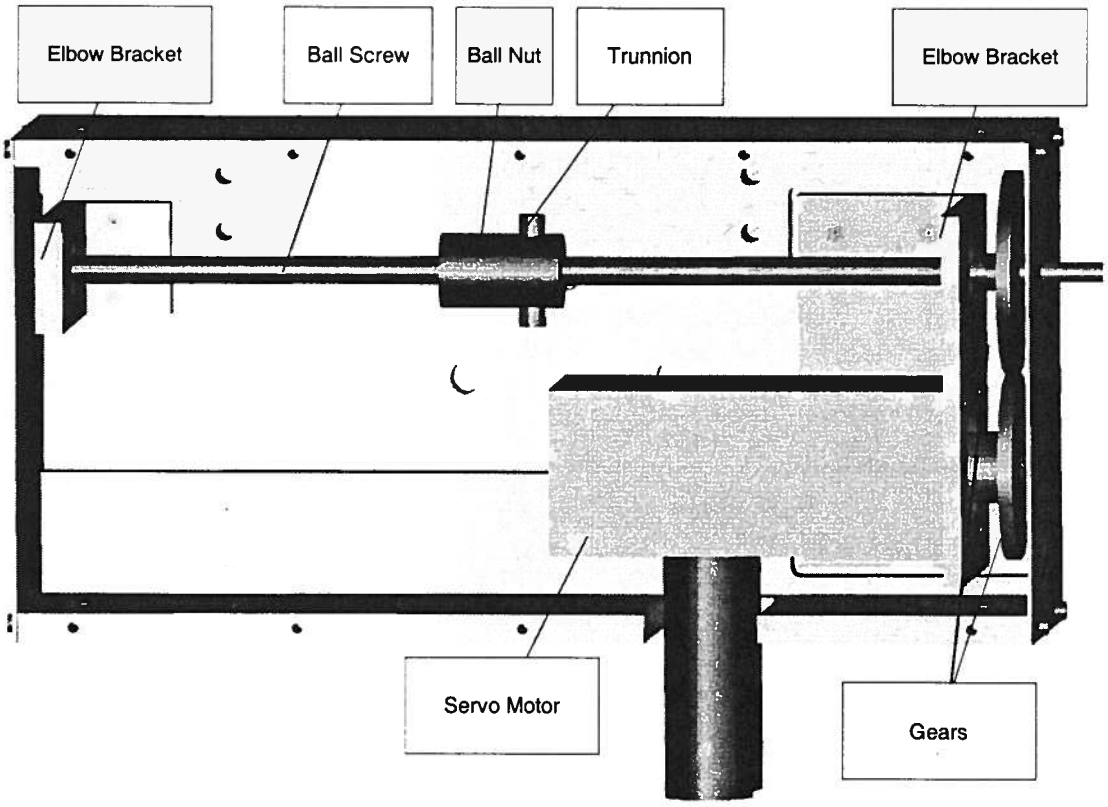

Figure 2.18 - Bottom View of Ground Enclosure with Bottom Panel Removed

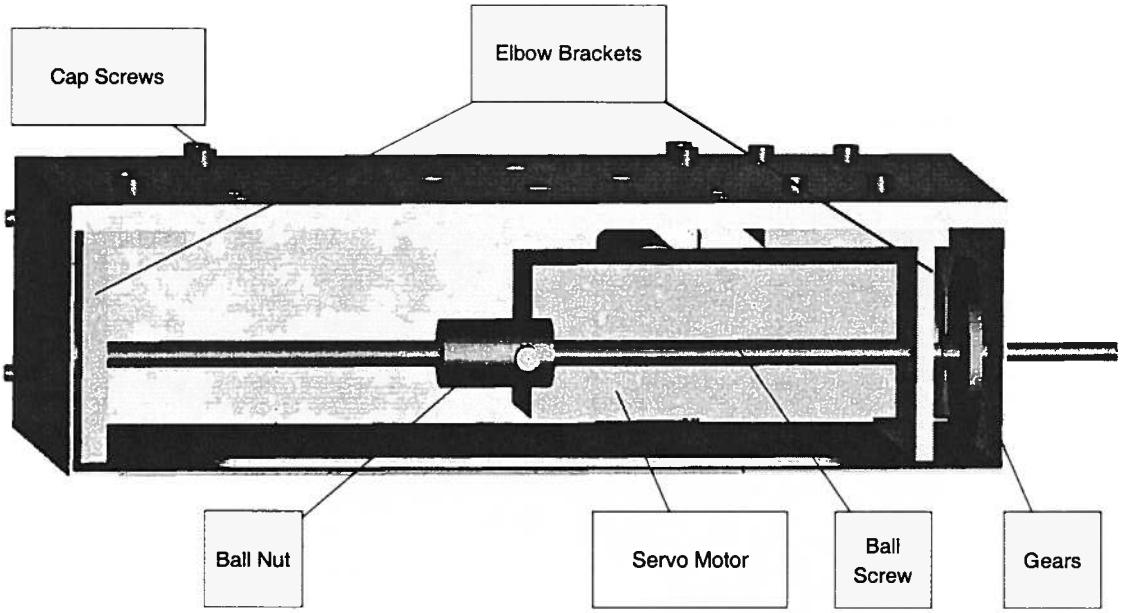

Figure 2.19 - Side View of Ground Enclosure with One Side Removed

The ground link enclosure also provides support and protection for the servomotor. An elbow bracket was used to mount the servomotor. The same elbow bracket was used to mount the ball screw to ensure that the distance between the ball screw and servomotor was tightly controlled. To allow for electrical access for the servomotor a small slot was cut into the side of the enclosure.

2.3.2 Revolute Joint Design

The joint design for each of the eight pin joints of the spray gun orientation mechanism consisted of a shoulder screw, a bronze thrust bearing and a bronze flange bearing. This selection of materials provided a close allowance fit between the shoulder

screw and the flange bearing and low friction during movement. Additionally, these components will provide an inexpensive precision assembly.

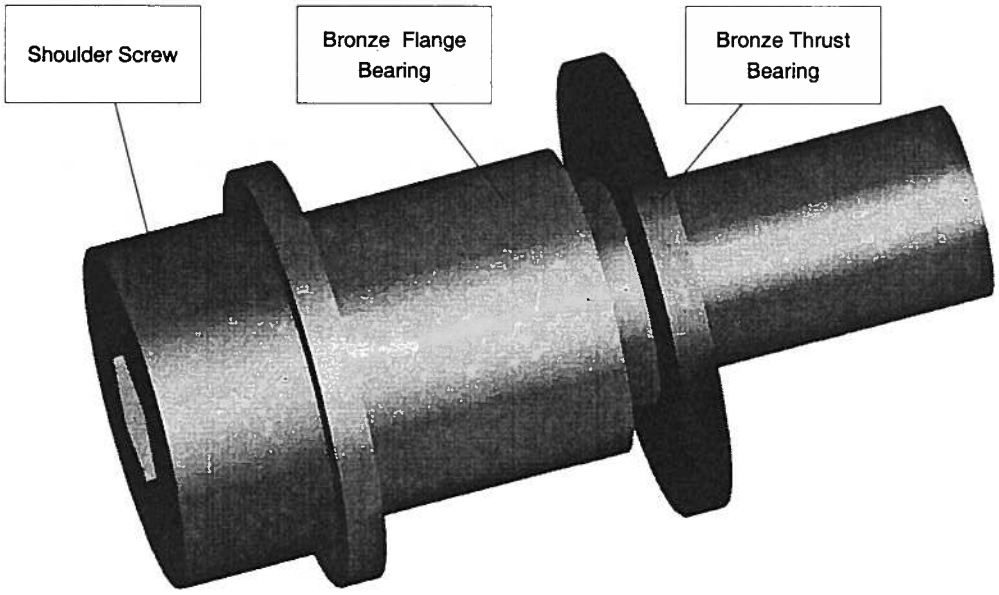

Figure 2.20 - Revolute Joint Components

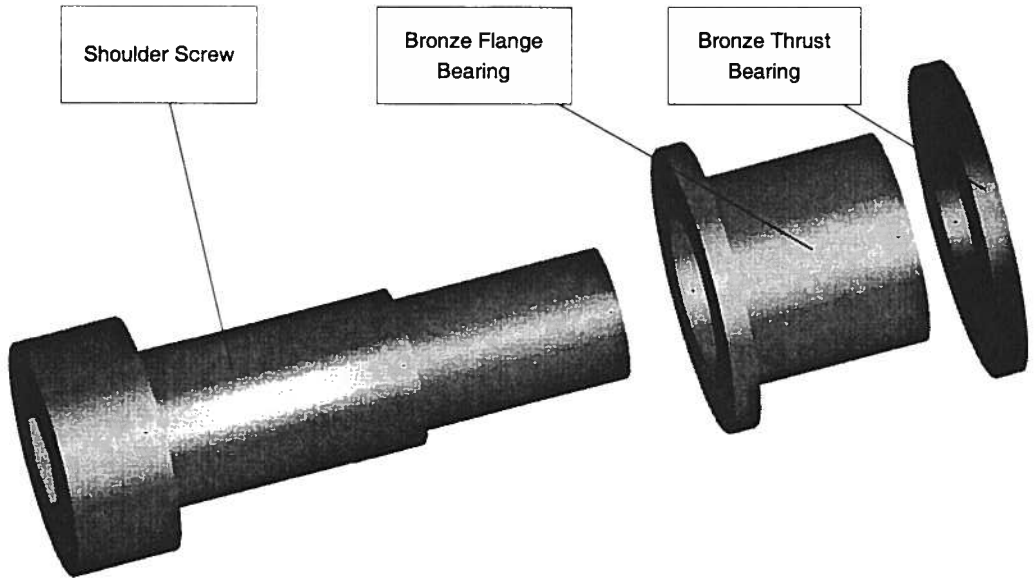

Figure 2.21 - Revolute Joint Components Exploded View

2.3.3 Rocker Link Design

The rocker links provided the connection between the ground link and the coupler link of the four bar mechanism. Each rocker link had two parallel bars and a perpendicular bar that connected the two parallel bars. With the small joint clearances and the large spacing of the parallel bars, the design allowed for only negligible out of plane motion.

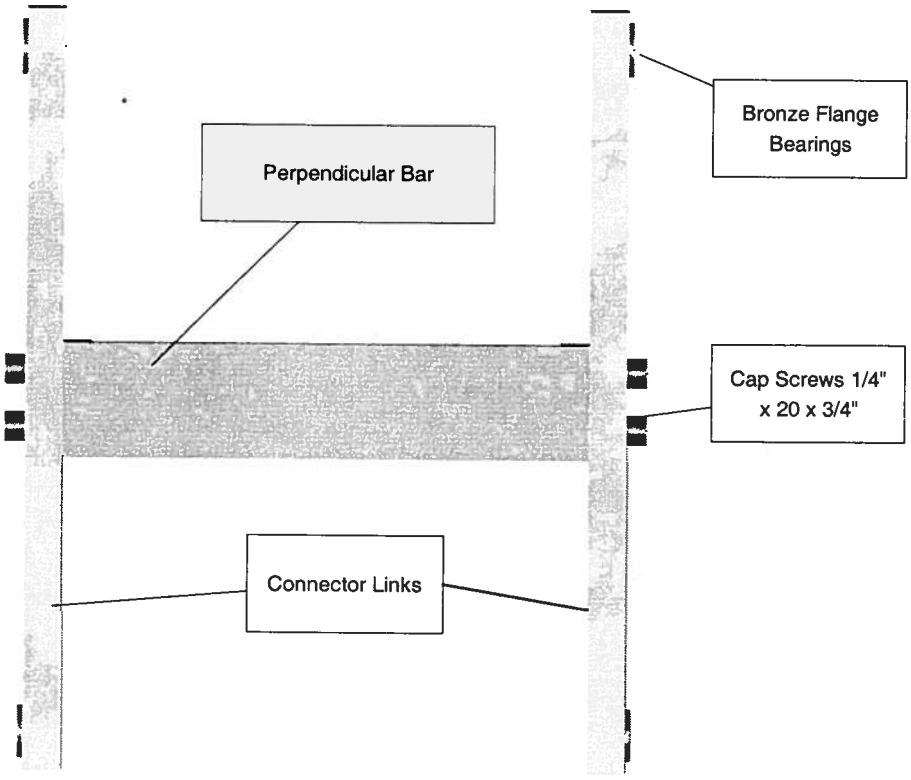

Figure 2.22 - Rocker Link

2.3.4 Coupler Design

The coupler link provided support for the nozzle and acts as the coupling link in the four bar mechanism. To fulfill these functions the coupler was designed as a rectangular plate that could provide a mounting surface for the nozzle elbow bracket and connection points at the plate's corners for the joints of the four bar mechanism.

The coupler provided support for the nozzle with an elbow bracket mounted to the top of the coupler with the use of socket cap screws. The nozzle aimed down through a square opening of the coupler. The nozzle was centered and in line with the rotary axis of the end effecter when the coupler was aligned parallel to the ground.

The coupler provided mounting surfaces at the four corners of the coupler to accommodate the joints of the four bar mechanism. The spacing between opposing joints helped to reduce the extent of possible out of plane motion by the four bar mechanism. Out of plane motion would decrease the accuracy of the paint system.

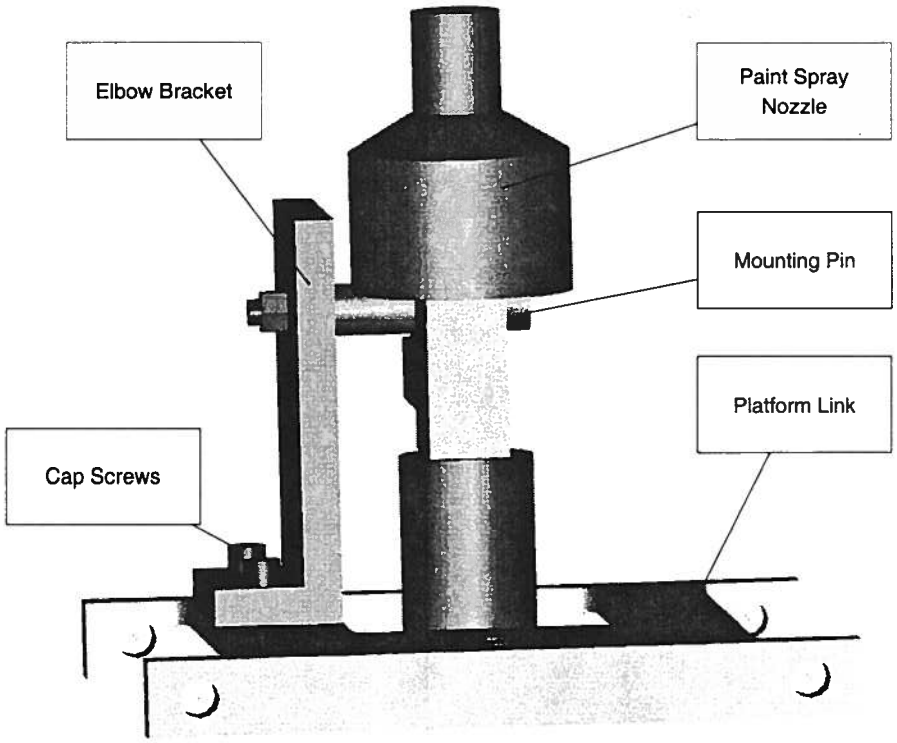

Figure 2.23 - Coupler Design

2.3.5 Yoke Design

The yoke provided the connection between the coupler and the ball screw. To accomplish the task, the yoke must provide mounting surfaces for both the coupler and the trunnion attached to the ball nut.

The yoke was rigidly attached to the coupler with the use of an elbow bracket. Socket cap screws secured the yoke to the coupler and assure a rigid connection.

To accommodate the small vertical translation inherent in the approximate straight-line motion, a ball end joint was used to couple the ball nut and the yoke. The ball end joint could accommodate the small vertical translation because it was offset from the center of rotation of the ball nut. As the coupler and ball nut moved, the ball end joint allowed the ball nut to rotate as needed to accommodate the small vertical translation in the coupler motion. The rotation of the ball nut could accommodate the small vertical translation of the yoke while not placing loads on the ball screw that could cause the ball screw to bind. A HDPE sleeve bearing provides the bearing surface between the trunnion and the ball end joint.

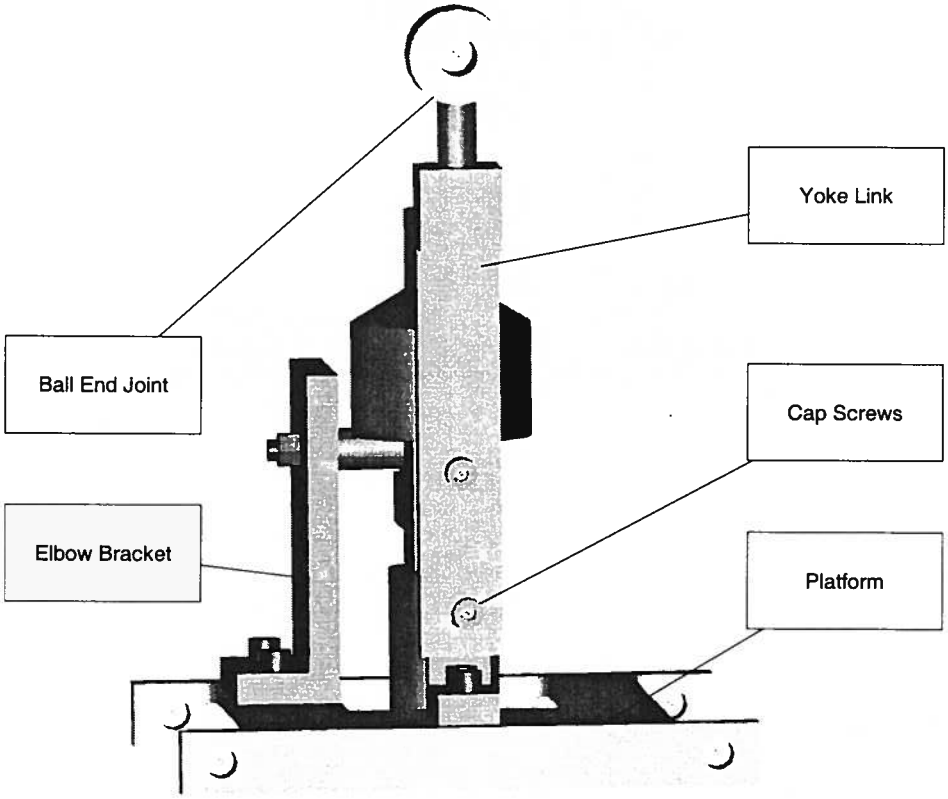

Figure 2.24 - Yoke Design with Coupler

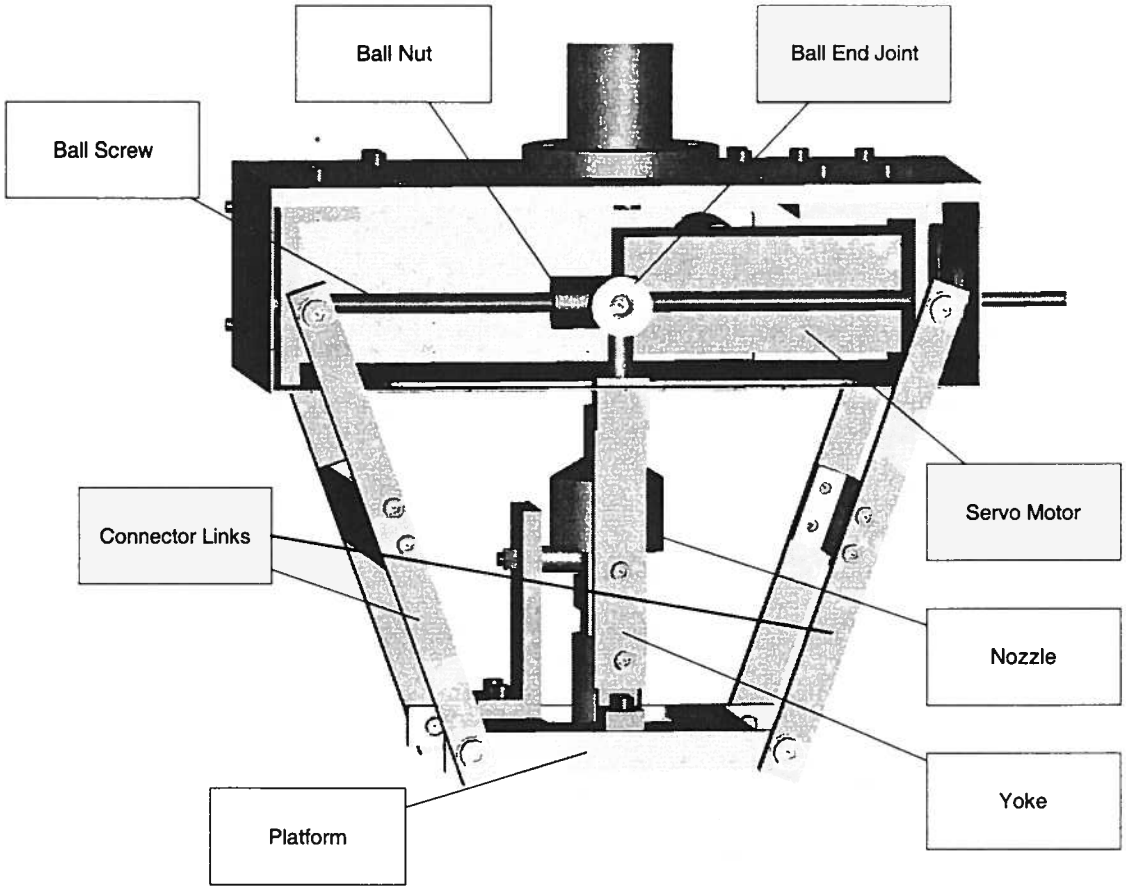

Figure 2.25 - Yoke Design with Spray Gun Orientation Mechanism

CHAPTER 3: YAW ROTATION JOINT DESIGN

The yaw rotation joint controlled the orientation of the spray gun's spray pattern in relation to the direction of motion of the robotic arm. Section 3.1 describes the development of the concept design of the yaw rotation joint. Section 3.2 lists the specifications for this joint and the components selected to fulfill these requirements. Section 3.3 describes the structural members designed to accommodate the chosen components and to provide support for the tilt mechanism.

3.1 Yaw Rotation Joint Concept Design

Because of the spray gun's rectangular fan pattern, the orientation of the paint gun relative to the motion of the robotic arm was important to painting an accurate roadway marking. The function of the yaw rotation joint was to maintain control of the orientation of the spray gun in relation to the direction of motion of the robotic arm. To achieve this functionality, the yaw rotation joint was based upon the previous concept design for the end effecter that employed an electric motor to turn a shaft that the tilt mechanism was mounted to. Because the previous yaw rotation joint design could not meet several performance targets and because of changes with the vertical extension joint, several improvements to the rotation joint's motor and structure were incorporated into the new design to improve the rotation joint's function.

3.2 Specifications and Selection of Components for the Yaw Rotation Joint

Based upon the path planning requirements of the robotic system, the yaw rotation joint must be capable of rotating the tilt mechanism at a maximum rate of 30° per second to maintain control of the orientation of the spray gun relative to the motion of the robotic arm.

The system should provide this performance with quick acceleration and minimal overshoot of the targeted rotation to assure accurate nozzle tip placement.

Ease of control and integration with the existing control hardware were also considered in the selection of components for the yaw rotation joint. The yaw rotation joint components should provide a simple control interface for the on board control computer.

Additionally, the yaw rotation joint needed to provide structural support for the tilt mechanism assembly to assure that the robotic system would be able to position and orientate the spray gun accurately within the desired painting region.

Figure 3.1 shows the rectangular paint pattern of the spray nozzle and its orientation relative to the paint spray line.

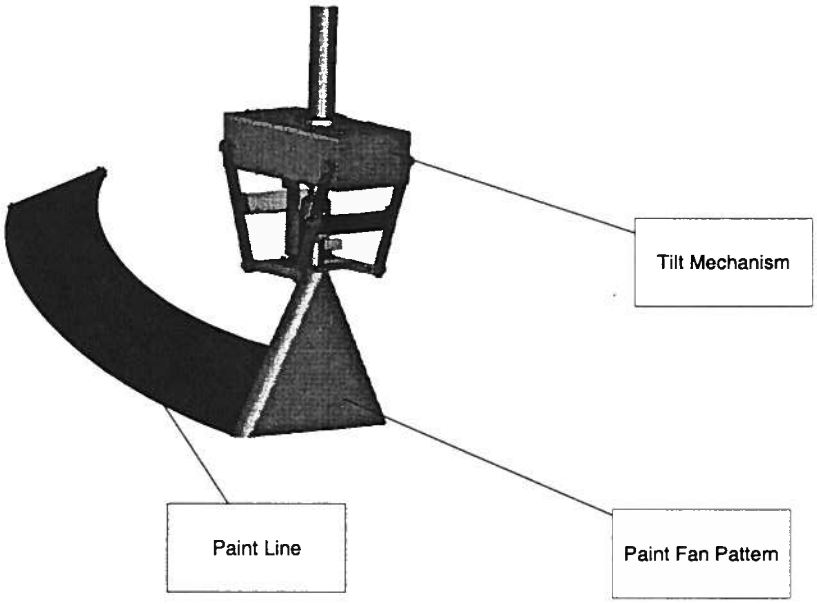

Figure 3.1 - Paint Fan Pattern

3.2.1 Torque Specifications for Yaw Rotation Joint Motor

Calculations for the torque specification for the yaw motor used several performance targets. The yaw rotation joint system should be able to create a 30°/s yaw rotation of the tilt mechanism with an acceleration time of 0.1 s to reach maximum speed during this move. From a CAD based simulation of the design of the tilt mechanism and cylinder, the tilt mechanism's inertia was estimated to be .138 kgm^2. With these assumptions and performance targets, the torque calculations using motion profile and equations found in Section 2.2.6 yielded a peak torque of 0.092 Nm [13 in-oz] for the actuator. To account for unknown forces from friction and cabling the calculated torque was tripled to reach a torque specification of 0.28 Nm [39 in-oz]. Appendix A includes calculations detailing the selection of a servo motor for the yaw rotation.

3.2.2 Gearbox vs. Pulley System

Another design decision involved the choice between a gearbox and a pulley system to transfer torque from the electric motor to the shaft upon which the tilt mechanism was mounted. Based upon the superior performance of the gearbox in regards to inertia matching, packaging size, and system compliance, a planetary gearbox was chosen to provide the transfer of torque between the motor and the shaft.

Inertia matching involved matching the motor's rotor inertia to that of the load's inertia. Close matching helped to assure stable system behavior. Gearing down the motor through the use of a pulley system or gearbox would reduce the apparent load's inertia felt by the motor. A comparison of available motors indicated that a 10:1 reduction would provide a reduced load inertia to motor rotor inertia ratio of 75:1. Manufacturer specification recommended an inertia ratio of 10:1 for high-speed applications. Although the design's

inertia ratio was higher than recommended, it would not impact performance because of the low motor speeds.

The gearbox and pulley systems' sizes also influenced the design decision between the gearbox and pulley system. For a large gear reduction, a pulley system would be large. A planetary gearbox would provide a more compact packaging solution because of its inline configuration of the shafts.

Consideration of the angular positioning compliance provided additional guidance in the selection of the planetary gearbox. Positioning compliance would reduce the accuracy of the paint line pattern by causing the paint pattern to overshoot or undershoot the desired orientation of the paint nozzle. The belt and pulley system would have much more compliance than the gearbox system due to the elastic nature of the belt.

3.2.3 Selection of a Servo Gear Motor

A review of motor specifications of available servomotors indicated a Compumotor SM231 AE servomotor with encoder feedback and a 10:1 planetary gearbox would adequately actuate the yaw rotation of the end effecter. The servomotor can provide 0.43 Nm [61 in-oz] of continuous input torque of and 1.28 Nm [181 in-oz] of peak input torque. Because of the low rotational speed of the tilt mechanism of the end effecter, a 10:1 gear reduction would not cause the servomotor to exceed its maximum rated speed.

The SM231 AE servomotor was favored over other servomotors and gearbox combinations because of its integrated design of the gearbox and servomotor. The servomotor and gearbox integration reduced the overall length of the assembly by eliminating the need for a separate shaft coupling between the servomotor and gearbox.

Precision of the servomotor encoder system was evaluated to ensure adequate position sensitivity. The encoder feedback had 1000 points per revolution of the motor shaft. A 10:1 planetary gearbox increased the resolution to 10000 points per revolution on the output shaft. This level of resolution cannot be realized because of a 6 arc-minute of backlash within the gearbox. The design would yield an accurate rotational position of the tilt mechanism because the required positioning tolerance derived from the path planning of the previous design is ±1°. Appendix A shows how the position sensitivity was determined for these components.

A Gemini GV-L3E servo drive provided the current to the servomotor and received encoder feedback from the motor shaft. The servo drive received commands from an Intel Celeron PC installed on the BASR vehicle.

The servomotor was configured with an electrically activated brake to help the motor maintain position during periods of inactivity. The brake will prevent the motor from overheating by eliminating the need to charge the coils during periods of inactivity. The brake will receive commands from the servo drive.

3.2.4 Yaw Rotation Joint Shaft Coupler

A helical beam coupling connected the servomotor shaft to the yaw rotation shaft. The helical beam coupling will allow for slight angular and positional misalignment between the servomotor shaft and the yaw rotation shaft. By allowing for the slight misalignment of the shafts, loading on the shaft support bearings will be reduced. The helical beam coupling was favored over other coupling designs because of its low cost, high torsional rigidity, and mechanical simplicity.

3.3 Detail Design of the Yaw Rotation Joint

The detail design of the rotation joint involved the design of a platform, a cylinder and shaft. The platform served as the interface plate between the pillow block bearings and the carriages of the vertical extension joint. The cylinder and shaft interfaced the pillow block bearings, gear motor, and tilt mechanism. The design of these members emphasized ease of manufacture and structural strength.

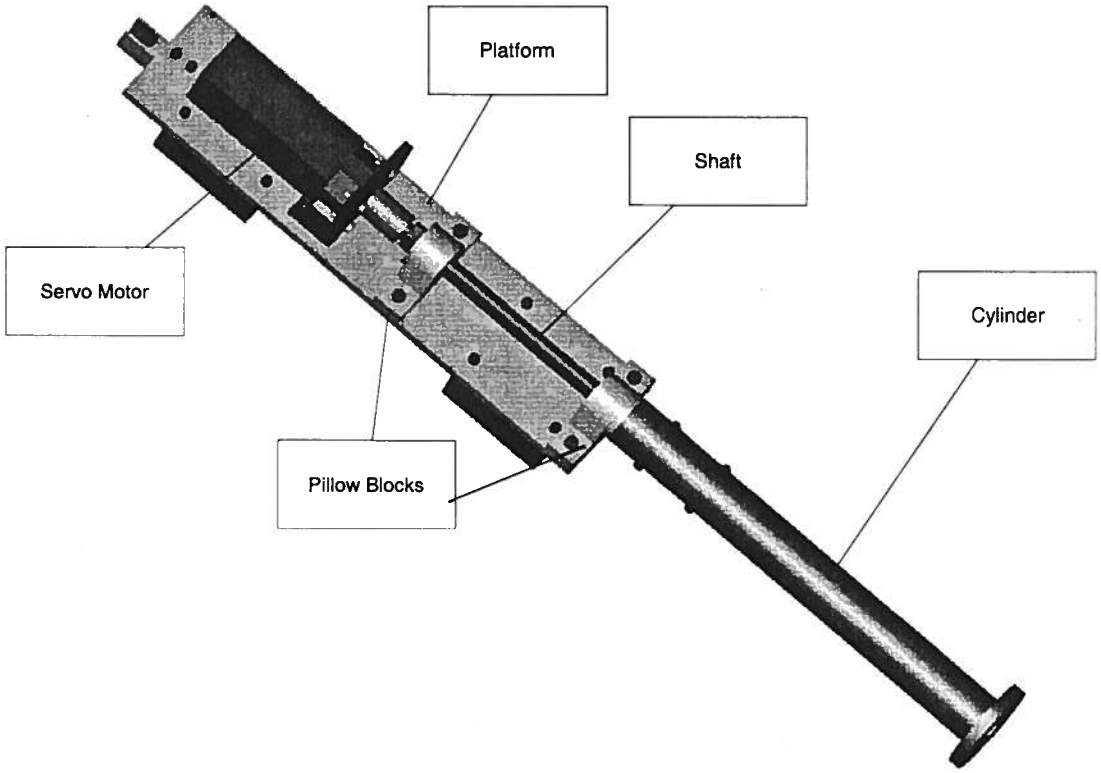

Figure 3.2 - Yaw Rotation Joint

3.3.1 Shaft Assembly

The shaft met the design needs of transmitting the motor torque to the tilt mechanism and securing the tilt mechanism to the end effecter to endure loads due to gravity and accelerations of the robotic arm.

A close tolerance clearance fit between the pillow block bearings and the shaft assured a secure fit of the shaft. The top of the shaft was threaded to allow a nut to be tightened to secure the lateral position of the shaft within the pillow blocks. Flats on the shaft surface allowed for the pillow block bearings' set screws to be tightened to prevent shaft slip within the bearings.

The top of the shaft was designed to fit the helical beam coupling.

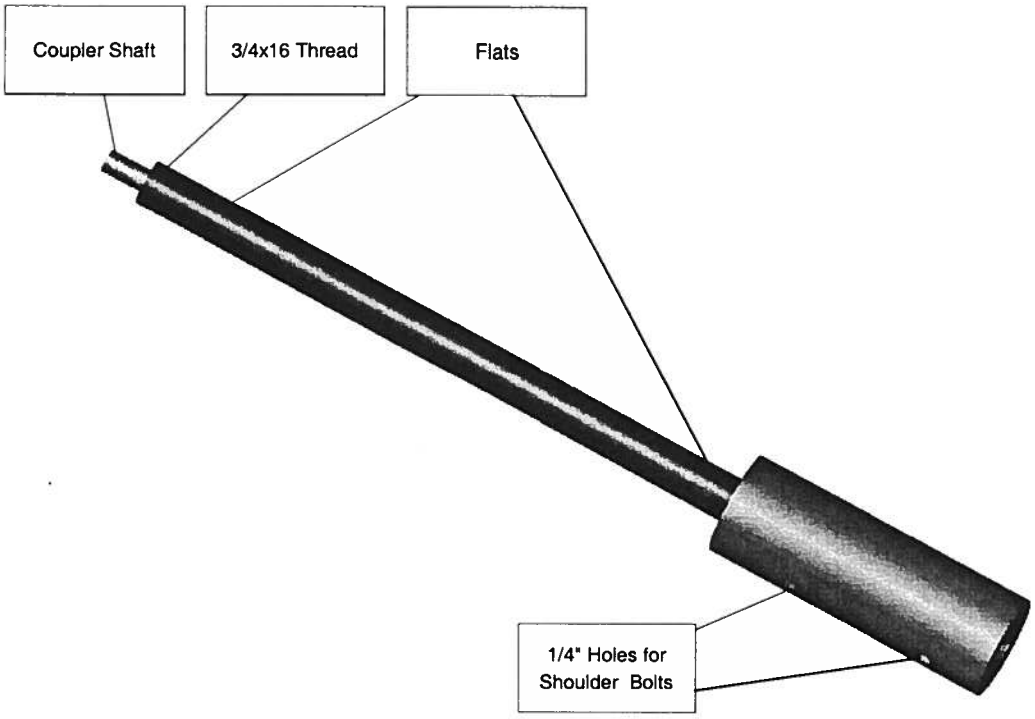

Figure 3.3 – Yaw Rotation Shaft

Two bearing pillow blocks provide support for the thrust and axial loading from yaw rotation shaft. A separation of .254 m [10"] of the bearing pillow block assemblies provided precise alignment of the shaft. The small loads on the bearings allowed for the use of deep groove Conrad style ball bearings. Fafnir SAS 0.019 m [¾"] pillow blocks will provide

adequate support for the thrust and axial loads and ample resistance to environmental contaminants.

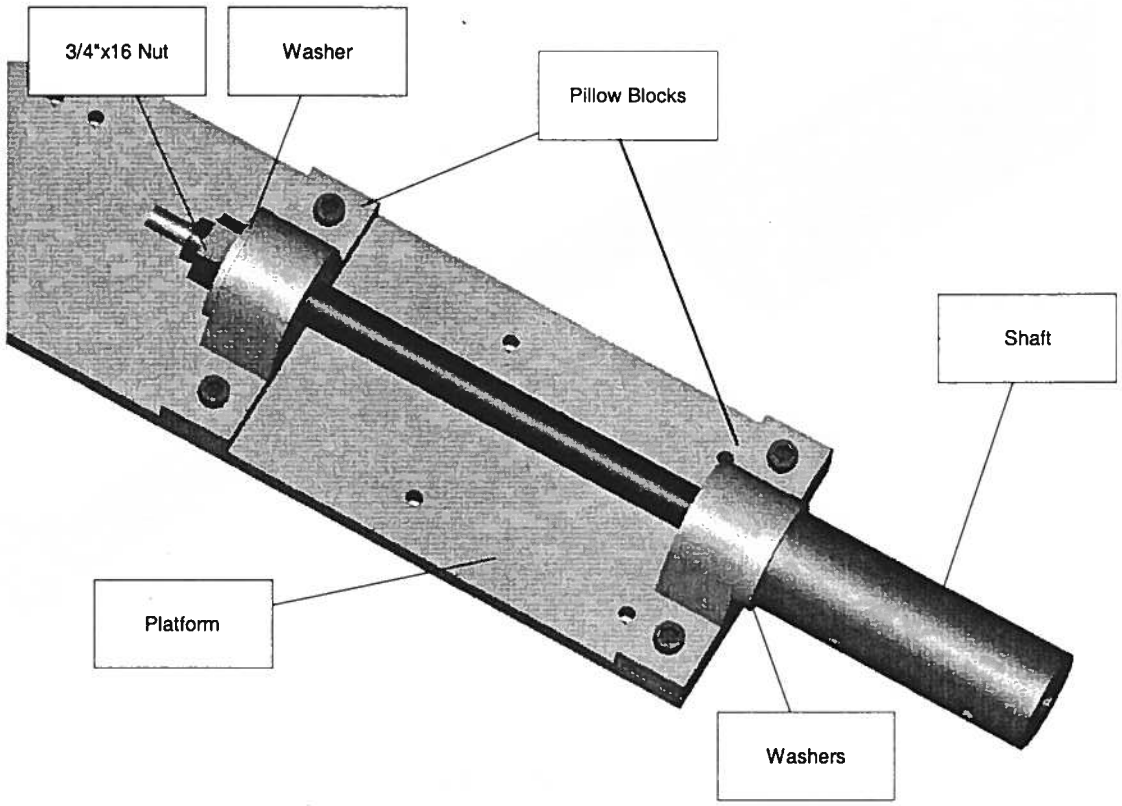

Figure 3.4 - Shaft Assembly

3.3.2 Cylinder

The cylinder design incorporated the need to provide a mounting interface between the shaft and cylinder and between the cylinder and the tilt mechanism. Additionally, its length spanned the distance between the bottom of the robot and the paint position of the nozzle above the ground.

The cylinder and shaft were assembled through a close tolerance clearance fit between the inside diameter of the cylinder and the outside diameter of the shaft. Two shoulder bolts hold the cylinder and shaft securely together.

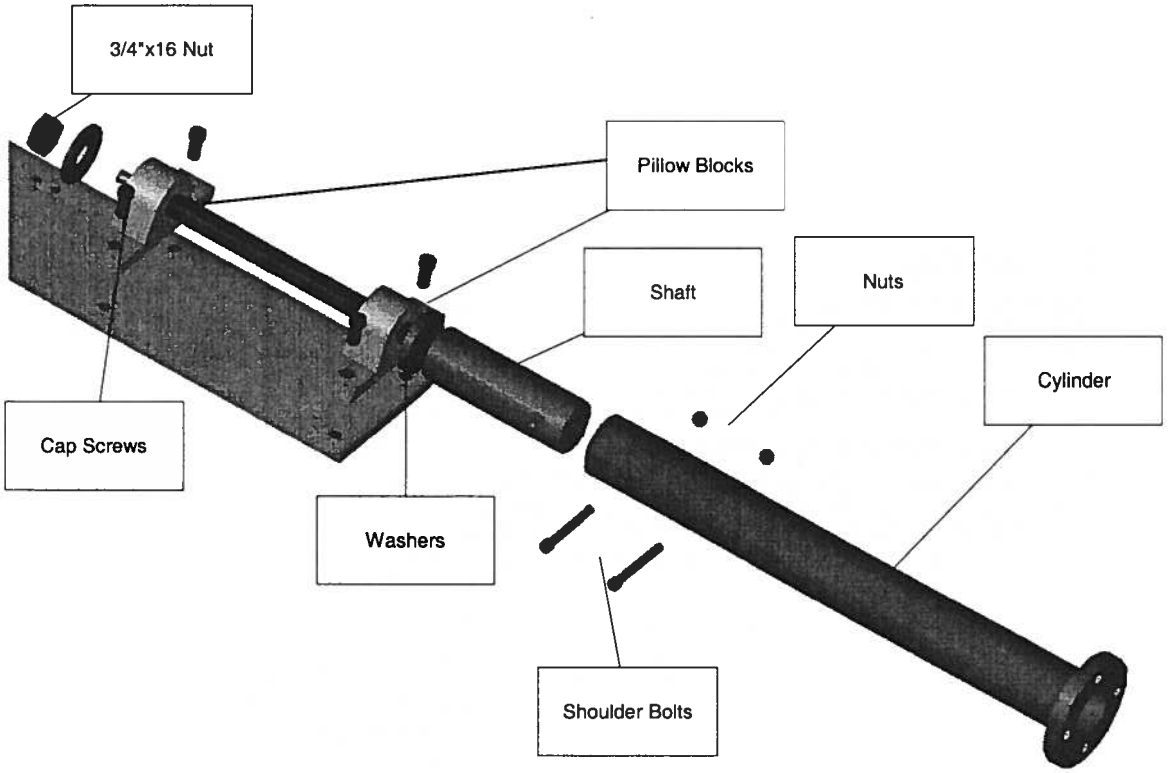

Figure 3.5 - Cylinder Shaft Assembly

To mount to the tilt mechanism, the cylinder was designed with a circular bolt bracket welded to the cylinder's base. Four cap screws fasten the cylinder and tilt mechanism together.

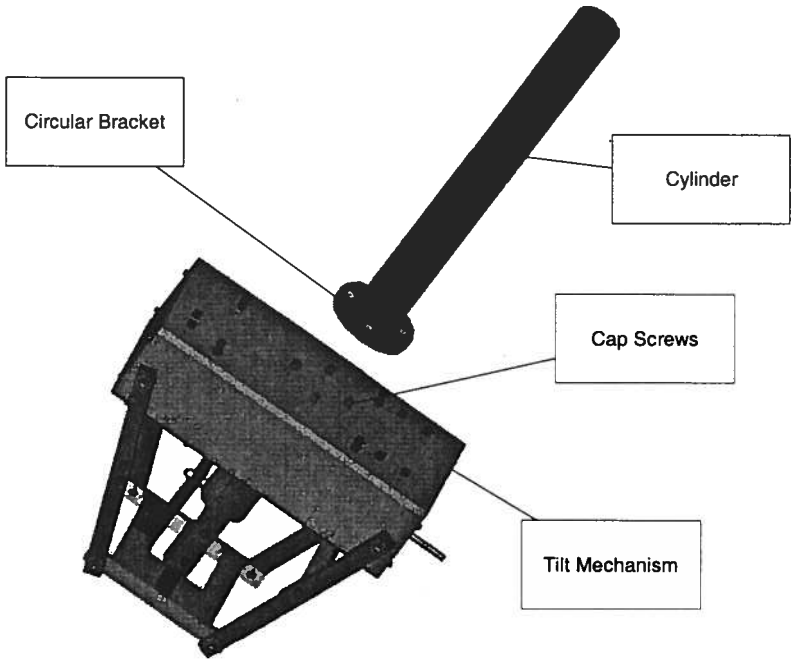

Figure 3.6 - Tilt Mechanism/Cylinder Interface

The location of the robotic arm also necessitated that the cylinder span 0.30 m [12"] to properly position the spray gun above the ground. To assure accurate positioning of the spray gun deflection calculations were performed to size the cylinder to ensure adequate rigidity. Through these calculations shown in Appendix A, a inside diameter of 0.0445 m [1.75"] and an outside diameter of 0.0508 m [2"] were chosen for the cylinder design.

3.3.3 Platform

The platform acted to provide an interface between the servo motor mount, bearing pillow blocks, and the carriages of the extension joint rail system. A rectangular aluminum plate was selected and sized to create a mounting surface for these components.

3.3.4 Servomotor Mount Assembly

An elbow bracket supported the servomotor and acted as an interface between the servomotor and platform. The servomotor was held to the elbow bracket with the use of four cap screws and nuts and washers. Four cap screws secured the elbow bracket and servomotor to the platform.

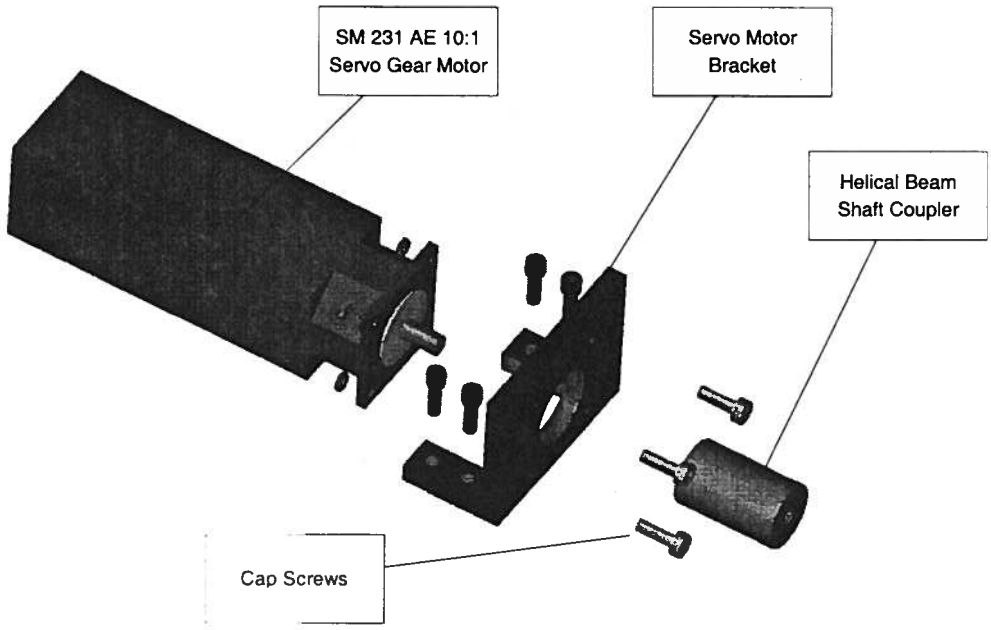

Figure 3.7 - Servo Gear Motor Assembly

CHAPTER 4: VERTICAL EXTENSION JOINT DESIGN

The vertical extension joint provided precise vertical positioning of the nozzle tip above the ground to control paint line thickness, and compensate for unwanted vertical motion of the nozzle tip caused by the tilt motion of the spray gun orientation mechanism and vibrations and deflections of the robotic arm. Section 4.1 describes the general concept of the design. Section 4.2 describes the required specifications and component selection. Section 4.3 details the design of several structural components.

4.1 Concept Design of Vertical Extension Joint

The vertical extension joint must maintain precise control over both the spray gun orientation mechanism's vertical position and its orientation while accurately measuring the relative vertical position of the spray gun orientation mechanism. The joint should be strong enough to resist loads and large enough to provide mounting surfaces for both the components of the yaw rotation joint and the robot arm. To meet these specifications, a rail carriage system was proposed where the carriage would carry the spray gun orientation mechanism and yaw rotation joint while riding upon a rail system. The rail system would allow the carriage to translate vertically and would maintain the alignment of the spray gun orientation mechanism with the robotic arm. An actuator would supply force to lift and lower the carriage.

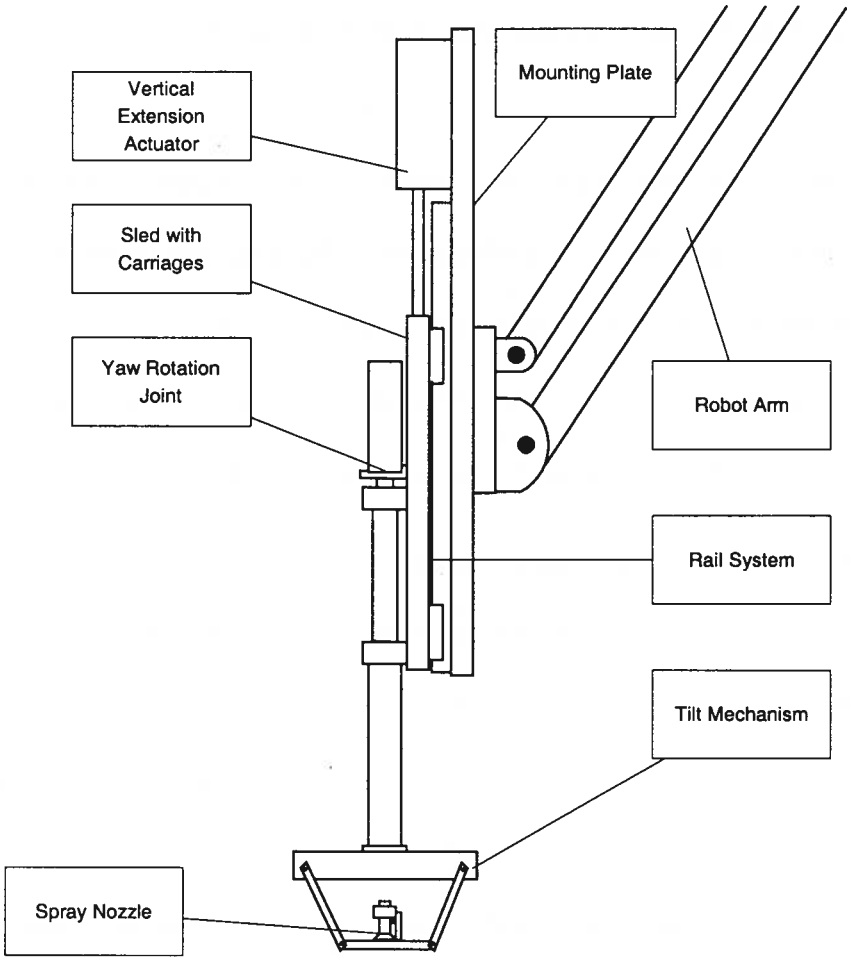

Figure 4.1 - Concept Design for Vertical Extension Joint

4.2 Vertical Extension Joint Component Specifications and Selection

The specifications for the vertical extension joint must be met to provide the trajectory of the spray gun to paint the roadway markings. The specifications were generated in response to the anticipated operation environment of the robot end effecter.

The vertical extension joint should have a vertical stroke of 0.254 m [10"] to accommodate the positioning needs of the nozzle tip according to the path planning requirements.

Force specifications for the actuator resulted from a need to compensate for vibrations of the robotic arm. The actuator should be able to correct for positioning errors caused by vibrations of 10 Hz and amplitude of 0.013 m [.5"]. Additionally, the force system should provide easy integration with existing control and power systems aboard the BASR truck.

The vertical extension joint design should also incorporate components that provide a simple means of sending vertical positional feedback about the location of the spray gun orientation mechanism to the onboard control computer. The positional feedback system should be rugged to operate in hostile outdoor environmental conditions.

4.2.1 Comparison of Actuation Methods for Vertical Extension

The previous design had incorporated a hydraulic actuator to supply force for actuating the vertical extension joint. The system performed less than adequately due to flaws in its positioning feedback system. The previous vertical extension design was reexamined to determine the necessary improvements to meet specifications derived from the path planning requirements. To accomplish this goal, ball screw and hydraulic actuation methods were examined to determine the possible advantages of each.

4.2.1.1 Ball Screw Actuation Method

A ball screw actuation method was considered due to the ease of feedback control. The rotation of the ball screw could be used to calculate the platform's translation and would be easy to measure since a rotary encoder could be mounted directly to the ball screw shaft. The encoder feedback could provide positional feedback to the control computer easily.

Torque calculations as shown in Appendix A were used to size the ball screw and servo motor system. Analysis of the loading conditions indicated that the rejection of robot arm vibrations would provide the largest torque demand on the servomotor. Therefore this

loading case was considered in the selection of a servomotor to power the proposed ball screw system. Torque calculations revealed that a required torque of 2.12 Nm [300 oz-in] was necessary to provide the motion to reject the expected vibrations of the robot arm. Inspection of manufacturer's servomotor specifications showed a Compumotor SM34 motor with a GV-U6E drive was required to meet this torque specification. A GV-U6E would require a 240VAC bus that would add additional complexity and expense to supply on a mobile platform such as a truck since only a 120VAC bus was currently available on the truck at the time of the analysis.

Torque Calculations [6]

$$T_{total} = T_{friction} + T_{acc} + T_{gravity}$$

$$T_{acc} = \frac{[\frac{J_{load}}{e} + J_{screw} + J_{motor}] \bullet \frac{\varpi_{screw}}{m_G}}{t_a}$$

$$T_{gravity} = \frac{M_{load} \bullet a_{gravity} \bullet p_{screw} \bullet m_G}{2\pi}$$

$$T_{friction} = estimated$$

where

$$J_{load} = \frac{M_{load} \bullet p_{screw}^2 \bullet m_G^2}{2\pi^2}$$

$$J_{screw} = \frac{\pi \bullet l \bullet \rho \bullet r^4 \bullet m_G^2}{2}$$

m_G = Gear Ratio
l = length of ball screw
r = radius of ball screw
ρ = density of ball screw
p_{screw} = pitch of ball screw

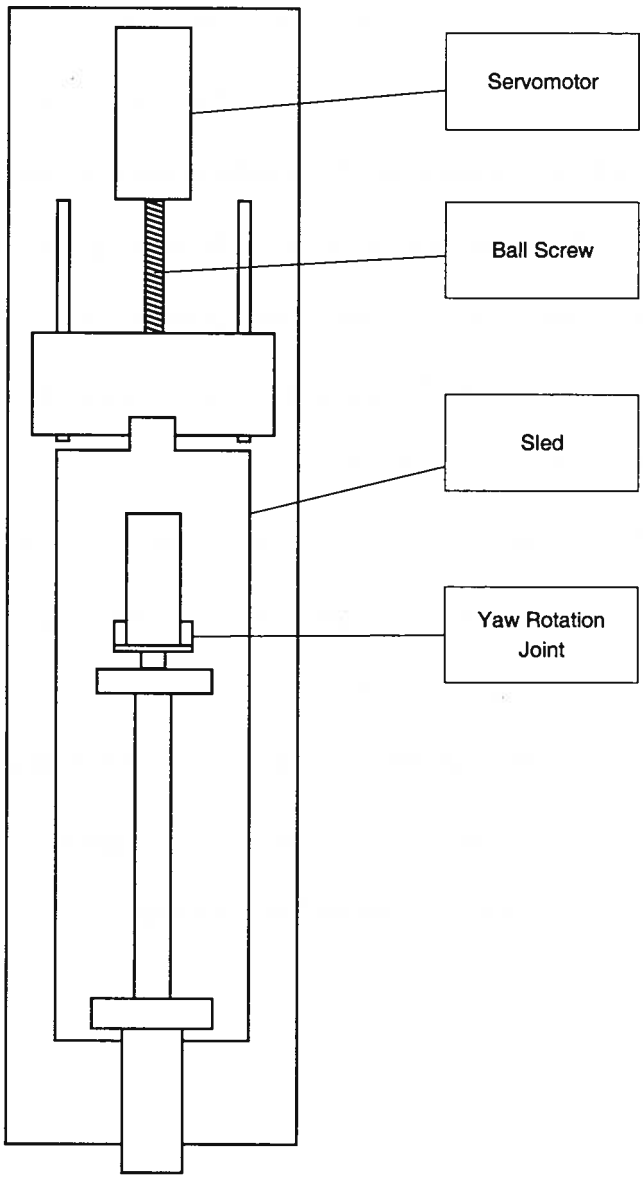

Figure 4.2 - Ball Screw Actuation Method

4.2.1.2 Hydraulic Actuation Method

The other design option for actuation of the vertical extension joint was to use the previous design's hydraulic actuator. To meet the system performance requirements, the hydraulic actuator must be able to correct for disturbances caused by vibrations in the arm

and provide the necessary travel to position the arm at the correct height above the roadway. Calculations and experimental work from the previous design showed the hydraulic actuator was capable of providing the necessary force to actuate the joint for the previous design.

The force needed to counteract the accelerations from vibrations within the arm was calculated assuming the same vibrations as in the ball screw specification phase. With a necessary acceleration of 24 m/s^2 and an estimated system mass of 35 kg, the required force of 840 N was within the $1.949*10^4$ N force ability of the Rexroth MS2 hydraulic actuator [1]. These calculations are shown in Appendix A.

The nozzle tip trajectory calculated from the path planning indicated that a 0.254 m [10"] stroke length would adequately position the nozzle tip above the roadway for all painting conditions encountered for roadway letter stenciling. The proposed design shared many similarities to the previous design. Because of the similarities the existing actuator should perform well if a new means of providing vertical position feedback is available. The use of existing hardware would also reduce the cost of modifications for this project.

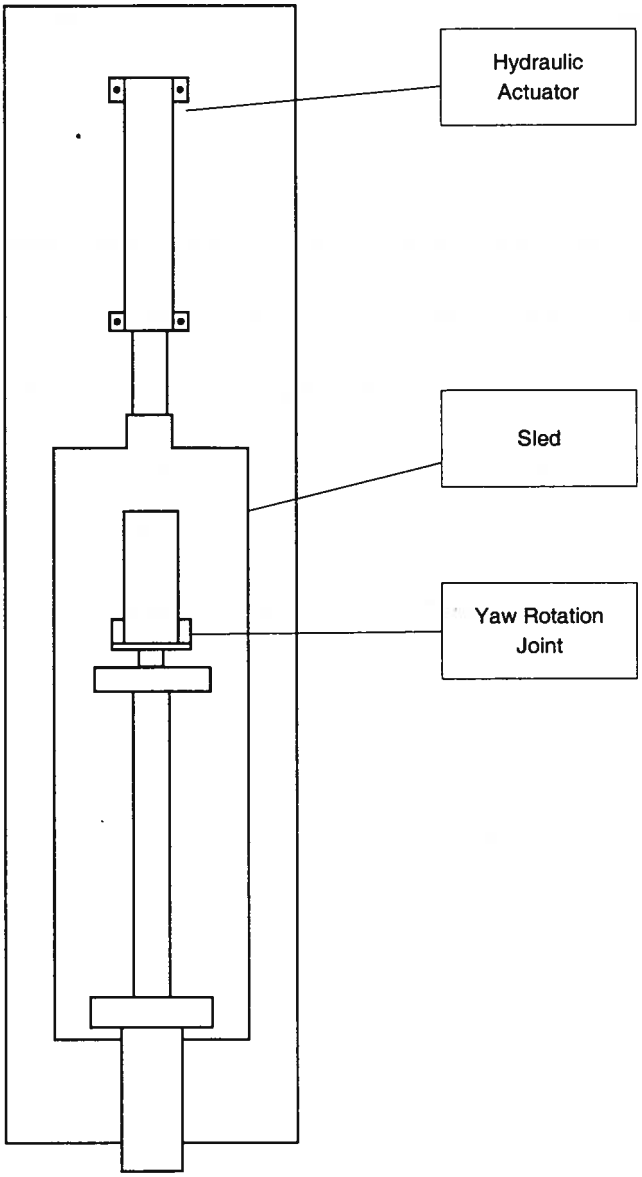

Figure 4.3 - Hydraulic Actuation Method

4.2.2 Cable Extension Transducer

The previous design used a rack and pinion system with encoder feedback to provide measurement of relative position of the vertical extension of the hydraulic actuator on the end effecter. The rotation of the pinion was transferred to the encoder shaft through a gear train. The resulting backlash from the use of a gear train introduced positioning errors that often

caused the previous design to vacillate as the end effecter moved up and down seeking the command position.

To improve the control of the hydraulic actuator a Celesco cable extension transducer would provide relative position information. The cable extension transducer measured translation through the extension and retraction of a cable. The cable's extension caused a shaft with a rotary encoder to turn. By attaching the cable to the moving sled, the encoder fed the sled's positional information to an Intel Celeron PC that was coordinating the motion of the robot. For this application a Celesco PT8150 cable extension transducer with a 0.635 m [25"] stroke range was chosen. The PT8150 had a resolution of 0.00013 m [.005"] and an accuracy of 0.00051 m [.02"]. The PT8150 could withstand hostile weather and vibration environments. Because the cable transducer was capable of highly accurate position sensing of the hydraulic actuator, the vertical translation joint should perform its motion without vacillation.

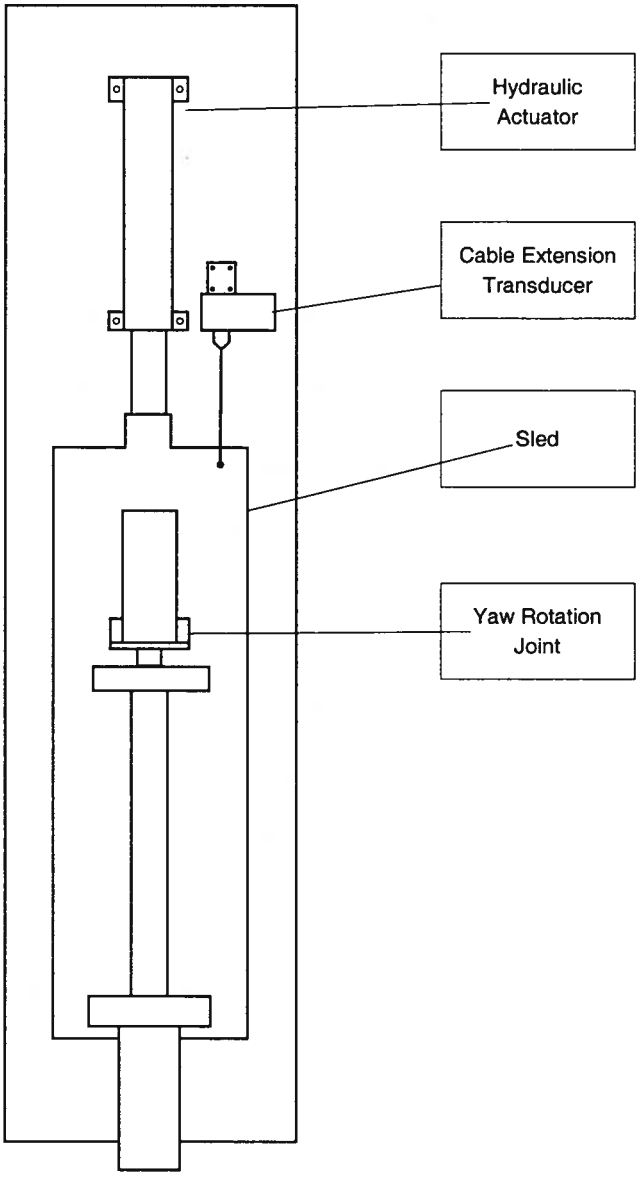

Figure 4.4 - Vertical Extension Joint with Cable Extension Transducer

4.2.3 Rail and Carriage System

The vertical extension joint's rail system accurately guided the vertical translation of the yaw rotation joint and spray gun orientation mechanism. To maintain control over the end effecter orientation the rail carriage system components were chosen based upon their ability to resist the expected moments about the extension axis. The use of two carriages allowed

the system to resist moments about axis perpendicular to the extension axis. Moment calculations as shown in Appendix A revealed that the assumed maximum side load on the spray gun orientation mechanism would not exceed the maximum load rating of the carriage bearings.

To resist contamination and rust, the carriages employed flouronyliner bearings. The flouronyliner feature a low friction journal type-sliding surface. The flouronyliner bearings will have a superior life over standard ball bearings because of the elimination of the moving parts susepetical to jamming from environmental debris. The flouronyliner bearings will also are resistant to rust and corrosion.

4.3 Vertical Extension Joint Structural Design

Several structural components serve as mounting interfaces for the components of the vertical extension joint. The connector bracket serves as the connection between the hydraulic actuator and the platform that the yaw rotation is mounted to. The cable extension transducer mount provides a mounting surface for the cable extension transducer. Finally, a rectangular plate provides the mounting surface for the components of the extension joint as well as a mounting surface to the robot arm.

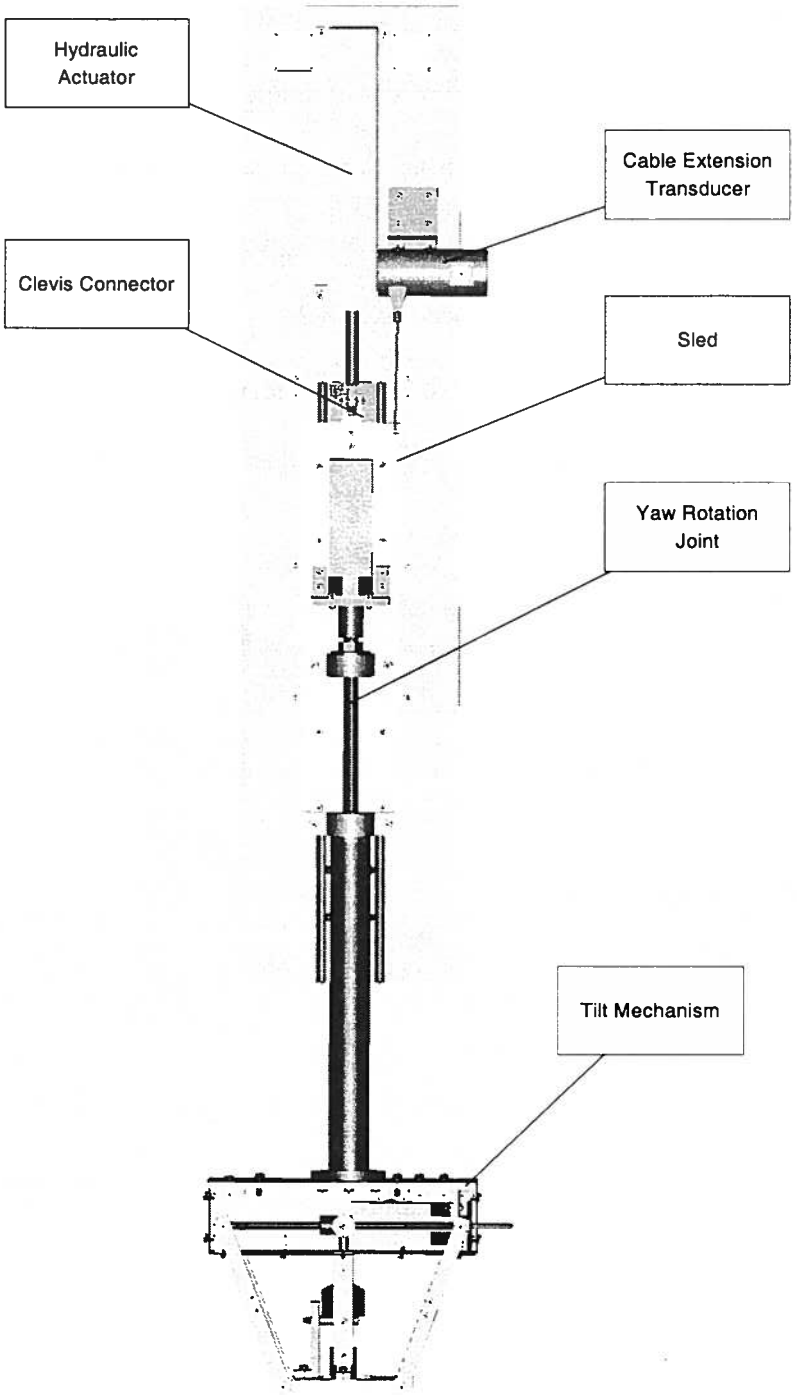

Figure 4.5 - Vertical Extension Joint Detail Design

4.3.1 Clevis Bracket and Clevis Pin

The clevis bracket connected the hydraulic actuator with the sled of the vertical extension joint. Because the piston of the hydraulic actuator would travel between the rails of the rail system, special considerations were taken to assure fit within these tight confines. The bracket mounts to the hydraulic actuator with a clevis pin. The clevis pin was held into the clevis bracket by two low head cap screws. The low head cap screws allowed for additional clearance of the rail system. Shear tearout calculations were performed to assure an adequate margin of safety to protect against failure. These calculation are shown in Appendix A.

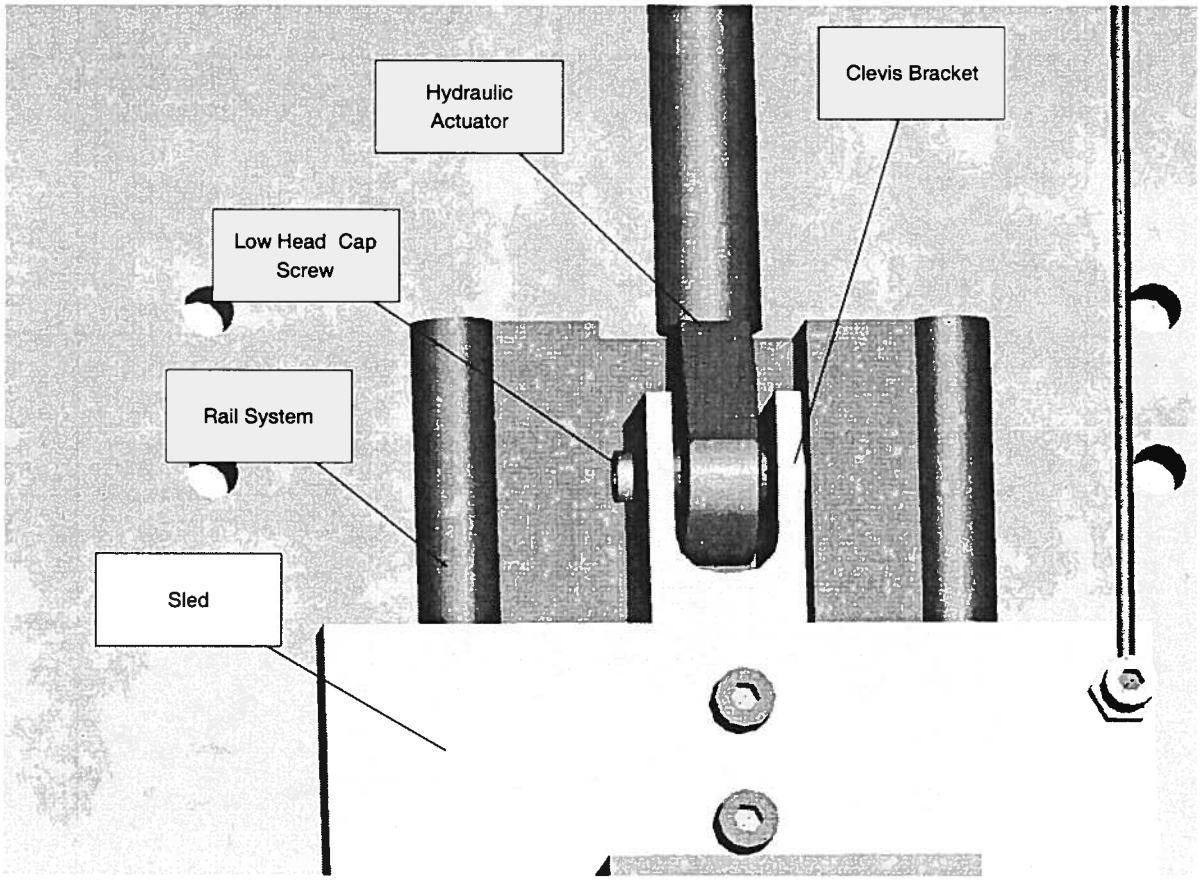

Figure 4.6 - Clevis Connector Design Detail

4.3.2 Cable Extension Transducer Mount

The cable extension transducer mount provided a mounting surface for the cable transducer. The mount was needed to rotate the transducer 90° to align the cable extension transducer's cable output with the motion of the sled.

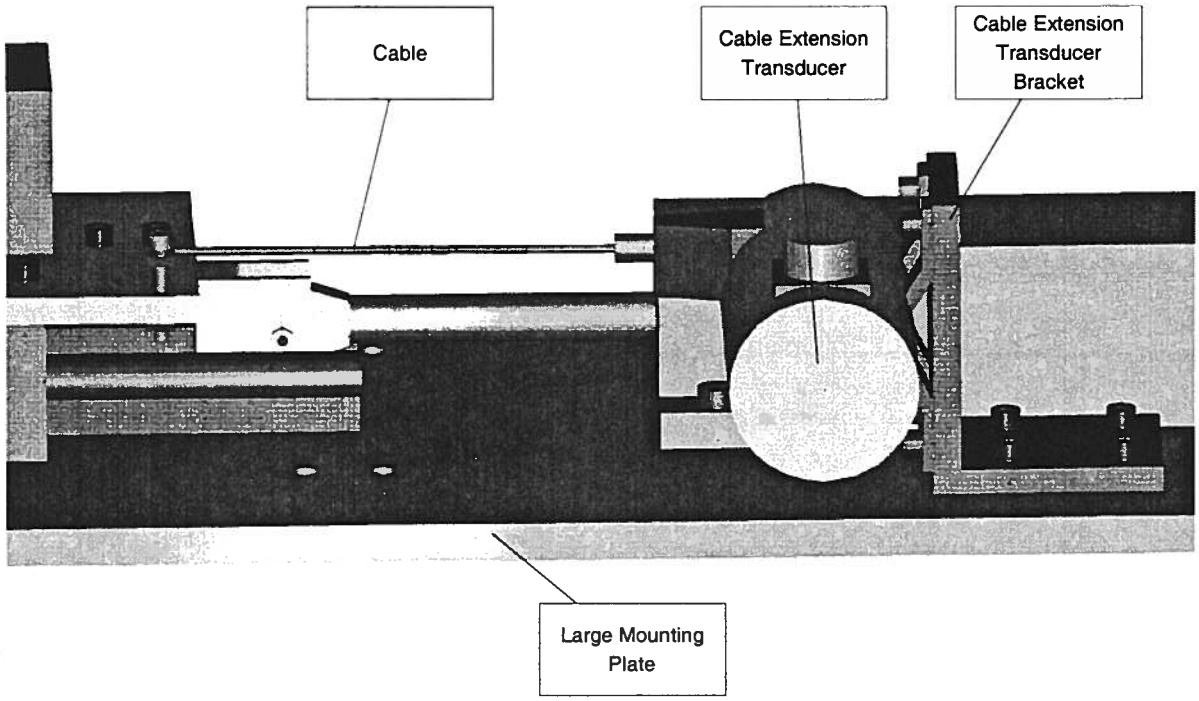

4.3.3 Large Mounting Plate

The large mounting plate provides a mounting surface for the components of the vertical extension joint and for connections to the robot arm.

CHAPTER 5: CONCLUSIONS AND RECOMMENDATIONS

5.1 Conclusions

The design of an end effecter tilt mechanism and its integration into the BASR end effecter design formed the basis of this thesis. A major design constraint was to not use a rotary actuator to achieve the tilting motion of the spray gun. An innovative design based on a four bar linkage was developed where a translatory motion was used to produce the necessary tilt motion. The actuation was performed using a ball screw mechanism. Additional modifications to the design were incorporated to improve end effecter performance and assure compatibility with other design changes.

The four bar mechanism supplied the orientation to control the paint distribution of the paint gun. The tilt motion allowed the paint distribution to remain acceptably constant even when the arm must paint letters containing sharp curves. The four bar mechanism provided a robust and easy to control tilt motion while maintaining a compact and light design. A servomotor with encoder feedback actuated the mechanism.

To provide for orientation control around the yaw axis of the end effecter, a rotation joint actuated by a servo gear motor was designed. The joint featured easy control and integration with existing hardware and simplicity in design.

A rail and carriage system actuated by a hydraulic cylinder controlled the spray gun's height off of the ground. A cable extension transducer provided position feedback.

5.2 Recommendations

Several improvements to the mechanical design of the end effecter could further increase performance of the end effecter by removing excess weight and reducing the complexity of assembly and cost of fabrication.

Since the arm was mounted to the bed of a Caltrans maintenance truck and the position of the paint gun during painting was between 0.3 m and 0.6 m [1' and 2'] off the ground, a substantial amount of structure was needed to span the distance between the base of the robot arm and the painting region. Substantial weight savings could be realized if the arm were mounted to a trailer or to low bed truck to eliminate this unnecessary height off of the roadway.

The design of the four bar mechanism added additional weight to the robot arm. Weight at the end of the arm decreases the arm's performance because of the increased arm's inertia. Further work could be done to simplify the mechanical design of the four bar mechanism to consolidate the functions of the mechanism onto fewer parts. Additionally, the overall size of the four bar mechanism could be minimized to reduce unwanted nozzle tip translations during tilt reorientations of the nozzle.

If a 240 VDC electric bus becomes available on a future design of the BASR the hydraulic actuator controlling the vertical extension of the end effecter should be replaced with a ball screw system. The substitution of a ball screw for hydraulic actuator would reduce the weight of the end effecter while also eliminating the need to run hydraulic supply lines to the end effecter.

BIBLIOGRAPHY

[1] McGrew, Richard A., *A Robotic End-Effector for Roadway Stenciling,* Masters Thesis, UC Davis, Ca., 1996.

[2] http://www.ahmct.ucdavis.edu/other/mark.htm

[3] http://www.appliedautonomy.com

[4] Molian, S., *Mechanism Design: The Practical Kinematics and Dynamics of Machinery 2nd ed.*, Elsevier Science, Kidlington, Oxford, UK, New York, NY, 1997.

[5] Erdman, A.G., Sandor, G.N., *Mechanism Design Analysis and Synthesis Vol I 2nd ed.*, Prentice Hall, Englewood Cliffs, N.J., 1991.

[6] Thomson, *Thomson Advanced Linear Motion Systems*, Thomson Industries, Port Washington, NY, 1990.

[7] Norton, Robert L. *Machine Design*, Prentice Hall, Upper Saddle River, N.J., 1998.

APPENDIX A: ENGINEERING CALCULATIONS

TABLE OF CONTENTS

Ball Screw Torque and Angular Velocity Calculations

Torque and angular velocity calculations were performed to define technical specifications for the servo motor system to power the tilt mechanism. Parameters were defined from path planning requirements and from the design characteristics of tilt mechanism assembly.

Assumptions:

Load on ball screw modeled as a linear slide pushing a 15 kg mass.

Angular motion of load neglected due to small angular velocity. Angular kinetic energy of platform and links is small.

Friction forces and forces from cabling neglected due to uncertainty of size. Sizing of motor by multiplying top calculated torque by 3.

Parameters:

g : Acceleration of Gravity : $9.8 m/s^2$
p : Ball Screw Pitch : $0.003175 m/rev$
l : Ball Screw Length : $0.445m$
r : Ball Screw Radius : $0.0048m$
ρ : Density of Steel : $7800 \text{ kg}/m^3$
I_m : Inertia of Motor Rotor : $1.80 \text{x} 10^{-5} \ kg/m^3$
m_l : Mass of Load : $15kg$
h : Height Load Raised : $0.01m$
d : Horizontal Distance Travel : $0.0107m$
t_t : Total Time of Move : $1s$
t_a : Time of Acceleration : $0.02s$
e : Effiency of Ball Screw : 0.9
m_G : Gear Ratio : 1.1 : 1

Calculations:

$$I_{ballscrew} = \frac{\pi \cdot l \cdot r^4}{2} = 2.8x10^{-6}\ kg/m^3$$

$$I_{load} = \frac{m_l \cdot p^2}{2 \cdot \pi^2} = 7.7x10^{-5}\ kg/m^3$$

$$V_{nut} = \frac{2 \cdot l}{2 \cdot ((t_t - 2 \cdot t_a) + 2 \cdot t_a)} = 0.11 m/s$$

$$\varpi_{ballscrew} = \frac{V_{nut}}{p} = 218\, rad/s$$

$$\omega_{motor} = \frac{w_{ballscrew}}{m_G} = 198\, rad/s$$

$$I_{reglectedballscrew} = p^2 \cdot I_{ballscrew} = 3.4x10^{-6} kg/m^2$$

$$I_{reflectedload} = p^2 \cdot I_{load} = 9.3x10^{-6}\ kg/m^2$$

$$T_a = \frac{(\frac{I_{reflectedload}}{p} + I_{reflectedballscrew} + I_{motor})}{\omega_{motor} / t_a} = 0.32\ Nm$$

Tilt Position Resolution Calculation:

Tilt position resolution calculation was performed to assure adequate resolution of tilt motor encoder. Tilt mechanism parameter was taken from linear regression of calculated horizontal position of connection point and tilt position of the platform of the 4 bar linkage.

Assumptions:

No backlash present

Parameters:

e_r : Encoder Resolution : 1000 pts/rev

p : Ball Screw Pitch : $0.0032 m/rev$

m_T : Tilt Mechanism Parameter : 137 °/in

m_G : Gear Ratio : 1.1 : 1

Calculations:

$$\text{Tilt Resolution}=\frac{p \cdot m_T}{m_G \cdot e_r} = .0005° / rev$$

Gear Tooth Bending Stress Calculation

These calculations were performed to assure adequate life of the gear train under anticipated loading by examining the bending stress.

Assumptions:

Transmitted torque assumed to be maximum torque servomotor capable of generating.

Parameters:

T : torque : $11.3lb-in$
p_d : diametrical pitch : 32
N : # of teeth : 84
J : AGMA bending geometry factor : 0.4
F: Face Width : 0.187
K_v : Dynamic Factor : 0.75

Calculations:

Tangential Force: $W_t = \frac{2 \cdot p_d \cdot T}{N} = 8.6lb$

Bending Stress: $\sigma_b = \frac{W_t \cdot p_d}{K_v \cdot F \cdot J} = 4910 psi$

Gear Tooth Surface Stress Calculation:

These calculations were performed to assure adequate life of the gear train under anticipated loading by examining the bending stress.

Assumptions:

Transmitted torque assumed to be maximum torque servomotor capable of generating.

Parameters:

T : torque : $11.3lb-in$

p_d : diametrical pitch : 32

N : # of teeth : 84

J : AGMA bending geometry factor : 0.4

F: Face Width : 0.187

C_v : Dynamic Factor : 0.75

ϕ : Pressure Angle : $0.349rad$

d_p : Pinion diameter

C : Center distance : $2.875in$

C_p : Elastic Coefficient = 2300

Calculations:

Tangential Force: $W_t = \frac{2 \cdot p_d \cdot T}{N} = 8.6lb$

Curvature of Pinion: $\rho_p = \sqrt{(r_p + \frac{1}{p_d})^2 - (r_p \cos\phi)^2} - \frac{\pi}{p_d}\cos\phi = .48$

Curvature of Gear: $\rho_g = C\sin\phi - \rho_p = .49$

Surface Geometry Factor: $I = \frac{\cos\phi}{\left(\frac{1}{\rho_g} + \frac{1}{\rho_g}\right) \cdot d_p} = .0803$

Surface Stress: $\sigma_c = C_p\sqrt{\frac{W_t}{F \cdot I \cdot d_p \cdot C_v}} = 36600psi$

Torque for Yaw Rotation Servo Gear Motor Calculation:

Torque calculation performed to find torque specification for yaw rotation servo gear motor. Moment of Inertia of Tilt motor found from CAD simulation of design.

Assumptions:

No friction

Parameters:

I_m : Inertia of Motor Rotor : $1.80\text{x}10^{-5}\ kg/m^3$

t_t : Total Time of Move : $1s$

t_a : Time of Acceleration : $0.1s$

I_{tilt} : Inertia of Tilt Mechanism : $1.38\text{x}10^{-2}\ kg/m^3$

θ : Angular Step : $0.528rad$

m_G : Gear Ratio : 0.1

Calculations:

$$\omega_{shaft} = \frac{2 \cdot \theta}{2 \cdot ((t_t - 2 \cdot t_a) + 2 \cdot t_a)} = 0.698 rad/s$$

$$I_{reflectedtilt} = m_G^2 \cdot I_{tilt} = .00138 kg/m^3$$

$$\omega_{motor} = m_G \cdot \omega_{shaft} = 6.98 rad/s$$

$$\alpha_{motor} = \frac{\omega_{motor}}{t_a} = 68 rad/s^2$$

$$T_{motor} = \alpha_{motor} \cdot (I_{reflectedtilt} + I_{motor}) = 0.099\ Nm$$

Yaw Rotation Position Resolution Calculation:

Yaw rotation position resolution calculation was performed to assure adequate resolution of yaw rotation motor encoder.

Assumptions:

No backlash present

Parameters:

e_r : Encoder Resolution : $1000\ pts/rev$

m_G : Gear Ratio : 10 : 1

Calculations:

$$\text{Yaw Rotation Resolution} = \frac{e_r}{m_G} = 10000\, pts / rev$$

Cylinder Design Calculation:

Calculation performed to assure adequate strength of structural member.

Assumptions:

Cylinder modeled as a cantilever beam.

Deflection small.

Uniform isotropic material.

Uniform cross section.

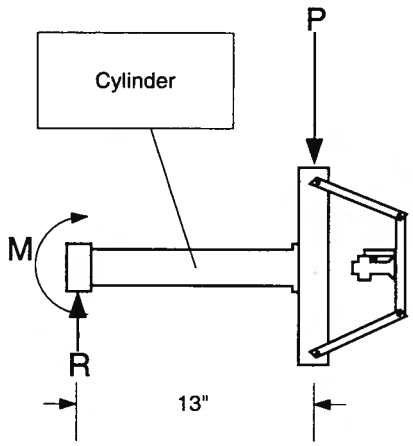

Parameters:

id : inside diameter of Cylinder : $0.0445m$ [1.75"]

od : outside diameter of Cylinder : $0.0508\, m$ [2"]

p : loading on cylinder : $450\, N$ [$100lb$]

l : Length of Cylinder : $0.33\, m$ [13"]

c : distance to outer fiber of cylinder : $0.0254\, m$ [1"]

Calculations:

Moment at base of Cylinder $M = l \cdot p = 149Nm$

Moment of Inertia of Cylinder $I = \frac{\pi \cdot \left(od^4 - id^4\right)}{64} = .134 \cdot 10^{-9} m^4$

Bending Beam Stress $\sigma_l = \frac{M \cdot c}{I} = 28MPa$

Vertical Actuator Ball Screw Torque Calculation:

Calculations performed to find technical specifications for servo motor selection for the vertical extension joint.

Assumptions:

Friction forces neglected.

Parameters:

m_G = Gear Ratio = 3 : 1

l : length of ball screw : $0.254m$

r : radius of ball screw : $0.0127m$

ρ : density of ball screw : $7800kg/m^3$

I_m : Polar Moment of Inertia : $2x10^{-5} kg/m^2$

m_l : mass of load : $30kg$

h : height load raised : $0.0127m$

t_t : total time of move : $0.06s$

t_a : efficiency of ball screw : 0.9

g : acceleration of gravity : $9.8m/s^2$

Calculations:

$$I_{ballscrew} = \frac{\pi \cdot l \cdot r^4}{2} = 8.1x10^{-5}\ kg/m^3$$

$$I_{load} = \frac{m_l \cdot p^2}{2 \cdot \pi^2} = 9.8x10^{-4}\ kg/m^3$$

$$V_{nut} = \frac{2 \cdot l}{2 \cdot [(t_t - 2 \cdot t_a) + 2 \cdot t_a]} = 0.42\,m/s$$

$$\omega_{ballscrew} = \frac{V_{nut}}{p_{screw}} = 104 rad/s$$

$$\omega_{motor} = \frac{\omega_{ballscrew}}{m_G} = 314 rad/s$$

$$I_{reflectedballscrew} = p_{screw}^2 \cdot I_{ballscrew} = 9.0x10^{-6}\ kg/m^2$$

$$I_{refleectedload} = p_{screw}^2 \cdot I_{load} = 1.1x10^{-4}\ kg/m^2$$

$$T_{acc} = \frac{\left(\frac{I_{reflectedload}}{e} + I_{screw} + I_{motor}\right) \cdot \frac{\omega_{screw}}{m_G}}{t_a} = 1.57 Nm\,[222 in-oz]$$

$$T_{gravity} = \frac{m_l \cdot g \cdot p_{screw} \cdot m_G}{2\pi} = 0.396 Nm\,[56.0 in-oz]$$

$$T_{friction} = estimated = 0.5 Nm\,[70 in-oz]$$

$$T_{total} = T_{friction} + T_{acc} + T_{gravity} = 2.5 Nm\,[350 in-oz]$$

Hydraulic Actuator Force Calculation

Calculations based upon previous end effecter design with new end effecter weight substituted into the mass of the load.

Assumptions:

Friction forces neglected.

Parameters:

$$m_{load} = 35kg$$

$$a_{load} = 24 m/s^2$$

Calculations:

$$F = m_{load} \cdot a_{load} = 840N$$

Moment and Force Calculations for Side Loading of Linear Slide Bearings [6]

Calculations performed to assure that the anticipated loading does not exceed manufacturer's specifications for maximum load given a set travel life length. Several loading situations were considered to find worst-case scenario.

Assumptions:

Load case assumed to be vertical application with simultaneous 100lb loads applied in directions shown in figure.

Solutions to load cases superimposed to find extreme load case.

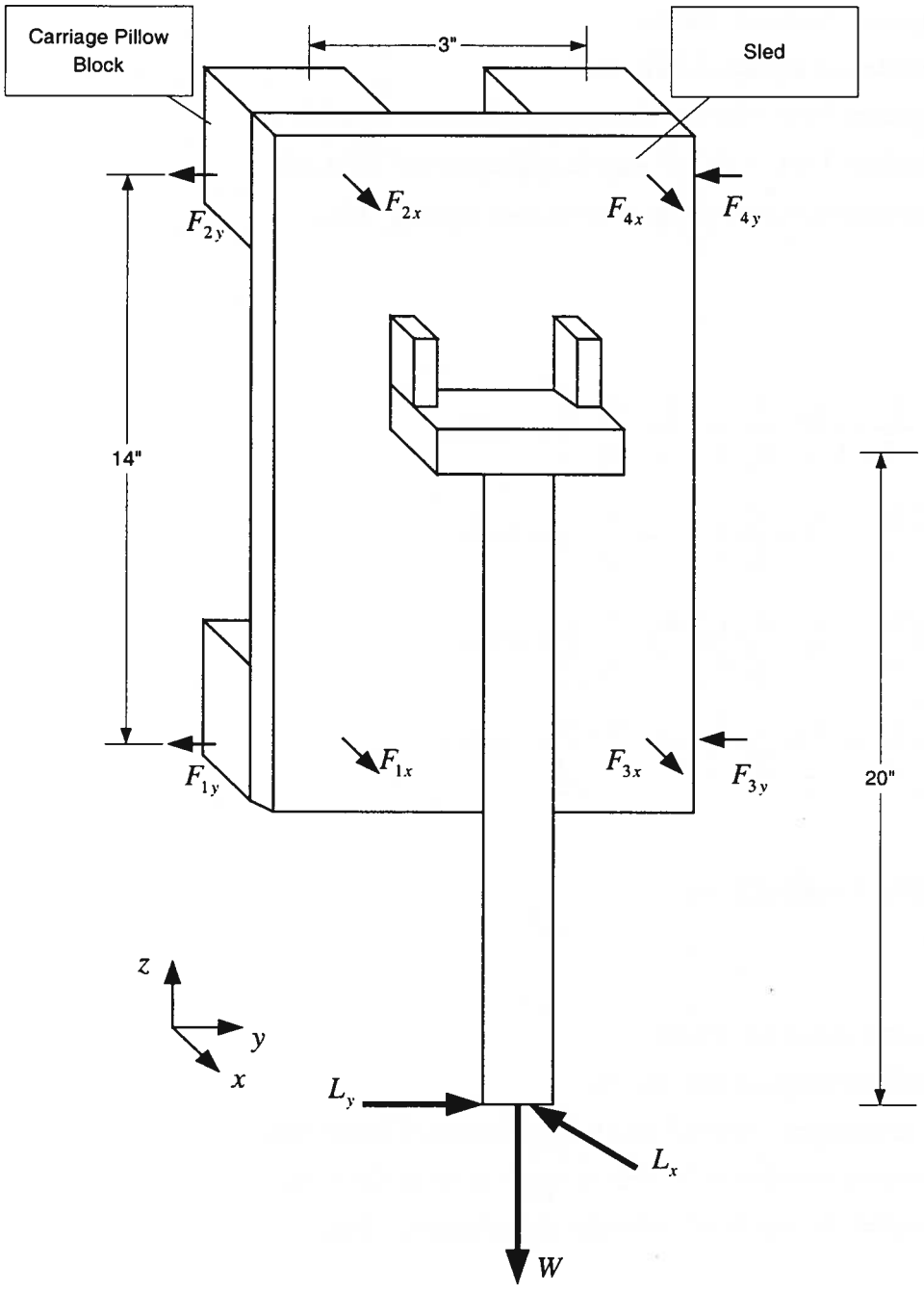

Calculation for L_x Loading Case

Parameters:

L_x : load in x direction : $100lbs$

d_1 : separation distance of rails : $3in$

d_z : z distance from center of sled to application of load : $20in$

d_y : y distance from center of sled to application of load : $0in$

d_0 : separation between pillowblocks along bearing : $14in$

Calculations:

$$F_{1x} = -\left[\frac{L_x}{4} + \left(\frac{L_x}{2}\cdot\frac{d_z}{d_0}\right) - \left(\frac{L_x}{2}\cdot\frac{d_y}{d_1}\right)\right] = -96lbs$$

$$F_{2x} = -\left[\frac{L_x}{4} - \left(\frac{L_x}{2}\cdot\frac{d_z}{d_0}\right) - \left(\frac{L_x}{2}\cdot\frac{d_y}{d_1}\right)\right] = 46lbs$$

$$F_{3x} = -\left[\frac{L_x}{4} - \left(\frac{L_x}{2}\cdot\frac{d_z}{d_0}\right) + \left(\frac{L_x}{2}\cdot\frac{d_y}{d_1}\right)\right] = 46lbs$$

$$F_{4x} = -\left[\frac{L_x}{4} + \left(\frac{L_x}{2}\cdot\frac{d_z}{d_0}\right) + \left(\frac{L_x}{2}\cdot\frac{d_y}{d_1}\right)\right] = -96lbs$$

Calculation for L_y Loading Case

Parameters:

L_y : load in y direction : $100lbs$

d_1 : separation distance of rails : $3in$

d_z : z distance from center of sled to application of load : $20in$

d_x : x distance from center of sled to application of load : $4in$

d_0 : separation between pillowblocks along bearing : $14in$

Calculations:

$$F_{1x} = F_{2x} = \left(\frac{L_y}{2} \cdot \frac{d_x}{d_1}\right) = 67lbs$$

$$F_{3x} = F_{4x} = -\left(\frac{L_y}{2} \cdot \frac{d_x}{d_1}\right) = -67lbs$$

$$F_{1y} = F_{4y} = -\left[\frac{L_y}{4} + \left(\frac{L_x}{2} \cdot \frac{d_z}{d_0}\right)\right] = -96lbs$$

$$F_{2y} = F_{3y} = \frac{L_y}{4} + \left(\frac{L_x}{2} \cdot \frac{d_z}{d_0}\right) = 96lbs$$

Calculation for Weight of End Effecter Loading Case

Parameters:

W : load in y direction : $80lbs$

d_1 : separation distance of rails : $3in$

d_y : y distance from center of sled to application of load : $0in$

d_x : x distance from center of sled to application of load : $4in$

d_0 : separation between pillowblocks along bearing : $14in$

Calculations:

$$F_{1x} = F_{4x} = \frac{W}{2} \cdot \frac{d_x}{d_0} = 11lbs$$

$$F_{2x} = F_{3x} = -\left[\frac{W}{2} \cdot \frac{d_x}{d_0}\right] = -11lbs$$

$$F_{1y} = F_{2y} = F_{3x} = F_{4x} = \frac{W}{2} \cdot \frac{d_y}{d_0} = 0lbs$$

Clevis Pin Shear Tearout Calculations [7]

Calculations performed to ensure that components were strong enough to perform under expected loading with suitable safety factors. Loads assumed based upon mass and expected accelerations of end effecter during use.

Assumptions:

Loading condition results from weight of mechanism

Uniform isotropic materials

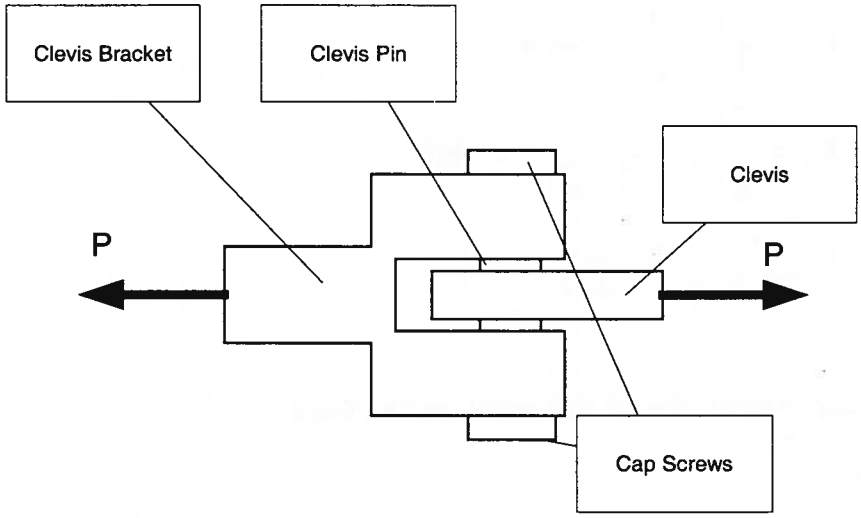

Parameters:

d_{cap} : diameter of #10 cap screw : $0.190in$

t : thickenss of clevis bracket side : $0.155in$

P : Load : $200lb$

h : distance from edge of hole to outside of part : $0.5in$

Calculations:

Direct Shear in # 10 Cap Screw

$$A_{shear} = \frac{\pi d^2}{4} = 0.0284in^2$$

$$\tau_{xy} = \frac{P}{A_{shear}} = 7000psi$$

Direct Bearing of Clevis Bracket

$$A_{shear} = t \cdot d_{cap} = .03in^2$$

$$\sigma = \frac{P}{A_{shear}} 6800psi$$

Tearout Failure for Clevis Bracket

$$A_{shear} = 2 \cdot (t \cdot h) = 0.0778in^2$$

$$\tau = 2600psi$$

APPENDIX B: ASSEMBLY AND DETAILED DRAWINGS

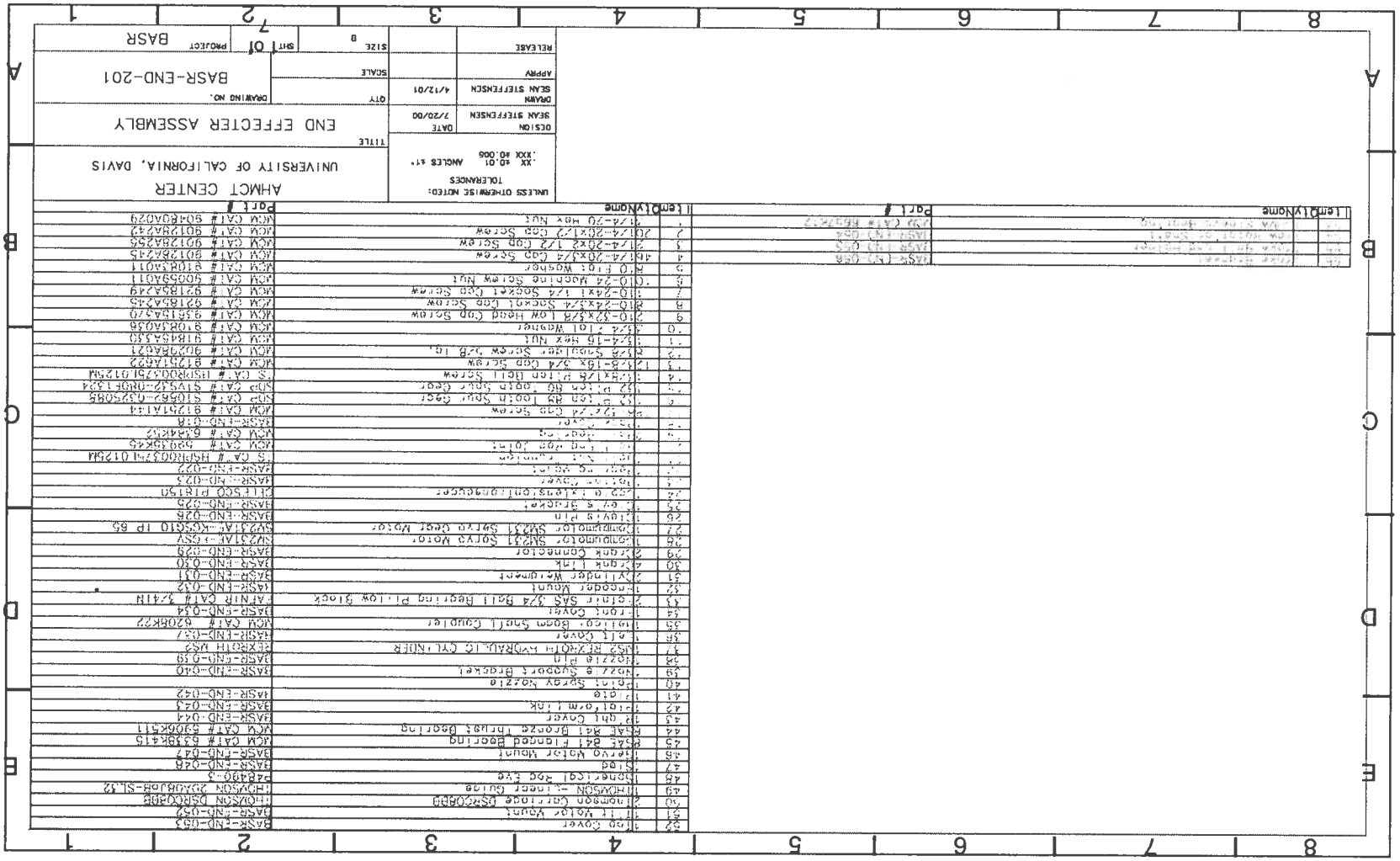

ITEM	QTY	NAME	PART #
1	1	Base Plate	BASR-END-001
2	1	Motor Mount	BASR-END-002
3	1	Motor Cover	BASR-END-003
4	1	Top Cover	BASR-END-004
5	1	Bottom Cover	BASR-END-005
6	1	Side Cover	BASR-END-006
7	1	Front Cover	BASR-END-007
8	1	Rear Cover	BASR-END-008
9	1	Motor Plate	BASR-END-009
10	1	Gear Plate	BASR-END-010
11	1	Gear Cover	BASR-END-011
12	1	Gear Plate	BASR-END-012
13	1	Gear Cover	BASR-END-013
14	1	Gear Plate	BASR-END-014
15	1	Gear Cover	BASR-END-015
16	1	Gear Plate	BASR-END-016
17	1	Gear Cover	BASR-END-017
18	1	Gear Plate	BASR-END-018
19	1	Gear Cover	BASR-END-019
20	1	Gear Plate	BASR-END-020
21	1	Gear Cover	BASR-END-021
22	1	Gear Plate	BASR-END-022
23	1	Gear Cover	BASR-END-023
24	1	Gear Plate	BASR-END-024
25	1	Gear Cover	BASR-END-025
26	1	Gear Plate	BASR-END-026
27	1	Gear Cover	BASR-END-027
28	1	Gear Plate	BASR-END-028
29	1	Gear Cover	BASR-END-029
30	1	Gear Plate	BASR-END-030
31	1	Gear Cover	BASR-END-031
32	1	Gear Plate	BASR-END-032
33	1	Gear Cover	BASR-END-033
34	1	Gear Plate	BASR-END-034
35	1	Gear Cover	BASR-END-035
36	1	Gear Plate	BASR-END-036
37	1	Gear Cover	BASR-END-037
38	1	Gear Plate	BASR-END-038
39	1	Gear Cover	BASR-END-039
40	1	Gear Plate	BASR-END-040
41	1	Gear Cover	BASR-END-041
42	1	Gear Plate	BASR-END-042
43	1	Gear Cover	BASR-END-043
44	1	Gear Plate	BASR-END-044
45	1	Gear Cover	BASR-END-045
46	1	Gear Plate	BASR-END-046
47	1	Gear Cover	BASR-END-047
48	1	Gear Plate	BASR-END-048
49	1	Gear Cover	BASR-END-049
50	1	Gear Plate	BASR-END-050
51	1	Gear Cover	BASR-END-051
52	1	Gear Plate	BASR-END-052

ITEM	QTY	NAME	PART #
1	1	Base Plate	BASR-END-001
2	1	Motor Mount	BASR-END-002
3	1	Motor Cover	BASR-END-003
4	4	1/4-20x1/2 Cap Screw	MCM CA1# 90128A245
5	1	M10 Flat Washer	MCM CA1# 810K340011
6	2	10-24 Machine Screw Nut	MCM CA1# 90059A011
7	1	10-24x1 1/4 Socket Cap Screw	MCM CA # 92185A249
8	2	10-24x3/4 Socket Cap Screw	MCM CA # 92185A245
9	2	10-32x3/8 Low Head Cap Screw	MCM CA1# 95515A470
10	1	1/4 Flat Washer	MCM CA1# 91025A050
11	1	1/4-18 Hex Nut	MCM CA1# 91845A530
12	1	5/16 Shoulder Screw 3/8 Lg.	MCM CA1# 90029A021
13	12	1/2-13x 3/4 Cap Screw	MCM CA1# 81251A622
14	1	3/8x1/8 Pilot Dell Screw	S CA1# HSMR0037M012SW
15	2	1/2 Plain Nu Solid Dowel	SDP CA1# S10A67-05Z50B5
16	2	1/2 Plain Hex Solid Dowel	SDP CA1# S1V542-08R0F1324
17	1	1/2-20 Cap Screw	MCM CA1# 81251A144
18	1	1/2x1/4 Cap Screw	MCM CA1# 81251A022
19	1	1/4-20 Hex Nut	MCM CA1# 90480A029
20	2	1/4-20x1/2 Cap Screw	MCM CA1# 90128A242
21	2	1/4-20x2 1/2 Cap Screw	MCM CA1# 90128A255
22	4	1/4-20x3/4 Cap Screw	MCM CA1# 90128A245
23	1	M10 Flat Washer	MCM CA1# 810K340011
24	2	10-24 Machine Screw Nut	MCM CA1# 90059A011
25	2	10-24x1 1/4 Socket Cap Screw	MCM CA # 92185A249
26	2	10-24x3/4 Socket Cap Screw	MCM CA # 92185A245
27	2	10-32x3/8 Low Head Cap Screw	MCM CA1# 95515A470
28	1	1/4 Flat Washer	MCM CA1# 91025A050
29	1	1/4-18 Hex Nut	MCM CA1# 91845A530
30	1	5/16 Shoulder Screw 3/8 Lg.	MCM CA1# 90029A021
31	12	1/2-13x 3/4 Cap Screw	MCM CA1# 81251A622
32	1	3/8x1/8 Pilot Dell Screw	S CA1# HSMR0037M012SW
33	2	1/2 Plain Nu Solid Dowel	SDP CA1# S10A67-05Z50B5
34	2	1/2 Plain Hex Solid Dowel	SDP CA1# S1V542-08R0F1324
35	1	1/2-20 Cap Screw	MCM CA1# 81251A144
36	1	1/2x1/4 Cap Screw	MCM CA1# 81251A022
37	1	1/4-18 Hex Nut	MCM CA1# 90480A029
38	2	1/4-20x1/2 Cap Screw	MCM CA1# 90128A242
39	2	1/4-20x2 1/2 Cap Screw	MCM CA1# 90128A255
40	4	1/4-20x3/4 Cap Screw	MCM CA1# 90128A245
41	1	M10 Flat Washer	MCM CA1# 810K340011
42	2	10-24 Machine Screw Nut	MCM CA1# 90059A011
43	2	10-24x1 1/4 Socket Cap Screw	MCM CA # 92185A249
44	2	10-24x3/4 Socket Cap Screw	MCM CA # 92185A245
45	2	10-32x3/8 Low Head Cap Screw	MCM CA1# 95515A470
46	1	1/4 Flat Washer	MCM CA1# 91025A050
47	1	1/4-18 Hex Nut	MCM CA1# 91845A530
48	1	5/16 Shoulder Screw 3/8 Lg.	MCM CA1# 90029A021
49	12	1/2-13x 3/4 Cap Screw	MCM CA1# 81251A622
50	1	3/8x1/8 Pilot Dell Screw	S CA1# HSMR0037M012SW
51	2	1/2 Plain Nu Solid Dowel	SDP CA1# S10A67-05Z50B5
52	2	1/2 Plain Hex Solid Dowel	SDP CA1# S1V542-08R0F1324
53	1	1/2-20 Cap Screw	MCM CA1# 81251A144
54	1	1/2x1/4 Cap Screw	MCM CA1# 81251A022
55	1	1/4-18 Hex Nut	MCM CA1# 90480A029
56	2	1/4-20x1/2 Cap Screw	MCM CA1# 90128A242
57	2	1/4-20x2 1/2 Cap Screw	MCM CA1# 90128A255
58	4	1/4-20x3/4 Cap Screw	MCM CA1# 90128A245
59	1	M10 Flat Washer	MCM CA1# 810K340011
60	2	10-24 Machine Screw Nut	MCM CA1# 90059A011
61	2	10-24x1 1/4 Socket Cap Screw	MCM CA # 92185A249
62	2	10-24x3/4 Socket Cap Screw	MCM CA # 92185A245
63	2	10-32x3/8 Low Head Cap Screw	MCM CA1# 95515A470
64	1	1/4 Flat Washer	MCM CA1# 91025A050
65	1	1/4-18 Hex Nut	MCM CA1# 91845A530
66	1	5/16 Shoulder Screw 3/8 Lg.	MCM CA1# 90029A021
67	12	1/2-13x 3/4 Cap Screw	MCM CA1# 81251A622
68	1	3/8x1/8 Pilot Dell Screw	S CA1# HSMR0037M012SW
69	2	1/2 Plain Nu Solid Dowel	SDP CA1# S10A67-05Z50B5
70	2	1/2 Plain Hex Solid Dowel	SDP CA1# S1V542-08R0F1324
71	1	1/2-20 Cap Screw	MCM CA1# 81251A144
72	1	1/2x1/4 Cap Screw	MCM CA1# 81251A022
73	1	1/4-18 Hex Nut	MCM CA1# 90480A029
74	2	1/4-20x1/2 Cap Screw	MCM CA1# 90128A242
75	2	1/4-20x2 1/2 Cap Screw	MCM CA1# 90128A255
76	4	1/4-20x3/4 Cap Screw	MCM CA1# 90128A245
77	1	M10 Flat Washer	MCM CA1# 810K340011
78	2	10-24 Machine Screw Nut	MCM CA1# 90059A011
79	2	10-24x1 1/4 Socket Cap Screw	MCM CA # 92185A249
80	2	10-24x3/4 Socket Cap Screw	MCM CA # 92185A245
81	2	10-32x3/8 Low Head Cap Screw	MCM CA1# 95515A470
82	1	1/4 Flat Washer	MCM CA1# 91025A050
83	1	1/4-18 Hex Nut	MCM CA1# 91845A530
84	1	5/16 Shoulder Screw 3/8 Lg.	MCM CA1# 90029A021
85	12	1/2-13x 3/4 Cap Screw	MCM CA1# 81251A622
86	1	3/8x1/8 Pilot Dell Screw	S CA1# HSMR0037M012SW
87	2	1/2 Plain Nu Solid Dowel	SDP CA1# S10A67-05Z50B5
88	2	1/2 Plain Hex Solid Dowel	SDP CA1# S1V542-08R0F1324
89	1	1/2-20 Cap Screw	MCM CA1# 81251A144
90	1	1/2x1/4 Cap Screw	MCM CA1# 81251A022
91	1	1/4-18 Hex Nut	MCM CA1# 90480A029
92	2	1/4-20x1/2 Cap Screw	MCM CA1# 90128A242
93	2	1/4-20x2 1/2 Cap Screw	MCM CA1# 90128A255
94	4	1/4-20x3/4 Cap Screw	MCM CA1# 90128A245
95	1	M10 Flat Washer	MCM CA1# 810K340011
96	2	10-24 Machine Screw Nut	MCM CA1# 90059A011
97	2	10-24x1 1/4 Socket Cap Screw	MCM CA # 92185A249
98	2	10-24x3/4 Socket Cap Screw	MCM CA # 92185A245
99	2	10-32x3/8 Low Head Cap Screw	MCM CA1# 95515A470
100	1	1/4 Flat Washer	MCM CA1# 91025A050
101	1	1/4-18 Hex Nut	MCM CA1# 91845A530
102	1	5/16 Shoulder Screw 3/8 Lg.	MCM CA1# 90029A021
103	12	1/2-13x 3/4 Cap Screw	MCM CA1# 81251A622
104	1	3/8x1/8 Pilot Dell Screw	S CA1# HSMR0037M012SW
105	2	1/2 Plain Nu Solid Dowel	SDP CA1# S10A67-05Z50B5
106	2	1/2 Plain Hex Solid Dowel	SDP CA1# S1V542-08R0F1324
107	1	1/2-20 Cap Screw	MCM CA1# 81251A144
108	1	1/2x1/4 Cap Screw	MCM CA1# 81251A022
109	1	1/4-18 Hex Nut	MCM CA1# 90480A029
110	2	1/4-20x1/2 Cap Screw	MCM CA1# 90128A242
111	2	1/4-20x2 1/2 Cap Screw	MCM CA1# 90128A255
112	4	1/4-20x3/4 Cap Screw	MCM CA1# 90128A245
113	1	M10 Flat Washer	MCM CA1# 810K340011
114	2	10-24 Machine Screw Nut	MCM CA1# 90059A011
115	2	10-24x1 1/4 Socket Cap Screw	MCM CA # 92185A249
116	2	10-24x3/4 Socket Cap Screw	MCM CA # 92185A245
117	2	10-32x3/8 Low Head Cap Screw	MCM CA1# 95515A470
118	1	1/4 Flat Washer	MCM CA1# 91025A050
119	1	1/4-18 Hex Nut	MCM CA1# 91845A530
120	1	5/16 Shoulder Screw 3/8 Lg.	MCM CA1# 90029A021
121	12	1/2-13x 3/4 Cap Screw	MCM CA1# 81251A622
122	1	3/8x1/8 Pilot Dell Screw	S CA1# HSMR0037M012SW
123	2	1/2 Plain Nu Solid Dowel	SDP CA1# S10A67-05Z50B5
124	2	1/2 Plain Hex Solid Dowel	SDP CA1# S1V542-08R0F1324
125	1	1/2-20 Cap Screw	MCM CA1# 81251A144
126	1	1/2x1/4 Cap Screw	MCM CA1# 81251A022
127	1	1/4-18 Hex Nut	MCM CA1# 90480A029
128	2	1/4-20x1/2 Cap Screw	MCM CA1# 90128A242
129	2	1/4-20x2 1/2 Cap Screw	MCM CA1# 90128A255
130	4	1/4-20x3/4 Cap Screw	MCM CA1# 90128A245
131	1	M10 Flat Washer	MCM CA1# 810K340011
132	2	10-24 Machine Screw Nut	MCM CA1# 90059A011
133	2	10-24x1 1/4 Socket Cap Screw	MCM CA # 92185A249
134	2	10-24x3/4 Socket Cap Screw	MCM CA # 92185A245
135	2	10-32x3/8 Low Head Cap Screw	MCM CA1# 95515A470
136	1	1/4 Flat Washer	MCM CA1# 91025A050
137	1	1/4-18 Hex Nut	MCM CA1# 91845A530
138	1	5/16 Shoulder Screw 3/8 Lg.	MCM CA1# 90029A021
139	12	1/2-13x 3/4 Cap Screw	MCM CA1# 81251A622
140	1	3/8x1/8 Pilot Dell Screw	S CA1# HSMR0037M012SW
141	2	1/2 Plain Nu Solid Dowel	SDP CA1# S10A67-05Z50B5
142	2	1/2 Plain Hex Solid Dowel	SDP CA1# S1V542-08R0F1324
143	1	1/2-20 Cap Screw	MCM CA1# 81251A144
144	1	1/2x1/4 Cap Screw	MCM CA1# 81251A022
145	1	1/4-18 Hex Nut	MCM CA1# 90480A029
146	2	1/4-20x1/2 Cap Screw	MCM CA1# 90128A242
147	2	1/4-20x2 1/2 Cap Screw	MCM CA1# 90128A255
148	4	1/4-20x3/4 Cap Screw	MCM CA1# 90128A245
149	1	M10 Flat Washer	MCM CA1# 810K340011
150	2	10-24 Machine Screw Nut	MCM CA1# 90059A011
151	2	10-24x1 1/4 Socket Cap Screw	MCM CA # 92185A249
152	2	10-24x3/4 Socket Cap Screw	MCM CA # 92185A245
153	2	10-32x3/8 Low Head Cap Screw	MCM CA1# 95515A470
154	1	1/4 Flat Washer	MCM CA1# 91025A050
155	1	1/4-18 Hex Nut	MCM CA1# 91845A530
156	1	5/16 Shoulder Screw 3/8 Lg.	MCM CA1# 90029A021
157	12	1/2-13x 3/4 Cap Screw	MCM CA1# 81251A622
158	1	3/8x1/8 Pilot Dell Screw	S CA1# HSMR0037M012SW
159	2	1/2 Plain Nu Solid Dowel	SDP CA1# S10A67-05Z50B5
160	2	1/2 Plain Hex Solid Dowel	SDP CA1# S1V542-08R0F1324
161	1	1/2-20 Cap Screw	MCM CA1# 81251A144
162	1	1/2x1/4 Cap Screw	MCM CA1# 81251A022
163	1	1/4-18 Hex Nut	MCM CA1# 90480A029
164	2	1/4-20x1/2 Cap Screw	MCM CA1# 90128A242
165	2	1/4-20x2 1/2 Cap Screw	MCM CA1# 90128A255
166	4	1/4-20x3/4 Cap Screw	MCM CA1# 90128A245
167	1	M10 Flat Washer	MCM CA1# 810K340011
168	2	10-24 Machine Screw Nut	MCM CA1# 90059A011
169	2	10-24x1 1/4 Socket Cap Screw	MCM CA # 92185A249
170	2	10-24x3/4 Socket Cap Screw	MCM CA # 92185A245
171	2	10-32x3/8 Low Head Cap Screw	MCM CA1# 95515A470
172	1	1/4 Flat Washer	MCM CA1# 91025A050
173	1	1/4-18 Hex Nut	MCM CA1# 91845A530
174	1	5/16 Shoulder Screw 3/8 Lg.	MCM CA1# 90029A021
175	12	1/2-13x 3/4 Cap Screw	MCM CA1# 81251A622
176	1	3/8x1/8 Pilot Dell Screw	S CA1# HSMR0037M012SW
177	2	1/2 Plain Nu Solid Dowel	SDP CA1# S10A67-05Z50B5
178	2	1/2 Plain Hex Solid Dowel	SDP CA1# S1V542-08R0F1324
179	1	1/2-20 Cap Screw	MCM CA1# 81251A144
180	1	1/2x1/4 Cap Screw	MCM CA1# 81251A022
181	1	1/4-18 Hex Nut	MCM CA1# 90480A029
182	2	1/4-20x1/2 Cap Screw	MCM CA1# 90128A242
183	2	1/4-20x2 1/2 Cap Screw	MCM CA1# 90128A255
184	4	1/4-20x3/4 Cap Screw	MCM CA1# 90128A245
185	1	M10 Flat Washer	MCM CA1# 810K340011
186	2	10-24 Machine Screw Nut	MCM CA1# 90059A011
187	2	10-24x1 1/4 Socket Cap Screw	MCM CA # 92185A249
188	2	10-24x3/4 Socket Cap Screw	MCM CA # 92185A245
189	2	10-32x3/8 Low Head Cap Screw	MCM CA1# 95515A470
190	1	1/4 Flat Washer	MCM CA1# 91025A050
191	1	1/4-18 Hex Nut	MCM CA1# 91845A530
192	1	5/16 Shoulder Screw 3/8 Lg.	MCM CA1# 90029A021
193	12	1/2-13x 3/4 Cap Screw	MCM CA1# 81251A622
194	1	3/8x1/8 Pilot Dell Screw	S CA1# HSMR0037M012SW
195	2	1/2 Plain Nu Solid Dowel	SDP CA1# S10A67-05Z50B5
196	2	1/2 Plain Hex Solid Dowel	SDP CA1# S1V542-08R0F1324
197	1	1/2-20 Cap Screw	MCM CA1# 81251A144
198	1	1/2x1/4 Cap Screw	MCM CA1# 81251A022
199	1	1/4-18 Hex Nut	MCM CA1# 90480A029
200	2	1/4-20x1/2 Cap Screw	MCM CA1# 90128A242
201	2	1/4-20x2 1/2 Cap Screw	MCM CA1# 90128A255
202	4	1/4-20x3/4 Cap Screw	MCM CA1# 90128A245
203	1	M10 Flat Washer	MCM CA1# 810K340011
204	2	10-24 Machine Screw Nut	MCM CA1# 90059A011
205	2	10-24x1 1/4 Socket Cap Screw	MCM CA # 92185A249
206	2	10-24x3/4 Socket Cap Screw	MCM CA # 92185A245
207	2	10-32x3/8 Low Head Cap Screw	MCM CA1# 95515A470
208	1	1/4 Flat Washer	MCM CA1# 91025A050
209	1	1/4-18 Hex Nut	MCM CA1# 91845A530
210	1	5/16 Shoulder Screw 3/8 Lg.	MCM CA1# 90029A021
211	12	1/2-13x 3/4 Cap Screw	MCM CA1# 81251A622
212	1	3/8x1/8 Pilot Dell Screw	S CA1# HSMR0037M012SW
213	2	1/2 Plain Nu Solid Dowel	SDP CA1# S10A67-05Z50B5
214	2	1/2 Plain Hex Solid Dowel	SDP CA1# S1V542-08R0F1324
215	1	1/2-20 Cap Screw	MCM CA1# 81251A144
216	1	1/2x1/4 Cap Screw	MCM CA1# 81251A022
217	1	1/4-18 Hex Nut	MCM CA1# 90480A029
218	2	1/4-20x1/2 Cap Screw	MCM CA1# 90128A242
219	2	1/4-20x2 1/2 Cap Screw	MCM CA1# 90128A255
220	4	1/4-20x3/4 Cap Screw	MCM CA1# 90128A245
221	1	M10 Flat Washer	MCM CA1# 810K340011
222	2	10-24 Machine Screw Nut	MCM CA1# 90059A011
223	2	10-24x1 1/4 Socket Cap Screw	MCM CA # 92185A249
224	2	10-24x3/4 Socket Cap Screw	MCM CA # 92185A245
225	2	10-32x3/8 Low Head Cap Screw	MCM CA1# 95515A470
226	1	1/4 Flat Washer	MCM CA1# 91025A050
227	1	1/4-18 Hex Nut	MCM CA1# 91845A530
228	1	5/16 Shoulder Screw 3/8 Lg.	MCM CA1# 90029A021
229	12	1/2-13x 3/4 Cap Screw	MCM CA1# 81251A622
230	1	3/8x1/8 Pilot Dell Screw	S CA1# HSMR0037M012SW
231	2	1/2 Plain Nu Solid Dowel	SDP CA1# S10A67-05Z50B5
232	2	1/2 Plain Hex Solid Dowel	SDP CA1# S1V542-08R0F1324
233	1	1/2-20 Cap Screw	MCM CA1# 81251A144
234	1	1/2x1/4 Cap Screw	MCM CA1# 81251A022
235	1	1/4-18 Hex Nut	MCM CA1# 90480A029
236	2	1/4-20x1/2 Cap Screw	MCM CA1# 90128A242
237	2	1/4-20x2 1/2 Cap Screw	MCM CA1# 90128A255
238	4	1/4-20x3/4 Cap Screw	MCM CA1# 90128A245
239	1	M10 Flat Washer	MCM CA1# 810K340011
240	2	10-24 Machine Screw Nut	MCM CA1# 90059A011
241	2	10-24x1 1/4 Socket Cap Screw	MCM CA # 92185A249
242	2	10-24x3/4 Socket Cap Screw	MCM CA # 92185A245
243	2	10-32x3/8 Low Head Cap Screw	MCM CA1# 95515A470
244	1	1/4 Flat Washer	MCM CA1# 91025A050
245	1	1/4-18 Hex Nut	MCM CA1# 91845A530
246	1	5/16 Shoulder Screw 3/8 Lg.	MCM CA1# 90029A021
247	12	1/2-13x 3/4 Cap Screw	MCM CA1# 81251A622
248	1	3/8x1/8 Pilot Dell Screw	S CA1# HSMR0037M012SW
249	2	1/2 Plain Nu Solid Dowel	SDP CA1# S10A67-05Z50B5
250	2	1/2 Plain Hex Solid Dowel	SDP CA1# S1V542-08R0F1324
251	1	1/2-20 Cap Screw	MCM CA1# 81251A144
252	1	1/2x1/4 Cap Screw	MCM CA1# 81251A022
253	1	1/4-18 Hex Nut	MCM CA1# 90480A029
254	2	1/4-20x1/2 Cap Screw	MCM CA1# 90128A242
255	2	1/4-20x2 1/2 Cap Screw	MCM CA1# 90128A255
256	4	1/4-20x3/4 Cap Screw	MCM CA1# 90128A245
257	1	M10 Flat Washer	MCM CA1# 810K340011
258	2	10-24 Machine Screw Nut	MCM CA1# 90059A011
259	2	10-24x1 1/4 Socket Cap Screw	MCM CA # 92185A249
260	2	10-24x3/4 Socket Cap Screw	MCM CA # 92185A245
261	2	10-32x3/8 Low Head Cap Screw	MCM CA1# 95515A470
262	1	1/4 Flat Washer	MCM CA1# 91025A050
263	1	1/4-18 Hex Nut	MCM CA1# 91845A530
264	1	5/16 Shoulder Screw 3/8 Lg.	MCM CA1# 90029A021
265	12	1/2-13x 3/4 Cap Screw	MCM CA1# 81251A622
266	1	3/8x1/8 Pilot Dell Screw	S CA1# HSMR0037M012SW
267	2	1/2 Plain Nu Solid Dowel	SDP CA1# S10A67-05Z50B5
268	2	1/2 Plain Hex Solid Dowel	SDP CA1# S1V542-08R0F1324
269	1	1/2-20 Cap Screw	MCM CA1# 81251A144
270	1	1/2x1/4 Cap Screw	MCM CA1# 81251A022
271	1	1/4-18 Hex Nut	MCM CA1# 90480A029
272	2	1/4-20x1/2 Cap Screw	MCM CA1# 90128A242
273	2	1/4-20x2 1/2 Cap Screw	MCM CA1# 90128A255
274	4	1/4-20x3/4 Cap Screw	MCM CA1# 90128A245
275	1	M10 Flat Washer	MCM CA1# 810K340011
276	2	10-24 Machine Screw Nut	MCM CA1# 90059A011
277	2	10-24x1 1/4 Socket Cap Screw	MCM CA # 92185A249
278	2	10-24x3/4 Socket Cap Screw	MCM CA # 92185A245
279	2	10-32x3/8 Low Head Cap Screw	MCM CA1# 95515A470
280	1	1/4 Flat Washer	MCM CA1# 91025A050
281	1	1/4-18 Hex Nut	MCM CA1# 91845A530
282	1	5/16 Shoulder Screw 3/8 Lg.	MCM CA1# 90029A021
283	12	1/2-13x 3/4 Cap Screw	MCM CA1# 81251A622
284	1	3/8x1/8 Pilot Dell Screw	S CA1# HSMR0037M012SW
285	2	1/2 Plain Nu Solid Dowel	SDP CA1# S10A67-05Z50B5
286	2	1/2 Plain Hex Solid Dowel	SDP CA1# S1V542-08R0F1324
287	1	1/2-20 Cap Screw	MCM CA1# 81251A144
288	1	1/2x1/4 Cap Screw	MCM CA1# 81251A022
289	1	1/4-18 Hex Nut	MCM CA1# 90480A029
290	2	1/4-20x1/2 Cap Screw	MCM CA1# 90128A242
291	2	1/4-20x2 1/2 Cap Screw	MCM CA1# 90128A255
292	4	1/4-20x3/4 Cap Screw	MCM CA1# 90128A245
293	1	M10 Flat Washer	MCM CA1# 810K340011
294	2	10-24 Machine Screw Nut	MCM CA1# 90059A011
295	2	10-24x1 1/4 Socket Cap Screw	MCM CA # 92185A249
296	2	10-24x3/4 Socket Cap Screw	MCM CA # 92185A245
297	2	10-32x3/8 Low Head Cap Screw	MCM CA1# 95515A470
298	1	1/4 Flat Washer	MCM CA1# 91025A050
299	1	1/4-18 Hex Nut	MCM CA1# 91845A530
300	1	5/16 Shoulder Screw 3/8 Lg.	MCM CA1# 90029A021
301	12	1/2-13x 3/4 Cap Screw	MCM CA1# 81251A622
302	1	3/8x1/8 Pilot Dell Screw	S CA1# HSMR0037M012SW
303	2	1/2 Plain Nu Solid Dowel	SDP CA1# S10A67-05Z50B5
304	2	1/2 Plain Hex Solid Dowel	SDP CA1# S1V542-08R0F1324
305	1	1/2-20 Cap Screw	MCM CA1# 81251A144
306	1	1/2x1/4 Cap Screw	MCM CA1# 81251A022
307	1	1/4-18 Hex Nut	MCM CA1# 90480A029
308	2	1/4-20x1/2 Cap Screw	MCM CA1# 90128A242
309	2	1/4-20x2 1/2 Cap Screw	MCM CA1# 90128A255
310	4	1/4-20x3/4 Cap Screw	MCM CA1# 90128A245
311	1	M10 Flat Washer	MCM CA1# 810K340011
312	2	10-24 Machine Screw Nut	MCM CA1# 90059A011
313	2	10-24x1 1/4 Socket Cap Screw	MCM CA # 92185A249
314	2	10-24x3/4 Socket Cap Screw	MCM CA # 92185A245
315	2	10-32x3/8 Low Head Cap Screw	MCM CA1# 95515A470
316	1	1/4 Flat Washer	MCM CA1# 91025A050
317	1	1/4-18 Hex Nut	MCM CA1# 91845A530
318	1	5/16 Shoulder Screw 3/8 Lg.	MCM CA1# 90029A021
319	12	1/2-13x 3/4 Cap Screw	MCM CA1# 81251A622
320	1	3/8x1/8 Pilot Dell Screw	S CA1# HSMR0037M012SW
321	2	1/2 Plain Nu Solid Dowel	SDP CA1# S10A67-05Z50B5
322	2	1/2 Plain Hex Solid Dowel	SDP CA1# S1V542-08R0F1324
323	1	1/2-20 Cap Screw	MCM CA1# 81251A144
324	1	1/2x1/4 Cap Screw	MCM CA1# 81251A022
325	1	1/4-18 Hex Nut	MCM CA1# 90480A029
326	2	1/4-20x1/2 Cap Screw	MCM CA1# 90128A242
327	2	1/4-20x2 1/2 Cap Screw	MCM CA1# 90128A255
328	4	1/4-20x3/4 Cap Screw	MCM CA1# 90128A245
329	1	M10 Flat Washer	MCM CA1# 810K340011
330	2	10-24 Machine Screw Nut	MCM CA1# 90059A011
331	2	10-24x1 1/4 Socket Cap Screw	MCM CA # 92185A249
332	2	10-24x3/4 Socket Cap Screw	MCM CA # 92185A245
333	2	10-32x3/8 Low Head Cap Screw	MCM CA1# 95515A470
334	1	1/4 Flat Washer	MCM CA1# 91025A050
335	1	1/4-18 Hex Nut	MCM CA1# 91845A530
336	1	5/16 Shoulder Screw 3/8 Lg.	MCM CA1# 90029A021
337	12	1/2-13x 3/4 Cap Screw	MCM CA1# 81251A622
338	1	3/8x1/8 Pilot Dell Screw	S CA1# HSMR0037M012SW
339	2	1/2 Plain Nu Solid Dowel	SDP CA1# S10A67-05Z50B5
340	2	1/2 Plain Hex Solid Dowel	SDP CA1# S1V542-08R0F1324
341	1	1/2-20 Cap Screw	MCM CA1# 81251A144
342	1	1/2x1/4 Cap Screw	MCM CA1# 81251A022
343	1	1/4-18 Hex Nut	MCM CA1# 90480A029
344	2	1/4-20x1/2 Cap Screw	MCM CA1# 90128A242
345	2	1/4-20x2 1/2 Cap Screw	MCM CA1# 90128A255
346	4	1/4-20x3/4 Cap Screw	MCM CA1# 90128A245
347	1	M10 Flat Washer	MCM CA1# 810K340011
348	2	10-24 Machine Screw Nut	MCM CA

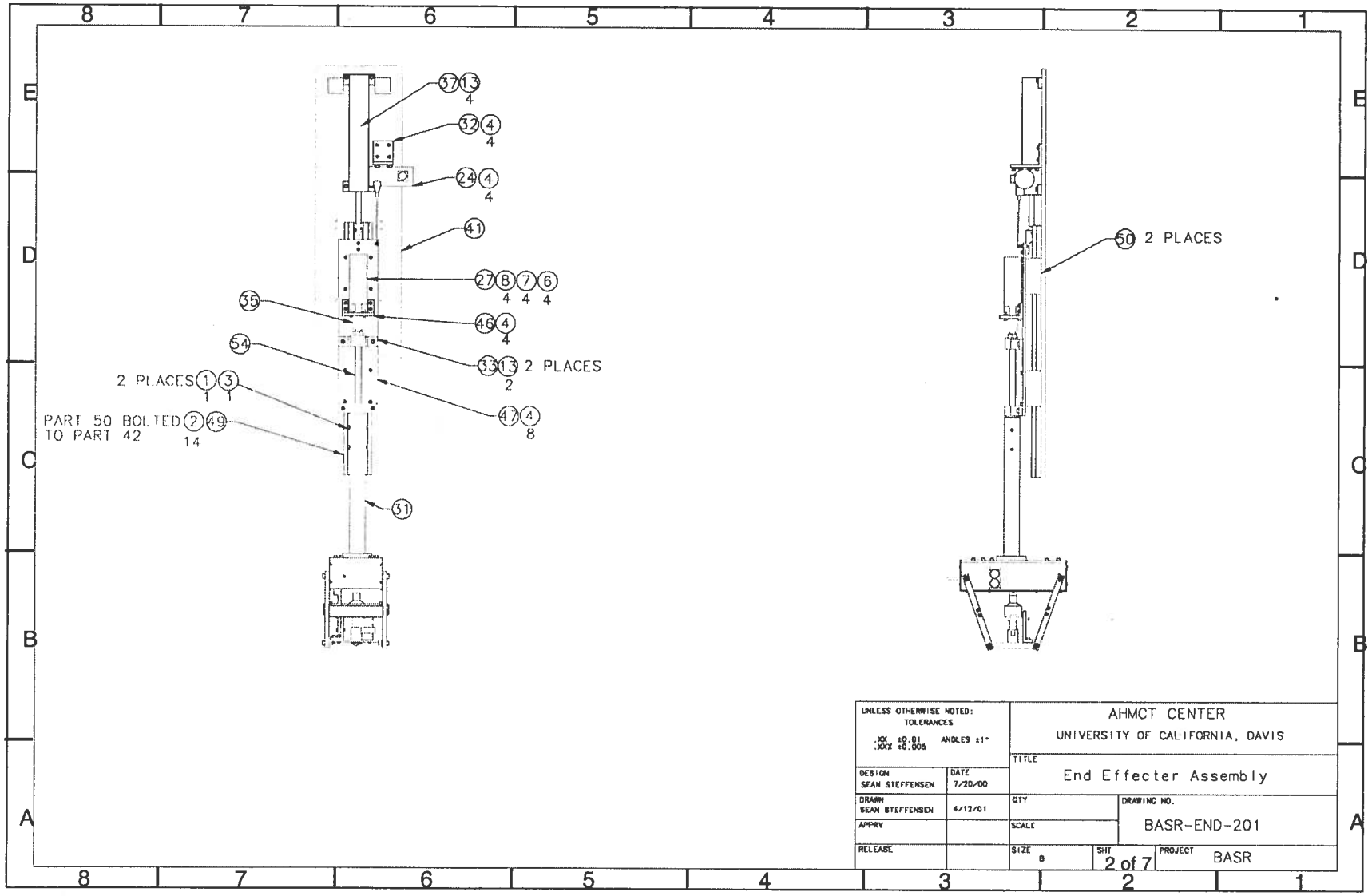

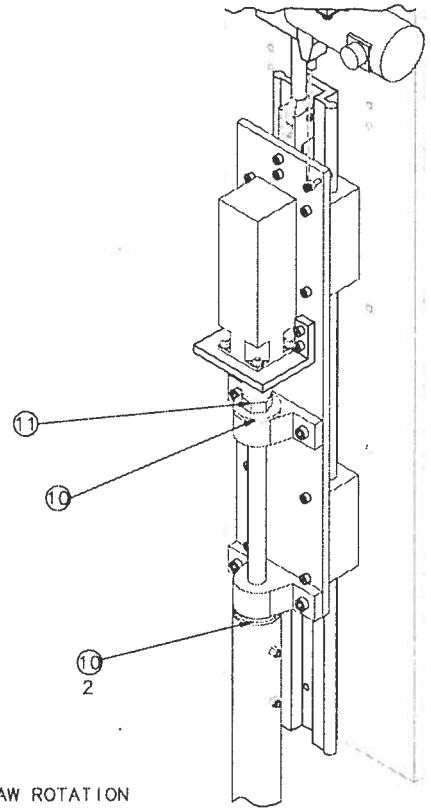

DETAIL VIEW OF YAW ROTATION JOINT

UNLESS OTHERWISE NOTED: TOLERANCES .XX ±0.01 .XXX ±0.005 ANGLES ±1°		AHMCT CENTER UNIVERSITY OF CALIFORNIA, DAVIS	
		TITLE: End Effecter Assembly	
DESIGN: SEAN STEFFENSEN	DATE: 7/20/00		
DRAWN: SEAN STEFFENSEN	4/12/01	QTY	DRAWING NO.: BASR-END-201
APPRV		SCALE	
RELEASE		SIZE: B	SHT: 3 of 7 PROJECT: BASR

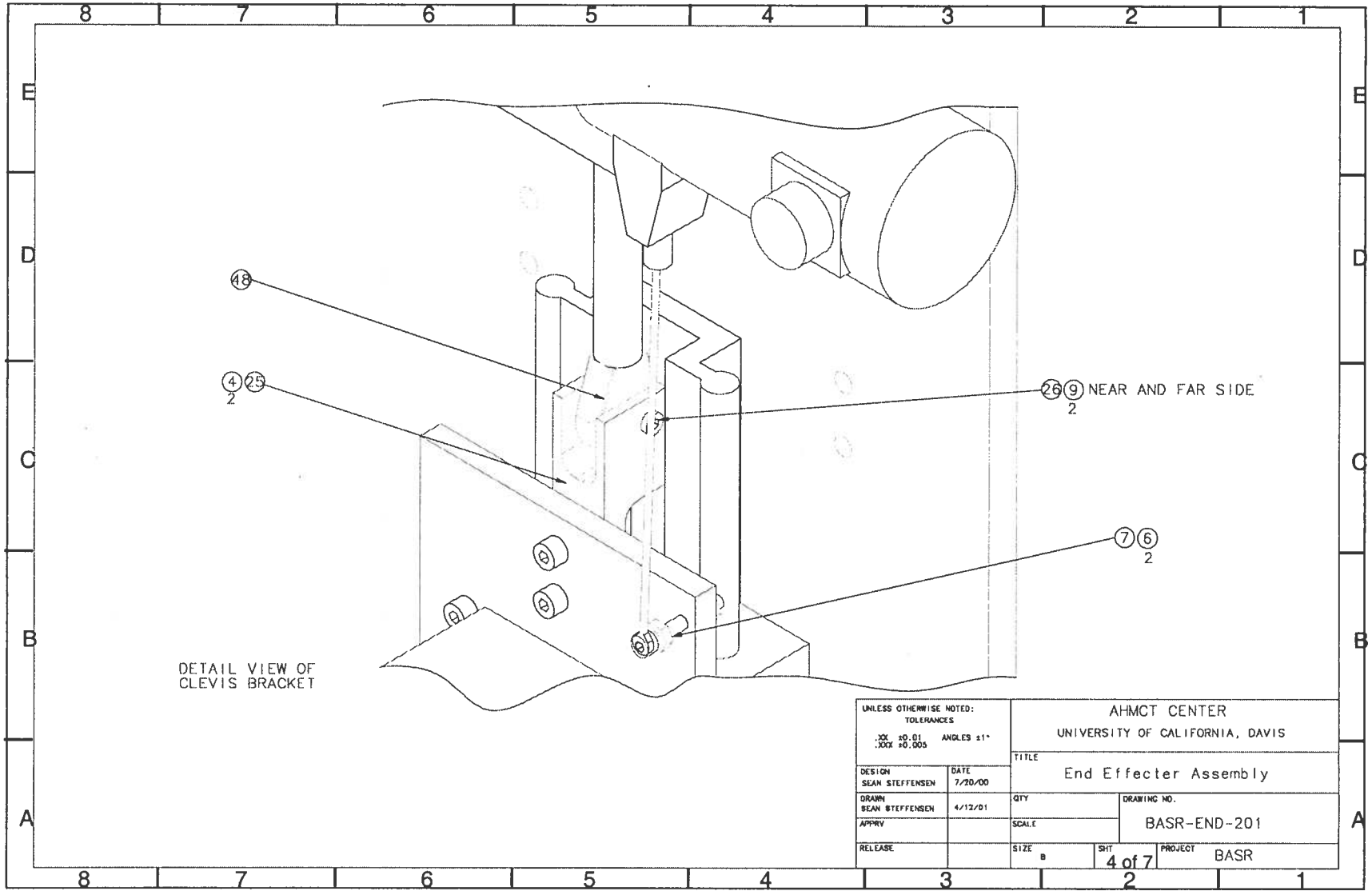

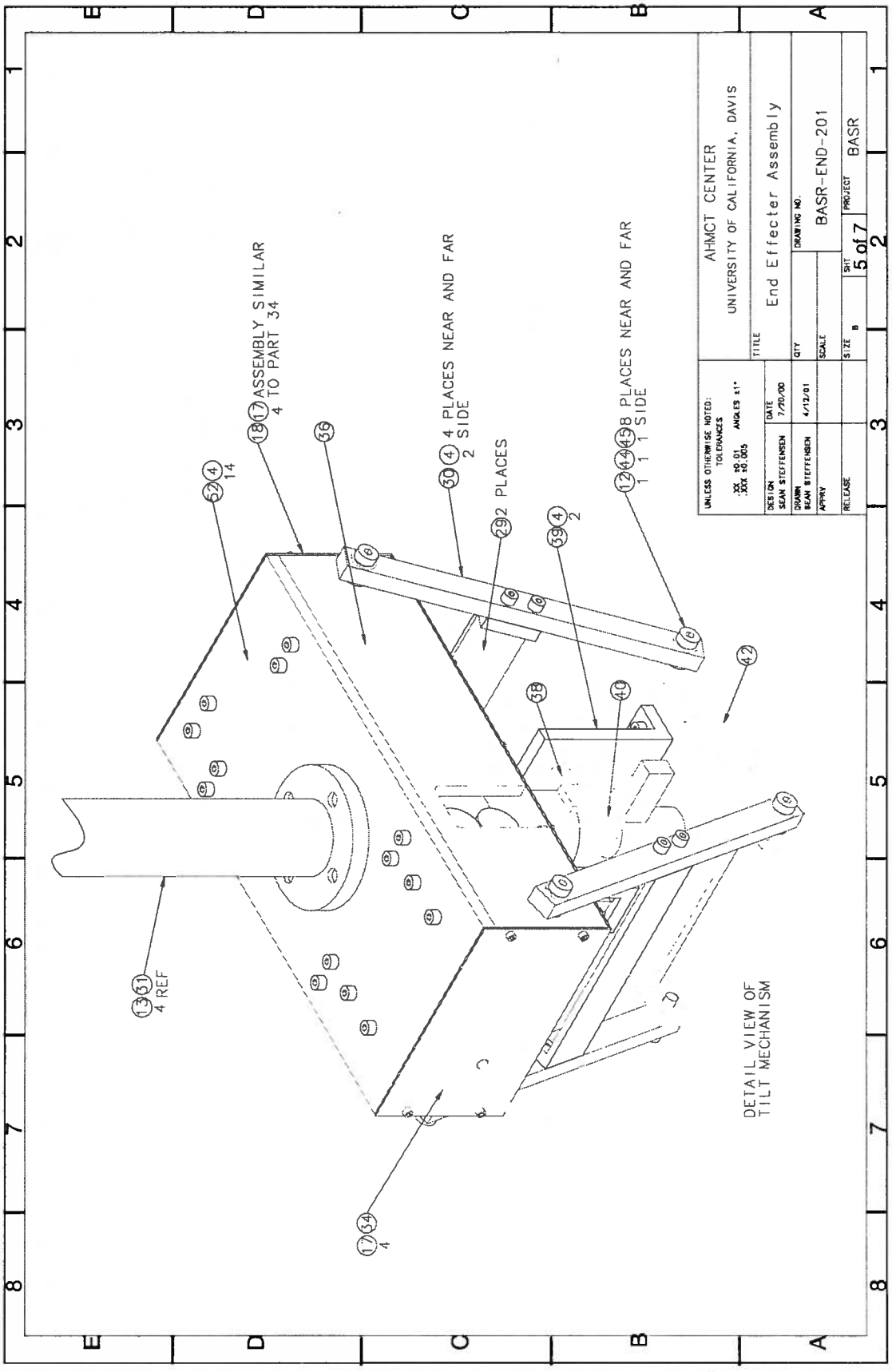

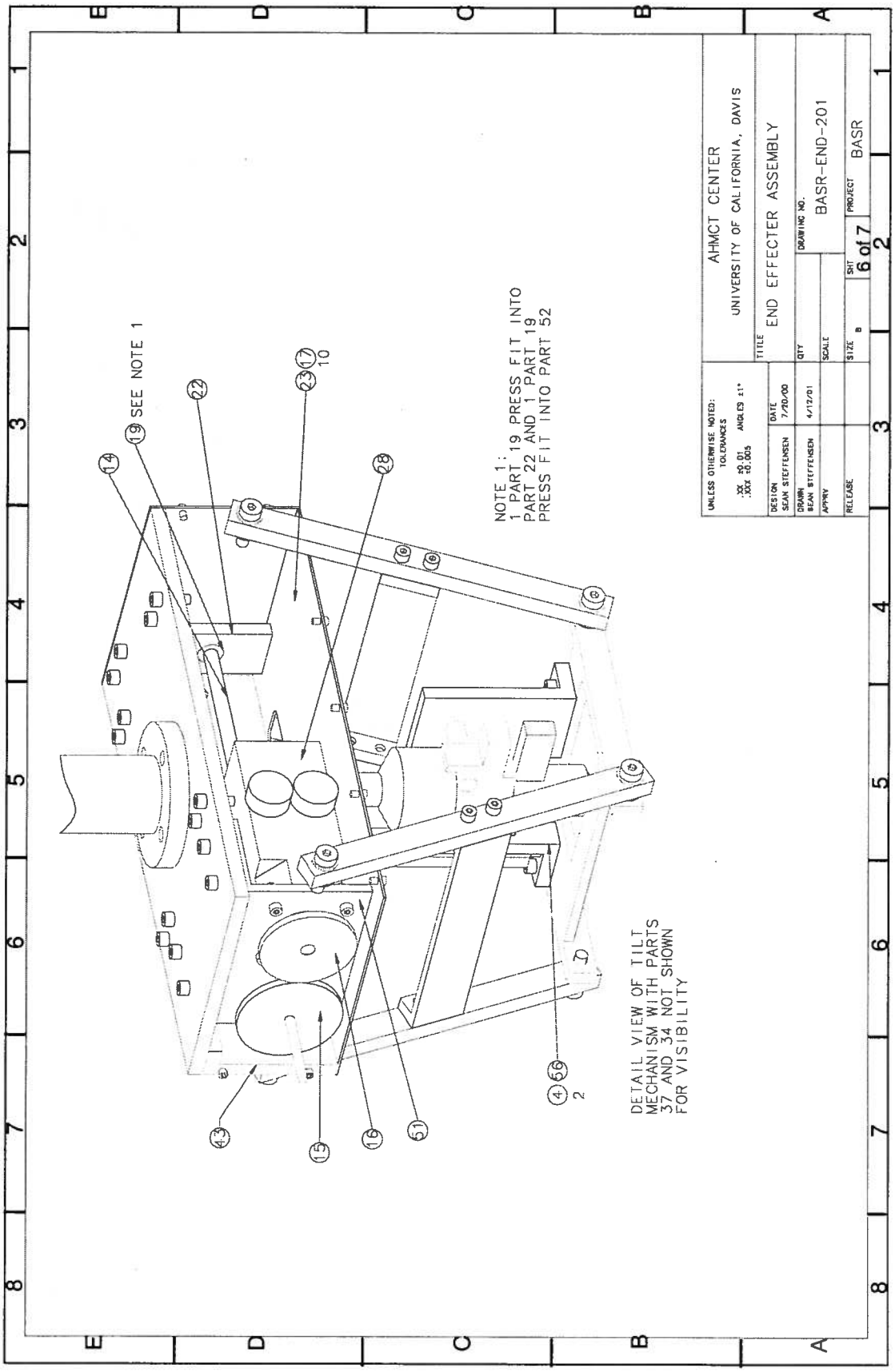

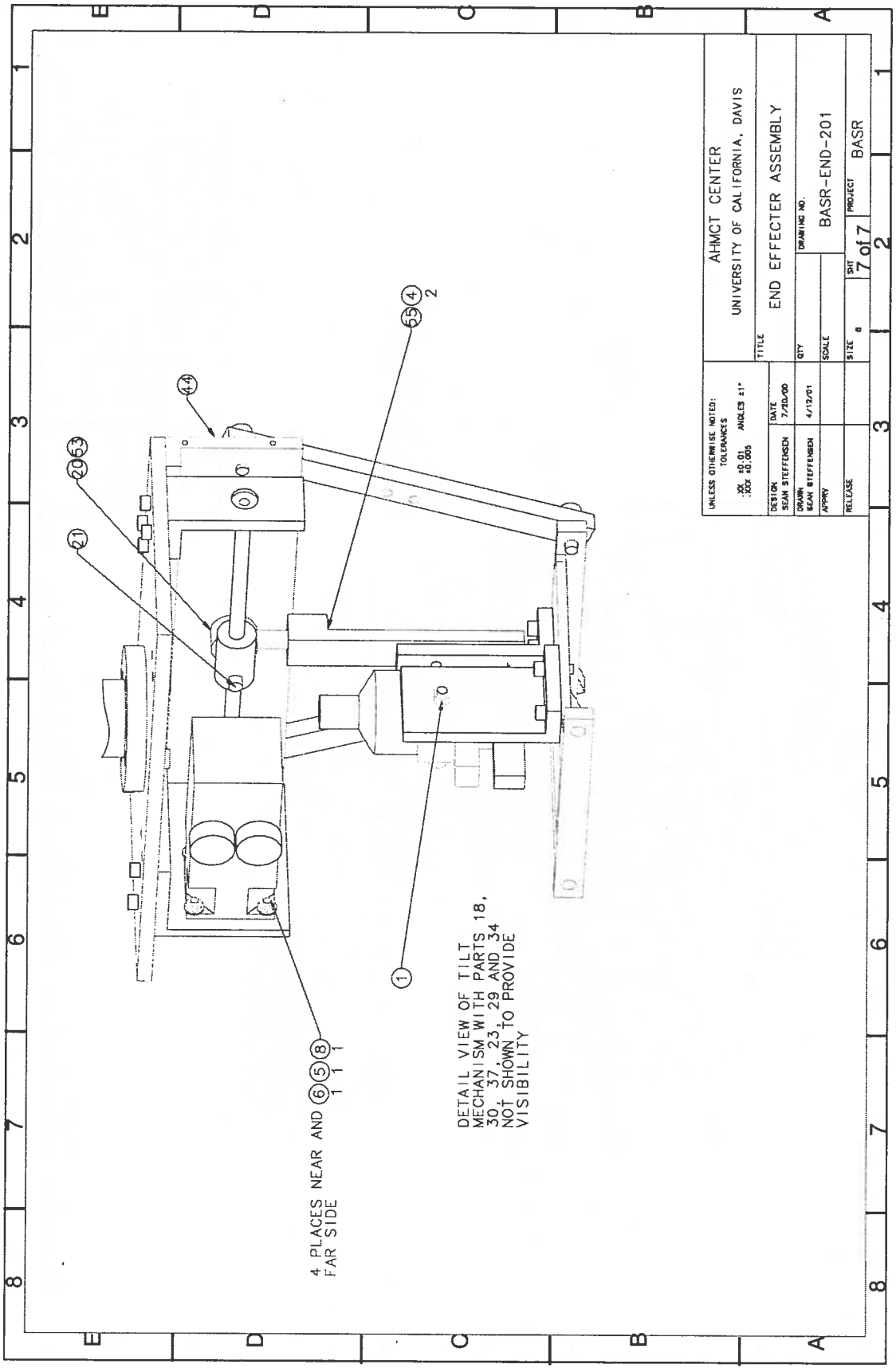

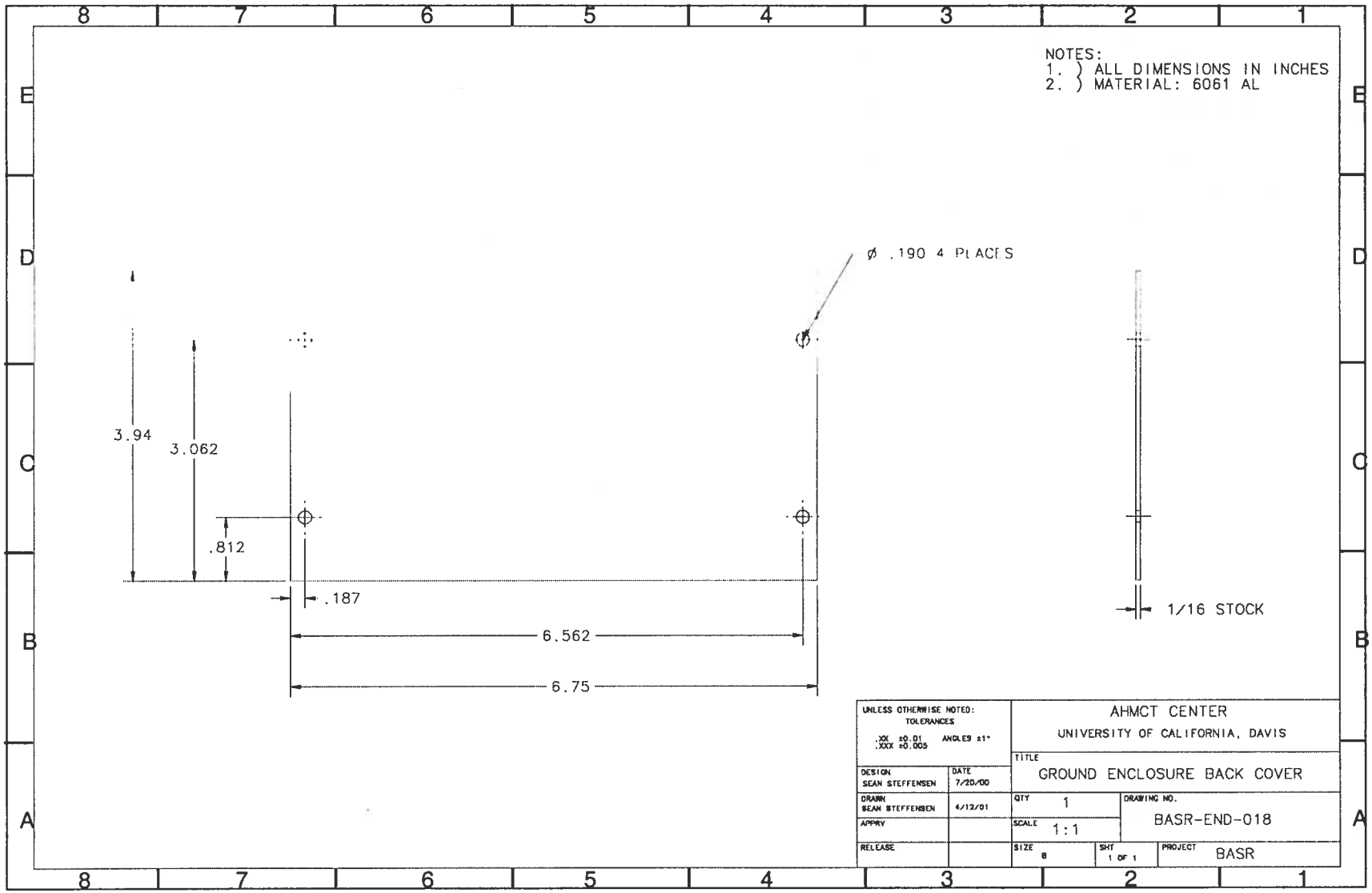

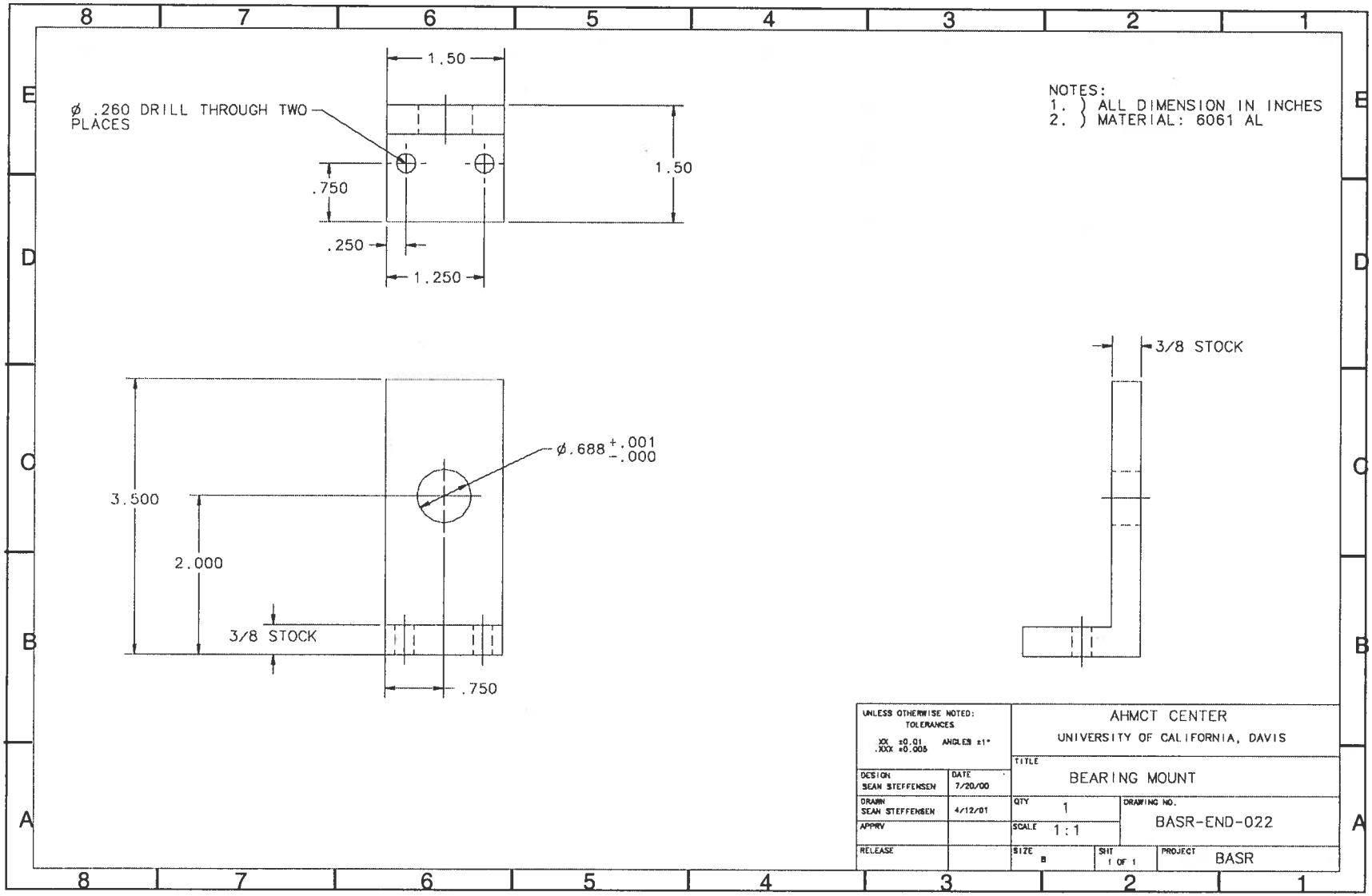

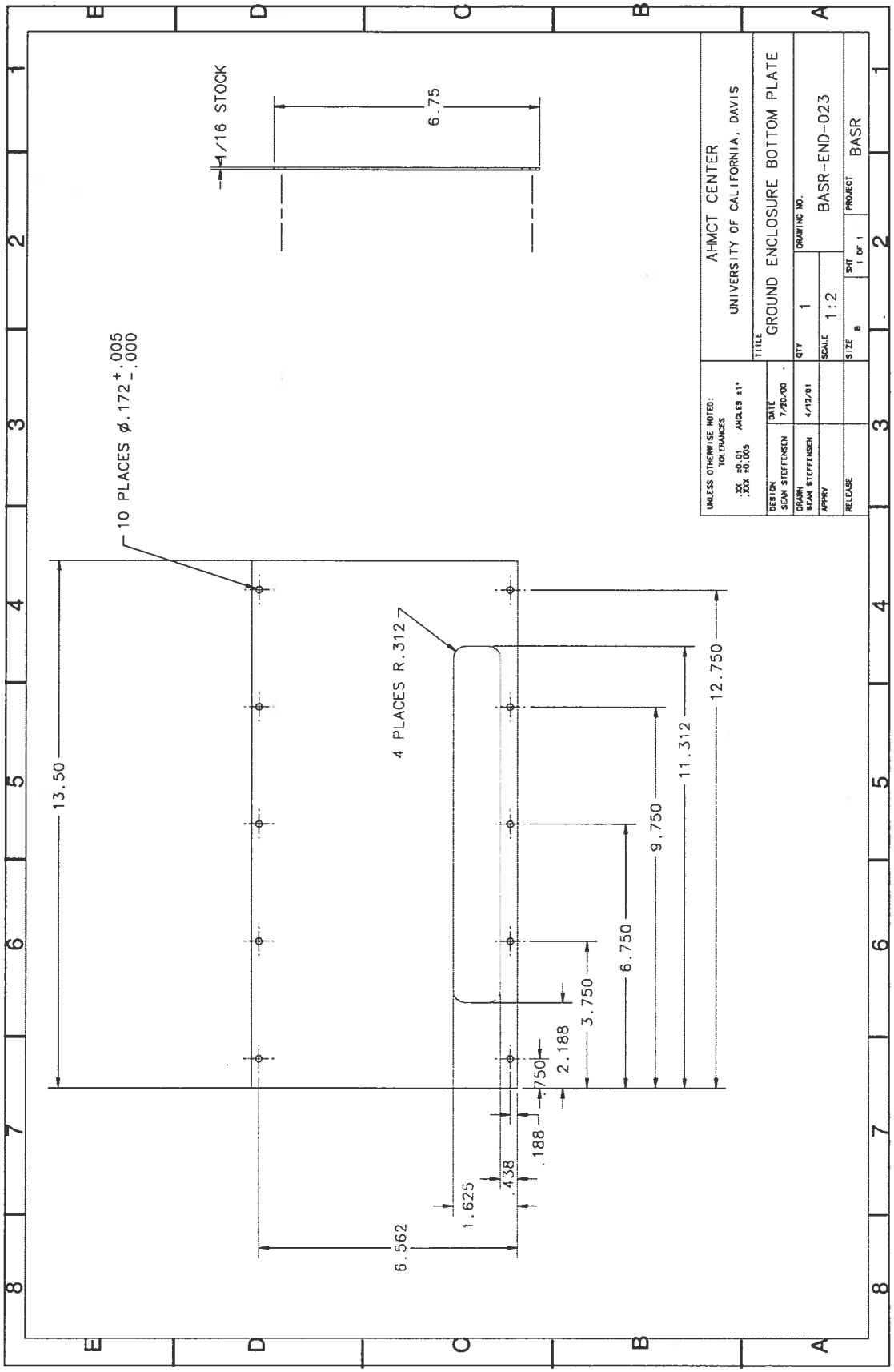

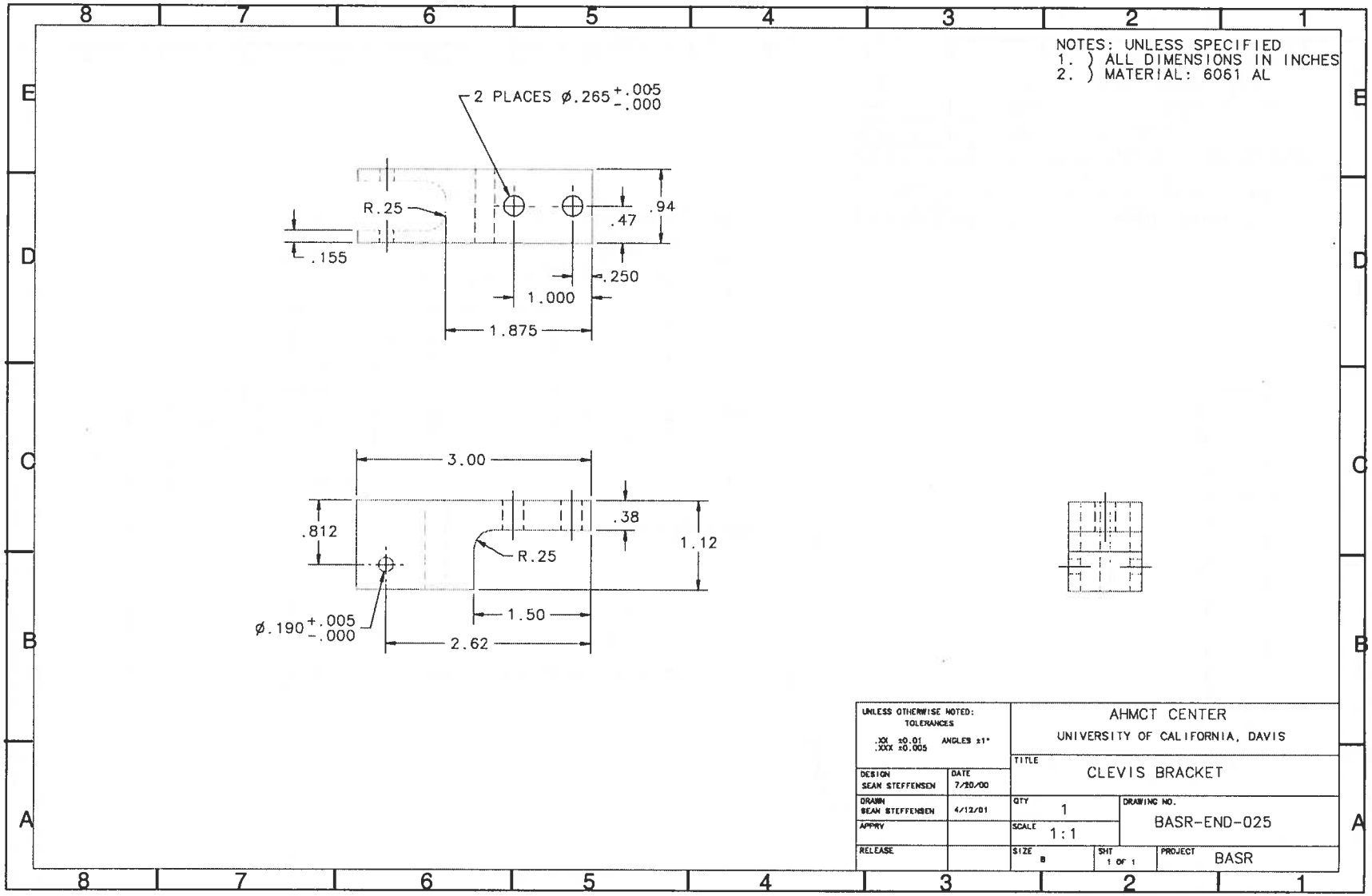

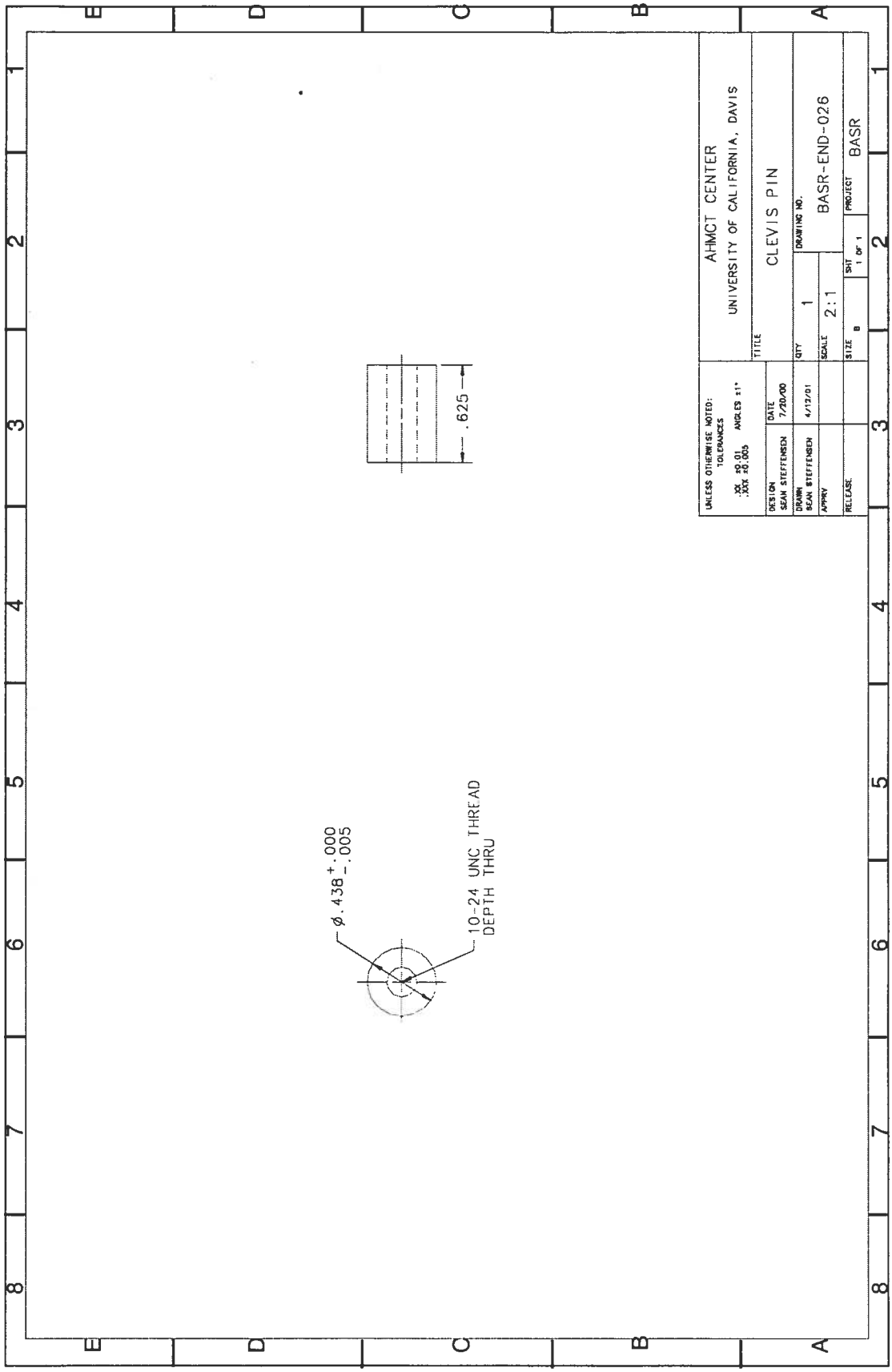

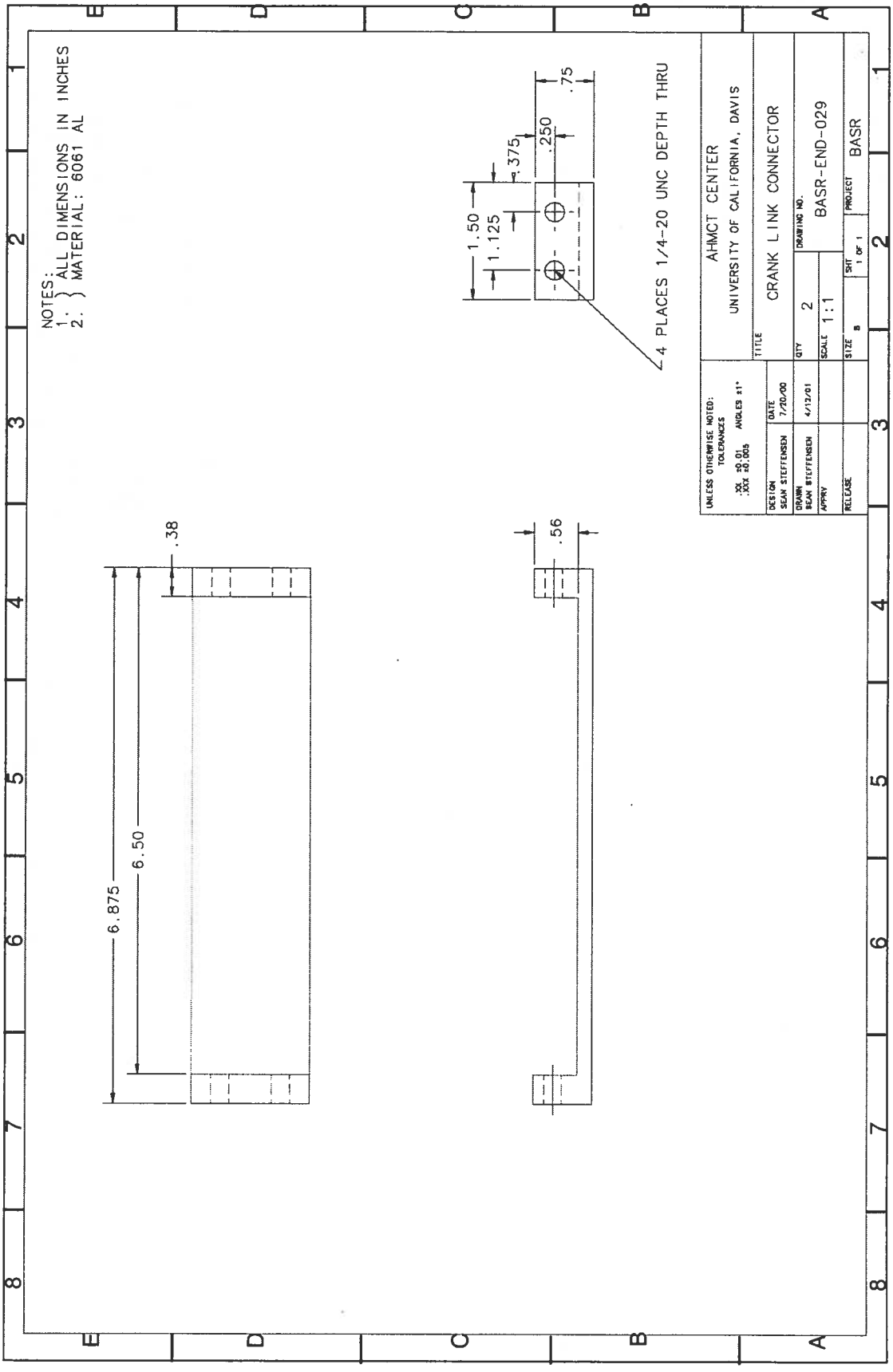

NOTES:
1.) ALL DIMENSIONS IN INCHES
2.) MATERIAL: 6061 AL

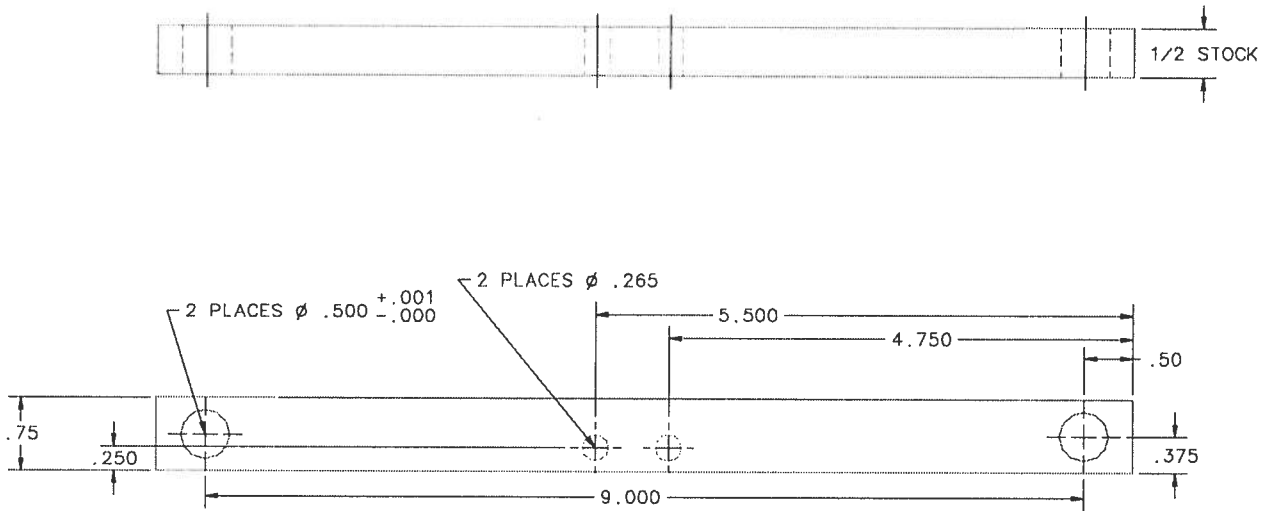

UNLESS OTHERWISE NOTED: TOLERANCES .XX ±0.01 .XXX ±0.005 ANGLES ±1°	AHMCT CENTER UNIVERSITY OF CALIFORNIA, DAVIS
DESIGN SEAN STEFFENSEN — DATE 4/12/01	TITLE: CRANK LINK
DRAWN SEAN STEFFENSEN — 4/12/01	QTY 2 — DRAWING NO. BASR-END-030
APPRV	SCALE 1:1
RELEASE	SIZE B — SHT 1 OF 1 — PROJECT

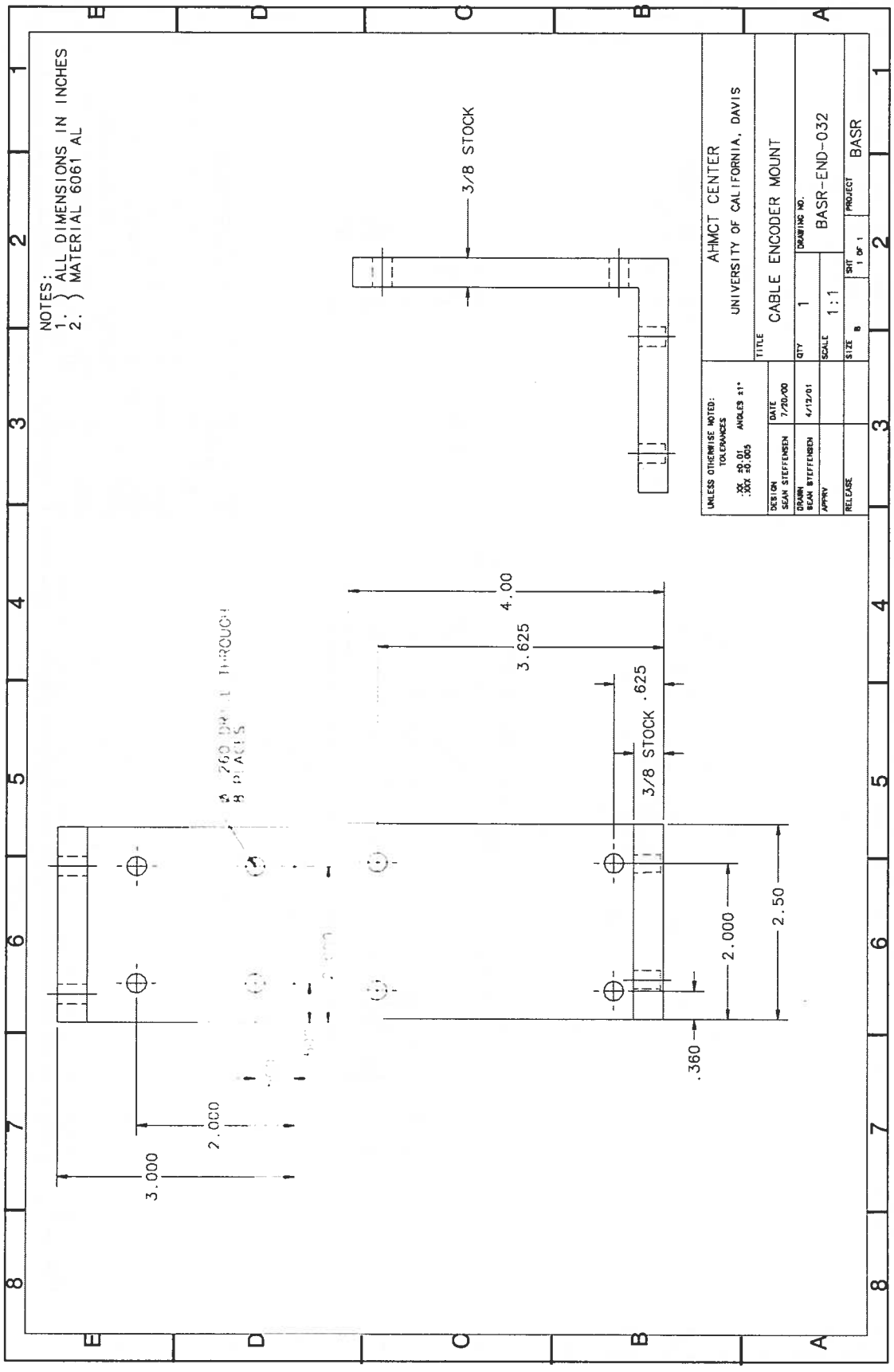

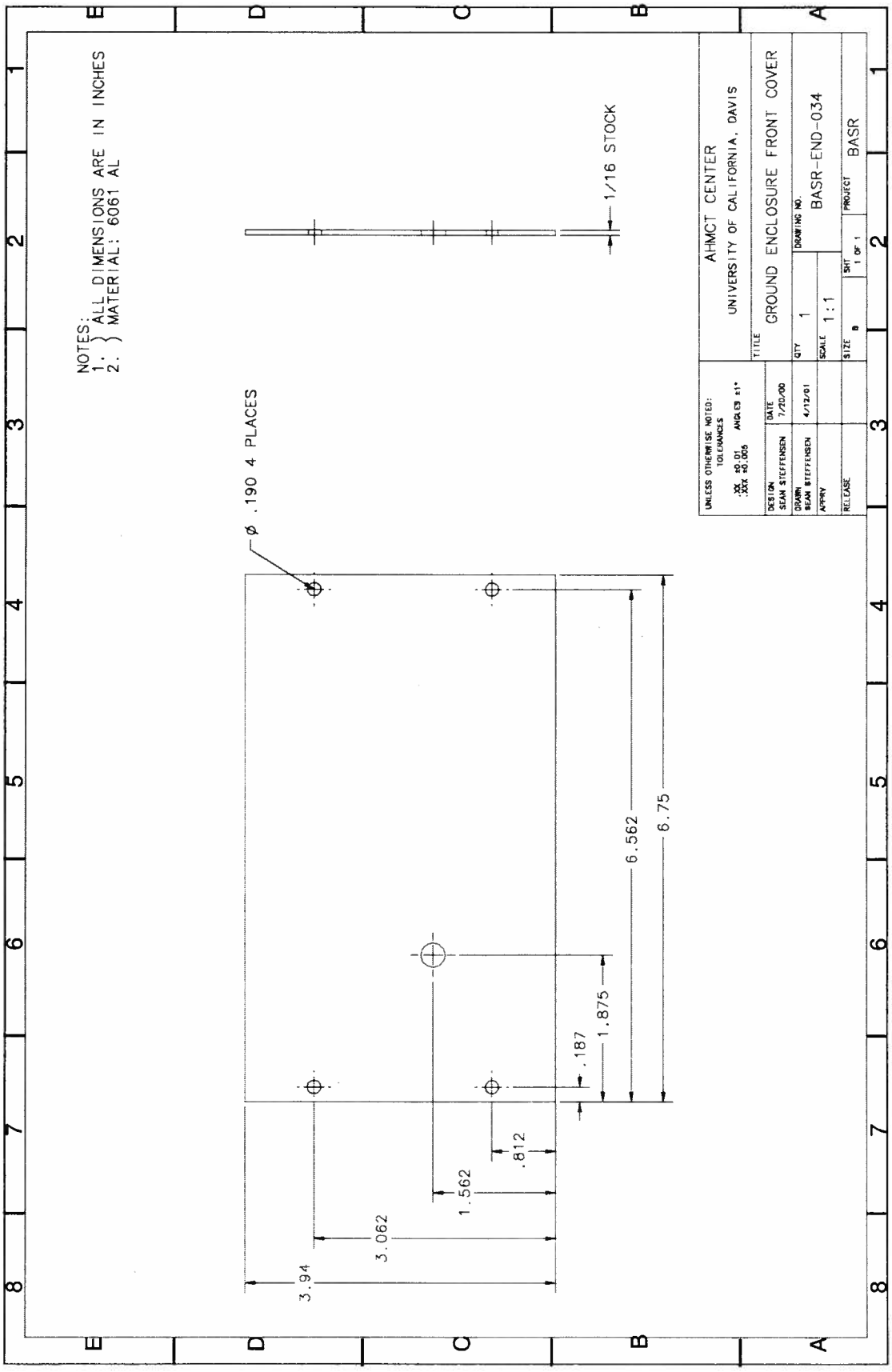

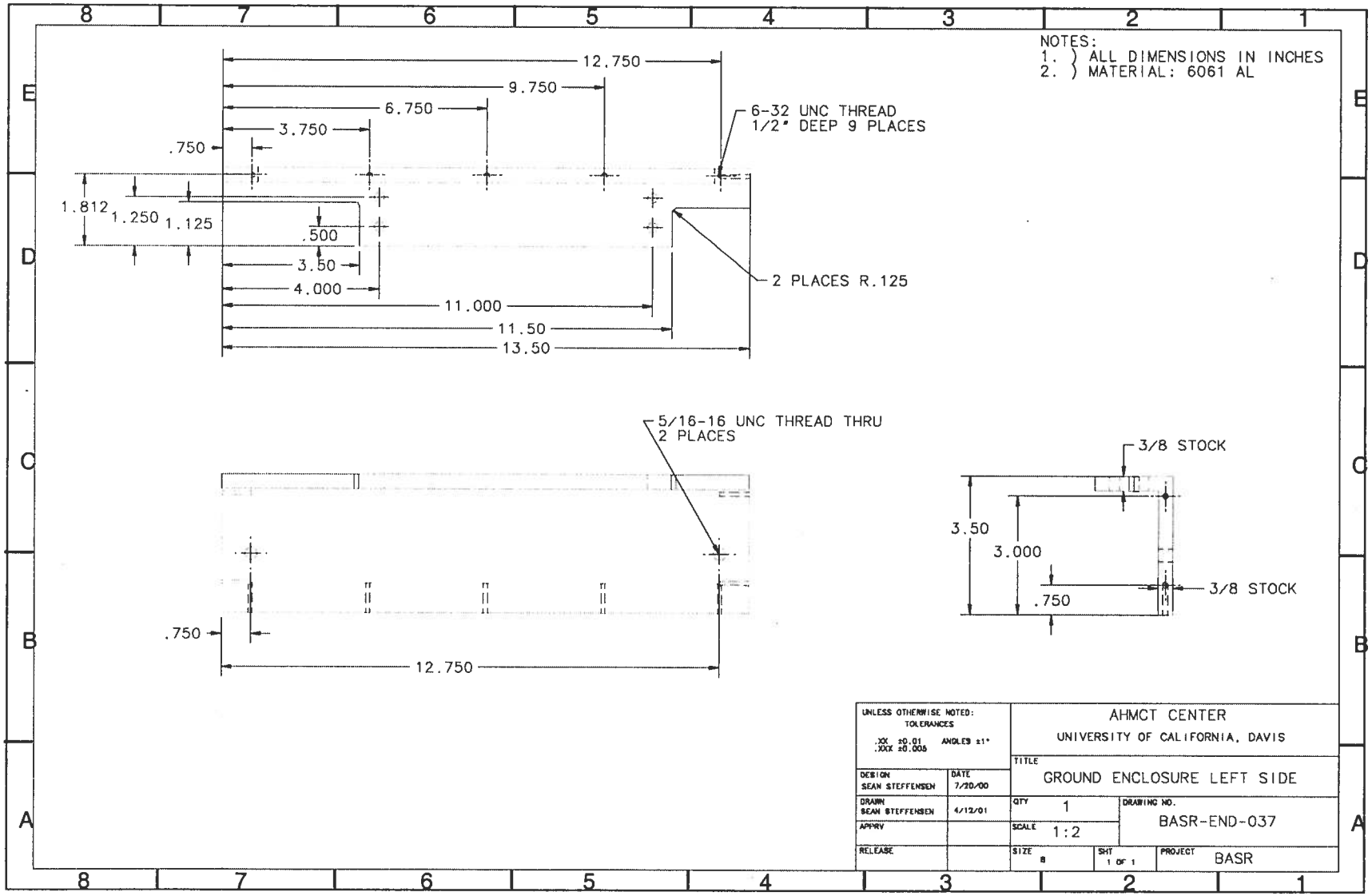

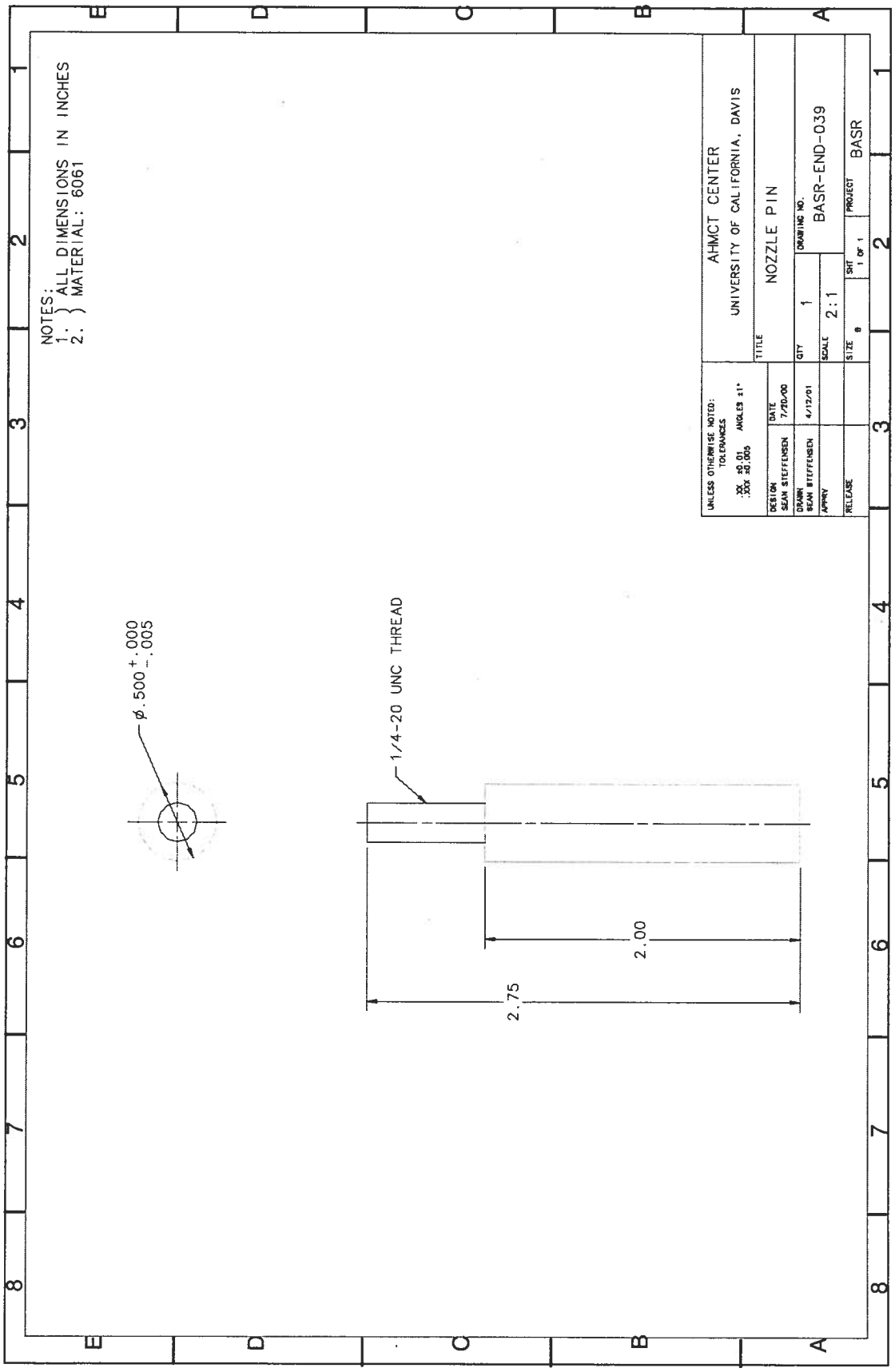

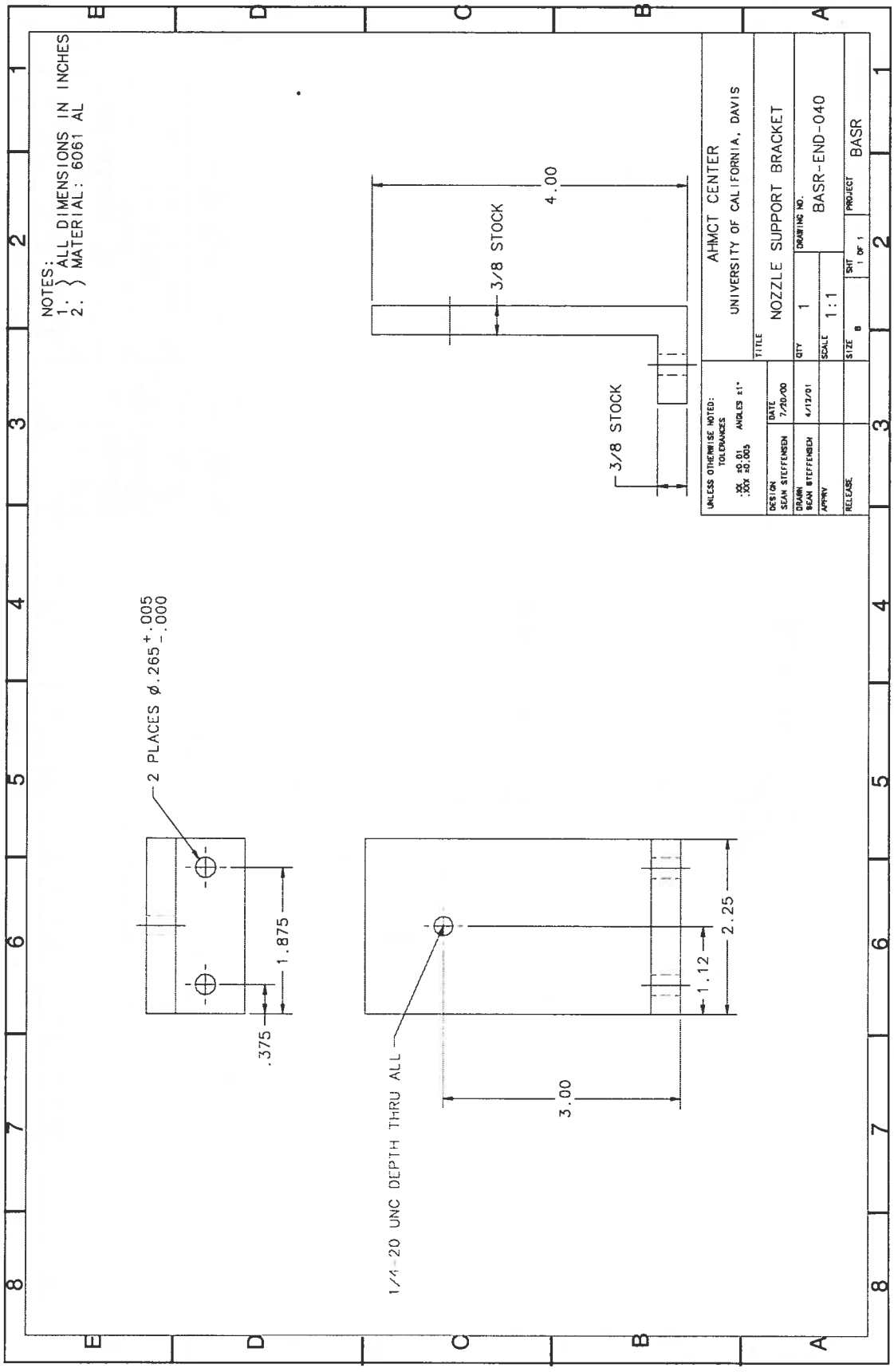

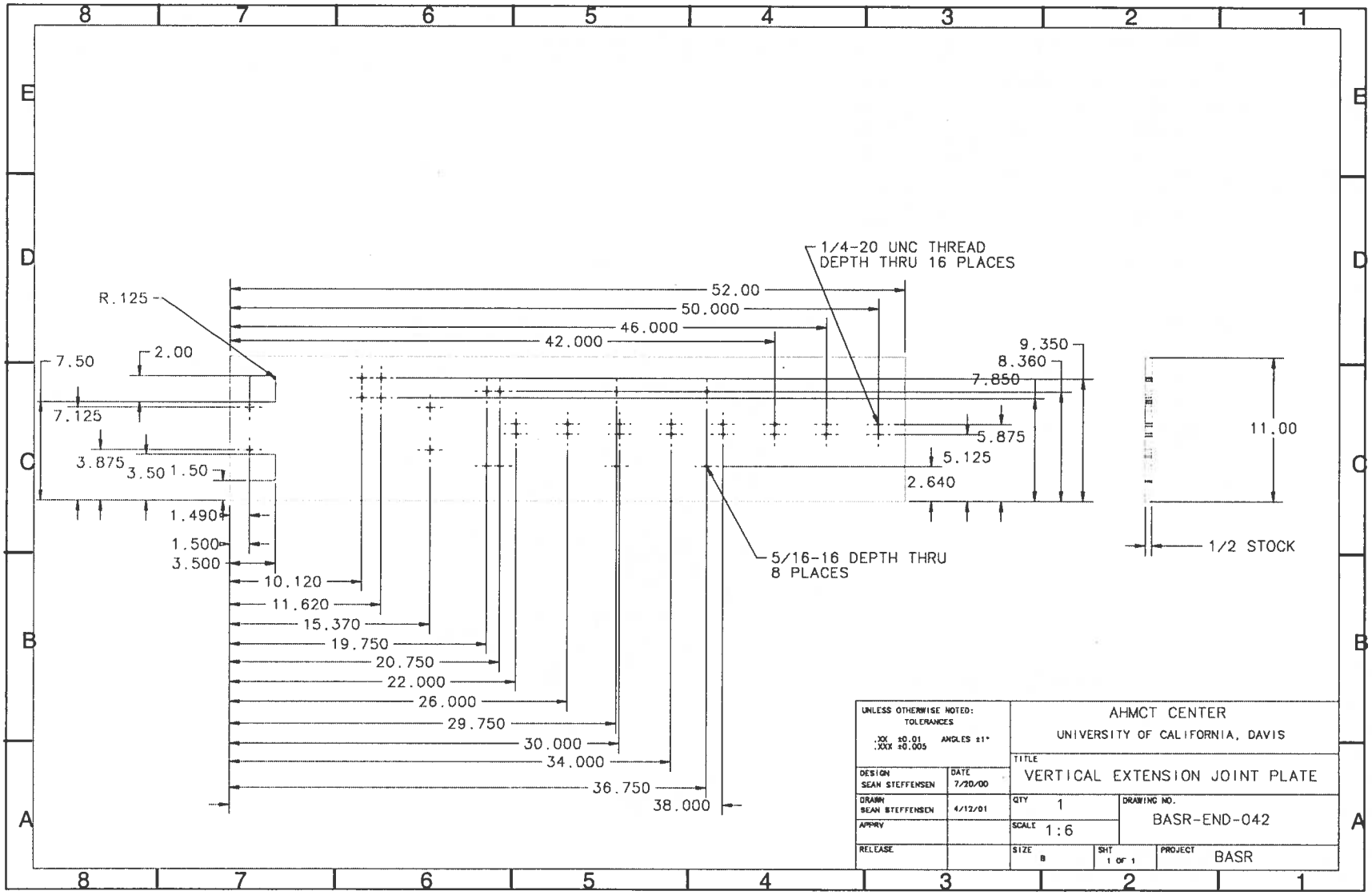

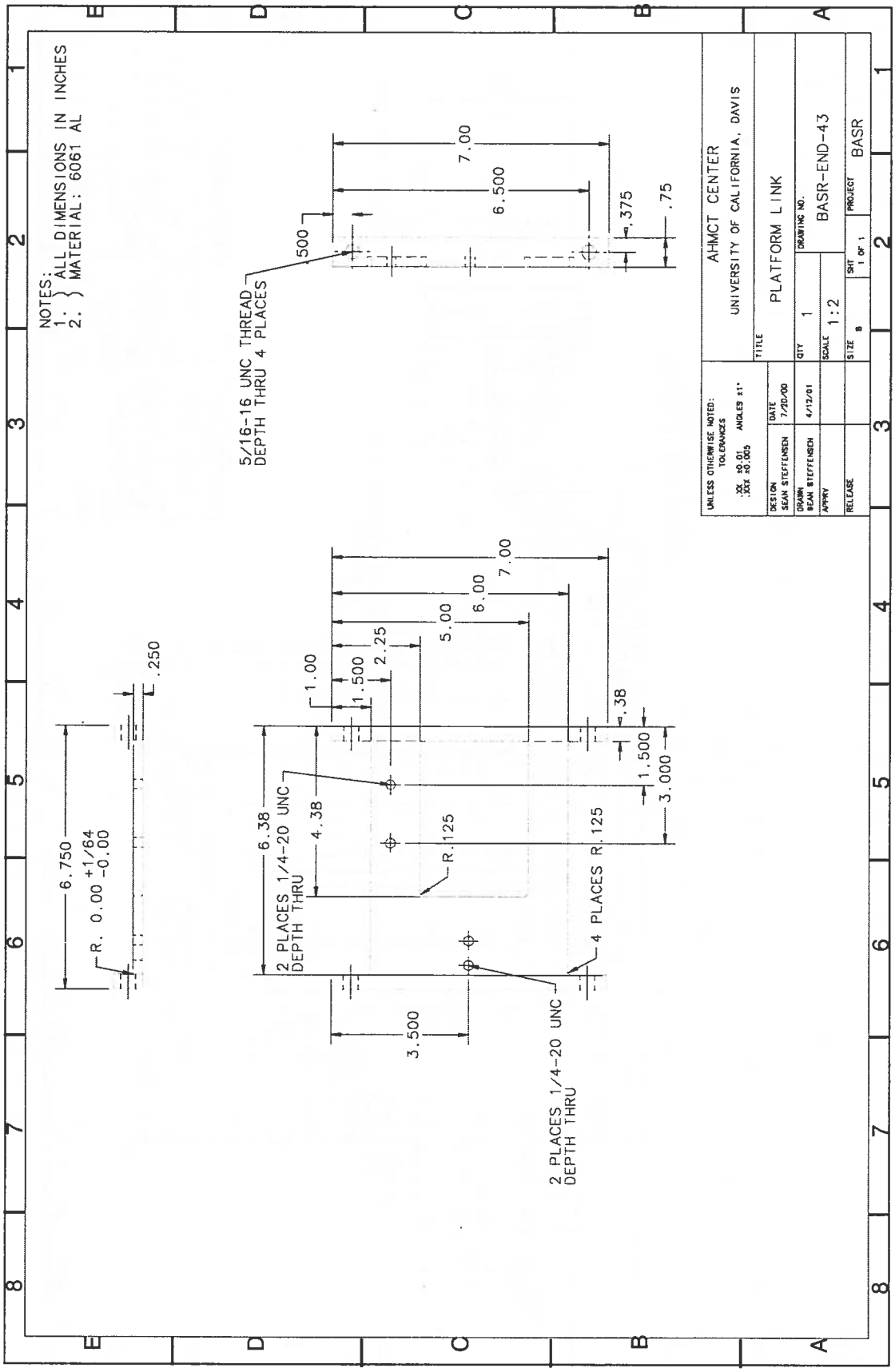

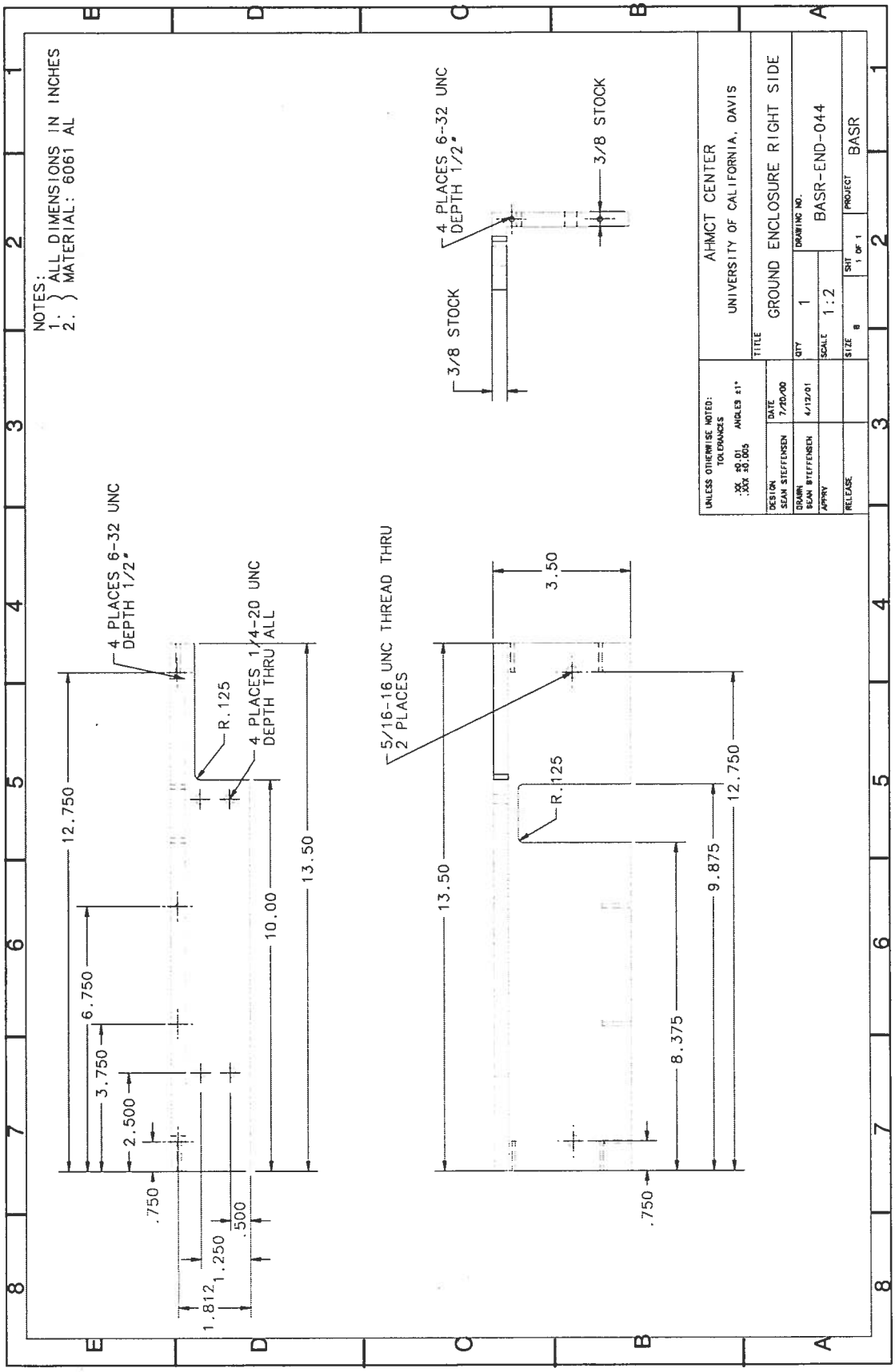

NOTES:
1.) ALL DIMENSIONS IN INCHES
2.) MATERIAL: 6061 AL

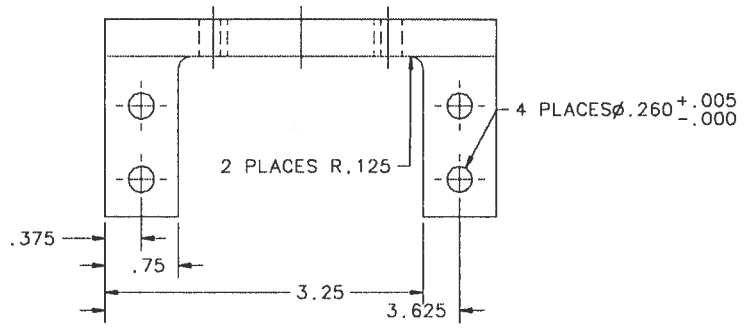

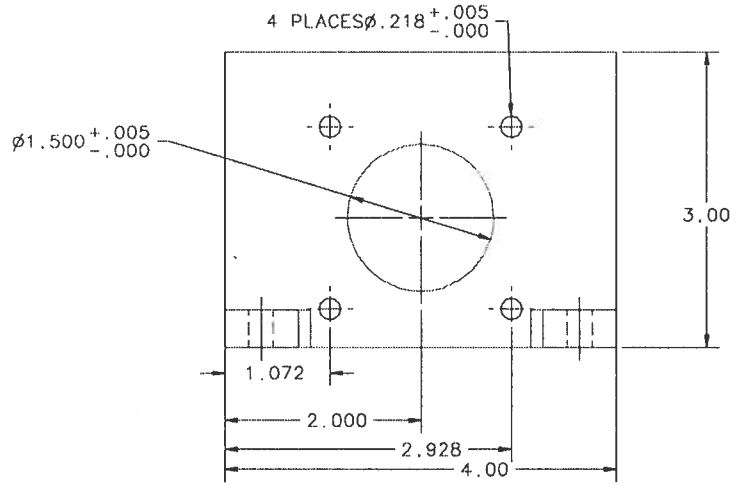

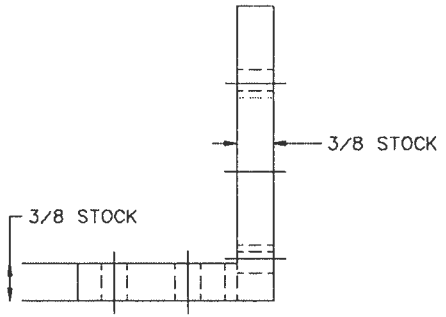

UNLESS OTHERWISE NOTED: TOLERANCES .XX ±0.01 .XXX ±0.005 ANGLES ±1°	AHMCT CENTER, UNIVERSITY OF CALIFORNIA, DAVIS
DESIGN SEAN STEFFENSEN / DATE 7/20/00	TITLE: SERVO GEAR MOTOR MOUNT
DRAWN SEAN STEFFENSEN / 4/12/01	QTY 1 / DRAWING NO. BASR-END-047
APPRV	SCALE 1:2
RELEASE	SIZE B / SHT 1 OF 1 / PROJECT BASR

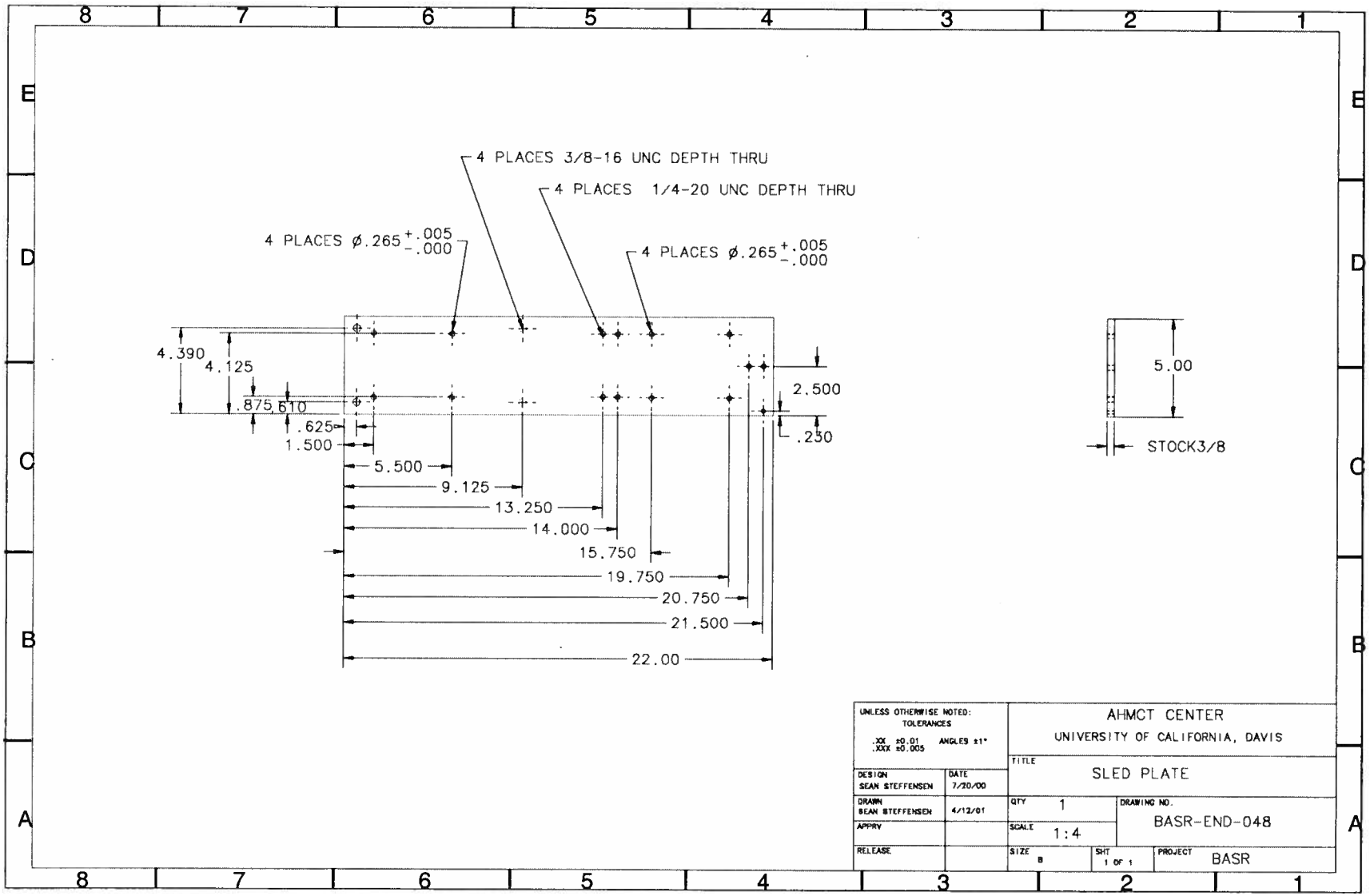

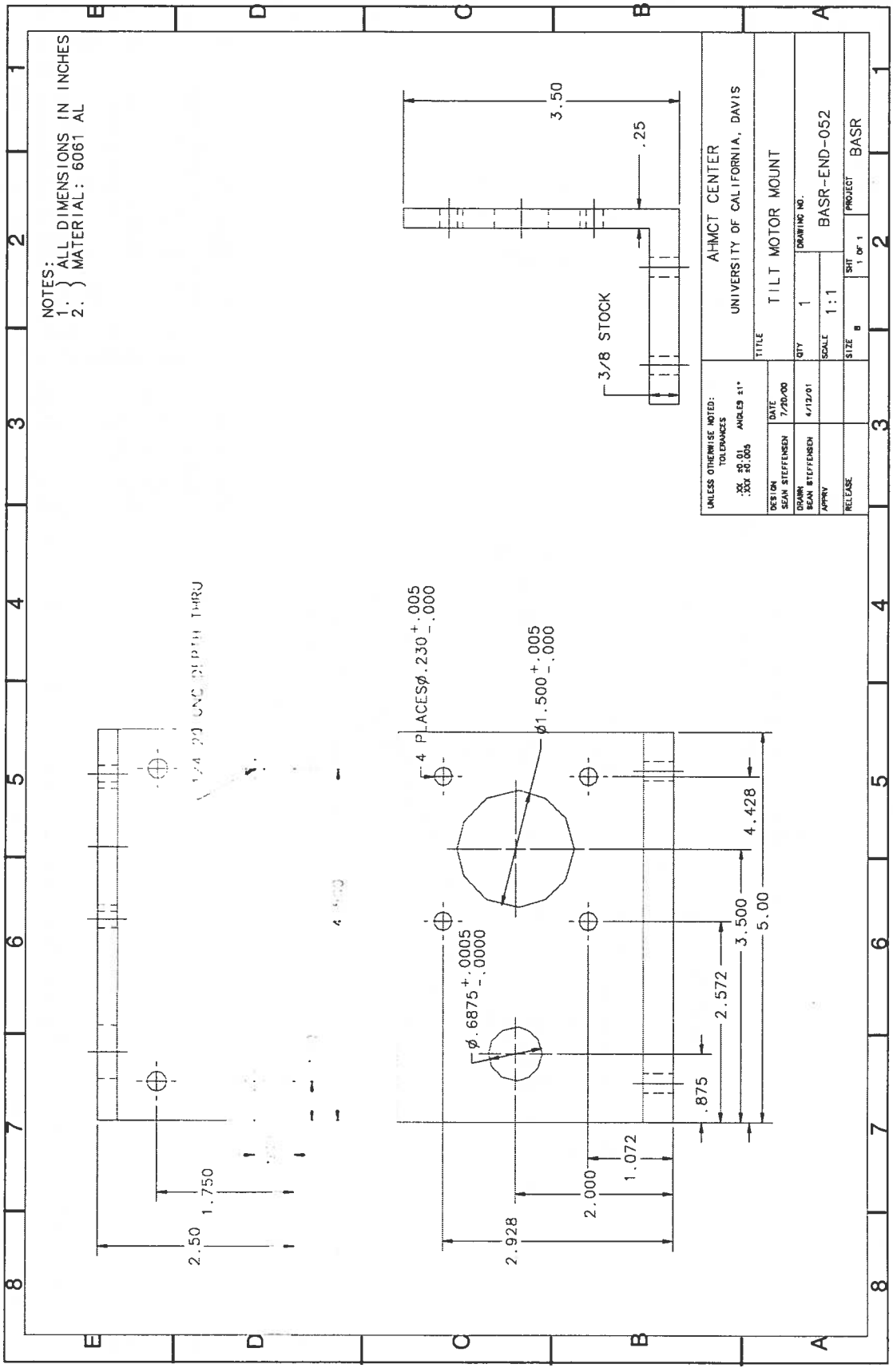

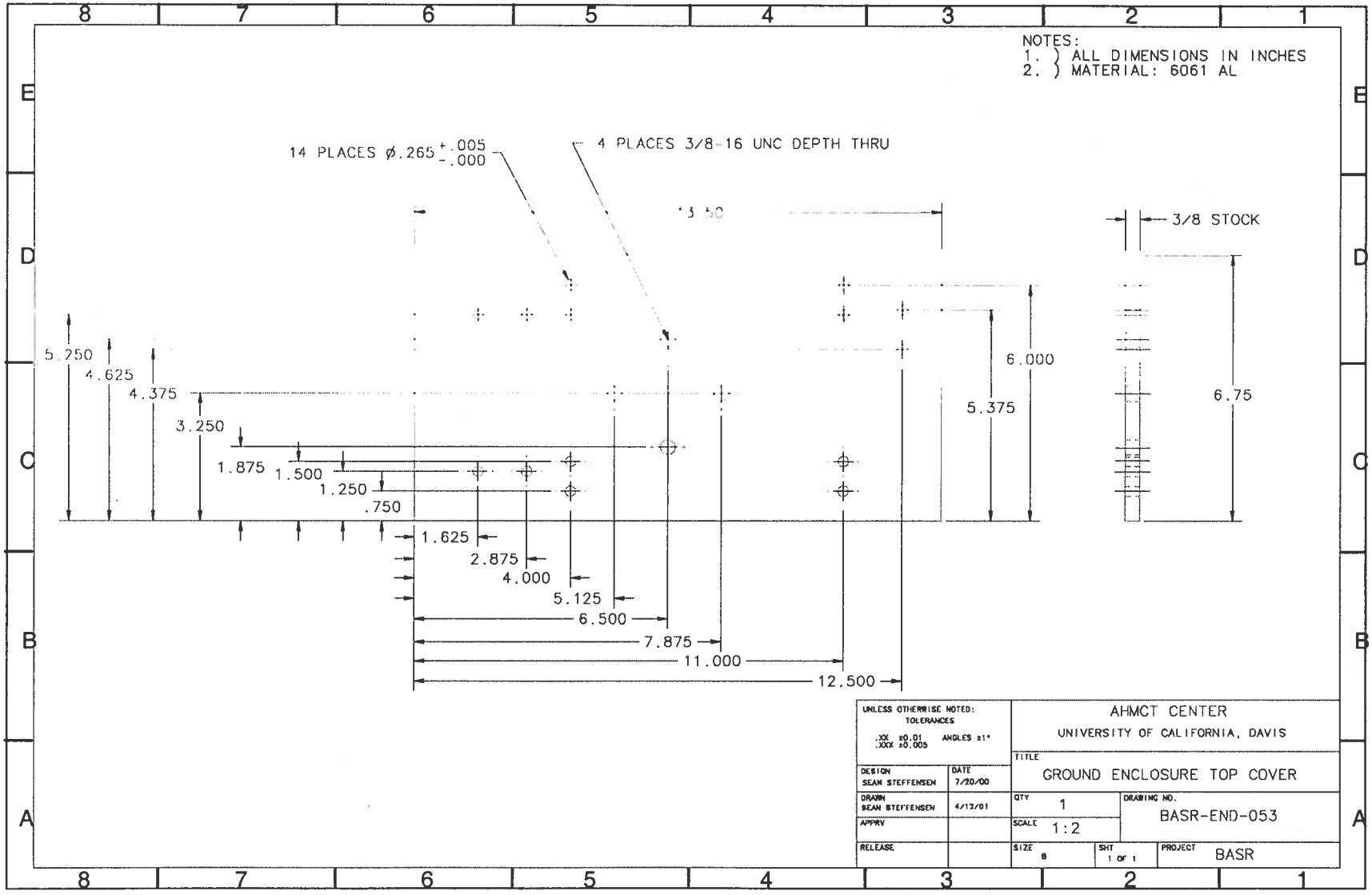

NOTES:
1.) ALL DIMENSIONS IN INCHES
2.) MATERIAL: 6061 AL

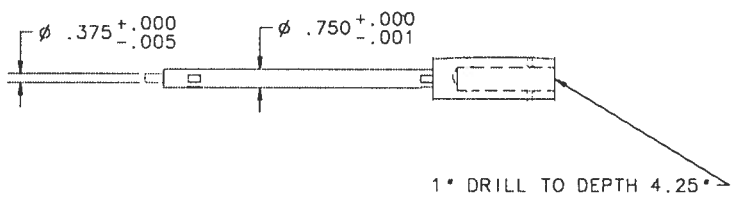

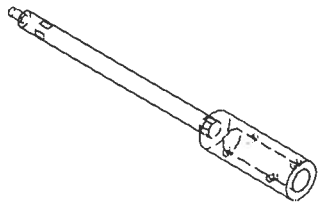

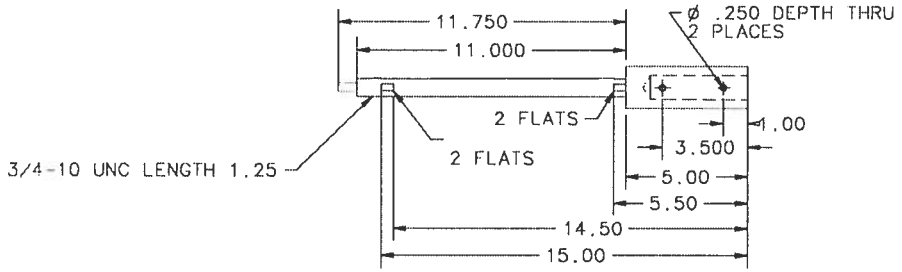

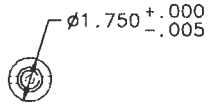

UNLESS OTHERWISE NOTED: TOLERANCES .XX ±0.01 .XXX ±0.005 ANGLES ±1°		AHMCT CENTER UNIVERSITY OF CALIFORNIA, DAVIS	
DESIGN SEAN STEFFENSEN	DATE 7/20/00	TITLE YAW ROTATION CYLINDER	
DRAWN SEAN STEFFENSEN	4/12/01	QTY 1	DRAWING NO. BASR-END-054
APPRV		SCALE 1:4	
RELEASE		SIZE B / SHT 1 OF 1	PROJECT BASR

NOTES:
1.) ALL DIMENSIONS IN INCHES UNLESS OTHERWISE SPECIFIED.
2.) MATERIAL: 6061 AL

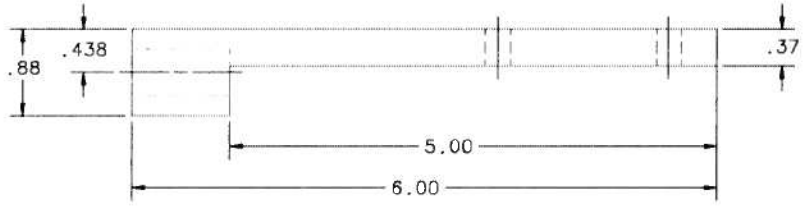

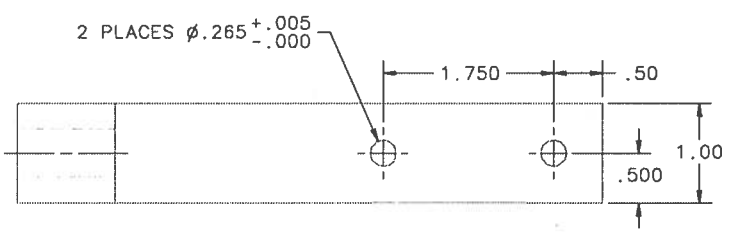

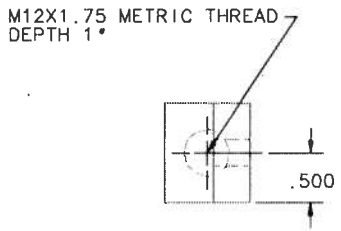

UNLESS OTHERWISE NOTED: TOLERANCES .XX ±0.01 .XXX ±0.005 ANGLES ±1°		AHMCT CENTER UNIVERSITY OF CALIFORNIA, DAVIS	
DESIGN SEAN STEFFENSEN	DATE 7/20/00	TITLE YOKE BALL END HOLDER	
DRAWN SEAN STEFFENSEN	4/12/01	QTY 1	DRAWING NO. BASR-END-055
APPRV		SCALE 1:1	
RELEASE		SIZE B	SHT 1 OF 1 PROJECT BASR